Scaled Experimental and Numerical Investigations of Auroral Radiation Phenomena

Sandra Louise M^{c}Conville

(B.Sc. Hons., MSc., The University of Strathclyde)

Department of Physics

The University of Strathclyde

Thesis Submitted for the Degree of Ph.D.

September 2009

Abstract

In the auroral regions of the Earth's magnetosphere particles are accelerated downwards into an increasing magnetic field where conservation of the magnetic moment, under the influence of magnetic compression, leads to the formation of a horseshoe distribution in velocity space. This process is correlated with the emission of Auroral Kilometric Radiation (AKR), predominantly polarised in the X-mode. Satellites have observed radiation at a frequency ~300kHz, close to the local cyclotron frequency corresponding to kilometre wavelengths. Powers of GW levels have been recorded with efficiencies of radiation emission ~1% of the precipitated electron kinetic energy. The radiation is emitted from the auroral density cavity (a region of plasma depletion spanning ~9000km at ~1.5-3R_E (Earth Radii) from the Earth's core) where the plasma density is ~1cm^{-3}, corresponding to a plasma frequency of ~9kHz. A cyclotron maser instability driven by the horseshoe distribution in electron velocity space is thought to be the generation mechanism of AKR. The scaled laboratory and numerical simulations presented in this thesis have been devised to reproduce such an instability allowing detailed study of the radiation conversion efficiency, polarisation and spectral content as a function of the electron distribution in velocity space for comparison with the satellite observations in the magnetosphere.

Frequency measurements showed operation at 4.42GHz close to cut-off for the TE_{01} mode measured by antenna scans. For two cathode flux density settings of 0.01T and 0.02T, radiation powers of ~19kW and 35kW were obtained from electron beams of 12-34A respectively corresponding to efficiencies of 2% and 1.4%. These were close to numerical predictions of 20kW and 50kW respectively. Analysis of the electron distributions in velocity space was able to explain this variation of output power with cathode flux density in terms of the population of high pitch angle electrons.

To more completely replicate the magnetospheric conditions, a Penning trap was constructed and inserted into the interaction region of the experiment to generate a background plasma. The discharge current and voltage were investigated as a function

of the magnetic flux density, neutral pressure/density and discharge gas. A plasma probe was used to measure the properties of the plasma. Measurements gave plasma frequencies ~160-300MHz which correspond to $\frac{\omega_{ce}}{\omega_p} \sim 30$ where ω_{ce}~5.21GHz, the cyclotron frequency dictated by the decreased dimensions of the interaction waveguide required by the Penning trap. An RF signal of 62.6kW was generated from an electron beam of 70kV and 60A with an efficiency of emission of 1.5%. When the plasma density was increased the amplitude of the microwave signals significantly decreased and simultaneously their statistical reliability dramatically reduced. At the maximum measured background plasma frequency of 300MHz and magnetic field strength of 0.222T, the output signal amplitude was reduced by a factor of 18 and generation of any microwave radiation was very sporadic. For an increased field of 0.229T, the microwave power decreased by a factor of 4 as the plasma frequency increased from 0-300MHz.

Table of Contents

Acknowledgements

Firstly, I would very much like to thank my supervisor, Dr. Kevin Ronald. Thank you for all your help and guidance, it was greatly appreciated! You can go on holiday now and relax !

I would also like to thank the rest of the ABP group for all their cooperation and support throughout my period of study, in particular; Mr. Dinwoodie and Mr. Barclay for their help in building and maintaining the experimental apparatus, Prof. Phelps and Dr. Cross for guidance, Dr. Speirs for his ‘humour’ in the office and help in the laboratory and for making my Ph.D study a pleasant and enjoyable time.

Writing for hours and carrying out extensive experimental work can be difficult without someone there to make light of the situation. I would therefore like to thank Karen Gillespie whom I shared an office with. Thankyou for all the wee lunches to destress, for the nights out to relax, and for being there as a great friend even when things got rough on both sides. Thankyou.

I would like to thank very much my Mum and Dad, and my two sisters Lisa and Rachel, I love you all. Lumpy, look what I did while you were travelling the world! And Rachet, I wonder if you could make physicists trendy with some new lab coat designs?! You all helped me to get through this in your own special way with cups of tea, helicopter stories or a great night out! I hope you enjoy the read!

I would like to send a big thankyou to all my friends whom I ignored for months whilst having to study! To all the boys and all the girlies, thankyou for all still being there now that I’m finished!

Lastly, but by no means least, I would like to thank my boyfriend Chris. You have had to endure my mood swings and have stayed up to make sure I was ok on the nights I had to work late. You gave me the boost I needed to get everything finished. I love you and thank you, x.

“I am an Absolute Instability”

- S.L.M^{c}Conville

Turning over finished boiled eggs to smash all over again!

“The Spring has Sprung,
The Grass has Ris,
I wonder where the Birdies Is?
The Birdies on the Wing...well!...I thought the Wing was on the Bird!”

- Grandad Eaton

Bending down to pick up your own big toe!

“Hey up Kiddo,
Vim made a Rat trap bigger than a Cat trap,
cannibal cannibal cease boom raa !”

- Grandad M^{c}Conville

List of Figures

List of Tables

Nomenclature

A	area of cathode
A_0	$1.20 \times 10^{6} Am^{-2}deg^{-2}$
a,b	waveguide dimensions
a_e	emitting area
a_r	radius of circular waveguide
α	pitch factor
$\underline{B}$	magnetic flux density
$\underline{B}_z$	magnetic flux along the z axis
β	propagation constant; $\beta^2 = k^2 - k_c^2$
β_f	field enhancement factor
c	speed of light, $3 \times 10^{8} ms^{-2}$
$\underline{D}$	electric flux density (C/m^2)
d	distance between electrodes
Δd	thickness of dielectric inclusion
∇_t^2	transverse gradient operator
$\underline{E}$	electric field strength
E	energy
E_c	specific energy per unit mass
E_F	Fermi energy
e	electron charge, 1.602×10^{-19} C
e_{sp}	charge of specific species, electron/ion
ε	cold plasma dielectric tensor
ε_0	permittivity of free space, $8.854 \times 10^{-12} F/m$
ε_r	relative permittivity
$\underline{F}$	Lorentz force
f_{co}	cut-off frequency
f_{cs}	collision frequency of species
f_K	Klimontovich distribution function
ϕ_B	height of potential barrier
ϕ_m	work function of metal

$\Delta\phi$	change in work function due to applied electric field
g_p	plasma parameter
γ	relativistic factor (Lorentz-Fitzgerald factor)
γ_{sp}	ratio of specific heats; C_p/C_v
$\underline{H}$	magnetic field strength, A/m
h	Planck's constant, 6.626×10^{-34} Js
η	charge to mass ratio, e/m
I_A	Alfven current
I_0	beam current ($I_0=eN\beta_c$)
I	current
$I(v,\theta)$	differential scattering cross section where in this case; v is relative speed of scattered particle compared with target, θ is angle through which particle is scattered by collision
i	current associated with the electron orbit
$\underline{J}$	current density (A/m^2)
J_0	Richardson-Dushman current density
j	space charge density
k_B	Boltzman constant, $1.38 \times 10^{-23} JK^{-1}$
$\underline{k}$	wavenumber
$k_\perp$	perpendicular wave vector (associated with the required transverse field variations imposed by boundary conditions)
k_z	axial wave vector
κ	resistivity
λ	wavelength
λ_D	Debye length
λ_{mfp}	mean free path
m_0	rest mass of electron, 9.11×10^{-31}kg
m,n	waveguide mode numbers
m_i,m_e	mass of ions, electrons
m_{sp}	mass of specific species, electron or ion

μ_0	permeability of free space, 4π x 10^{-7} H/m
μ_m	vector magnetic dipole moment of an electron orbit
μ'	(first root of $J_0'(x)$), Bessel root for specific mode of radiation
n_0	neutral gas
$\underline{n}$	unit vector normal to cathode surface
n	number density
n_c,n_a	number density of electrons at the cathode, anode
n_n	number density of stationary targets
n_i,n_e	number density of ions, electrons
$n\underline{v}_{ave}$	particle flux density
N	total number of electrons per unit length in the axial direction
P	perveance
P	pressure
θ	pitch angle
θ_m	pitch angle of the orbit in the weak field region
θ_{res}	resonant angle
R_E	Earth radii, ~6400km
R_m	mirror ratio
r	radius of electron orbit
r_e	electron radius
r_L	Larmor radius
ρ	charge density (C/m^3)
ρ_m	mass density
S	harmonic number
σ	conductivity tensor
$\sigma_{sc,s}$	collision cross section of the species
σ_{sc}	total collision cross section
t	time
t_{col}	collapse time of acceleration potential
t_d	time for vaporisation to occur

τ_c	collision time
T	temperature
$<U>$	mean speed of colliding particles
$<U_s>$	mean speed of mobile species
V	accelerating voltage
V_{pr}	probe voltage
V_s	potential difference across pre-sheath
$\underline{v}$	electron velocity, $\underline{v} = (v_\perp^2 + v_z^2)^{\frac{1}{2}}$
v_A	Alfven velocity
v_c,v_a	drift velocity of electrons at the cathode, anode
v_{max}	maximum velocity
v_{pl}	plasma expansion velocity
v_p	phase velocity
v_g	group velocity
$v_\perp$	magnitude of transverse velocity component
v_z	axial velocity component
ω	angular frequency
ω_{ce}	angular electron cyclotron frequency
ω_{co}	angular cut-off frequency
ω_D	angular Doppler shifted frequency
ω_{pi},ω_{pe}	angular ion, electron plasma frequency
ω_w	angular frequency of the wave

Chapter 1 : Introduction & Background

Chapter 1 : Introduction & Background

1.1 Background on Auroral Kilometric Radiation

Auroral Kilometric Radiation, (AKR), is found to occur in the polar regions of the Earth's magnetosphere and has been observed by various satellites since ~1974. AKR can be described as intense narrow band radio emission which occurs in short duration bursts at frequencies of around 50-800kHz, [Mutel et al 2004]. The radiation frequency observed by satellite measurements at any given altitude extends down to the local electron cyclotron frequency and has a peak in emission intensity at around 300kHz. The wave propagation is in the X mode (polarised and propagating perpendicular to the static magnetic field) and has been shown to have a peak power ~10^9W, and this corresponds to an estimated radiation efficiency ~1% of the precipitated electron kinetic energy [Pritchett & Strangeway 1985, Gurnett 1974]. For a naturally occurring process this efficiency is unusually high which implies that a collective non-linear process is taking place and has therefore driven significant research in this field to explain these findings, [Burinskaya & Rauch 2007, Bingham et al 1999, 2004, Vorgul et al 2005]. In these polar regions of the magnetosphere there exists an area of plasma depletion, the auroral density cavity (a region spanning ~9000km where the plasma frequency is less than the cyclotron frequency, $\frac{\omega_{ce}}{\omega_p} \sim 30$), in which particles precipitating in the Earth's magnetosphere are accelerated into the increasing magnetic field at the Earth's poles. This region is situated ~3200km above the Earth's surface, Figure 1.1. In the absence of collisions and given that the field increases slowly compared to the electron oscillation period, the adiabatic conservation of the magnetic moment comes into effect, increasing the pitch angle, $\theta = \text{atan}\left(\frac{v_\perp}{v_z}\right)$, of each electron. Since the electrons enter the Earth's magnetic dipole with a spread in velocity, those electrons with small components of velocity perpendicular to the magnetic field lines undergo an increase in their rotational velocity component on their descent towards the Earth's atmosphere. By this process the initially largely rectilinear beam of electrons is transformed into a horseshoe velocity distribution function where in the inner boundary, $\frac{\partial f}{\partial v_\perp} > 0$. The horseshoe distribution has been shown to be unstable to a cyclotron resonance maser type

interaction, [Bingham and Cairns 2000, 2002], and it has been proposed that this may be the mechanism required to explain the production of AKR in these regions of space, [Benson 1985, Delory et al 1998, Ergun et al 1998, 2000].

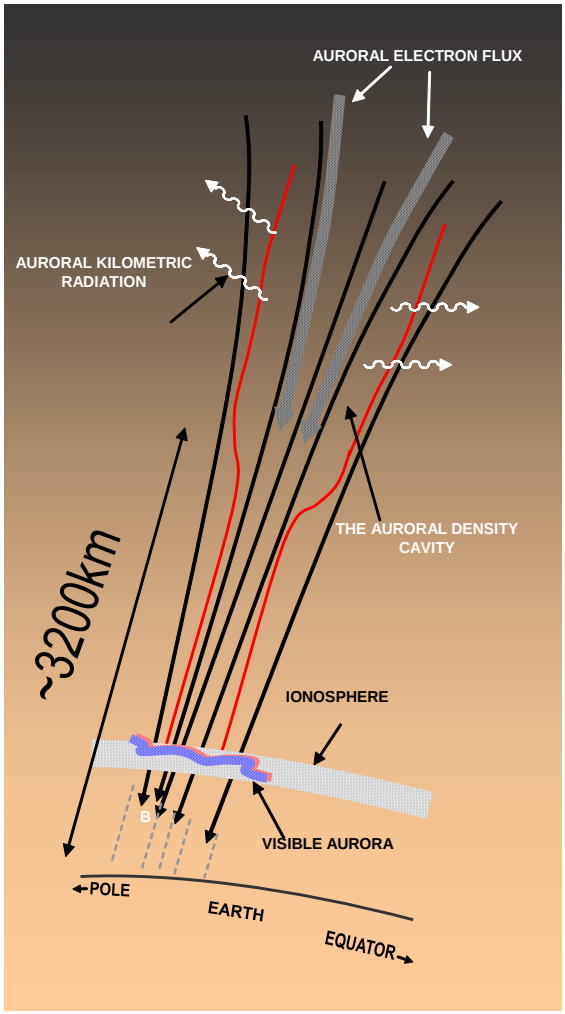

Figure 1.1: Illustration of the terrestrial auroral process

The Earth is not the only planet in the solar system to produce non-thermal planetary radio emissions due to cyclotron maser radiation. There has been significant interest around other magnetized planets showing signs of similar dynamics in polar regions - Jupiter, Saturn, Uranus and Neptune - as well as one of Jupiter's moons, Io, [Ergun et al 2000, Pritchett et al 2002, Zarka et al 2001]. Studies have also suggested that the cyclotron maser instability may be responsible for microwave emission (~GHz

frequencies) from stellar objects such as UV Ceti, [Bingham et al 2001] and CU Virginis [Kellett et al 2007].

1.2 Satellite Observations and Measurements

Various satellites have been constructed with progressively refined instrumentation over the years allowing data to be collected about the AKR region and the radio emissions of the Earth (closest source for research). Different satellites have provided different viewpoints of the source region, i.e. some cross directly within the source region whilst others pass round about taking measurements from a distance. As satellite technology has developed, the precision and sophistication of measurements has increased.

1.2.1 Satellite Timeline

1965-1974 - **Electron-2** satellite, [Benediktov et al 1965] first recorded AKR as intense non-thermal natural emission from the Earth with powers of 10^7-10^9W [Gurnett 1974].

1970 - First widely documented observation of AKR was reported as “High-pass noise” in VLF radio data collected by the **OGO-1** satellite, [Dunckel et al 1970].

1974-1985 - The extent of the auroral density cavity (the AKR source region) was first mapped by Calvert [Calvert 1981]. Density measurements were extrapolated from wave data collected by the University of Iowa “**Hawkeye**” satellite. Data from **Hawkeye** showed the density of plasma within the auroral density cavity to be less than $1cm^{-3}$ from 1.8-3R_E, (Earth radii ~ 6400km), [Calvert 1981]. This value of electron density corresponds to a plasma frequency of ~9kHz, [Gurnett 1974, Gurnett & Green 1978]. **Hawkeye** observed AKR signals whilst in Earth orbit situated at 20R_E above the northern hemisphere [Benson & Calvert 1979] using a long dipole antenna to take electric field measurements. Use of ray tracing calculations demonstrated the dominance of the X-mode over the O-mode in AKR, [Green et al

1977]. Evidence from **Voyager** also favoured the extraordinary wave mode and was confirmed by **ISIS 1** observations at the source. **ISIS 1** [Benson and Calvert, 1979], could simultaneously receive AKR signals and reveal the plasma density by sounder echoes and resonances. It used an ionospheric sounder to sweep between 100kHz and 2MHz at around 3500km, [Benson 1985]. The satellite was positioned in the source region and observed that the plasma in the AKR source region is quite low density and suggests that the ratio of ω_p to ω_c has to be < 0.2 for the AKR generation, [Calvert 1982]. **ISIS-1** and **Hawkeye** complemented each other by making observations at the lower and higher altitude portions of the AKR source region, respectively.

1978-1982 - R-X mode polarisation first indicated in data collected by the **Voyager 1** and **2** probes [Kaiser et al 1978]. As the two **Voyager** spacecraft were heading to outer planets they reported the dominance of the X-mode over the O-mode by direct polarization measurements. This method was also used by the satellite DE-1 which confirmed the X-mode dominance, [Shawhan & Gurnett 1982].

1978-1993 - The Swedish satellite, **Viking**, conducted a very successful magnetospheric research mission, carrying experimental equipment to measure electric fields, magnetic fields, charged particles, waves, and auroral images and was the first satellite to cross the central part of the AKR source region at ~$1R_E$ above the auroral zone. Electron distributions within the auroral density cavity were measured and AKR emission spectra recorded. The observations that were taken by **Viking** substantially increased knowledge about AKR, [Roux et al, 1993]. Observed data led to the suggestion that the energy source for AKR is a population of downward accelerated electrons with a large perpendicular velocity produced by a combination of parallel accelerating electric field and converging magnetic field lines and not a loss cone as had been previously postulated. Both ring and horseshoe distribution functions have been observed by this satellite, [Perraut et al 1990]. Plasma densities inside the AKR source region were measured to be of the order $1cm^{-3}$, typically a factor of 5-10 below that of surrounding regions, coinciding with data from **Hawkeye**. R-X mode waves are a dominant feature in **Viking** RF observations but are

usually accompanied by L-O mode waves at a factor of 10-100 lower amplitudes [Gurnett and Green 1978, Kaiser et al 1978, Shawhan and Gurnett 1982, Benson 1985, Mellott et al 1986].

1998-1999 – The **FAST** (**F**ast **A**uroral **S**napsho**T**) Explorer satellite mission observed charged particle distributions and wave data from the AKR source region which, compared to previous measurements, were greatly improved in frequency and time resolution, [Delory et al 1998, Pritchett et al 1999]. It crossed Earth's auroral zones collecting high resolution data. It was designed to observe and measure the plasma physics of the aurora at both of the poles of the Earth and with its orbit taking it into the charged particle environment of the aurora it was able to observe and measure properties such as electric and magnetic fields, plasma waves, thermal plasma density and temperature [Strangeway et al 1998]. To measure the AKR spectra it used a plasma wave tracker instrument. Electron distribution contour plots were obtained in this source region [Delory et al 1998]. Results from previous satellite missions by **Freja** and **Viking** informed the design of the enhanced instruments onboard **FAST**. The instruments allow for measurement of wavelength, phase velocity and AC and DC magnetic fields, [Carlson et al 1998].

2000 – The **Cluster 2** mission consists of four identical satellites which fly in formation to study the interaction between the solar wind and the Earth's magnetosphere in three dimensions. Charged particle and electromagnetic field measurements are recorded from outside the AKR source region. Each of the four satellites carries a suite of eleven instruments that measure electric and magnetic fields, electrons, protons and ions and plasma waves. It can measure the time variation of transient particle flows in the auroral zone. At the time of writing this thesis, the **Cluster** orbit is now taking the four satellites into the regions of the auroral density cavity and further enhancement of the collected data may soon be available.

1.3 Original Theories of AKR

Due to correlation between the electron cyclotron frequency and the radio frequency, it was postulated quite early that the mechanism behind AKR is that of the cyclotron maser instability [Chu 2004, Sprangle & Drobot 1977, Twiss 1985]. Given a suitable magnetic field configuration and exploiting the conservation of the magnetic moment, an electron population forms with a high rotational component of kinetic energy. There comes a point, as the magnetic flux density is continually increased, where in order to conserve its magnetic moment all of an individual electrons kinetic energy must be transformed into rotational energy. This causes the electrons descent towards the Earth's surface to cease and starts to reverse its journey back up along the magnetic field lines due to mirroring. The component of the electrons which does not mirror before reaching the Earth's atmosphere is said to be in the 'loss cone'. In a theory proposed back in 1979 by Wu and Lee, [and again by Melrose and Dulk 1982], AKR was caused by an instability in the positive gradient in the $v_\perp$ electron density distribution profile of the magnetically mirrored auroral electron flux, [Wu & Lee 1979, Ungstrup et al 1990], the 'loss cone model'. This process directly generates the X mode. Later a study of the observations and data collected by Viking suggested the need for an alternative theory. It was proposed that whilst the free energy for the AKR wave growth came from electron distributions which had $\frac{\partial f}{\partial v_\perp} > 0$, that the loss cone model was insufficient to explain the observed AKR power levels, [Louarn et al 1990]. The loss cone theory has therefore been challenged by others, proposing that the instability is indeed driven by a positive gradient in the $v_\perp$ profile but of the earthward accelerated auroral electron flux. Bingham and Cairns proposed that the X mode growth was driven by the horseshoe shaped velocity distribution in the earthward accelerated auroral electron flux, and this theory appears to offer a better explanation for the frequencies and efficiencies of AKR that are observed. [Vorgul et al 2004, Bingham and Cairns 2000, 2002]

1.4 Group History at Strathclyde

The Atoms Beams and Plasma (ABP) group at Strathclyde is involved in diverse research projects in the field of beam-wave interactions and free electron physics,

including experimental programmes, numerical simulations and cathode & beam formation physics. These include the AKR (auroral kilometric radiation simulation) experiment, gyrotron amplifier and oscillator projects and 2D Bragg free electron maser experiments. The research carried out in the group focuses on two radiation FEM processes; Cherenkov and bremsstrahlung. The work conducted at Strathclyde is of interest to applications in industry due to the high efficiency of electromagnetic radiation that can be produced. Megawatt level radiation at frequencies of 1-100GHz has been achieved by investigations of the CRM instability, FEL's, gyrotrons [Cross et al 1995] and dielectric [Yin et al 1999] & corrugation loaded waveguides. In 1996, the group demonstrated a saturated FEL oscillator [Ginzburg et al 1996] leading to further research into the physics of high gain FEL amplifiers. The CARM (Cyclotron Auto Resonance Maser) instability experiments [Cooke et al 1996] were the first observations of the CARM at the second harmonic and the group were also the first to document results on a new type of broadband gyrotron amplifier [Denisov et al 1998, Bratman et al 2000] with high output power and efficiency.

In the field of cathode and beam formation physics, Strathclyde were the first to document the use of both cold field enhanced emission [Garven et al 1996] and pseudospark discharges [Yin et al 1999], in high power microwave devices. The emission of electrons from velvet surfaces in Pierce configurations [Cooke et al 1996, Denisov et al 1998] and explosive electron emission in coaxial diodes [Ronald 1996, Ronald et al 1998], was also investigated.

The group has collaborated with different companies and universities on some of the aforementioned work ranging from the researchers in the mathematics department at the University of St. Andrews to researchers at the Institute of Applied Physics in Nizhny Novgorod, Russia, and staff members of e2v and TMD technologies. It is due to the strong background in electron beam and especially cyclotron instabilities that led onto the group becoming involved in the laboratory simulation of magnetosphere cyclotron radiation.

1.5 Initial AKR Work at Strathclyde

The ABP group at Strathclyde became involved in the study of AKR from an experimental point of view in collaboration with the University of St. Andrews (undertaking the theoretical investigation) and with scientists from the Rutherford Appleton laboratory who were able to supply astrophysical data. It was realised that satellite data provided an essential benchmark but that to be able to replicate the 'system' of AKR emission in a controlled laboratory experiment to provide data to compare to the natural phenomena, would substantially enhance the understanding of the mechanisms.

A laboratory experiment was constructed to reproduce major features of the natural phenomena. The experiment had to be scaled to laboratory dimensions as kilometre band radiation was obviously too large to accommodate. Therefore the length of the experimental apparatus in total was shortened in scale to ~1-2m from the ~9000km of the interaction region in the magnetosphere whilst the resonant frequency was scaled to the GHz range by increasing the magnetic flux density corresponding to centimetre wavelengths, as opposed to the 10's-100's kHz frequencies of the natural process. The apparatus offered complete control of the parameters controlling the instability which meant that direct comparisons of the electron distribution function and instability efficiency could be performed. This led to accurate measurements of powers and frequencies as functions of beam parameters and compression ratios which could then be compared to the theoretical predictions and astrophysical data.

Initial work focused on the characterisation of the electron beam as it traversed through the system whilst experiencing an increasing magnetic field. Due to the specifications of the resonance and operating mode, the magnetic field plateau in this case was 0.48T, resonant frequency 11.7GHz and coupling to the TE_{03} mode. At this resonance the apparatus is highly overmoded with $\lambda <<$ than the smallest experimental dimension, this made mode differentiation analysis more difficult than say for a single mode resonance. The reason for persevering at these settings was the relatively close

representation it gave of the magnetospheric conditions. [Speirs et al 2005, Cairns et al 2005]

1.6 Present AKR Research Program

The present work has focused on more detailed beam characterisation to enhance the understanding of the impact of the electron distribution on the microwave radiation. One of the key aims of this work is to investigate whether there is enough free energy in the AKR emission process to account for the efficiency of radiation emission ~1-2%, as is measured in the magnetosphere. This work was compared with that previously documented by Speirs [Speirs et al 2005, 2008] in the initial work. The present research started by lowering the resonance frequency to 4.42GHz enabled by coupling to the TE_{01} mode. This was achieved whilst operating with a plateau magnetic field of 0.18T. The advantage of this modification was that it gave an excess of 'spare' magnetic field with which to further map the electron distribution.

Results demonstrating and characterising the excitation of the TE_{01} mode at 4.42GHz, will be presented. This will include electron beam characterisation as it traverses through the interaction waveguide, measurements of the radiation mode structure, polarisation and propagation properties, radiation power and spectral content. These results are discussed and analysed in light of the mapping of the distribution function in velocity phase space. Detailed comparison of the impact of the electron number density in velocity space on the conversion efficiency from electron kinetic to wave field energy is presented.

To aid in the design of the experiment and enhance insight into the internal dynamics, a computer PiC programme KARAT was exploited to enable numerical simulations of the experiment. This meant that as well as comparing results in the laboratory to theoretical predictions and geophysical measurements, a comparison to numerical simulation could also be undertaken.

Further experiments were carried out to improve comparisons to the magnetospheric conditions by introducing a background plasma. This was the second key objective of this investigation; to study the effect that the addition of a background plasma had on the generated microwave radiation. This was achieved by design and construction of a 'Penning type' trap which was inserted into the interaction region of the experiment. IV characteristics of the discharge were investigated as a function of the background gas type and pressure to find stable operating regimes. With the insertion of a plasma probe the plasma characteristics were measured including electron temperature, T_e, electron number density, n_e and therefore the electron plasma frequency, ω_{pe}. The plasma frequency could be controlled by variation of the discharge current (0.8mA-2.5mA) and this allowed the impact of the plasma density (in the range $3.2x10^{14}m^{-3}$ to$1.1x10^{15}m^{-3}$) on the radiation emission to be investigated, in the limit $\frac{\omega_{ce}}{\omega_p} \sim 10-30$. Results investigating the impact of the plasma frequency on the radiation emitted for resonance with the TE_{01} mode at 5.21GHz will be presented, detailing the optimum magnetic field setting, the statistical nature of the generation of microwaves and the efficiency of the radiation emission.

Chapter 2 : Theory

Chapter 2 : Theory

2.1 Introduction

This chapter will describe fundamental physical processes important in understanding the auroral radiation emission behaviour and the experiment which was created to reproduce this effect. The sections that make up this chapter shall discuss plasma and electron beam properties, plasma probes, the CRM instability, electron emission processes and microwave waveguide and resonator theory.

2.2 CRM Instability

The CRM [Twiss 1985, Chu 1978, 2004, Chu & Lin 1988] (Cyclotron Resonance Maser) instability arises between an electron beam gyrating in an external magnetic field and an electromagnetic wave. It is the most widely applied mechanism for cyclotron energy extraction, used in the gyrotron [Nusinovich 2004, Petelin 1993, 1999, Flyagin et al 1977, Granatstein & Alexeff 1987], and requires that the electron beam gyro-frequency be slightly lower than that of the microwave frequency by a few percent. The CRM instability involves an interaction between the AC field components of an electromagnetic wave with a gyrating electron beam leading to electron bunching which produces a suitable state for energy transfer with the RF field, see Figure 2.1. In the CRM instability bunching occurs azimuthally and is of a relativistic nature due to the energy dependant electron cyclotron frequency, [Sprangle & Drobot 1977, Sprangle et al 1977], shown in Equation 2.2.1.

.

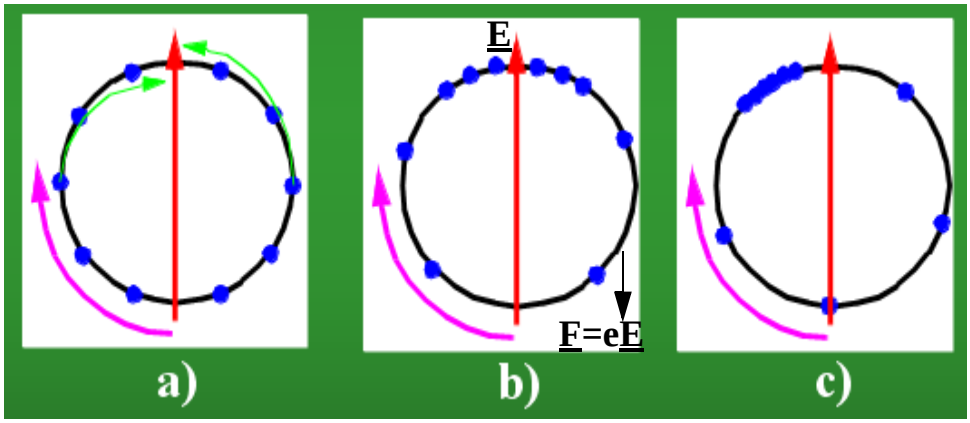

Figure 2.1: CRM bunching process. Red Arrow-AC electric field, Blue Dots-electron orbit, Pink Arrow-direction of rotation

$$\omega_{ce} = \frac{eB}{\gamma m_0} \qquad \text{Equation 2.2.1}$$

ω_{ce}	angular electron cyclotron frequency
e	electron charge
B	magnetic flux density
γ	relativistic factor
m_0	rest mass of electron

A simple way of understanding the CRM mechanism is to think of a group of electrons interacting with an electric field. Figure 2.1 depicts the physical principles of how the cyclotron maser works with regards to the formation of electron bunching [Granatstein & Alexeff 1987]. As is shown in a), the electrons start off uniformly distributed around a helical path unaffected by any interaction with the RF field at this point. The electrons co-rotate with the transverse electric field of an electromagnetic wave in the clockwise direction. The electrons will go around in an orbit at a constant radius known as the Larmor radius, r_L. This can be obtained starting with an expression whereby the Lorentz force is equal to the centrifugal force, Equation 2.2.2:

$$ev_{\perp}B_z = \frac{\gamma m_0 v_{\perp}^2}{r_L} \qquad \text{Equation 2.2.2}$$

$v_\perp$ magnitude of perpendicular velocity component

r_L Larmor radius

B_z magnetic field along z-axis

This can then be rearranged to give the expression for the Larmor radius:

$$r_L = \frac{\gamma m_0 v_\perp}{eB_z} \qquad \text{Equation 2.2.3}$$

The electron orbit circumference is given by $2\pi r_L$ which is substituted into the equation for the period, Equation 2.2.4, and leads to an expression for the relativistic cyclotron frequency, ω_{ce}, as previously shown in Equation 2.2.1.

$$\text{Period} = \frac{2\pi r_L}{v_\perp} = \frac{2\pi\gamma m_0}{eB_z} \qquad \text{Equation 2.2.4}$$

In these equations, γ is the Lorentz-Fitzgerald factor and is represented by Equation 2.2.5.

$$\gamma = 1 + \frac{eV}{m_0 c^2} = \left[1 - \frac{v^2}{c^2}\right]^{-\frac{1}{2}} \qquad \text{Equation 2.2.5}$$

c speed of light, $3\text{x}10^8 \text{ms}^{-2}$

V accelerating voltage

v electron velocity, $v = (v_\perp^2 + v_z^2)^{\frac{1}{2}}$

As the electrons travel around their helical trajectory they interact with the transverse (to their drift motion) components of the electromagnetic wave which leads to those electrons on the left of the red arrow in Figure 2.1 being subject to deceleration whilst those on the right of the red arrow are subject to acceleration, Figure 2.1b). As the electrons exchange energy with the transverse electric field the modified relativistic factor modulates their cyclotron frequency, Equation 2.2.1.

The electrons that are decelerated increase their cyclotron frequency due to their decreasing energy and therefore are advanced in phase. Those that are accelerated are conversely retarded in phase. Consequently, the electrons are then grouped together at the position of the electric field phase in an azimuthal bunch, Figure 2.1b), and can emit radiation coherently once they are in a suitable phase to allow for net energy

transfer with the RF field. In order for energy transfer to occur between the beam and wave it is required that $\underline{v} \cdot \underline{E}$ is finite, i.e. non-zero, where $\underline{E}$ is the electric field. At the resonant bunch formation position the bunch does not satisfy this. However, if the wave frequency is a little higher than ω_{ce} then the bunch forms on the left side, Figure 2.1c), and is in decelerating phase. The difference in the frequencies is called the detuning.

$$\omega_D = S\omega_{ce} + k_z v_z \qquad \text{Equation 2.2.6}$$

$$\omega_w \geq \omega_D \qquad \text{Equation 2.2.7}$$

Where:

ω_w	frequency of the wave
ω_D	Doppler shifted frequency
S	harmonic number
k_z	axial wave vector
v_z	axial velocity component

The Doppler effect has to be accounted for when the resonance condition is being calculated, and is given by Equation 2.2.6. The resonant frequency can be approximated with this equation and the requirement for energy extraction is shown in Equation 2.2.7. If the detuning becomes too large, more than a few percent, then the resonance condition is not strong enough to modulate the beam. Saturation occurs when the Doppler shifted frequency exceeds that of the wave.

When a high spread in velocity or energy is present, a different approach must be taken in order to describe the instability mathematically. One must use a kinetic approach to the interaction between the electron beam and the electromagnetic fields, based on the Vlasov equation. This work is being undertaken at the Rutherford Appleton Laboratory (RAL) and St. Andrews University. In this project mathematical PiC methods are used in order to investigate the instability numerically and these will be discussed in Chapter 4.

2.3 Waveguide Theory

In this experiment both rectangular and cylindrical waveguides were used in the AKR apparatus and it is therefore necessary to have an understanding of waveguide theory. This section explains electromagnetic (EM) propagation through waveguide as described by Maxwell's equations which can then be applied to both rectangular and circular waveguide as necessary.

2.3.1 Electromagnetic Theory

To understand the way in which EM waves propagate through a waveguide, one must refer back to Maxwell's Equations [Radmanesh 2001]. The fundamental versions of these equations are shown below in Equations 2.3.1 to 2.3.4.

Maxwell's first two equations, shown in Equation 2.3.1 and 2.3.2, give Gauss' law for $\underline{E}$ and $\underline{B}$ fields respectively.

$$\underline{\nabla} \bullet \underline{E} = \frac{\rho}{\varepsilon} \qquad \text{Equation 2.3.1}$$

$$\underline{\nabla} \bullet \underline{B} = 0 \qquad \text{Equation 2.3.2}$$

Maxwell's third equation represents Faraday’s Law.

$$\underline{\nabla} \times \underline{E} = -\frac{\partial \underline{B}}{\partial t} \qquad \text{Equation 2.3.3}$$

Maxwell's fourth equation is an altered version of Ampere’s law.

$$\underline{\nabla} \times \underline{B} = \mu \underline{J} + \varepsilon\mu \frac{\partial \underline{E}}{\partial t} \qquad \text{Equation 2.3.4}$$

Alongside the four fundamental Maxwell's equations there are also two constituent equations as shown in Equation 2.3.5 and 2.3.6;

$$\underline{D} = \varepsilon \underline{E} \qquad \text{Equation 2.3.5}$$

$$\underline{B} = \mu \underline{H} \qquad \text{Equation 2.3.6}$$

These two equations, along with Equations 2.3.1 to 2.3.4 can be used together to give the general propagation expressions for electric and magnetic waves, in this case

assuming that there are no free charges or current, [Woan 2000]. See Equations 2.3.7 and 2.3.8 respectively.

$$\nabla^2 \underline{E} = \mu\varepsilon \frac{\partial^2 \underline{E}}{\partial t^2} \qquad \text{Equation 2.3.7}$$

$$\nabla^2 \underline{B} = \mu\varepsilon \frac{\partial^2 \underline{B}}{\partial t^2} \qquad \text{Equation 2.3.8}$$

$\underline{D}$	electric flux density, C/m^2
ε_0	permittivity of free space, F/m
$\underline{E}$	electric field strength, V/m
$\underline{H}$	magnetic field strength, A/m
$\underline{J}$	current density, A/m^2
ρ	charge density, C/m^3
t	time, s
μ	permeability of free space, H/m

One has to consider boundary conditions when solving the above equations, [Collin 2001]. It is required that the tangential component of the electric field go to zero at the walls of the metallic waveguide, as the walls will short any such field. Also, the normal component of the magnetic field must be at zero at the walls, as current would flow to negate such a field. It is because of these boundary conditions that TEM (Transverse Electro-Magnetic) modes cannot propagate in hollow waveguide, only TE (Transverse Electric) or TM (Transverse Magnetic).

2.3.2 Rectangular Waveguide

•Dispersion

The plot below in Figure 2.2, is a dispersion diagram for any smooth waveguide and shows the angular frequency ω asymptotically approaching the light line as k_z increases. Equation 2.3.9 shows the dispersion relation for any smooth waveguide

$$\omega_w = c[k_z^2 + k_\perp^2]^{\frac{1}{2}} \qquad \text{Equation 2.3.9}$$

$k_\perp$	perpendicular wave vector, associated with the required transverse

field variations imposed by the boundary conditions

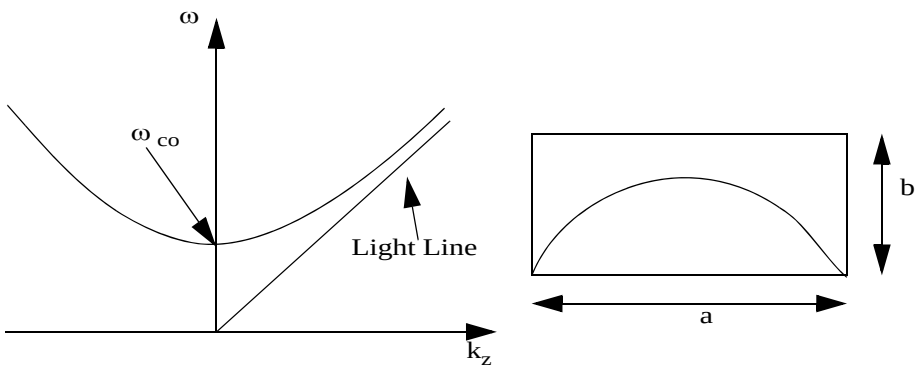

Figure 2.2: Dispersion plot and representation of a mode inside rectangular waveguide

The minimum frequency for a hollow waveguide is given by Equation 2.3.10:

$$\omega_{co} = ck_{\perp} \qquad \text{Equation 2.3.10}$$

ω_{co} angular cut-off frequency

Where for rectangular waveguide:

$$k_{\perp} = \left[\left[\frac{m\pi}{a}\right]^2 + \left[\frac{n\pi}{b}\right]^2\right]^{\frac{1}{2}} \qquad \text{Equation 2.3.11}$$

m,n waveguide mode numbers

a,b waveguide dimensions

The bracketed terms are the wave variations for particular modes where m and n are the number of half wave variations along dimensions a and b respectively. Substituting Equation 2.3.11 into Equation 2.3.9 allows an alternative expression for the dispersion ω of a rectangular waveguide to be written, shown in Equation 2.3.12.

$$\omega = c\left[k_z^{\,2} + \left[\frac{m\pi}{a}\right]^2 + \left[\frac{n\pi}{b}\right]^2\right]^{\frac{1}{2}} \qquad \text{Equation 2.3.12}$$

ω angular frequency

•Rectangular Waveguide Field Distribution Equations

The field distribution equations for rectangular waveguide are shown below in Equations 2.3.13 to 2.3.16 and Equations 2.3.17 to 2.3.20 for TE and TM modes respectively. Close to cut-off k_z goes to zero as do the H_x and H_y terms for the TE modes, whereas for the TM modes, it is the E_x and the E_y terms that go to zero at cut-off.

Field distribution equations for TE mode:

$$H_x = -\frac{jk_z}{k_c^2} \times \frac{\partial H_z}{\partial x} \qquad \text{Equation 2.3.13}$$

$$H_y = -\frac{jk_z}{k_c^2} \times \frac{\partial H_z}{\partial y} \qquad \text{Equation 2.3.14}$$

$$E_x = -\frac{j\omega\mu}{k_c^2} \times \frac{\partial H_z}{\partial y} \qquad \text{Equation 2.3.15}$$

$$E_y = \frac{j\omega\mu}{k_c^2} \times \frac{\partial H_z}{\partial x} \qquad \text{Equation 2.3.16}$$

Field distribution equations for TM mode:

$$H_x = \frac{j\omega\varepsilon}{k_c^2} \times \frac{\partial E_z}{\partial y} \qquad \text{Equation 2.3.17}$$

$$H_y = -\frac{j\omega\varepsilon}{k_c^2} \times \frac{\partial E_z}{\partial x} \qquad \text{Equation 2.3.18}$$

$$E_x = -\frac{jk_z}{k_c^2} \times \frac{\partial E_z}{\partial x} \qquad \text{Equation 2.3.19}$$

$$E_y = -\frac{jk_z}{k_c^2} \times \frac{\partial E_z}{\partial y} \qquad \text{Equation 2.3.20}$$

These components can be found using Equations 2.3.21 and 2.3.22 shown below for E_z and H_z which satisfy the appropriate boundary conditions stated earlier, and show the allowed modes in rectangular waveguide.

$$E_z = B_{k_z} \sin\left(\frac{m\pi x}{a}\right) \sin\left(\frac{n\pi y}{b}\right) \qquad \text{Equation 2.3.21}$$

$$H_z = A_{k_z} \cos\left(\frac{m\pi x}{a}\right) \cos\left(\frac{n\pi y}{b}\right) \qquad \text{Equation 2.3.22}$$

2.3.3 Circular Waveguide

The waveguides used in the interaction region of the experiments were circular waveguides of diameter 8.22cm and 7.02cm. Theory shows that the transverse field distributions are given by Bessel roots and Bessel functions described below.

•Details of Wave Propagation in Circular Waveguide

To solve Maxwell's equations and the wave equations in cylindrical coordinates the Bessel roots (which arise as the cylindrical polar form of the transverse Laplacian) must be used due to the cylindrical boundaries. Starting with the generalised wave equation for circular waveguides it can be written that:

$$(\nabla_t^2 + \mu\varepsilon\omega^2 - k_z^2)\begin{bmatrix} \underline{E} \\ \underline{H} \end{bmatrix} = 0 \qquad \text{Equation 2.3.23}$$

Where the transverse gradient operator is $\nabla_t^2 = \nabla^2 - \frac{\partial^2}{\partial z^2}$

Writing the transverse Laplacian in cylindrical polar coordinates gives Equation 2.3.24.

$$\left[\frac{1}{r} \cdot \frac{\partial}{\partial r}\left(r\frac{\partial}{\partial r}\right) + \frac{1}{r^2} \cdot \frac{\partial^2}{\partial \phi^2} + \mu\varepsilon\omega^2 - k_z^2\right]\psi = 0 \qquad \text{Equation 2.3.24}$$

r radial coordinate

ϕ azimuthal coordinate

Where in this form of the expression, ψ is used to represent E_z and H_z for TM and TE modes respectively. The solutions of Equation 2.3.24 have the form of Bessel Functions.

This then allows one to write the dispersion relation for cylindrical waveguide which takes the same form as rectangular waveguide but the transverse structure is described by Bessel functions and their roots, Equation 2.3.25;

$$k_z^{\,2} = \varepsilon\mu\omega^2 - \frac{\mu'^{\,2}_{m,n}}{a_r^{\,2}} \qquad \text{Equation 2.3.25}$$

μ' (first root of $J_0'(x)$) Bessel root for specific mode of radiation, 3.832 for TE_{01}

a_r radius of circular waveguide

The cut-off frequency, f_{co}, for a circular waveguide for TE modes, can be obtained in the following way:

$$f_{co} = \frac{ck_\perp}{2\pi} \qquad \text{Equation 2.3.26}$$

Substituting for $k_\perp$ leads to Equation 2.3.27:

$$f_{co} = \frac{c\mu'_{m,n}}{2\pi a_r} \qquad \text{Equation 2.3.27}$$

•Cylindrical Field Distribution Equations

By solving Equation 2.3.24 and applying the appropriate boundary conditions, solutions in the form of the field distribution equations are obtained as given below.

TM modes: [Pozar 1998, Sander 1987]

$$E_r = \left(-\frac{jk_z}{k_c}\right)(A\sin m\phi + B\cos m\phi)J'_m(k_c r)e^{-jk_z z} \qquad \text{Equation 2.3.28}$$

$$E_\phi = \left(-\frac{jk_z m}{k_c^{\,2} r}\right)(A\cos m\phi - B\sin m\phi)J_m(k_c r)e^{-jk_z z} \qquad \text{Equation 2.3.29}$$

$$H_r = \frac{j\omega\varepsilon m}{k_c^{\,2} r}(A\cos m\phi - B\sin m\phi)J_m(k_c r)e^{-jk_z z} \qquad \text{Equation 2.3.30}$$

$$H_\phi = \left(-\frac{j\omega\varepsilon}{k_c}\right)(A\sin m\phi + B\cos m\phi)J'_m(k_c r)e^{-jk_z z} \qquad \text{Equation 2.3.31}$$

TE modes: [Pozar 1998, Sander 1987]

$$E_r = \frac{j\omega\mu m}{k_c^2 r}(A\cos m\phi - B\sin m\phi)J_m(k_c r)e^{-jk_z z} \qquad \text{Equation 2.3.32}$$

$$E_\phi = \frac{j\omega\mu}{k_c}(A\sin m\phi + B\cos m\phi)J'_m(k_c r)e^{-jk_z z} \qquad \text{Equation 2.3.33}$$

$$H_r = \left(-\frac{jk_z}{k_c}\right)(A\sin m\phi + B\cos m\phi)J'_m(k_c r)e^{-jk_z z} \qquad \text{Equation 2.3.34}$$

$$H_\phi = \left(-\frac{jk_z m}{k_c^2 r}\right)(A\cos m\phi - B\sin m\phi)J_m(k_c r)e^{-jk_z z} \qquad \text{Equation 2.3.35}$$

A and B	arbitrary amplitude constants
$\underline{k}$	wavenumber
k_c	cut-off wavenumber; $k_c^2 = k^2 - \beta^2$
β	propagation constant

Looking at the equations given for TE modes; when m is set to zero, E_ρ and H_ϕ go to zero leaving:

$$E_\phi = \frac{j\omega\mu}{k_c}J'_m(k_c r)e^{-jk_z z} \qquad \text{Equation 2.3.36}$$

$$H_r = \left(-\frac{jk_z}{k_c}\right)J'_m(k_c r)e^{-jk_z z} \qquad \text{Equation 2.3.37}$$

For the TM modes, at m equal to zero, E_ϕ and H_ρ go to zero, leaving:

$$E_r = \left(-\frac{jk_z}{k_c}\right)J'_m(k_c r)e^{-jk_z z} \qquad \text{Equation 2.3.38}$$

$$H_\phi = \left(-\frac{j\omega\varepsilon}{k_c}\right)J'_m(k_c r)e^{-jk_z z} \qquad \text{Equation 2.3.39}$$

As can be seen in Equations 2.3.28 to 2.3.35, when at a near cut-off resonance condition, hence k_z tending to zero, only the axial component of the magnetic field survives for the TE modes whereas it is the axial component of the electric field for the TM modes.

2.3.4 Choice of EM Modes for the AKR Experiment

In the auroral density cavity within the Earth's magnetosphere it has been postulated that there is an effective boundary which occurs when the plasma frequency exceeds the cyclotron frequency, causing the waves to 'reflect' back into the auroral density cavity, thus creating a boundary much like one at a metal wall of a circular waveguide [Burinskaya and Rauch 2007]. The radiation that occurs is observed to be polarised in the X-mode, Figure 2.3, which is polarised and propagating perpendicular to the static magnetic field and close to the cyclotron frequency. This implies a Doppler term of effectively zero for the resonance which in turn allows for strong coupling between the wave and the beam even in the case of large velocity spread, see Equation 2.2.6. Referring to the cylindrical field distribution equations, Equations 2.3.28 to 2.3.35, it is possible to conclude that near cut-off TE modes should be used in the laboratory experiment to give the best approximation in terms of polarisation and propagation properties to the X-mode.

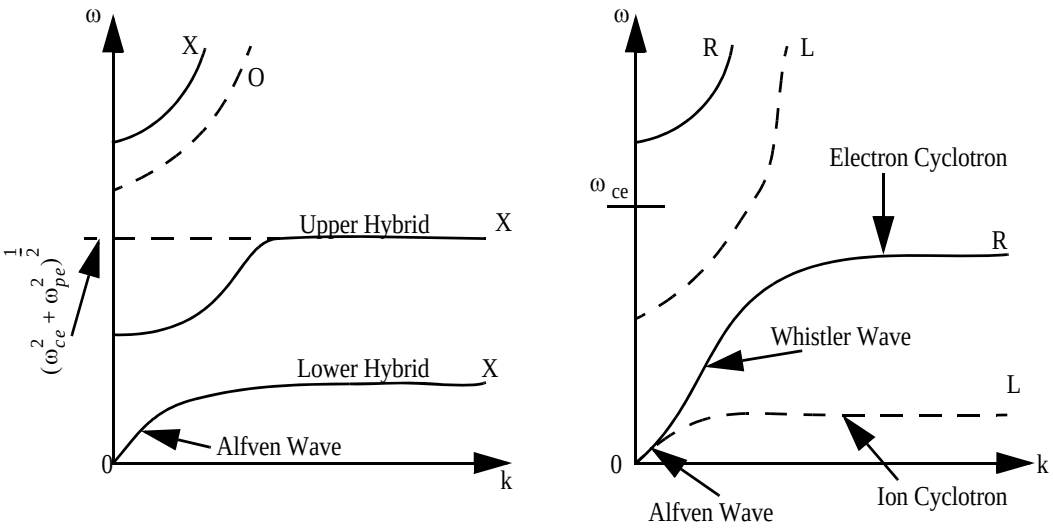

Figure 2.3: Dispersion diagrams for wave propagation, k⊥B and k//B, showing the X,O,R&L resonances

The circular waveguide in the interaction region of the experiment ran parallel to the direction of the static magnetic field and therefore the beam drift velocity. In order to obtain a zero Doppler term as in the auroral case, one needs to have a zero k_z term.

Referring to Equations 2.3.28 to 2.3.31, for a TM wave, when k_z=0, only the axial electric field components are left which are polarised parallel to the static magnetic field, like the O-mode. Looking at Equations 2.3.32 to 2.3.35, the TE mode with k_z=0 retains the transverse electric components and these propagate and are polarised perpendicular to the static magnetic field, similar to the X-mode. As this would give the closest representation of the auroral situation, the TE modes are used in the experiment, close to cut-off.

2.4 Electron Emission

2.4.1 Electron Energy Distribution in a Solid

To fully understand the way in which electrons are distributed in materials one needs to review Fermi-Dirac (FD) statistics, [Mandl 1988]. Since electrons are Fermions their statistical behaviour is subject to the Pauli exclusion principle and therefore only one particle can be in any one state.

The Fermi Dirac distribution is important in the process of electron emission from a cathode as it governs how the electrons are distributed in energy within the material as a function of the temperature. One can obtain the probability of an electron having a certain energy, within a metal/solid, by taking the product of the FD distribution function, Equation 2.4.1, with that of the density of states function, Equation 2.4.2. By integrating the result from 0 to E (energy) one may determine the total number of electrons with energy less than 'E'. If these equations shown below are plotted, they produce the traces shown in Figures 2.4 and 2.5 respectively.

$$F(E) = \frac{1}{1 + \exp\left[\frac{E - E_F}{k_B T}\right]} \qquad \text{Equation 2.4.1}$$

$$N(E) = 4\pi\left(\frac{2m_e}{h^2}\right)^{\frac{3}{2}} E^{\frac{1}{2}} \qquad \text{Equation 2.4.2}$$

$\int_0^E N(E) \cdot F(E) dE$ gives the number of electrons below an energy E.

k_B	Boltzmann constant, $1.38 \times 10^{-23} JK^{-1}$
h	Planck's constant, $6.626 \times 10^{-34} Js$
m_e	electron mass, $9.11 \times 10^{-31} kg$
E	energy
E_F	Fermi energy
T	temperature

a)

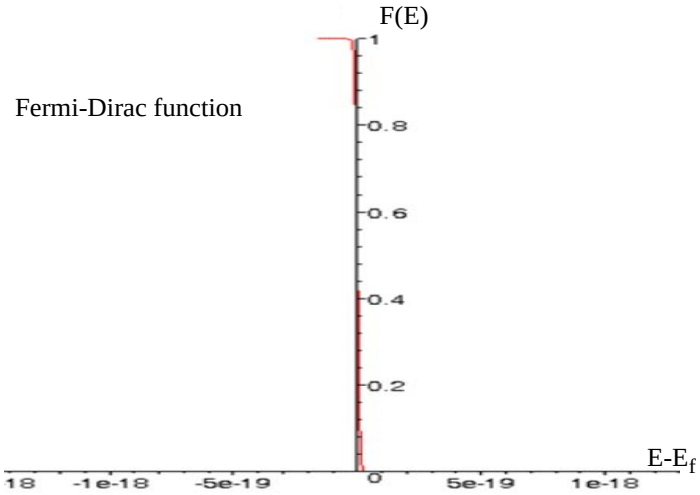

b)

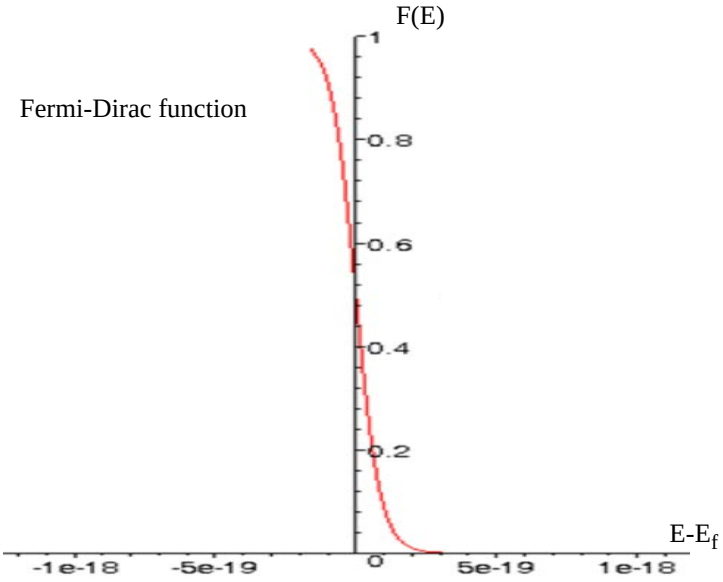

Figure 2.4: Fermi-Dirac function (where $E-E_f$ is measured in Joules) at; a) T=300K, b) T=3200K

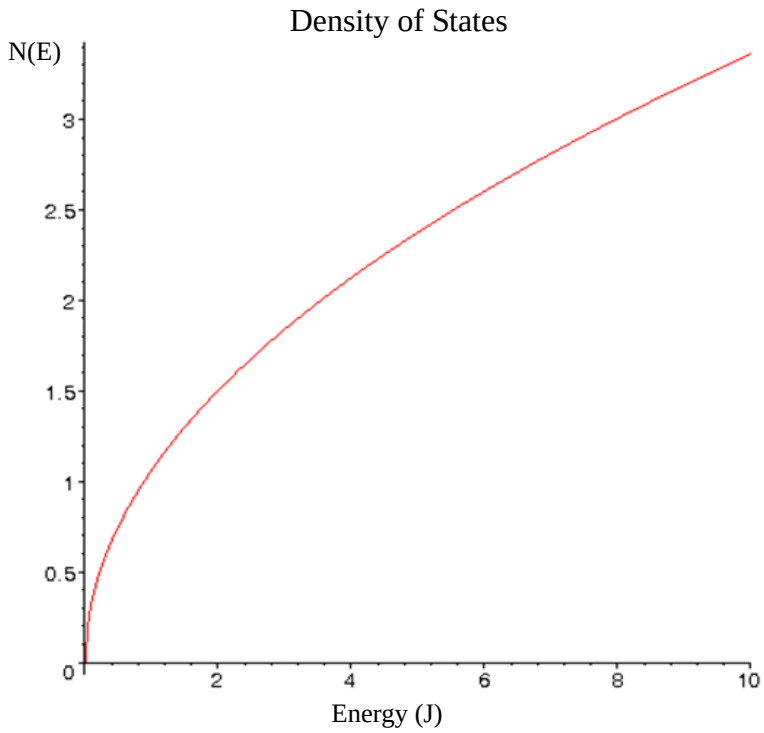

Figure 2.5: Density of states as a function of energy

At absolute zero, there is a Fermi energy E_F which defines the energy of the topmost occupied level. Fermions will fill up all the available energy states below this level E_F, with one particle in each state due to the Pauli exclusion principle. At higher temperatures some of the Fermions will be elevated to levels above the Fermi level. This results in a depopulation of energy states just below the Fermi energy. The probability of an energy state being filled above E_F increases with temperature but decreases with energy, whilst below E_F it decreases with temperature and increases with energy. The probability of finding an electron in an energy state of E_F is 0.5, independent of the temperature. For low temperatures, those energy states significantly below the Fermi energy have a probability of essentially one, and those significantly above the Fermi energy essentially zero.

2.5 Cathodes

Cathodes are charged negative with respect to any other nearby electrodes. If some part of the cathode emits electrons then these electrons will drift under the action of the electric field. The geometry and constituency of such cathodes and emitters is determined by the application requirements but certain ‘ideal’ characteristics for a cathode may still be defined:

- At the Space Charge Limit the cathode would freely emit electrons over a wide range of temperatures and applied fields
- There would be no emission of extraneous material
- Throughout all the heating cycles and particle bombardment, it would last forever and never need replacing
- It would be able to tolerate a poor vacuum environment and various gasses during the vacuum cycling period

[Gilmour 1986]

The following short descriptions look briefly at various cathodes, their emission mechanisms and certain restrictions that apply to the emission processes. One restriction that applies to all cathodes emitting into a vacuum is that of the Space Charge (SCL) or Child Langmuir Limit.

The space charge limit is the maximum limit of the electron emission current and occurs when the electric field at the cathode surface goes to zero due to the formation of an electron cloud. There is a link between the attainable diode current and the anode voltage due to the potential gradient between the cathode and anode increasing with the diode voltage, [Gilmour 1986]. Additional electrons may then leave the cathode to increase the space charge density and keep the cathode surface electric field at zero.

Due to continuity there will be a greater number density of electrons at the cathode as opposed to the anode. This is quantified by the relation between the number density of

electrons and their drift velocity as shown in Equation 2.5.1. Whilst at the cathode, the electrons have very little kinetic energy and so v_c is small requiring n_c to be large. Electrons that have been accelerated towards the anode have their potential energy turned into kinetic energy and so v_a is large, making n_a small to keep the balance.

$$en_cv_c = en_av_a = J \qquad \text{Equation 2.5.1}$$

The relation between the voltage and limiting current is known as the Child-Langmuir law in a space charge limited diode and is shown below, for a parallel plane diode.

$$I = PV^{\frac{3}{2}} \qquad \text{Equation 2.5.2}$$

$$P = \left[\frac{4}{9}\right]\left[\frac{A\varepsilon_0(2\eta)^{\frac{1}{2}}}{d^2}\right] \qquad \text{Equation 2.5.3}$$

A	area of the cathode
d	distance between electrodes
I	current
n_c/n_a	number density of electrons at the cathode/anode
η	charge to mass ratio, e/m
P	perveance
v_c/v_a	drift velocity of electrons at the cathode/anode

Other diode geometries, such as cylindrical and spherical, all obey Equation 2.5.2 but the perveance expression will differ using appropriate parameters for the specific geometry.

2.5.1 Thermionic Cathodes

A thermionic cathode is one which exhibits the mechanism of thermionic emission whereby the material is heated to induce electron emission. The Fermi Dirac function, Equation 2.4.1, describing the distribution of electrons in a metal, influences the way the electrons are emitted from the cathode surface.

Thermionic emission current density increases with electron temperature and the Schottky effect. As the temperature of the material is increased the number and energy of electrons in the high-energy tail part of the distribution which have the energy they require to surpass the surface potential barrier increases. The surface potential barrier is given by Equation 2.5.4:

$$\phi_B = (\phi_m - \Delta\phi) \qquad \text{Equation 2.5.4}$$

$\Delta\phi$ change in work function due to applied E field

ϕ_m work function of metal

ϕ_B height of the potential barrier

Only those electrons with sufficient energy and momentum to overcome the potential barrier of the metal (the work function) will escape the solid. The rate at which electrons in the material are able to leave the surface to fill the vacuum gap is dependant on the temperature of the electrons and the work function of the solid.

Referring to what is known as the Richardson-Dushman equation, Equation 2.5.5 shows the resultant emission current density $\underline{J}$ where it can be seen that for high emission to be obtained, one needs a low work function and high temperatures.

$$\underline{J} = A_0 T^2 \exp\left(-\frac{e\phi_m}{k_B T}\right) \qquad \text{Equation 2.5.5}$$

A_0 Richardson's constant, $1.20 \times 10^6 Am^{-2}deg^{-2}$

Lowering the potential barrier, due to the applied electrostatic field across the cathode, is known as the Schottky effect, [Gilmour 1986] and increases electron emission. By changing the barrier height by a very small amount $\Delta\phi$, one can obtain a significant effect on the current, as it will exponentially increase the number of electrons with sufficient escape energy (via the Fermi-Dirac distribution).

Equation 2.5.5, [Llewellyn-Jones 1957], may be altered by taking into consideration the lowering of the potential barrier and $\Delta\phi$. $\Delta\phi$ is expressed in Equation 2.5.6 and when substituted into the Richardson Dushman equation it gives Equation 2.5.7.

$$\Delta\phi = \left(\frac{e\underline{E}\cdot\underline{n}}{4\pi\varepsilon_0}\right)^{\frac{1}{2}} \qquad \text{Equation 2.5.6}$$

$$J = J_0 \exp \Delta\phi \qquad \text{Equation 2.5.7}$$

J_0 Richardson-Dushman current density

$\underline{n}$ unit vector normal to cathode surface

2.5.2 Field Enhanced Emission

The electron emission due to the tunnelling effect is a process where an electric field is applied to the cathode, similar to the Schottky effect, but in this case the E-field is much larger. The application of this electric field reduces the width of the potential barrier at the surface of the cathode and the more the field is increased, the narrower the barrier becomes, Figure 2.6, [Gilmour 1986].

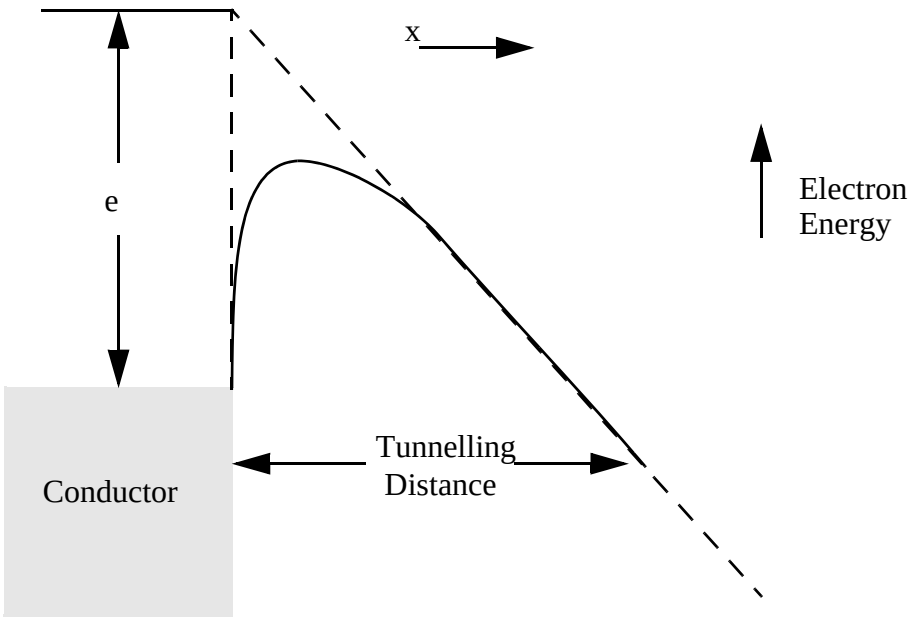

Figure 2.6: Illustration of surface barrier penetration by electrons

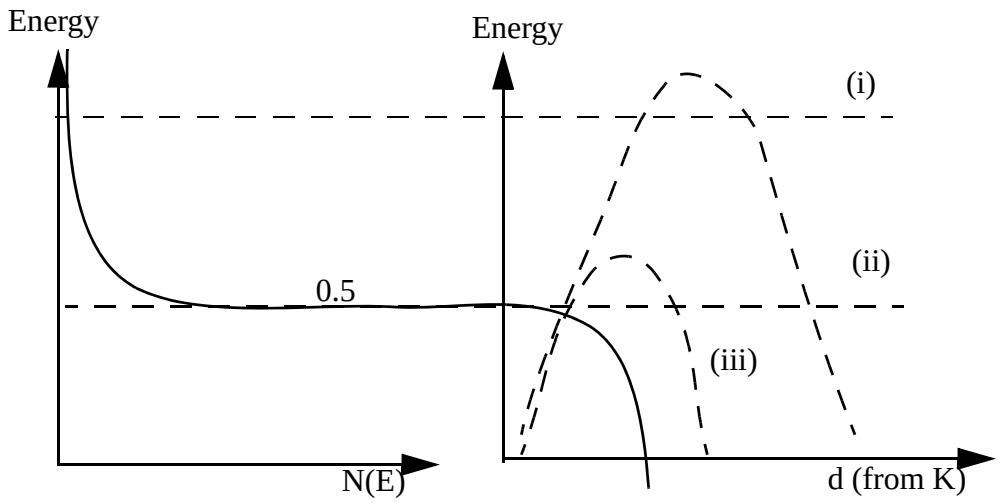

Figure 2.7: Comparison of electron energies in a warm metal and surface barrier under varying electric field strengths

Consider the potential barriers illustrated in Figure 2.7. Electrons with energy above position (i) can either emit over the top of the barrier by heating, or they may be emitted by barrier tunnelling since they are only a little below the surface barrier potential and therefore experience a weak decay of their wavefunction over a short distance ‘d’ from the cathode. In contrast, electrons at position (ii) perceive a high, wide barrier and therefore their wavefunction decays very rapidly and over a long distance. However, as the electric field is increased the barrier shape reconfigures to that at point (iii). Here many more electrons may be thermionically emitted but as the barrier is now thin at the Fermi energy (where the electron distribution is much higher), a finite chance of tunnelling arises. As both the number density of electrons in the metal (exceeding a given energy) and the tunnelling probability increase rapidly with the electric field strength this may quickly dominate the thermionic emission giving way to the field emission regime. This process can be represented by what is known as the Fowler-Nordheim equation, Equation 2.5.8, [Ronald 1996], depending on the properties of the material. Experiments show that the onset of the dominant field enhanced electron emission occurs at much lower E-fields than this formula would predict. This is believed to be associated with field enhancement of microscopic protrusions on the cathode surface.

$$J = \frac{A_{FN}\left|\underline{E}\right|^2 \exp -\frac{B_{FN}\phi_m^{\frac{3}{2}}}{\left|\underline{E}\right|}}{\phi_m} \qquad \text{Equation 2.5.8}$$

A_{FN} $1.54\text{x}10^{-6}$ AeV/V^2

B_{FN} $6.83\text{x}10^{9}$ $Vm^{-1}eV^{-3/2}$

By careful analysis of the Fowler Nordheim equation and fitting the experimental data, estimations of the effective emission areas and the field enhancement factors can be obtained. This is achieved by plotting a logarithmic form of Equation 2.5.8 using experimental measurements of diode current and voltage. By specifying the work function ϕ_m, of the material, the field enhancement factor β, can be obtained from the slope of a straight line (the gradient) and the emitting area, ‘a’, from the y intercept as can be seen in [Mesyats and Proskurovsky 1989]. The geometries of the 'whiskers' (tips of fibre material) determine the value of the field enhancement factor one can achieve (the factor by which the local electric field at a discontinuity exceeds the field for a smooth electrode). Typical values have bases $\leq 1\mu m$ that taper to radii $\leq$ 10's of nanometers. These particular dimensions correspond to field enhancement factors $\geq$ 100. The obtained values of β and ‘a’ allow the cathode to be characterised in greater detail with regards to the microprotrusions on its surface. Modern microscopy techniques allow correlation with such macroscopic measurements.

Under certain conditions this type of emission can affect or limit the operating voltage of an electron gun as it may act as a precursor to breakdown [Kukreja 2005]. This can lead to cases of breakdown within the gun as the field emission current flows through a point on the cathode, causing it to heat up, melt and vaporize. This leads to explosive emission discussed later. Breakdown can also occur when the anode is heated which can happen due to electrons accelerating in the vacuum gap and transferring energy to a section on the anode surface. Due to the immense heating that can occur with field emission, this process is not usually used in thermionic cathodes so as not to damage the thermionic emission surface.

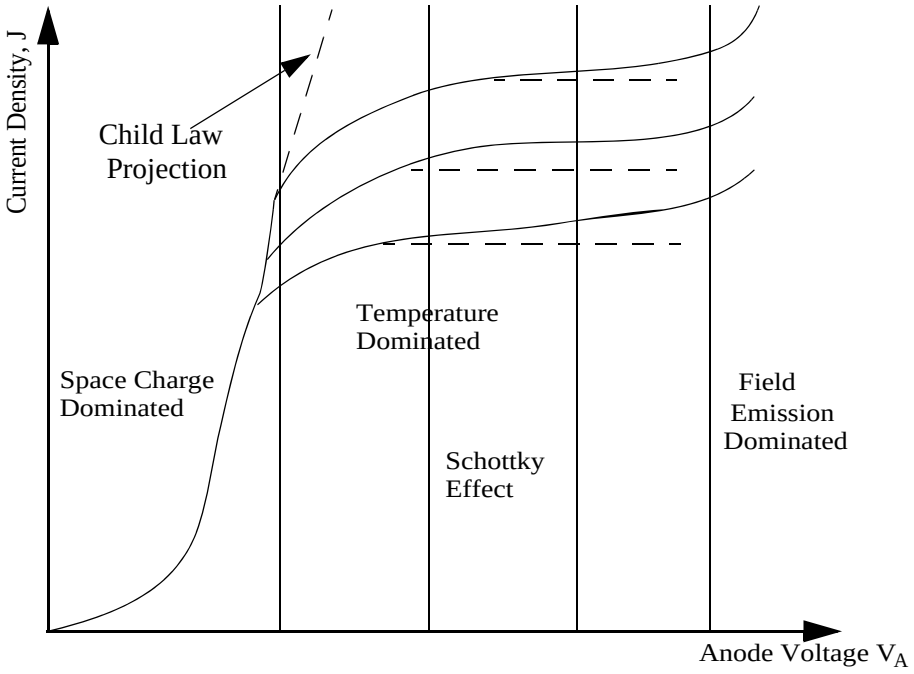

Figure 2.8: Ranges of different emission regimes

The different areas where SCL, temperature limit and field emission occur can be seen in Figure 2.8, [Gilmour 1986].

2.5.3 Hot Electron Model of Emission

The hot electron model was a physical interpretation of the non-metallic emission process and was proposed by Latham and his co-workers [Latham, 1983]. This model is an alternative theory to explain results based on the emissions from insulating inclusions in the cathode surface. As such it represents an alternative description for electron field emission.

In the hot electron model one may envisage an insulating microscopic inclusion on a metallic surface. The applied electric field penetrates the inclusion and bends the conduction and valence bands in the insulator. This induces Schottky barrier emission from the metal conduction band to the insulator conduction band and accelerates these electrons until they induce avalanche ionisation of the valence electrons which in turn

move under the influence of the electric field. Ultimately these electrons are then able to escape over the potential barrier by thermionic emission and have a new energy value of a few eV below the Fermi level, i.e. the electric potential energy drops over the dielectric. Electron holes in the valence band that are created within this region drift towards the metal increasing the electric field by creating a positive space charge region near the metal-dielectric interface. This sustains the emission from the metal surface.

Referring to Equation 2.5.5, if the electron temperature is written as shown below and substituted into the Richard Dushman equation, one obtains the expression in Equation 2.5.9 which can be seen to be of the same form as the Fowler Nordheim equation with regard to its dependence on the E-field, however it is based on an entirely different theoretical model.

$$T_e = \left(\frac{2e\Delta d}{3k_B\varepsilon_r d}\right)V$$

$$I = A_0 a_e \left(\frac{2e\Delta d}{3k_B\varepsilon_r d}\right)^2 V^2 \exp\left(\frac{-\phi}{\left(\frac{2\Delta d}{3\varepsilon_r d}\right)V}\right) \qquad \text{Equation 2.5.9}$$

a_e	emitting area
ε_r	relative permittivity
Δd	thickness of dielectric inclusion
d	distance between electrodes

2.5.4 Vacuum Spark/Explosive Emission Cathodes

When a cold cathode is subject to a strong electric field the electron field emission process increases rapidly giving small regions (the field enhanced regions) a very high current density causing explosive vaporisation of the cathode material, hence the name explosive-electron-emission (EEE) cathode. Such cathodes are used in pulsed systems to generate a high voltage, short duration electron beam. The vapour cloud formed in the explosive emission process is initially uncharged. Strong bombardment by electrons from the underlying and very hot metallic substrate ionises this very

dense material forming a cathode flare plasma. This plasma can be thought of as a highly conductive plasma ball and expands into the vacuum at around 1-10cm/μs whilst freely emitting electrons into the vacuum. The cathode temperature is sustained by ion bombardment whilst the pressure of the plasma cloud on the liquid surface forms new 'enhanced' emission sites. Due to this expansion of the CF (cathode flare) plasma the cathode-anode gap will ultimately be shorted when it reaches the grounded electrode forming a vacuum arc discharge. The expansion of the plasma can be measured and is described by the plasma expansion velocity, v_{pl}. This is achieved by measuring the electrode separation, d, and the time taken for a complete collapse of the acceleration potential, t_{col} and using Equation 2.5.10:

$$v_{pl} = \frac{d}{t_{col}} \qquad \text{Equation 2.5.10}$$

The rate at which the plasma flare expands is not strongly affected by the electric field strength, but depends strongly on the properties of the cathode material such as the conductivity, resistivity and density. Equation 2.5.11 shows the specific energy (per unit mass) that is required to cause the solid to vaporise (which is of the form $J^2\kappa$), the density, and the time required for vaporisation to occur, t_d.

$$E_c = \frac{J^2 t_d \kappa}{\pi^2 \rho_m} \qquad \text{Equation 2.5.11}$$

E_c	specific energy
κ	resistivity
ρ_m	mass density

These factors have to be taken into account when predicting the velocity rate of the plasma expansion, the formula for which can be seen in Equation 2.5.12, which shows how it depends on the adiabatic parameter γ_{sp} and specific energy.

$$v_{max} = \left(\frac{4\gamma_{sp}E_c}{\gamma_{sp}-1}\right)^{\frac{1}{2}} = \left(\frac{2\gamma_{sp}}{\gamma_{sp}-1}\right)^{\frac{1}{2}} v_\infty \qquad \text{Equation 2.5.12}$$

Where;

$$v_\infty = (2E_c)^{\frac{1}{2}} \qquad \text{Equation 2.5.13}$$

v_{max} maximum velocity

γ_{sp} ratio of specific heats; C_p/C_v

This type of cathode is important in high peak power pulsed applications. They do not require heater devices for electron emission but are subject to disadvantages such as high emittance and non-uniform emission [Shiffler et al 2002]. Applications for use of explosive emission cathodes include intense X-ray sources, microwave experiments (as in this thesis) and in general, when the need arises for a very high current electron beam.

In the AKR simulation experiment the explosive emission cathode used [Mesyats and Proskurovsky 1989] had a velvet emitter [Miller 1998] used to induce plasma formation by field emission from the tips of the fibres. Velvet has a plasma expansion velocity of ~$2x10^6$cm/s. Other materials include Tungsten 2-2.5 x 10^6cm/s, Aluminium 2.4 x 10^6cm/s, Copper 2.4 x 10^6cm/s, etc., all rough values [Mesyats and Proskurovsky 1989]. The expanding outer limit of the plasma cloud is, in effect, the new emission surface as it grows and emits more electrons, therefore, the expansion velocity at the front of the flare is extremely important. Reduction of the flare velocity, by minimising E_c, allows for closer gap spacing and potentially a lower operating voltage for the electron gun.

2.6 Plasma Theory

2.6.1 Introduction

Plasma is often referred to as the fourth state of matter existing at an energy state exceeding solid, liquid and gas. It is an electrically energised and active matter in a gaseous state and in general consists of three components.

1. Electrically neutral gas molecules
2. Charged particles in the form of positive ions, negative ions and electrons
3. Quanta of electromagnetic radiation (photons) permeating the plasma-filled space [von Engel 1983, 1994]

It is the most common form of matter, making up approximately 99% of the visible universe. There are two important conditions that must be satisfied when defining the plasma state:

i) Its extent must be considerably larger than a single Debye length, λ_D. i.e. it needs to be larger than the sphere of influence of a single charged particle.

ii) It must have charge neutrality i.e. $n_e \approx n_i$

n_e/n_i number density of electrons/ions

Plasma is formed when a material is subjected to sufficient energy to form and sustain ionisation. The plasma is generally characterised by its plasma density and a measure of the energy of the charged particles, usually given in terms of temperature. Generally n_e and n_i of a low temperature plasma are equal quantities, however, in such plasmas the degree of ionisation may be small, < 1 in 10^4 and so neutral gas, n_o, predominates. Non-thermal plasmas operate at low gas pressures typically ~ a few $\rightarrow$ 100's mTorr, with electron temperatures ~ $10^4 \rightarrow 10^5$ K, with ion and neutral temperatures at around background 'room' temperature. Generally in low pressure plasmas: $kT_e >> kT_i$ and $kT_i \approx kT_o$

2.6.2 Plasma Characteristics

The expression for the electron plasma frequency is given below in Equation 2.6.1, with the complementing ion plasma frequency given in Equation 2.6.2, and as is clearly seen, the expressions are identical except for the differing variables corresponding to electron or ion species. The assumption made here is that there are only singly ionised ions.

$$\omega_{pe} = \left(\frac{n_e e^2}{\varepsilon_0 m_e} \right)^{\frac{1}{2}} \qquad \text{Equation 2.6.1}$$

$$\omega_{pi} = \left(\frac{n_i e^2}{\varepsilon_0 m_i}\right)^{\frac{1}{2}} \qquad \text{Equation 2.6.2}$$

ω_{pi}/ω_{pe}	angular ion/electron plasma frequency
m_i/m_e	mass of ions/electrons (9.11×10^{-31}kg)

The electron cyclotron frequency is shown, as stated earlier in Equation 2.2.1, and similarly the ion cyclotron frequency, very much lower than the electron case. For most plasma the value of γ is usually ~1 and can be dismissed from the equations below, however, it is included here for completeness.

$$\omega_{ce} = \frac{eB}{\gamma m_e}$$

$$\omega_{ci} = \frac{eB}{\gamma m_i}$$

The corresponding Larmor radii, previously stated in Equation 2.2.3, for the electron and ion species is expressed below.

$$r_L = \frac{m_{sp} v_\perp}{e_{sp} B}$$

e_{sp}	charge of specific species, electron or ion
m_{sp}	mass of specific species, electron or ion

The collision frequency, Equation 2.6.3, is the average rate at which inter-particle collisions take place, assumed (for simplicity) to be between a mobile species and a stationary one. The collisional cross section is shown in Equation 2.6.4 and the collision time is in Equation 2.6.5. [Diver 2001]

$$f_{cs} = n_n \sigma_{sc,s} \langle U_s \rangle \qquad \text{Equation 2.6.3}$$

f_{cs}	collision frequency of species
n_n	number density of stationary targets
$\sigma_{sc,s}$	collision cross section of the species
$\langle U_s \rangle$	mean speed of mobile species

$$\sigma_{sc} = 2\pi \int_0^{\pi} I(v, \theta) d\theta \qquad \text{Equation 2.6.4}$$

σ_{sc} total collision cross section

$I(v,\theta)$ differential scattering cross section where in this case; v is the relative speed of scattered particle compared with target, and θ is the angle through which the particle is scattered by collision

$$\tau_c = \frac{1}{n_n \sigma_{sc} \langle U \rangle} \qquad \text{Equation 2.6.5}$$

τ_c collision time

$\langle U \rangle$ mean speed of colliding particles

The mean free path in Equation 2.6.6 represents the average distance a particle moves before successive collisions/interactions. [Diver 2001]

$$\lambda_{mfp} = (n_n \sigma_{sc})^{-1} \qquad \text{Equation 2.6.6}$$

λ_{mfp} mean free path

The Debye length, λ_D, is the maximum extent to which a localised disruption in the potential is observed. Beyond a Debye sphere, radius λ_D, the plasma remains effectively neutral.

$$\lambda_D = \left(\frac{\varepsilon_0 k_B T_e}{n_e e^2} \right)^{\frac{1}{2}} \qquad \text{Equation 2.6.7}$$

$$g_p = \frac{e^2}{\varepsilon_0 k_B T_e \lambda_D} = \frac{1}{n_e \lambda_D^3} \ll 1 \qquad \text{Equation 2.6.8}$$

g_p plasma parameter

It is necessary that $n_e \lambda_D^3 >> 1$, shown in Equation 2.6.8, as this implies that a large number of electrons are present within the Debye sphere. This is necessary to reduce

the effect of a significant resultant force on any given particle due to ‘collisions’. This is quantified in the plasma parameter shown in Equation 2.6.8.

2.7 Models for Describing Plasma Behaviour

2.7.1 Single Particle (Orbital) Model

The single particle model uses the Lorentz force equation (Equation 2.7.1), along with Newton’s 2nd Law and the equations of motion, allowing the particle trajectories to be calculated whilst ignoring collective effects.

$$\underline{F} = e(\underline{E} + \underline{v} \times \underline{B}) \qquad \text{Equation 2.7.1}$$

$\underline{F}$ Lorentz force

By solving these equations the orbit of a single charged particle in prescribed electric and magnetic fields can be determined. It provides information on the plasma based on the behaviour of individual electrons and ions. This model is useful in assessing the impact of an applied magnetic field describing the Larmor radius and the cyclotron frequency of the charged particles, Section 2.2. The time comes to use a different model to describe plasma, such as the fluid and statistical descriptions, whenever the charge distributions or current densities are significant. However, the single particle model forms one part of the basis of PiC code simulation approaches where the impact of the other charged particles is dynamically calculated into the field components. The trapping of particles by an inhomogeneous magnetic field - the mirror effect - is an example of the behaviour described using this model.

The invariance of the magnetic moment of a gyrating particle, Equation 2.7.2, is the basis for one of the primary schemes for plasma confinement: the magnetic mirror.

$$\underline{\mu}_m = \pi r^2 i \hat{\underline{z}} = \frac{\gamma m v_\perp^2}{2B} \hat{\underline{z}} \qquad \text{Equation 2.7.2}$$

$\underline{\mu}_m$ vector magnetic dipole moment of an electron orbit

i current associated with the electron rotational orbit

r radius of electron orbit

As a particle moves from a weak field region to a strong field region in the course of its thermal motion, it sees an increasing B-field and therefore its $v_{\perp}$ must increase in order to keep μ_m constant. Since its total energy must remain constant, v_z must necessarily decrease. The smallest pitch angle θ of a confined particle is given by:

$$\sin^2\theta_m = \frac{B_0}{B_m} \equiv \frac{1}{R_m} \qquad \text{Equation 2.7.3}$$

R_m mirror ratio

θ_m pitch angle of the orbit in the weak field region

All particles at initial condition B_0 having pitch angles of between 90° and θ_m° will be reflected. Equation 2.7.3 defines the boundary of a region in velocity space called the ‘loss cone’. Particles with $\theta < \theta_m$ will not mirror, unless the field is increased above B_m.

2.7.2 Fluid Model

This model is different to the particle model as it ignores the motion of the individual particles and treats the macroscopic motion of the plasma as a fluid, averaging over the Larmor orbits of the particles and therefore losing microscopic detail. The microscopic plasma properties are, in effect, wiped out and the macroscopic plasma dynamics described in terms of well chosen electric, magnetic and mechanical fluid properties. This model hence develops hydrodynamics to become magneto hydrodynamics (MHD) i.e. a conducting fluid in electric and magnetic fields. The set of fluid equations include the continuity equation, Equation 2.7.4, the conservation of momentum, Equation 2.7.5, and Maxwell's equations (refer to Equations 2.3.1 to 2.3.4). The equation of state which relates pressure to number density is given in Equation 2.7.6.

The continuity equation relates to the conservation of matter which requires that the total number of particles in a volume can change only if there is a net flux of particles across the surface which bounds that volume.

$$\frac{\partial n}{\partial t} + \underline{\nabla} \cdot (n\underline{v}) = 0 \qquad \text{Equation 2.7.4}$$

n number density

v velocity of particle

Equation 2.7.5 defines the conservation of momentum combining the effect of pressure, the Lorentz force and Newton's 2nd Law into the same expression.

$$mn\left(\frac{\partial}{\partial t} + \underline{v} \cdot \underline{\nabla}\right)\underline{v} = en(\underline{E} + \underline{v} \times \underline{B}) - \nabla P \qquad \text{Equation 2.7.5}$$

m mass of particle

P pressure (neglected for a cold plasma)

Equation 2.7.6 is the equation of state relating pressure to number density, however as mentioned before for a cold plasma, *P* tends to zero.

$$P = C\rho^{\gamma_{sp}} \qquad \text{Equation 2.7.6}$$

C constant

γ_{sp} ratio of specific heats C_p/C_v

Equations 2.7.4, 2.7.5, Maxwell's Equations (2.3.1 to 2.3.4) and Equation 2.7.6, are the plasma wave equations.

The fluid model is useful for describing large scale collective effects where the individual particles can be ignored.

2.7.3 Kinetic Theory

This is the most complete of the three (particle, fluid and kinetic) plasma models, but is also the most difficult to use to obtain results. It describes plasma via evolution of its distribution functions, Equations 2.7.7 and 2.7.8:

$$f_e(\underline{r}, \underline{v}, t) \qquad \text{Equation 2.7.7}$$

$$f_i(\underline{r}, \underline{v}, t) \qquad \text{Equation 2.7.8}$$

They describe the number density of particles in an infinitesimally small volume element centred at the point (r, v) at time t.

Information about the distribution of velocities of particles within the fluid element gets lost when using the fluid model. One needs to use a description that is in 6-dimensional (r, v) space, beginning with the distribution function, f(r, v, t), described by the kinetic theory. This introduces a description in microscopic detail that was not present within the fluid model.

One uses the kinetic equation, 2.7.9:

$$\frac{\partial f}{\partial t} + \underline{v} \cdot \frac{\partial f}{\partial \underline{r}} + \frac{\underline{F}}{m} \cdot \frac{\partial f}{\partial \underline{v}} = \left(\frac{\partial f}{\partial t}\right)_c \qquad \text{Equation 2.7.9}$$

In the case where $\left(\frac{\partial f}{\partial t}\right)_c$ is zero, we get collisionless plasma, and so giving the collisionless Bolztmann equation below, 2.7.10:

$$\frac{\partial f}{\partial t} + \underline{v} \cdot \frac{\partial f}{\partial \underline{r}} + \frac{\underline{F}}{m} \cdot \frac{\partial f}{\partial \underline{v}} = 0 \qquad \text{Equation 2.7.10}$$

This is obtained by integration of the Klimontovich distribution function, 2.7.11:

$$f_K(\underline{r}, \underline{v}, t) = \sum_{i=1}^{N} \delta[\underline{r} - \underline{r}_i(t)]\delta[\underline{v} - \underline{v}_i(t)] \qquad \text{Equation 2.7.11}$$

f_K Klimontovich distribution function

Equation 2.7.10 is known as the Vlasov equation when $\underline{F}$ is represented by Equation 2.7.1 (the Lorentz Force). The Vlasov-Maxwell equations are the starting point for most calculations in plasma kinetic theory. By integrating over $f(\underline{r},\underline{v},t)$ the fluid equations are obtained and so it is seen that the kinetic equation provides both a macroscopic and microscopic description of plasma.

The kinetic theory is required where one cannot average over particles, for example, where the particles have a mathematically complex distribution function and with an instability that critically depends on the structure in that distribution. This is relevant

in the present case as the horseshoe distribution function is itself a mathematically complex problem. The process of Landau damping can be described using this model; it is the effect of damping (exponential decrease as a function of time) of longitudinal space charge wave in plasma or a similar environment. This phenomenon prevents instability from developing, and creates a region of stability in the parameter space.

2.8 Unbounded Homogeneous Plasma Wave Theory

2.8.1 Introduction

From the early 1920's to the early 1940's, due to practical concerns, experimental studies were carried out in the laboratory and geophysically on the subject of radio wave propagation in plasmas. This led to the development of theory by, amongst others, Langmuir, Tonks, Hartree and Alfven. This research provided an important insight into the internal dynamical behaviour of plasmas.

Plasma waves tend to be non-linear phenomena. Real plasmas are non-linear inhomogeneous, anisotropic, dissipative and dispersive. The Vlasov equation, 2.7.10, can be used to predict expressions for the dispersion relations of many types of waves, for example, electron-cyclotron, ion-cyclotron, Bernstein modes, etc. The problem is fairly simple in a low temperature plasma unless there is a strong magnetic field. In the absence of a bias magnetic field the plasma has a simple cut-off behaviour but adding a magnetic field allows a number of waves to propagate at very low frequencies. Due to the wide discrepancy in their masses, some waves (usually high frequency ones) resonate with the electrons, whereas others tend to couple to the ion motion.

2.8.2 Basic Wave Concepts

The electric field in a plane wave is expressed in general by a superposition of two linearly independent solutions of the wave equation and is written in the form expressed in Equation 2.8.1. The z axis has in this case been chosen along the wave vector $\underline{k}$.

$$\underline{E}(z, t) = [E_{x0}\hat{\underline{x}} + E_{y0}e^{i\delta}\hat{\underline{y}}]\exp i(kz - \omega t + \alpha) \qquad \text{Equation 2.8.1}$$

E_x and E_y are both complex amplitudes and are shown below. E_{x0} and E_{y0} are both real and $\delta=\beta-\alpha$.

$$E_x = E_{x0}\exp(i\alpha) \qquad E_y = E_{y0}\exp(i\beta)$$

[Allen & Phelps 1977]

In general, the polarisation of an electromagnetic wave is elliptical and this can be seen if δ is set to be $\pm\pi/2$ and put into Equation 2.8.1. Special cases, where $E_{x0}=E_{y0}$ means the field becomes circularly polarised, and, if E_{x0} or E_{y0} = 0 then it becomes linearly polarised. If an electromagnetic wave is propagating perpendicular to a static magnetic field that is polarised along the z-axis, then the wave will have components in the O or X mode, (E_z and $E_\perp$ respectively). If the wave is propagating parallel to the magnetic field, then it is polarised in either the R or L mode. The orientation and magnitude of the static magnetic field determines the frequency and direction of individual particle motion for electrons and ions and therefore strongly influences the waves resonance and propagation, [Boyd & Sanderson 1969, 2003, Stix 1992]. The definitions arise since a wave polarised perpendicular to a strong magnetic field will give rise to particle motion that is subject to the Lorentz force, whereas if the E-field of the wave is parallel to B_0 then no such coupling will occur. Similarly different particle charges and masses give rise to different rotational resonances for circularly polarised waves propagating along B_0. Figure 2.9 illustrates the dispersion curve for an electromagnetic wave in an unmagnetised plasma.

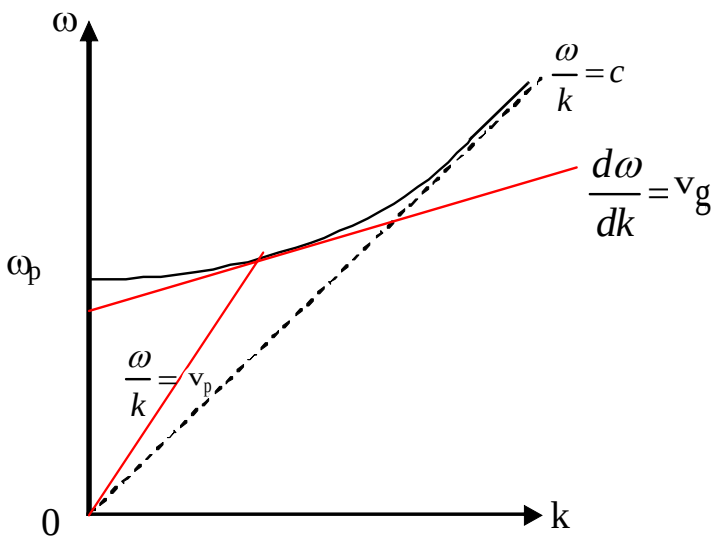

Figure 2.9: Dispersion curve for an electromagnetic wave, v_g is the group velocity, v_p is the phase velocity

Figure 2.9 also illustrates the definition and physical significance of the group and phase velocities. In this case the group velocity appears as the propagation velocity of a wave packet envelope. When the phase velocity is independent of wavelength there is no dispersion. An electromagnetic wave which propagates in a plasma is an example of normal dispersion where $v_g < v_p$.

2.9 Waves in Cold Plasma

2.9.1 Introduction

In cold plasma, the thermal speeds of the particles are much smaller than the phase speeds of the waves. The cold plasma wave equations provide a very good initial description of wave phenomena in collisionless plasmas. The general dispersion equation of a wave is:

$$F(\omega, k) = 0 \qquad \text{Equation 2.9.1}$$

Where F is a function linking ω and k. The linearized versions of the cold plasma equations are shown in Equations 2.9.2 to 2.9.7, where second order AC terms have been ignored.

$$\frac{\partial n_1}{\partial t} + \underline{\nabla} \cdot (n_0 \underline{v}_1) = 0 \qquad \text{Equation 2.9.2}$$

$$\frac{\partial \underline{v}_1}{\partial t} = \frac{e}{m}(\underline{E}_1 + \underline{v}_1 \times \underline{B}_0) \qquad \text{Equation 2.9.3}$$

$$\underline{\nabla} \times \underline{E}_1 = -\frac{\partial \underline{B}_1}{\partial t} \qquad \text{Equation 2.9.4}$$

$$\underline{\nabla} \times \underline{B}_1 - \frac{1}{c^2}\left(\frac{\partial E_1}{\partial t}\right) = \mu_0 \underline{j} = \mu_0 \sum en_0 \underline{v}_1 \qquad \text{Equation 2.9.5}$$

$$\underline{\nabla} \cdot \underline{E}_1 = \frac{q}{\varepsilon_0} = \frac{1}{\varepsilon_0} \sum en_1 \qquad \text{Equation 2.9.6}$$

$$\underline{\nabla} \cdot \underline{B}_1 = 0 \qquad \text{Equation 2.9.7}$$

It is assumed here that v_0 and E_0 are zero. B_1 and E_1 are the AC fields of the wave, $\underline{v}_1$ is the AC particle velocity, $\underline{B}_0$ is finite and n_0 is the background number density with n_1 a perturbation of this value.

2.9.2 Waves in Cold Magnetised Plasma

The wave equation for the electric field can be expressed (assuming all variables vary as $\exp i(\underline{k} \cdot \underline{r} - \omega t)$) as in Equation 2.9.8:

$$\underline{n} \times (\underline{n} \times \underline{E}_1) = -\underline{E}_1 - \frac{i}{\varepsilon_0 \omega} \underline{\sigma} \cdot \underline{E}_1 = -\varepsilon \cdot \underline{E}_1 \qquad \text{Equation 2.9.8}$$

σ conductivity tensor

ε cold plasma dielectric tensor

Where the dielectric tensor is written in matrix format as shown, choosing B_0 to be in the z-direction.

$$\varepsilon = \begin{bmatrix} S & -iD & 0 \\ iD & S & 0 \\ 0 & 0 & P \end{bmatrix} \qquad \text{Equation 2.9.9}$$

The components for the cold plasma dielectric tensor are given below:

$$S = \frac{1}{2}(R + L) = 1 - \frac{\omega_p^2(\omega^2 + \Omega_i\Omega_e)}{(\omega^2 - \Omega_i^2)(\omega^2 - \Omega_e^2)}$$

$$D = \frac{1}{2}(R - L) = \frac{\omega_p^2\omega\,(\Omega_i + \Omega_e)}{(\omega^2 - \Omega_i^2)(\omega^2 - \Omega_e^2)}$$

$$R = 1 - \frac{\omega_p^2}{(\omega + \Omega_i)(\omega + \Omega_e)}$$

$$L = 1 - \frac{\omega_p^2}{(\omega - \Omega_i)(\omega - \Omega_e)}$$

$$P = 1 - \frac{\omega_p^2}{\omega^2}$$

The wave propagation direction $\underline{n}$ is given by:

$$\underline{n} = (n\sin\theta, 0, n\cos\theta) \qquad \text{Equation 2.9.10}$$

It should be noted that the plasma frequency is written as $\omega_p^2 = \omega_{pi}^2 + \omega_{pe}^2$ and θ is the angle the wave makes with the magnetic field.

Equation 2.9.11 is written where $\underline{n} = \frac{c\underline{k}}{\omega}$ and is a dimensionless wave propagation vector thus allowing the matrix to be rewritten in the form shown in Equation 2.9.12.

$$(\underline{n}\cdot\underline{E})\underline{n} - n^2\underline{E} + \varepsilon\cdot\underline{E} = 0 \qquad \text{Equation 2.9.11}$$

$$\begin{bmatrix} S - n^2\cos^2\theta & -iD & n^2\cos\theta\sin\theta \\ iD & S - n^2 & 0 \\ n^2\cos\theta\sin\theta & 0 & P - n^2\sin^2\theta \end{bmatrix} \begin{bmatrix} E_x \\ E_y \\ E_z \end{bmatrix} = 0 \qquad \text{Equation 2.9.12}$$

The determinant of Equation 2.9.12 gives the cold plasma wave dispersion relation shown below;

$$An^4 - Bn^2 + C = 0 \qquad \text{Equation 2.9.13}$$

Where:

$$A = S\sin^2\theta + P\cos^2\theta \qquad \text{Equation 2.9.14}$$

$$B = RL\sin^2\theta + PS(1 + \cos^2\theta) \qquad \text{Equation 2.9.15}$$

$$C = PRL \qquad \text{Equation 2.9.16}$$

The following sections will look at waves travelling parallel ($\theta=0$) and perpendicular ($\theta=\pi/2$) to the magnetic field, their resonances and cut-offs.

In cold, non-streaming plasma there are no sources of free energy to drive instabilities and no dissipation terms to produce decaying waves which means that there can only be real solutions of n^2 from Equation 2.9.13. The values for n will either be pure real corresponding to wave propagation or will be pure imaginary corresponding to evanescence. The transition at which propagation goes to evanescence occurs when n^2 goes through zero or infinity. The first case at $n^2=0$ is called a cut-off, as it defines the frequency above or below which the wave ceases to propagate at any angle ($v_p \rightarrow \infty$). $n^2=0$ is a solution if C=0, i.e. P, R or L = 0:

P=0: $\omega = \omega_p$

R=0: $$\omega = \left[\omega_p^2 + \frac{(\Omega_i - \Omega_e)^2}{4}\right]^{\frac{1}{2}} - \frac{(\Omega_i + \Omega_e)}{2} \equiv \omega_R$$

L=0: $$\omega = \left[\omega_p^2 + \frac{(\Omega_i - \Omega_e)^2}{4}\right]^{\frac{1}{2}} + \frac{(\Omega_i + \Omega_e)}{2} \equiv \omega_L$$

The second case where $n^2 \rightarrow \infty$ defines a resonance. The wave is not necessarily stopped altogether, but has a defined cone of propagation. From Equation 2.9.13, if $n^2 \rightarrow \infty$ it is necessary that A=0 if the wave is to propagate and therefore $\tan^2\theta = -\frac{P}{S}$. This equation allows θ_{res}, the resonant angle, to be defined, giving:

$$\tan^2\theta_{res} = -\frac{P}{S} \qquad \text{Equation 2.9.17}$$

A wave that experiences a resonance will propagate either for:

a) $0 \le \theta < \theta_{res}$ but not $\theta_{res} < \theta \le \frac{\pi}{2}$

OR

b) $\theta_{res} < \theta \leq \frac{\pi}{2}$ but not $0 \leq \theta < \theta_{res}$

These are the principal resonances that define angles above or below which a particular wave frequency does not propagate. From Equation 2.9.17, the principal resonances, $\theta_{res} = 0$ and $\theta_{res} = \frac{\pi}{2}$ occur when Equations 2.9.18 and 2.9.19 are satisfied respectively:

$$P=0 \text{ or } S = \frac{1}{2}(R + L) \rightarrow \infty \qquad \text{Equation 2.9.18}$$

$$S=0 \qquad \text{Equation 2.9.19}$$

The former case where P=0 is a cut-off where $n^2=0$, as previously mentioned. The latter expression for S, in Equation 2.9.18, gives the following results for two different resonances, either:

$$R \rightarrow \infty \text{ as } \omega \rightarrow -\Omega_e = |\Omega_e| \qquad \text{Equation 2.9.20}$$

which is the electron cyclotron resonance, or:

$$L \rightarrow \infty \text{ as } \omega \rightarrow \Omega_i \qquad \text{Equation 2.9.21}$$

which is the ion cyclotron resonance.

The cyclotron resonances at $\theta = 0$ involve either electrons or ions, NOT both. For the perpendicular resonances at $\theta = \pi/2$ both ions and electrons are involved together and are consequently known as the hybrid resonances, [Boyd & Sanderson 1969, 2003]. The solution for the hybrid resonance can be written as two separate expressions, one for the upper hybrid and one for the lower hybrid;

$$\omega^2_{UH} \approx (\omega^2_p + \Omega^2_i + \Omega^2_e) \approx \omega^2_{pe} + \Omega^2_e \qquad \text{Equation 2.9.22}$$

$$\omega^2_{LH} \approx -\frac{\Omega_i \Omega_e(\omega^2_p - \Omega_i \Omega_e)}{\omega^2_p + \Omega^2_i + \Omega^2_e} \approx \begin{cases} |\Omega_i \Omega_e| & (\omega^2_p \gg \Omega^2_e) \\ \omega^2_{pi} + \Omega^2_i & (\omega^2_p \ll \Omega^2_e) \end{cases} \qquad \text{Equation 2.9.23}$$

•Resonances

Absorption of the wave energy by the plasma is an indication that a resonance has occurred, as opposed to cut-off where the wave is reflected. Also, contrary to the cut-off case, resonance conditions do depend on the direction of propagation of the wave relative to the magnetic field.

•Cut-offs

As cut-off is approached within the plasma, the wave magnetic field decreases whilst the electric field increases. At cut-off the wave is reflected and this itself gives rise to a useful diagnostic, plasma reflectometry, where measurement of time-of-flight and frequency allow plasma density profiles to be measured. The cut-off points are independent of the direction of propagation of the wave relative to the magnetic field.

2.9.3 Plasma With and Without a Magnetic Field

Two practical cases will be considered now, one where there is no static magnetic field present in the plasma, and one where a magnetic field is applied.

•Field Free Plasma

With no magnetic field there is no preferred direction of propagation and so as with Equation 2.9.11, n is assumed to be taken in the z direction. Equation 2.9.12 can be written in a simplified matrix form as there is now the condition where $\theta=0$ and so S=P and D=0:

$$\begin{bmatrix} 1-\frac{\omega_p^2}{\omega^2}-n^2 & 0 & 0 \\ 0 & 1-\frac{\omega_p^2}{\omega^2}-n^2 & 0 \\ 0 & 0 & 1-\frac{\omega_p^2}{\omega^2} \end{bmatrix} \begin{bmatrix} E_x \\ E_y \\ E_z \end{bmatrix} = 0 \qquad \text{Equation 2.9.24}$$

There are two solutions (corresponding to two types of wave) to this matrix. The first is with $\underline{E}=(0,0,E_z)$ and $\omega=\omega_p$. This corresponds to a longitudinal wave with k//E, the wave is propagating parallel to the electric field. Within the cold plasma limit, the

group velocity for the longitudinal case is $\underline{v}_g = \frac{d\omega}{dk} = 0$, meaning this particular wave does not propagate.

The second solution is that $E_z=0$ and $\omega^2=\omega_p{}^2+k_z{}^2c^2$ which is a transverse wave with $\underline{k}\perp\underline{E}$. The transverse wave has a stop band at $0<\omega<\omega_p$. ω_p is the natural frequency with which the plasma responds to any electric field and if this frequency is greater than the frequency of such a field, then the particles block out the electric field.

•Plasma with Magnetic Field Present

For the situation where there is a non-zero magnetic field, a further two cases can be studied. One where the wave propagates parallel to the magnetic field, Section 2.9.4, and one where it propagates perpendicular, Section 2.9.5.

2.9.4 Parallel Propagation: Ion & Electron Cyclotron Resonances

In the parallel case the wave propagates along the magnetic field and so has $\theta=0$, meaning that Equation 2.9.12 can be simplified to Equation 2.9.25:

$$\begin{bmatrix} S-n^2 & -iD & 0 \\ iD & S-n^2 & 0 \\ 0 & 0 & P \end{bmatrix} \begin{bmatrix} E_x \\ E_y \\ E_z \end{bmatrix} = 0 \qquad \text{Equation 2.9.25}$$

The dispersion relation for longitudinal waves is the same as in the field-free case, $P=0$ and $\omega^2=\omega_p{}^2$. There is no effect on this mode by the magnetic field as the plasma oscillations are in the same direction as the magnetic field and so there is no Lorentz force. Solutions for the transverse wave dispersion relation, for the R and L modes, are given in Equations 2.9.26 and 2.9.27 respectively.

$$n^2 = R = 1 - \frac{\omega_p^2}{(\omega+\Omega_i)(\omega+\Omega_e)} \qquad \text{Equation 2.9.26}$$

$$n^2 = L = 1 - \frac{\omega_p^2}{(\omega-\Omega_i)(\omega-\Omega_e)} \qquad \text{Equation 2.9.27}$$

The R mode, Figure 2.10, has a cut-off at ω_R and a principal resonance at $|\Omega_e|$. At both the lowest frequencies ($\omega \rightarrow 0$) and when $\omega \rightarrow \propto$ it is seen that $n^2>0$, and so the stop band for the R mode is between $|\Omega_e|$ and ω_R. An approximate dispersion relation for the R mode is shown in Equation 2.9.30. The L mode, Figure 2.11, has a cut-off at ω_L and a principal resonance at Ω_i. It also has $n^2>0$ at $\omega \rightarrow 0$ and $\omega \rightarrow \propto$, and thus has its stop band between Ω_i and ω_L. The approximate dispersion relation for the L mode is shown in Equation 2.9.31.

In the limit where $\omega \sim \Omega_e$ and $\Omega_e >> \Omega_i$, Equations 2.9.26 and 2.9.27 can be represented as in Equation 2.9.28 and Equation 2.9.29.

$$n^2 = R = 1 - \frac{\omega_p^2}{\omega\,(\omega + \Omega_e)} \qquad \text{Equation 2.9.28}$$

$$n^2 = L = 1 - \frac{\omega_p^2}{\omega\,(\omega - \Omega_e)} \qquad \text{Equation 2.9.29}$$

These can be further manipulated mathematically to give the forms shown below;

$$\omega^2 = k^2c^2 + \frac{\omega\,\omega_p^2}{\omega - |\Omega_e|} \qquad \text{Equation 2.9.30}$$

$$\omega^2 = k^2c^2 + \frac{\omega\,\omega_p^2}{\omega + |\Omega_e|} \qquad \text{Equation 2.9.31}$$

Equations 2.9.30 and 2.9.31 are valid in the intermediate frequency limit where $\omega \sim \Omega_e$.

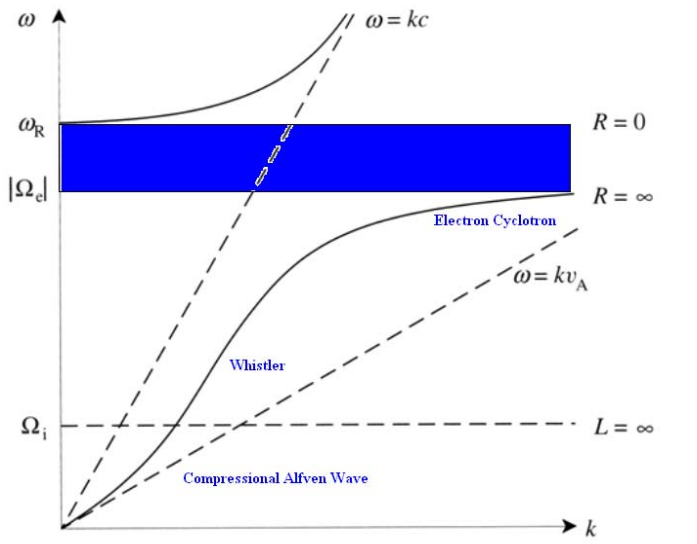

Figure 2.10: Dispersion diagram for R-mode EM waves

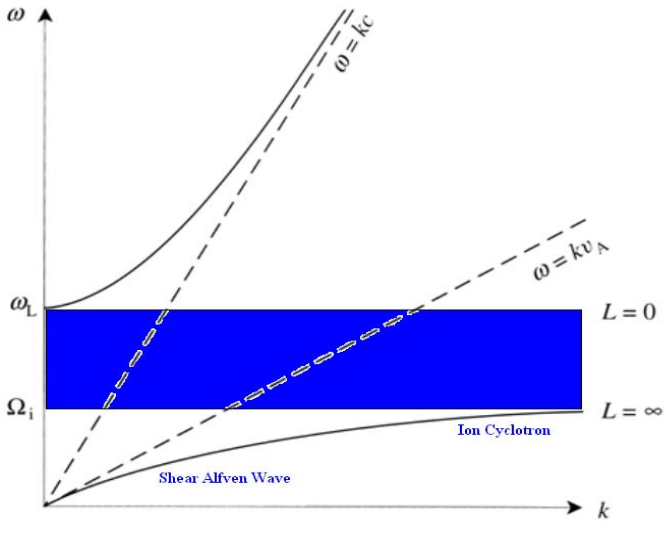

Figure 2.11: Dispersion diagram for L-mode EM waves

As can be seen from Figures 2.10 and 2.11 of the R and L modes, there are points on the plots referring to the electron cyclotron, ion cyclotron, whistler waves, and

compressional and shear Alfvén waves. The R-branch links to the compressional Alfven (and the L-branch to the shear Alfven) branch at low frequencies where $0 < \omega < \Omega_i$. The R-branch also links to the whistler waves, so called due to their descending pitch in audio frequency as they propagate along the magnetic field lines in the magnetosphere, [Bell & Buneman 1964, Koch 2006].

2.9.5 Perpendicular Propagation

In this case, k is perpendicular to B_0, and there is an angle of $\theta = \pi/2$. Looking back to Equation 2.9.12 a new version of the matrix is obtained, Equation 2.9.32.

$$\begin{bmatrix} S & -iD & 0 \\ iD & S - n^2 & 0 \\ 0 & 0 & P - n^2 \end{bmatrix} \begin{bmatrix} E_x \\ E_y \\ E_z \end{bmatrix} = 0 \qquad \text{Equation 2.9.32}$$

The ordinary, O mode polarised in the z direction is independent of magnetic field due to the electric field making the particles travel parallel to B, i.e. there is no Lorentz force. It has the simple dispersion relation shown in Equation 2.9.33 and a dispersion curve the same as that in Figure 2.9. The stop band for this mode occurs between $\omega=0$ and $\omega=\omega_p$.

$$n^2 = P \qquad \text{Equation 2.9.33}$$

The extraordinary, X mode has the dispersion relation shown in Equation 2.9.34 and a more complex dispersion diagram, shown in Figure 2.12.

$$n^2 = \frac{RL}{S} \qquad \text{Equation 2.9.34}$$

In terms of the electron and ion cyclotron frequencies, this equation can be extended to be represented as shown in Equation 2.9.35;

$$\omega^2 = \frac{1}{2}\left[\frac{(\omega + \Omega_i)(\omega + \Omega_e)}{(\omega + \Omega_i)(\omega + \Omega_e) - \omega_p^2} + \frac{(\omega - \Omega_i)(\omega - \Omega_e)}{(\omega - \Omega_i)(\omega - \Omega_e) - \omega_p^2}\right] k^2 c^2 \qquad \text{Equation 2.9.35}$$

As can be seen from the diagram below, it has stop bands at intervals in frequency between ω_{LH} to ω_L and between ω_{UH} and ω_R. Its cut-offs as $k \to 0$, occur at ω_R and ω_L, i.e. R=0 and L=0 respectively. Its resonances as $k \to \infty$, occur at the upper and lower hybrid frequencies, S=0. This thesis investigates experimental electron

cyclotron resonances close to cut-off where radiation emitted in the presence of a background plasma could be absorbed. This could be to do with the proximity of the R mode cut-off to the upper hybrid resonance point, Figure 2.12.

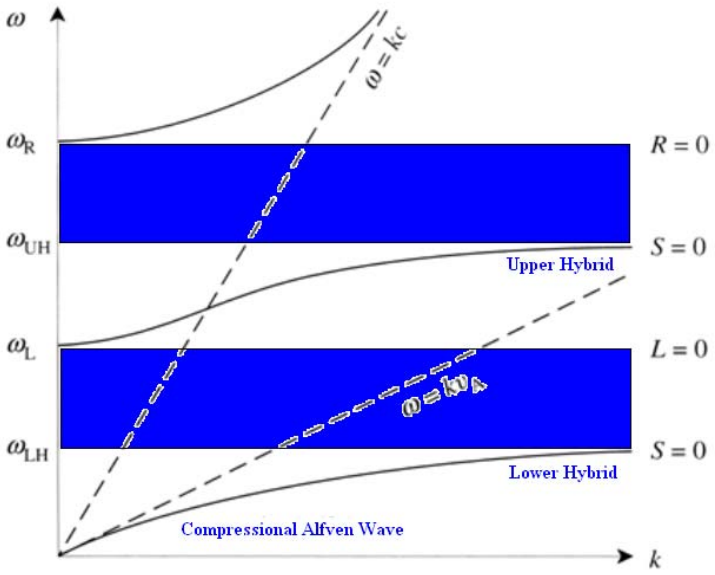

Figure 2.12: Dispersion diagram for X-mode EM waves

For low densities, where $\omega_p^2 \leq \Omega_e^2$, the resonance of the lower hybrid is mainly an ion resonance occurring when the ion motion is synchronised with the electric field. For the upper hybrid case at higher frequencies, it is the ions which are insignificant and the resonance occurs between the electrons and the electric field. The upper and lower hybrid resonances have already been shown in Equations 2.9.22 and 2.9.23.

2.10 Gas Discharges

A discharge may occur when a gas becomes ionised (which maybe a type of plasma), with typically equal quantities of positive and negative charges and a large number of neutrals. Low pressure discharges and plasmas are commonly used in applications. Most important in the industrial sense is in the microelectronics industry for surface treatment and etching for fabrication of integrated circuits, as well as deposition of thin protective coatings etc. Other major applications are in the light industry,

fluorescent and neon bulbs for signs etc. and for flat screen televisions. As part of the AKR experiment a low pressure discharge was formed using a variation of the Penning geometry, thus giving the effect of a background plasma to more precisely compare with the auroral scenario, where within the auroral density cavity the number density is of the order $1cm^{-3}$, plasma frequency 9kHz and the cyclotron frequency ~300kHz. Therefore with a cyclotron frequency ~5.21GHz in the laboratory a plasma frequency of ~160-300MHz is required which has corresponding number densities ~$3.18x10^{14}$-$1.12x10^{15}m^{-3}$.

2.10.1 Townsend Discharge

The Townsend discharge nominally takes place between two parallel plates, one being the cathode and the other the anode. A gas is placed between these two plates and is represented in Figure 2.13.

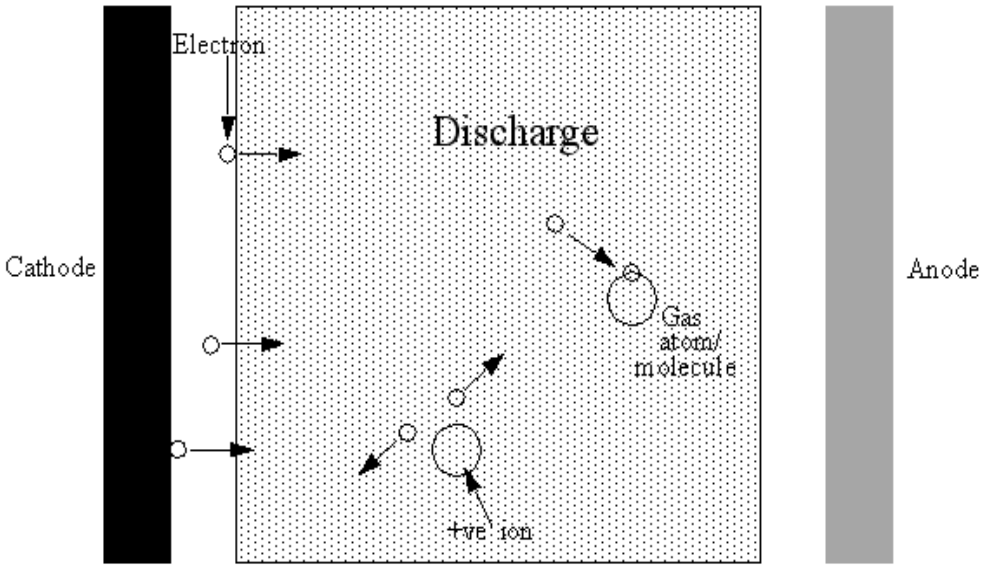

Figure 2.13: Collisions in the Townsend parallel plate geometry

The diagram in Figure 2.14 shows the voltage and current characteristics of a DC discharge, with attention to the Townsend as well as normal glow discharge, abnormal glow discharge and arc discharges.

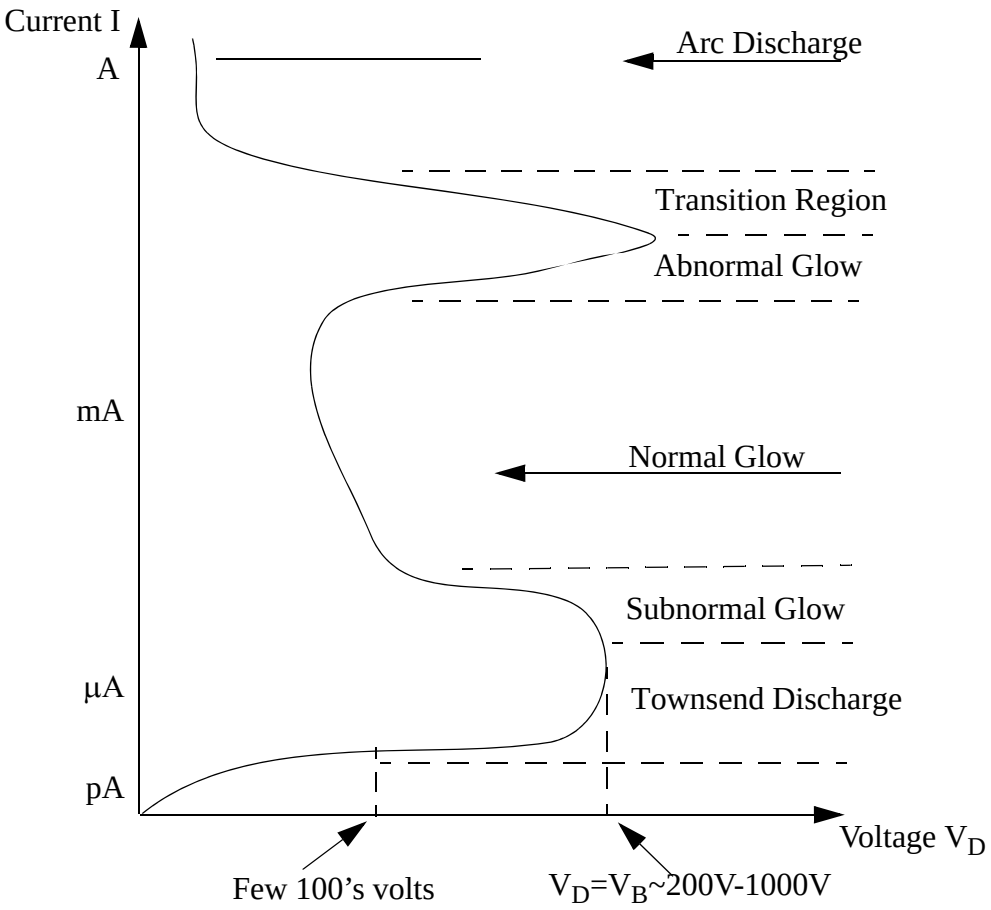

Figure 2.14: Illustration of typical current-voltage characteristics for a gas discharge

•Self Sustaining Discharges

The Townsend discharge can be started by injecting electrons by thermionic or photoelectric stimulation at the cathode, but can also self initiate when a high enough voltage is applied. In the case of the 'initiated start' with an electric field, electrons are emitted from the cathode surface and as normal make their way across the electrode spacing towards the anode. In a vacuum when there is no gas present, all the electrons are collected on the anode surface once they have transferred their potential to kinetic energy. When there is a gas present in the diode spacing the electron propagation properties are changed by collisions. If the incoming electrons have a certain minimum kinetic energy when colliding with the atoms in the gas they may knock an electron from its outer shell, leaving an ion behind. The minimum kinetic energy must

exceed the ionisation threshold of the neutrals. The bombarding electron shoots off in another direction following this inelastic collision having had its kinetic energy reduced. Its path length is altered as it now travels in a non-direct path to the anode, having more collisions along the way. The electron which has been knocked out of the gaseous atom now has increased potential energy due to the collision and starts to make its way to the anode in an equally indirect manner. The lengthened path of these electrons means that ionisation collisions are more probable since they spent more time within the gas. An avalanche effect is apparent as each electron on ionising collision creates a second electron, both of which then go on to create more electrons and so on. The ions that have now been produced are attracted to the cathode, and at an immense rate, travel back and bombard its surface in what is known as the cathode fall. This can result in secondary electrons being emitted. The point where the discharge becomes self sustained is when the expression in Equation 2.10.1 is satisfied:

$$\gamma(e^{\alpha d} - 1) = 1 \qquad \text{Equation 2.10.1}$$

α Townsend's first ionisation coefficient and relates to the number of ion/electron pairs that are created by a single electron per unit displacement from cathode to the anode

γ Townsend's second ionisation coefficient and relates to the number of secondary electrons that are emitted from the cathode per ion arriving

When the voltage across the discharge is increased the 1st Townsend coefficient tends to increase with increased electron temperature. This increases the bombardment of the cathode and increases the rate of the 2nd Townsend process. The criterion above is satisfied when one electron emitted from the cathode shall produce enough 'child' ions (directly or indirectly) in its path to the anode to yield at least one secondary electron to sustain the process, [Howatson 1976].

•Disadvantages of Parallel Plate Geometry

The main disadvantage of the parallel plate geometry found in the Townsend discharge, Figure 2.13, is its inability to work at low pressures. Decreasing pressures

corresponds to a decrease in atom density therefore the electrons which leave the cathode more often make a straight path to the anode without collisions, this means that the ionisation rate is very low and therefore so is the bombardment of the cathode by ions. This inhibits discharge ignition.

2.11 Super Critical Discharge Regimes

2.11.1 Normal Glow Discharge

A normal glow discharge occurs above Townsend ignition where current increases are associated with a decrease in voltage, an effect known as negative dynamic impedance. The current increases by covering a greater cathode region. The increased active volume compared to the perimeter area of the discharge column gives a reduced loss of charged particles, hence the drop in voltage required to sustain the discharge. This leads on to the regime of abnormal glow. [Chapman 1980]

2.11.2 Abnormal Glow Discharge

An abnormal glow discharge takes place when current is being carried on the entire cathode surface. The voltage begins to rise with current since the current density must increase.

2.12 Penning Discharge

2.12.1 Geometry and Advantages

The Penning geometry allows for effective trapping of the electrons (and ions) between two cathode plates. The setup is shown in Figure 2.15 and shows the electron trajectories as they are influenced by the magnetic field.

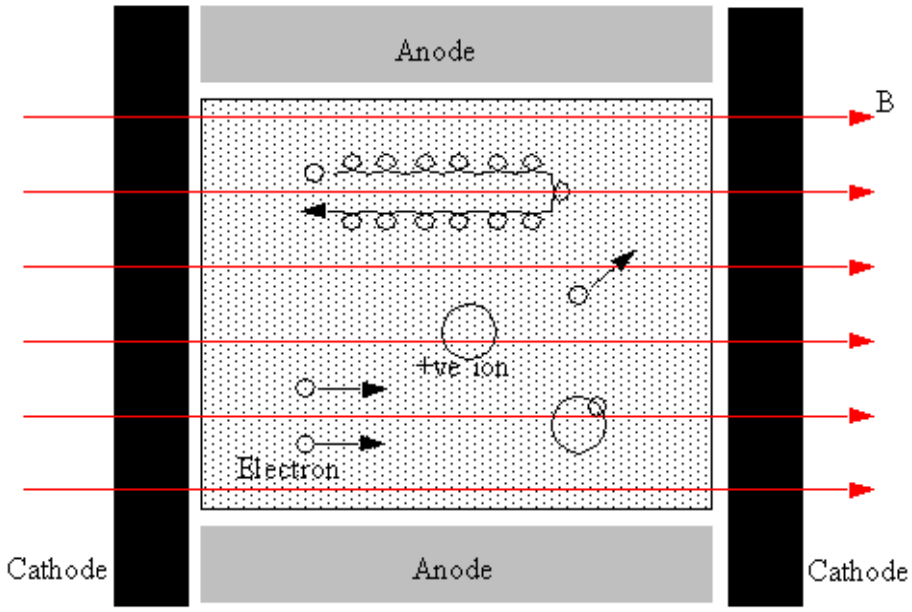

Figure 2.15: Penning Geometry

The Penning discharge uses the same principles of operation as that of the Townsend discharge process, but with crossed electric and magnetic fields. The main difference, and advantage, is that due to its geometry it can work at low pressures. Instead of a parallel plate setup, the Penning discharge operates with two cathodes on either side of a ring, or short cylindrical, anode, shown in Figure 2.15. In this configuration, even with low pressure, the discharge is started and will self sustain. This is due to the fact that if the electrons do not collide and ionise on the first trip through the cavity they do not go straight to the anode as they are prevented from doing so by the magnetic field. Instead they are spiralled towards the vicinity of the opposite cathode, are consequently repelled as they arrive there, and rebound back across the cavity. This results in the electrons having longer path lengths and staying within the region of the gas for longer thus increasing greatly the chance of ionisation and the discharge ignition, [Chambers et al 1998]. The design used in this experiment can be found in Section 3.8.

2.13 Probe Theory/Electric dipole antenna

In order to measure characteristics of a plasma, an electrostatic plasma probe may be deployed. The relevant theory required to interpret this diagnostic involving sheath theory, the Bohm criterion and RF antenna theory are discussed in the following sections.

2.13.1 Sheath Theory

When a plasma is brought into contact with a solid object, for example a probe, a boundary region forms, called a sheath. The sheath surrounding a probe is normally a few Debye length (Equation 2.6.7) in thickness. The sheath area is the part of the plasma where charge neutrality does not exist, as it does in the main plasma body, but instead has a net charge. Any inserted object is bombarded by electrons which therefore (if it is floating) acquires a negative charge and repels electrons from the immediate surrounding area i.e. the sheath region, leaving it to be positively charged. Equation 2.13.1 shows the reduced form of the non-linear differential 'sheath' equation. Assuming collisionless motion of ions;

$$\left(\frac{dV}{dx}\right)^2 = \frac{V^2}{\lambda_D^2}\left(1 - \frac{k_B T_e}{2E_s}\right) \qquad \text{Equation 2.13.1}$$

V electrostatic potential

E_s 'beam like' kinetic energy of ions

Equation 2.13.1 implies that $E_s \geq \frac{k_B T_e}{2}$ as the LHS of Equation 2.13.1 is positive. This is known as the Bohm criterion and implies that any ions which enter the sheath region must have a minimum kinetic energy of $\frac{1}{2}k_B T_e$ i.e. ions enter the sheath at the Bohm velocity, as given in Equation 2.13.8. The potential difference across the pre-sheath, V_s, is given by Equation 2.13.2. Notice these depend only on the electron temperature, not that of the ions:

$$V_s \geq \frac{k_B T_e}{2e} \qquad \text{Equation 2.13.2}$$

The Bohm model used to determine the electron number density is discussed at the end of Section 2.13.2.

2.13.2 Probe Theory

Understanding the theory of sheaths allows a conducting probe to be inserted into a plasma and used as a diagnostic. The current and voltage at the probe may be measured and an IV trace will be plotted. The electron temperature is found from the gradient of the logarithm of **j** against V_{pr}, where;

$$j = j_0 \exp\left(\frac{eV_{pr}}{kT_e}\right) \qquad \text{Equation 2.13.3}$$

and

$$\ln j = \ln j_0 + \frac{eV_{pr}}{kT_e} \qquad \text{Equation 2.13.4}$$

V_{pr} probe voltage

Once the value of T_e is known, it can be used in Equation 2.13.5 to find the value of the thermal velocity of the electrons. This in turn, along with a value for j (at the plasma potential) from the graph, leads to the number density of electrons within the bulk plasma, Equation 2.13.6. The plot of j versus V illustrates the relative values of the floating potential V_f and the plasma potential V_p.

$\frac{1}{2}mv_{th}^2 = \frac{3}{2}kT_e$ which rearranged gives:

$$v_{th} = \left(\frac{3kT_e}{m}\right)^{\frac{1}{2}} \qquad \text{Equation 2.13.5}$$

$$n_e = \frac{4j_0}{ev_{th}} \qquad \text{Equation 2.13.6}$$

j I/A and is taken from the plot and knowledge of the probe structure

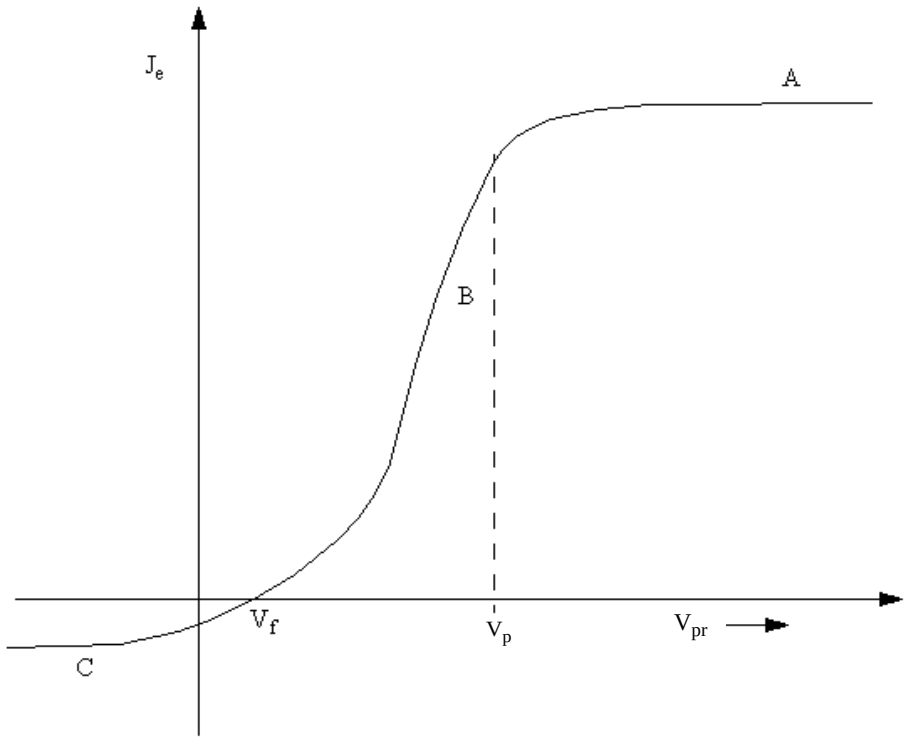

Figure 2.16: Example of plot obtained showing V_f, V_p and the point where the Ln is taken to allow for a value of T_e to be recorded

At the point marked V_p (the plasma potential) the potential of the electric probe is the same as that of the plasma. At this point charged particles flow towards the probe with the electrons dominating over the ions due to their smaller mass, and therefore it is electron current that is predominantly collected. The region at 'A' in Figure 2.16 is the saturation electron current. It is a relatively flat part of the plot providing the effective collection area of the probe stays relatively constant as the probe voltage is increased. This section of the curve corresponds to a positive probe potential (relative to V_p). If the probe bias is switched so that now the probe potential is negative (with respect to V_p), it will then attract ions and repel electrons. Therefore as is seen at region 'B' in the plot, the electron current at the probe falls off as V decreases. This region of the plot is called the transition region. The floating potential, V_f on the graph, is the point at which there is no net current flow as the probe has reached a sufficiently negative value at which it repels the excess thermal bombardment of electrons. When V

becomes large (negatively) one reaches an ion saturation current. This is region ‘C’ in Figure 2.16. It should be noted here some key differences between the ion and electron saturation collections:

- The first (most obvious) point is the mass difference, in that the ions are much heavier and slower moving than the electrons
- Secondly, the temperature of the electrons often differ from the that of the ions
- Lastly, in the presence of a magnetic field the motion of the electrons is more affected than that of the ions

If the gradient for the logarithm of the current is constant in the transition region then this confirms the Maxwellian distribution in the electrons. The ion temperature can not be measured using this method since the ions are already beam like as they enter the sheath region, as (at least at low pressures) they have less random energy than the electrons. Indeed the Bohm sheath criterion is written in terms that the ions must have a beam kinetic energy that exceeds the electron thermal energy and therefore any measurements taken by a probe can not be related back to the background bulk ion temperature.

It is important to note that the presence of a magnetic field can interfere with electron transport across the sheath. This is a complex problem and is strongly dependent on the plasma properties and probe configuration.

Equation 2.13.7 shows an alternative method of calculating the electron temperature as it can be difficult to pinpoint the proper gradient of the logarithmic plot when applying Equation 2.13.4.

$$T_e = \frac{\left|V_s - V_f\right| 2e}{k\left[1 + \mathrm{Ln}\left(\frac{2m_i}{\pi m_e}\right)\right]} \qquad \text{Equation 2.13.7}$$

The Bohm sheath criterion is another method which will be used in this research to estimate the plasma density. This method determined the number density of the

electrons based on an estimate of electron temperature, and uses the area of a cathode electrode as the ion collection surface. Starting with an expression for Bohm sheath velocity, i.e. the velocity of the ions as they cross the sheath-pre-sheath boundary, Equation 2.13.8, this is inserted into Equation 2.13.9, which can then be rearranged to obtain the number density.

$$v_{sh} = \left(\frac{kT_e}{m_i}\right)^{\frac{1}{2}} \qquad \text{Equation 2.13.8}$$

$$I_c = Anev_{sh} \qquad \text{Equation 2.13.9}$$

Where

A	area of electrode
I_c	ion current collected on the electrode

2.13.3 RF Antenna Probe Theory

•Using the probe with the spectrum analyser

A probe may be constructed to act as a short electric dipole. Equation 2.13.10 shows the electric field strength for such an idealised probe:

$$\underline{E} = \frac{p}{4\pi\varepsilon_0 r^3}(2\cos\theta\hat{r} + \sin\theta\hat{\theta}) \qquad \text{Equation 2.13.10}$$

This expression is for the condition where r<<λ', where r is the radial distance and $\lambda' = \frac{\lambda}{2\pi}$. So E falls off as the cube of the distance r for these static terms. If one moves far away from the dipole so that now r >> λ', then one is left with the radiation terms which now fall off as $\frac{1}{r}$.

$$\underline{E} = -\frac{[p]}{4\pi\varepsilon_0\lambda'^2 r}\sin\theta\hat{\theta} \qquad \text{Equation 2.13.11}$$

[p]	time retarded electric dipole moment; $[p] = t - \frac{r}{c}$

The expression in Equation 2.13.10 can be represented as a plot as is shown in Figure 2.17. The length of the arrows in the plot denote the strength of the field. (Logarithmic scale so dynamic range is extended). This equation describes the relationship between the electric field in the vicinity of the probe to the charges which appear on the probe terminals, in the limit that λ_D « probe length « λ.

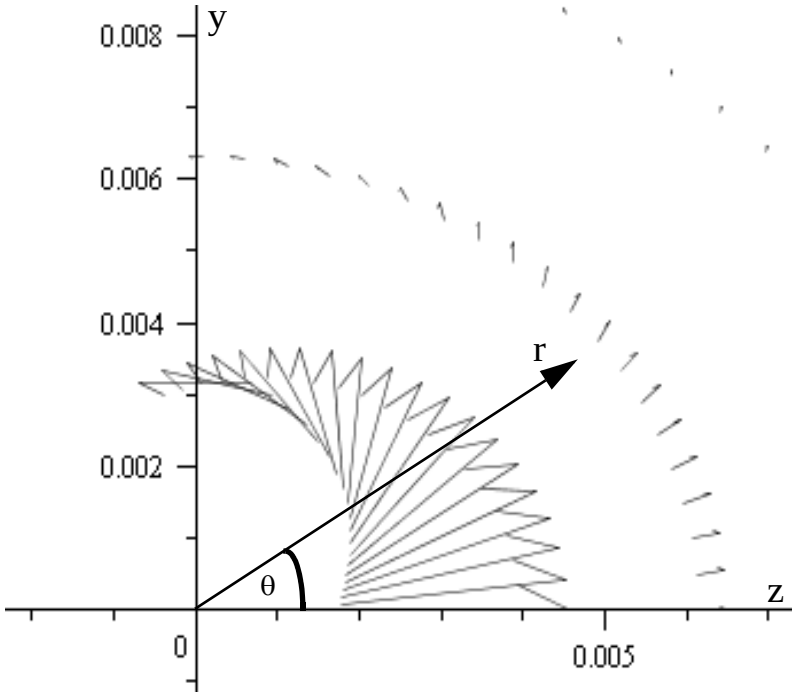

Figure 2.17: Electric field vector plot showing concentration of the field close to the dipole

As can be seen from the diagram, the electric field is concentrated at low values of r, i.e. close to the dipole and predominantly has an orientation along the z-axis, i.e. along the dipole. This implies that the antenna will strongly couple to those plasma oscillation signals that are associated with plasma motion along its length, i.e. along the magnetic field lines.

Chapter 3 : Apparatus and Experimental Techniques

Chapter 3 : Apparatus and Techniques

3.1 Introduction

The formation of an electron beam with a horseshoe distribution and the study of its RF emissions was achieved by constructing a scaled laboratory apparatus. This chapter deals with the design of the various components and their assembly to form the apparatus. The experiment at Strathclyde is presented as a laboratory plan in Figure 3.1.

An appropriate vacuum condition had to be achieved and maintained to eliminate collisions between beam electrons and any other particles, Section 3.2. To reproduce the magnetospheric geometry it is necessary to inject an electron beam, which already exhibits an initial spread in velocity into an increasing magnetic field. The electron emitter and other components forming the electron gun are discussed in Section 3.3. An HT firing circuit, Section 3.4, had to be created to energise the electron gun with pulses of 75-100kV. The magnet coils, and cooling system, which encapsulate the beam are discussed in Section 3.5. Section 3.6 describes the diagnostics required to measure the electron beam characteristics. Section 3.7 discusses the microwave receiver diagnostics used to carry out the antenna scans and spectral measurements, and Section 3.8 covers the plasma generation apparatus and diagnostics.

3.2 Vacuum Set-Up

The magnetospheric environment is highly non-collisional, meaning that the electrons traverse all length scales of interest without being subject to scattering by binary collisions with other particles. To replicate this in the experiment the mean free path must be increased until it substantially exceeds the distance traversed by the particles from their origin at the emitter until they reach the collector. So it is therefore necessary to remove the bulk of the gas molecules from the system, creating a vacuum. In our case, this vacuum was obtained by use of an Edwards RV12 rotary pump to reach the roughing pressure (~10^{-3}mBar) and an Edwards 100/300M oil diffusion pump for achieving high vacuum (~10^{-6}mBar). The electrons are subject to

a collision cross-section value between electrons and Nitrogen molecules of $q= 15x10^{-20}m^2$ [von Engel 1994], the mean free path for a background pressure 10^{-6}mBar is of the order λ=1km, significantly exceeding the 2m trajectories of the electrons.

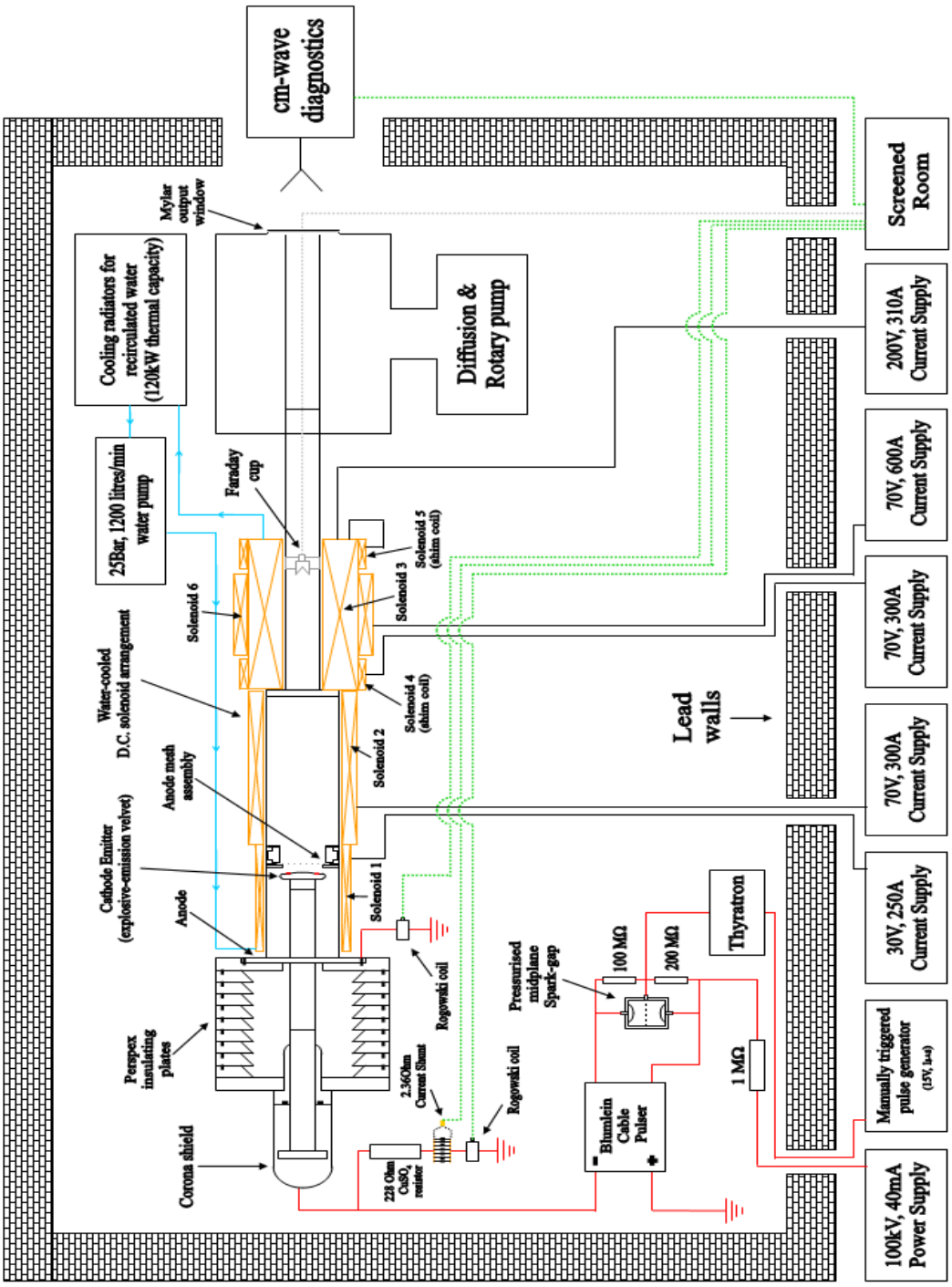

Figure 3.1: Schematic illustrating the configuration of major components of the apparatus

3.3 Electron Injector

The experiment used a vacuum spark cathode, see Section 2.5.4, to inject a high voltage, short duration electron beam. Such injectors are inherently pulsed since the cathode forms a plasma which given time would eventually expand to reach the anode and short circuit the accelerator gap. In pulsed operation the delay between each pulse allows the plasma to dissipate. Use of pulsed operation is also advantageous to help reduce the occurrence of breakdown and flashover, which is more likely to happen the longer the high voltage is maintained, thus simplifying the apparatus and especially the insulator design. In the AKR simulation experiment the explosive emission cathode [Mesyats and Proskurovsky 1989] used a velvet material emitter which had a plasma expansion velocity of ~$2x10^6$cm/s, Figure 3.2, from which the electrons are emitted, with the nose-cone of the cathode face pointing towards the central hole in the mesh anode that lies immediately downstream, Figures 3.3 and 3.4. The nose cone of the cathode varied the angle made between the electric and magnetic fields in the vicinity of the emitter as at the inner edge E_r is greater than at the outer edge. This induces an initial spread in the electron velocity as they are injected into the vacuum. By placing the injector in the fringing magnetic field the flux density linking the emitter is also a function of r. Hence the degree of magnetic compression experienced as the electrons drift through the experiment is a function of their source position at the gun. As a result of this geometry the beam will have an initial spread in velocity and may form a horseshoe distribution in velocity space after an appropriate degree of magnetic compression. The anode and cathode were separated by an acrylic insulating stack with a corona shield covering the air-side of the cathode stalk. The anode-cathode gap could be adjusted and was set at 1.5cm or 2cm, this spacing determined by the plasma expansion velocity of the red velvet shown in Figure 3.2. A sparse anode mesh, Figure 3.3, was placed in front of the cathode to increase the electric field on the cathode surface to further enhance field emission, allowing a critical value of electric field to be obtained of ~30kV/cm, necessary to initiate explosive electron emission. The wires are made from copper, and are spaced sufficiently so as not to block the propagation of the beam as it passes through and down towards the interaction region. The purpose of the velvet is to induce plasma

formation by field emission from the tips of the fibres. This type of emission can significantly affect the operating voltage of the electron gun [Kukreja 2005]. Figure 3.4 shows the orientation of the cathode to the anode mesh and the 1.5-2cm gap spacing to allow for the expansion velocity of the ‘velvet’ plasma flare.

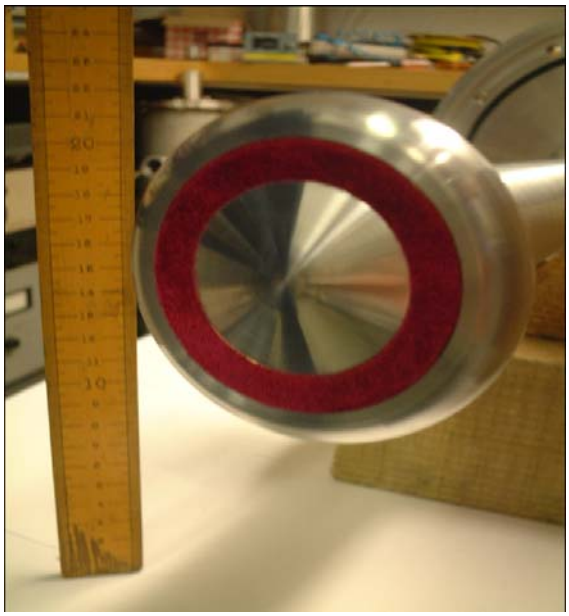

Figure 3.2: Cathode face showing annular red velvet emitter and the central domed nose cone

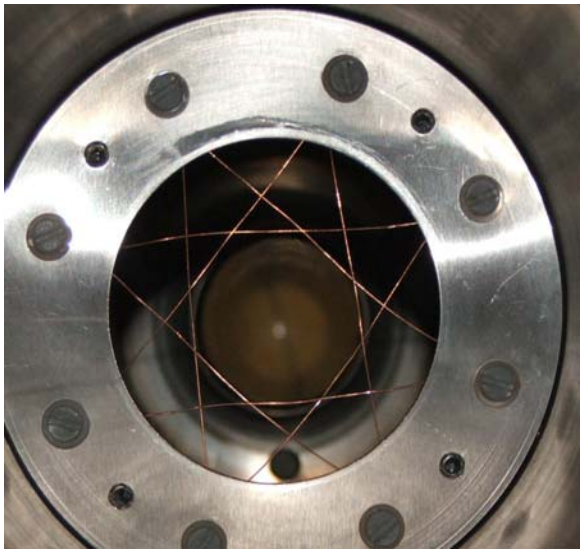

Figure 3.3: Anode mesh constructed from copper wiring to concentrate the accelerating field onto the cathode surface

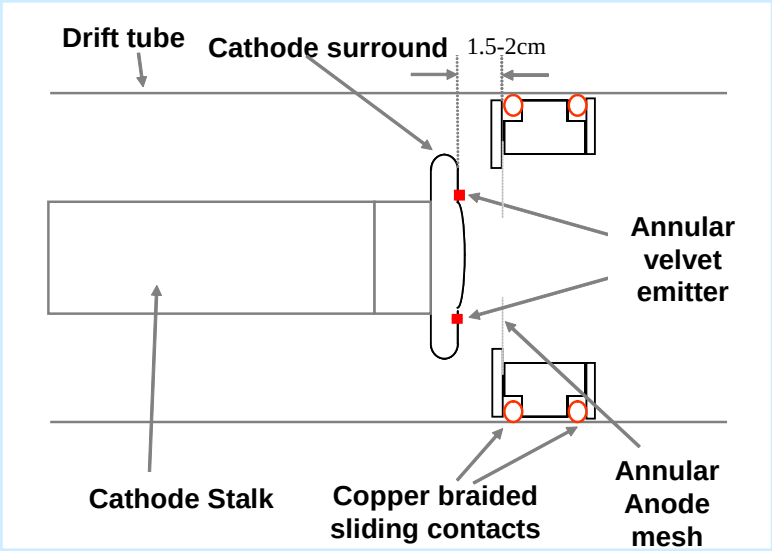

Figure 3.4: Schematic diagram showing the position of the cathode in relation to the anode mesh

3.4 Firing Circuit

3.4.1 Blumlein

The vacuum spark electron gun was powered by 75kV, 100ns pulses from a Blumlein [Somerville et al 1990] power supply, Figure 3.5. The quad cable Blumlein discharges into the electron gun in parallel with an ionic resistor to an earth connection. The cables were charged in parallel and discharged in series and when wired in an appropriate manner can be used to give an amplified output signal whilst maintaining a rectangular output pulse. The Blumlein circuit was triggered by a mid-plane spark gap, Section 3.4.3. The ionic resistor that is between the high voltage end of the Blumlein and ground is made up of a saturated copper sulphate ($CuSO_4$) solution which has the advantage of being able to withstand huge peak powers without damage. The combination of the 206Ω matching ionic resistor and a 1V/A Rogowski coil allowed the current through this branch of the experiment to be measured which in turn gave the value of the Blumlein output voltage.

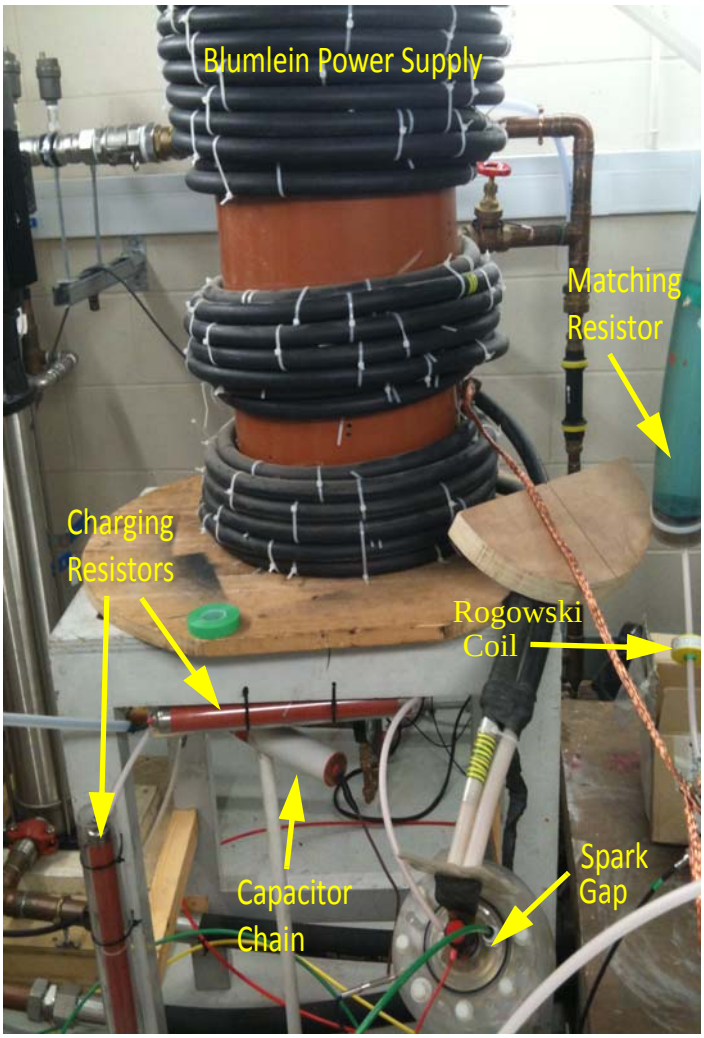

Figure 3.5: Blumlein pulsed power supply, mid plane spark gap, matching resistor and HT safety apparatus assembled in the lab

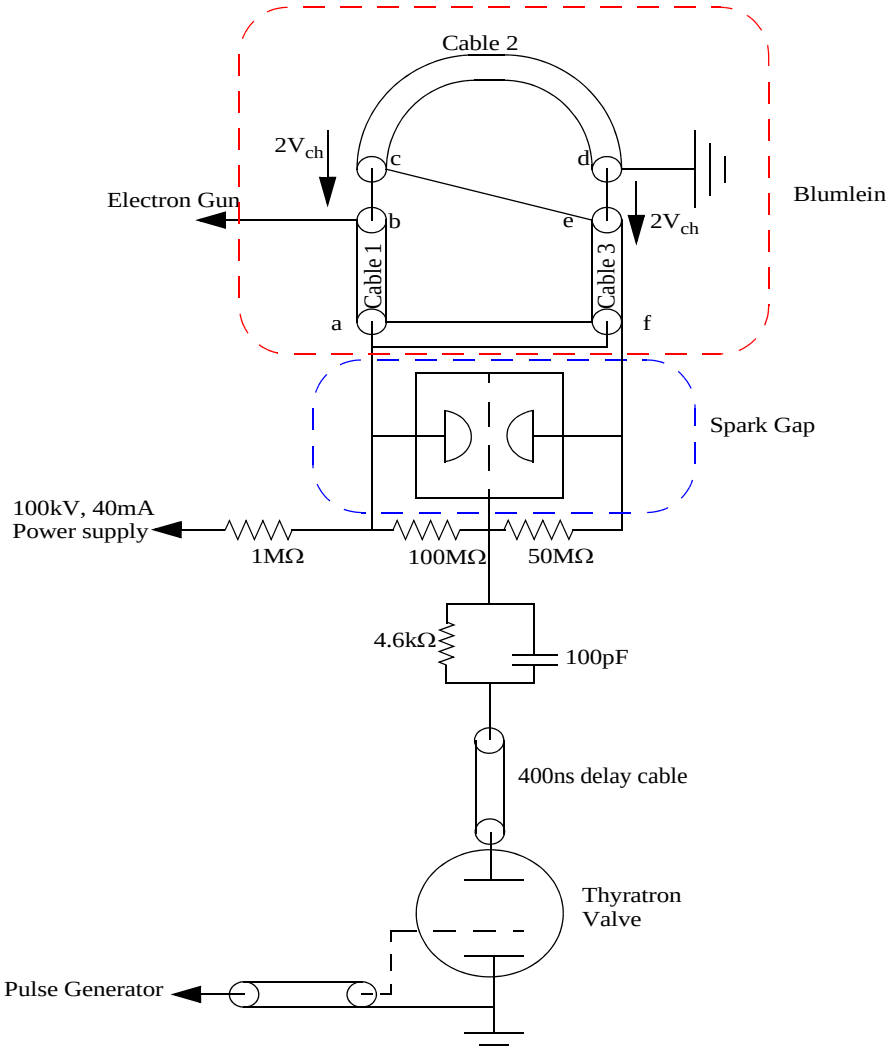

Figure 3.6: Schematic of charging circuit illustrating connections between and values of the components connecting the thyratron, spark gap and charging PSU

When the cables are fully charged to voltage V_{ch}, Figure 3.6, the spark gap switch closes which fires the Blumlein generator. Between the points b+c and e+d, there forms a voltage of $2V_{ch}$ and by further making a connection between points c+e, a voltage of $4V_{ch}$ can be obtained across points b+d. As is shown, d is connected to earth and this produces a negative voltage at b with respect to the charging polarity.

The cables were inductively wound around a former, which enabled the dipole antenna impedance, Z_d, to be made as large as possible and this in turn maximises the

efficiency and pulse wave shape. To calculate the output voltage V_L, one needs the cable impedance Z_c, the charging voltage V_{ch} and the load impedance Z_L that can all be linked together in Equation 3.4.1:

$$V_L = \frac{4V_{ch}Z_L}{4Z_c + Z_L} \qquad \text{Equation 3.4.1}$$

In this case, the charging voltage was ~50kV, the cables have an impedance of 50Ω and voltage rating of 100kV, a pulse duration of 100ns and an output impedance of 200Ω. The Blumlein is charged through a charging resistor of impedance ~1MΩ, used to ensure that the systems charging power is decoupled from the transients of the Blumlein and to limit the maximum charging currents at a safe level. The equivalent circuit for this set-up is shown in Figure 3.6, meanwhile, Figure 3.7 shows the 'load' connections to the Blumlein.

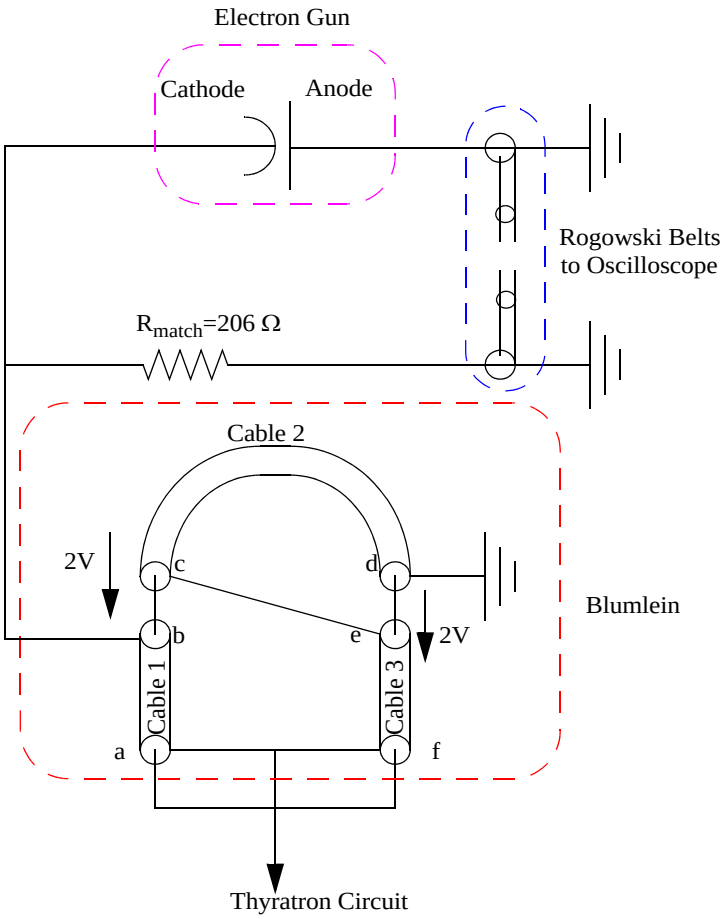

Figure 3.7: Blumlein equivalent schematic, 'load' side connections

3.4.2 $CuSO_4$ Matching Resistor

As stated earlier, the output of the Blumlein is connected to an ionic resistor, which, in this case, is made up of saturated Copper Sulphate, $CuSO_4$, solution. Ionic solutions in water are good conductors of high power pulsed currents. When a voltage is applied across it, positively charged ions, cations, travel towards the cathode, whilst negatively charged ions, anions, travel towards the anode. Disadvantages of this type of resistor are that their resistance will vary with temperature, they cannot be used with DC currents due to the fact that this will cause the solution to electrolyse and they do not have an entirely linear conductivity. A particular advantage of using an ionic resistor is that, due to it consisting of a large bulk of water, specific heat capacity of $4.2 kJkg^{-1}K^{-1}$, it can withstand huge peak powers without being damaged. Accelerating potential was measured by sensing the current through the 206Ω matching ionic resistor by a Rogowski belt and recorded by a deep memory oscilloscope. The resistance was calibrated at low (<30kV) output voltage with a voltage probe and checked for linearity against the charging voltage up to the operating voltage of the apparatus.

3.4.3 Pressurised Mid-Plane Spark Gap

The spark gap is made up of two (or more) conducting electrodes that are separated by a gap which is filled with some type of gas in this case nitrogen. A spark bridges the gap when a suitable voltage is applied across it. The spark ionises the air and reduces its electrical resistance to nearly zero, very quickly. The middle electrode of this particular device must be kept at the correct DC potential to gradiate the field strength and this is achieved by a 100MΩ:50MΩ resistance divider in parallel with the spark gap, Figure 3.6. A thyratron, Section 3.4.4, is used to short half of the gap, inducing breakdown in the other half thus creating the switch needed to convert the Blumlein to series wiring.

3.4.4 Thyratron

A thyratron is a gas filled tube which is used as a high voltage electrical switch. This type of device first came about in the 1920's although the first commercial devices did

not appear until around 1928. Nowadays, the semiconductor equivalent, the thyristor, has in most cases replaced the thyratron although the latter is still favoured for use in switching mechanisms requiring high voltages and in harsh electrical environments, such as in the experiment in this thesis. In this case the thyratron Figure 3.6, has a grid in place between the thermionic cathode and the anode. The grid is normally kept at a negative state in order to keep the charge in place. To trigger the device, the grid is switched rapidly to a positive state to produce a short circuit as electrons are thermionically emitted from the thyratron cathode and ionise the background hydrogen gas in the main body of the switch causing a rapid collapse of the impedance between ground and HT electrodes.

3.5 Coils and Cooling

3.5.1 Water Cooled Solenoids

To provide a magnetic field region comparable to that experienced by particles in the magnetosphere, a system of magnet solenoids was created to encompass the electron beam as it traversed through the system, Figures 3.8 to 3.10, and to provide a controlled degree of magnetic compression. The solenoids were constructed using OFHC (Oxygen Free High Conductivity) copper tubing, coated with a thin plastic sheath for electrical insulation, wound around non-magnetic formers. A different number of layers were used on each solenoid, the tubing came to a total length of greater than 1km, with an inside diameter of 2mm and an outside diameter of 7mm. Independent control of the individual solenoids allowed fine control of the magnetic compression profile. Figure 3.8 shows how the solenoids have been labelled numbered one through to six. Solenoid 1, the cathode coil, is run by a 30V, 250A switched mode power supply and is made up of 2 layers and is 0.45m long with an ID of 0.21m (as does solenoid 2). This coil surrounded the electron accelerator and was used to define the magnetic field which the electrons would experience as they were injected from the gun into the anode can. Solenoid 2 is made up of four layers, is half a meter in length, and is run by a 70V, 300A switched mode power supply, although in practice it was only used at 40A. Its purpose is to transport the electrons into the interaction region of the experiment and acts as the transition between the low field

electron gun region and the high field interaction region. Solenoid 3 is made up of 10 layers and is half a meter long and has an ID of 0.10m. This coil encases the interaction region and holds the magnetic field plateau at a steady maximum magnetic field. Solenoids 4 and 5 are made up of 2 layers and are 0.11m long. They are called the shimming coils and are each powered separately, solenoid 4 by a 70V, 300A supply, and solenoids 3 and 5 are driven in series by a 210V, 310A linear regulator. The shim coils allow the short thick solenoid 3 to provide the flat central plateau, 20cm in length at approximately a meter and a half downstream from the cathode, up to 0.5T in magnitude and also allow balancing of the field profile to compensate for the presence of solenoid 2. Solenoid 6 was a reserve coil, not used in this experiment, capable of providing a very high (>0.7T), peaked magnetic field profile to aid in mirroring the electrons, should it be required. Figure 3.8 shows the solenoids as they are set up in the laboratory. The inner diameters of the magnet solenoids must accommodate the experimental vacuum envelope and so determined the diameters of the evacuated anode can/beam tunnel (16cm) and interaction space (8.28cm) respectively, illustrated in Figure 3.9, which is a representation of the experiment as programmed into the PiC code KARAT [McConville et al 2008]. Figure 3.10 shows a schematic of the magnet coils along side the magnetic field profile along the length of the system. The operational objectives of the magnet coil arrangement is to provide a convergent axial magnetic field over the length of the coils which would end with a peak uniform section at a maximum of 0.18T, for the AKR experiments and 0.21T, for the Penning experiments with the background plasma. The electrons were subject to magnetic compression as they passed into solenoid 2 and reached a maximum magnetic field in the centre of solenoid 3. Adiabatic motion of the electrons must be satisfied as much as possible during the magnetic compression stage.

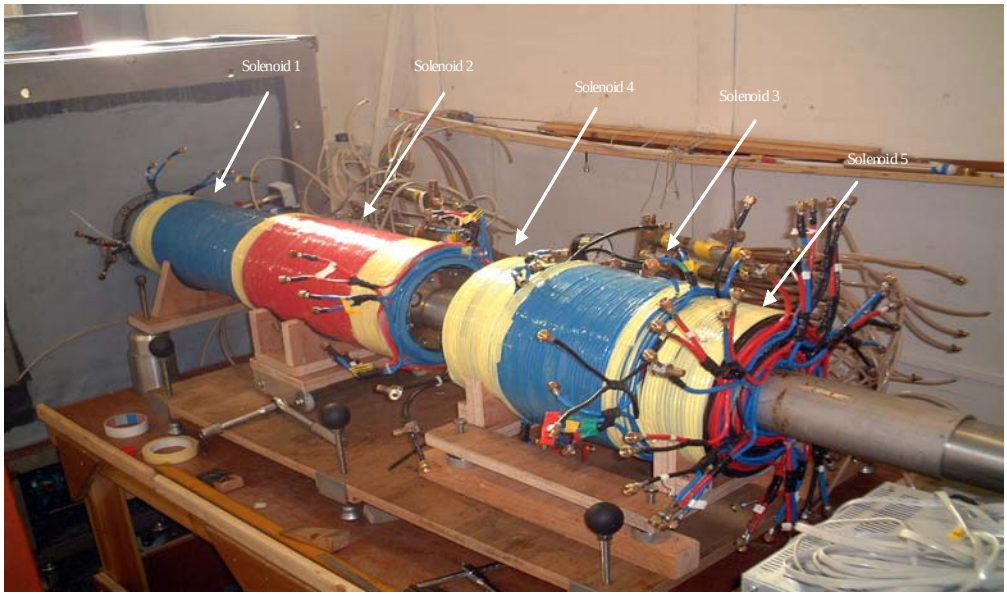

Figure 3.8: Solenoids of the magnetic field system during assembly in the laboratory

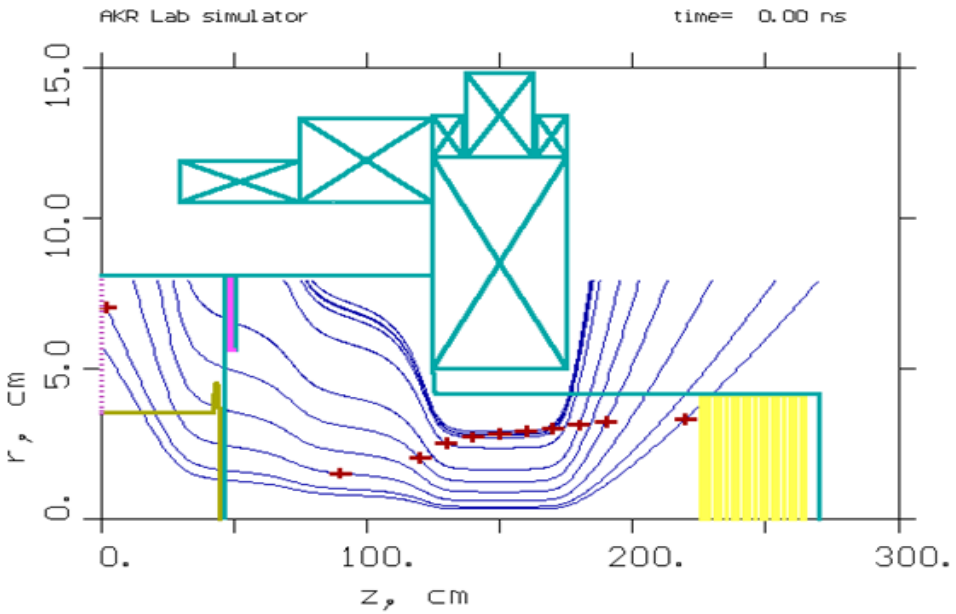

Figure 3.9: KARAT representation of experimental apparatus-notice the extreme foreshortening of the z-axis

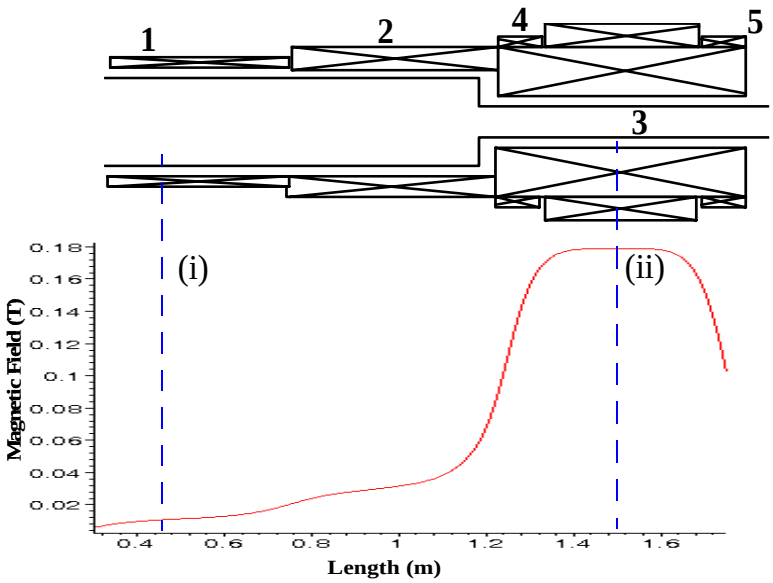

Figure 3.10: Schematic of solenoids and a plot of the corresponding magnetic field profile

For the cooling of the solenoids, a vertical multistage booster pump was used which allowed the copper tubing that made up the layers of the solenoids to be core cooled by water at ~22Bar. The laboratory was equipped with a $10m^3hr^{-1}$, 4bar water cooling system and so to provide the necessary 20Bar, a boost pump was installed rated at $5m^3hr^{-1}$ and 16Bar. This provided an acceptable flow rate of water through the 20m long, 2mm ID pipes enabling each one to carry 300A. This was sufficient to allow the solenoids to be driven by total electrical power of 120kW.

3.5.2 Hall Probe Measurements

The following plots show the Hall probe field measurements for the separate coils making up the experiment (see Figures 3.11 to 3.14). This allows the predictions from the analytical calculations in Maple, see Appendix 3, to be compared with what was actually obtained experimentally. By doing this the accuracy of the maple simulation can be confirmed giving reassurance that the code models the solenoids properly. This allows the magnetic field of the experiment to be precisely tuned using the script without having to measure the flux densities of the system each time. The script estimates the magnetic field situated on the axis of a set of solenoids having been

supplied with the values of the currents flowing in each coil along with the coil winding parameters.

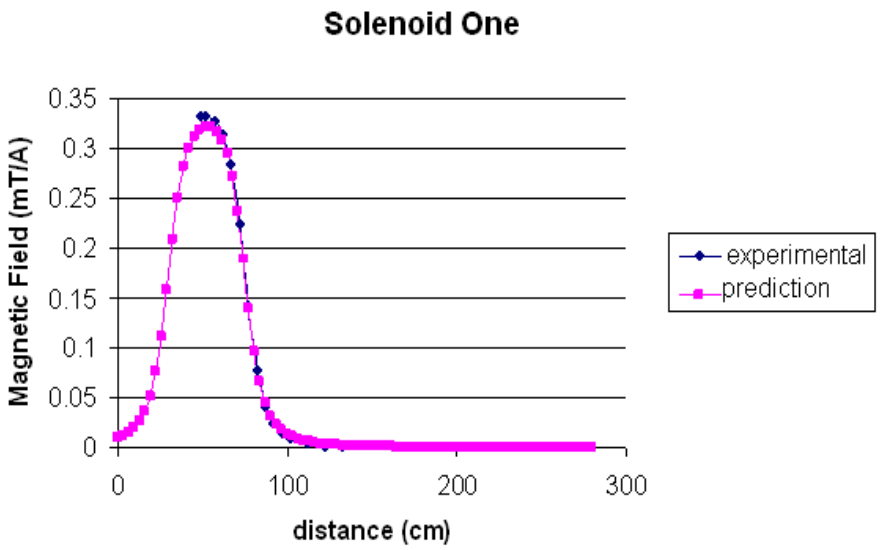

Figure 3.11: Hall probe measurement of solenoid 1compared to Maple predictions

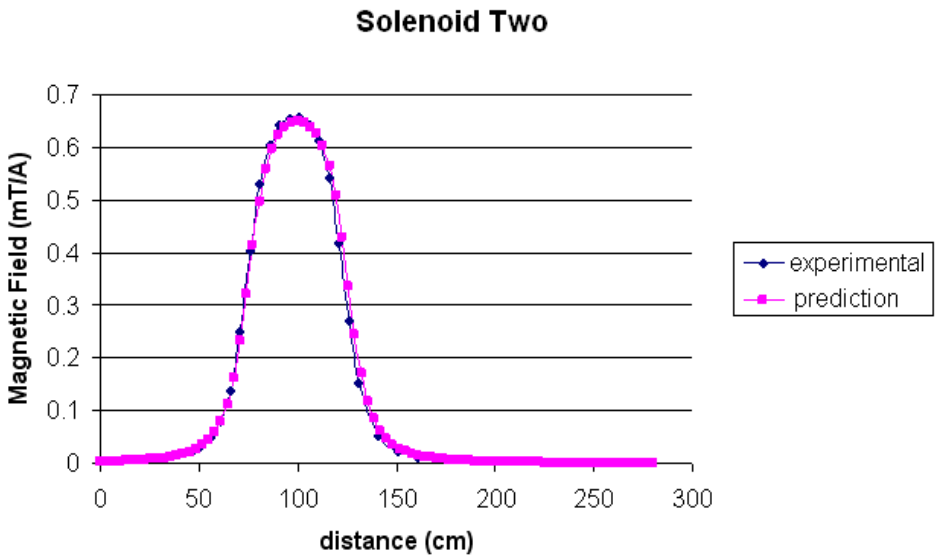

Figure 3.12: Hall probe measurement of solenoid 2 compared to Maple predictions

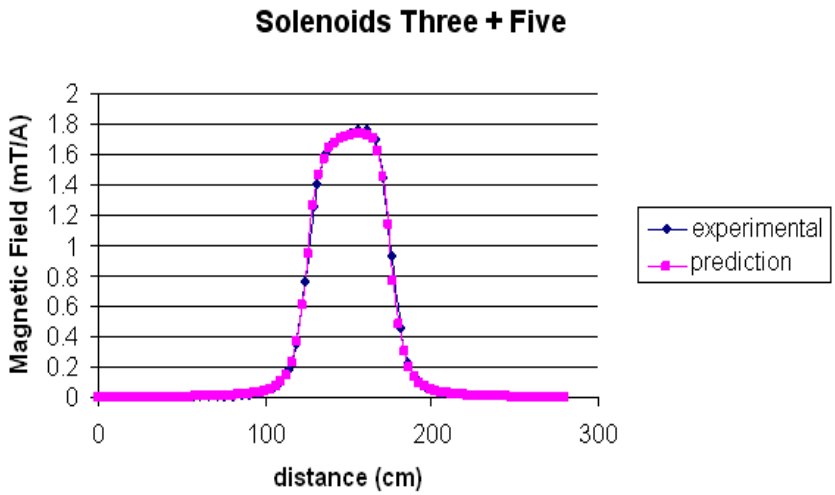

Figure 3.13: Hall probe measurement of solenoids 3 and 5 compared to Maple predictions

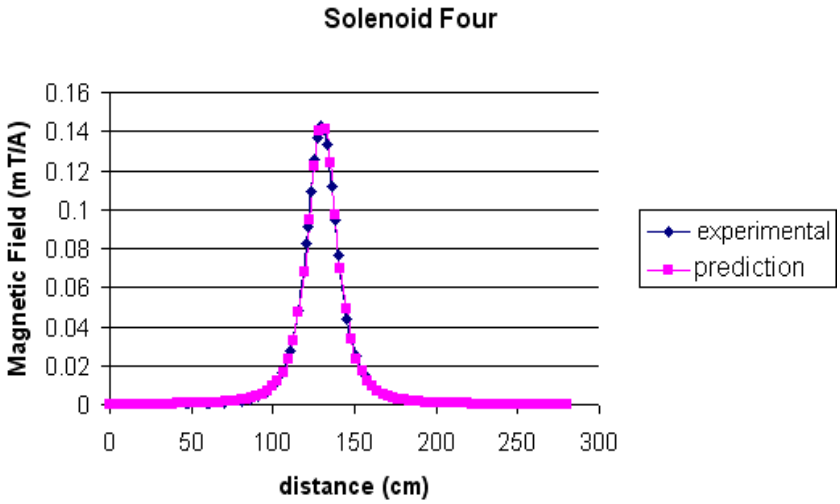

Figure 3.14: Hall probe measurement of solenoid 4 compared to Maple predictions

3.6 Voltage and Current Diagnostics

Diagnostics apparatus was required to allow the behaviour of the experiment to be measured. In particular it was necessary to measure the beam energy, current, electron

distribution, microwave frequency, power and polarisation in order to compare the experimental measurements with satellite observations.

3.6.1 Rogowski Coils

One type of Rogowski coil is a coil of wire that is wound on a toroidal former which encircles a current carrying conductor or say, an electron beam, Figure 3.15. The coil is threaded by the magnetic field created by the current which links the torus. The alternating magnetic field produced by the current induces a voltage in the coil that is proportional to the rate of change of current as a result of Faraday's Law.

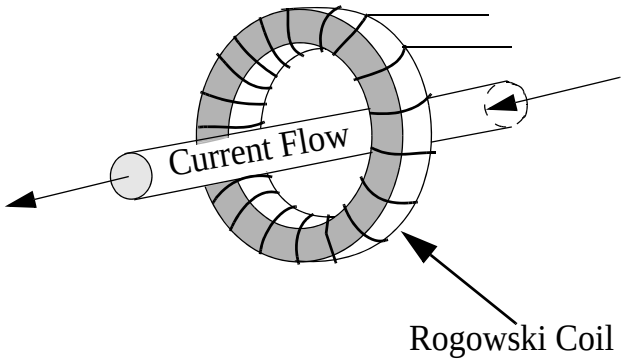

Figure 3.15: Rogowski coil current transformer

Air cored Rogowski coils are inherently linear with no saturable components, however, the ones that were used in this project are filled with a mu–metal magnetic material and this makes them potentially non-linear due to the saturable material. The coil in effect acts as a transformer and the windings in the coils must be as uniform as possible to prevent magnetic pick-up from other sources of magnetic fields.

There are a great range of frequencies and currents that can be measured using Rogowski coils. For high enough currents and frequencies the output from the coil may cause voltage breakdown, and so in these cases, coils are used that have a low mutual inductance.

A primary advantage of a Rogowski coil is that it is not directly connected to the circuit which it is measuring and can be insulated from the high potential of the conductor where the pulsed current is being measured. It also allows the position of the detector to be independent of the experimental ground.

The diode voltage was measured using a non contact method by determining the current flowing through the matching ionic resistor in the firing circuit by a Rogowski belt. The diode current was obtained by a Rogowski belt diagnostic placed in the ground connection of the anode, Figure 3.7. In both cases the measurements were recorded on an oscilloscope, after a suitable attenuation had been applied.

3.6.2 Faraday Cup

The Faraday cup is a device that is used to capture and measure the current of a beam of charged particles. The Faraday cup is illustrated in Figures 3.16 to 3.18, it had a conical beam collector and was placed in the interaction region of the experimental waveguide to measure the electron beam current during the beam transport measurements. When performing the microwave instability experiments, the cup had to be removed from the system as it effectively blocks the output waveguide reflecting all signals. Therefore the beam current cannot be measured simultaneously with the microwave measurements. A schematic drawing of the Faraday cup is shown in Figure 3.16, and shows the connections to the oscilloscope, the front and back faces of the device are shown in Figures 3.17 and 3.18 respectively. The conical face helps reduce the escape of secondary electrons. A sliding contact was provided to ground the 50Ω resistor by a sliding nitrile rubber piston ring sheathed in copper braiding. This 50Ω output was shunted by a 50Ω co-axial line to a CRO, also terminated in a 50Ω impedance. Hence the total shunt impedance to ground was 25Ω .

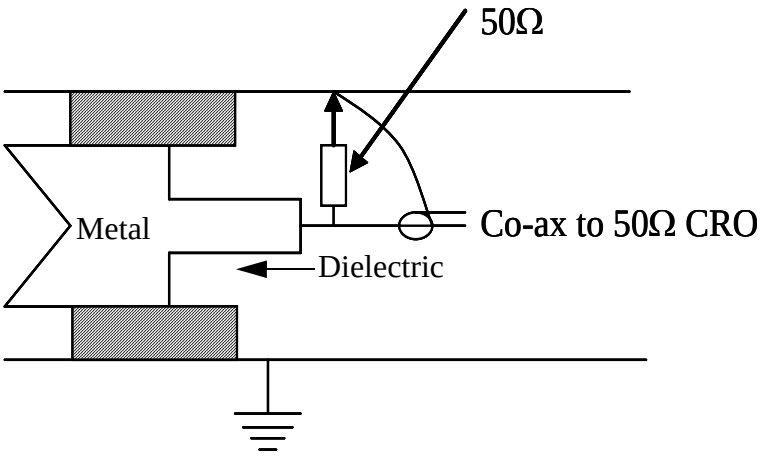

Figure 3.16: Schematic of Faraday cup, showing conical beam collector and electrical output structure

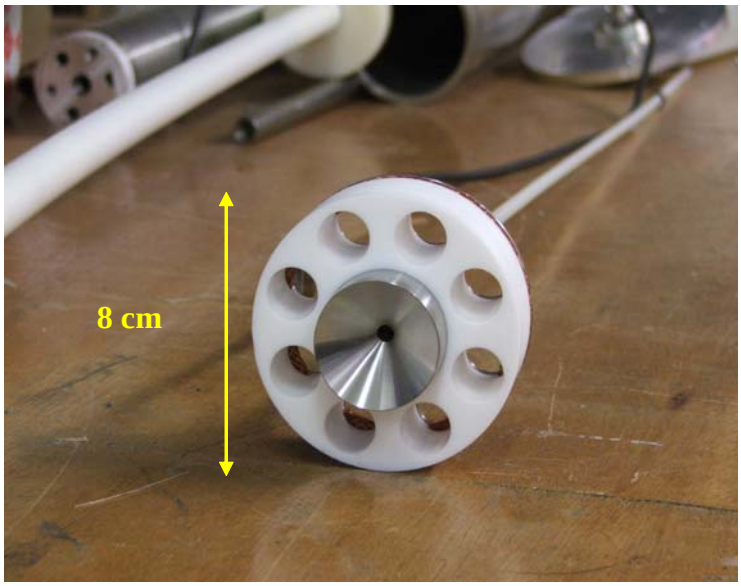

Figure 3.17: Beam collection face of the Faraday cup, note the dielectric support with through holes for vacuum pressure equalisation

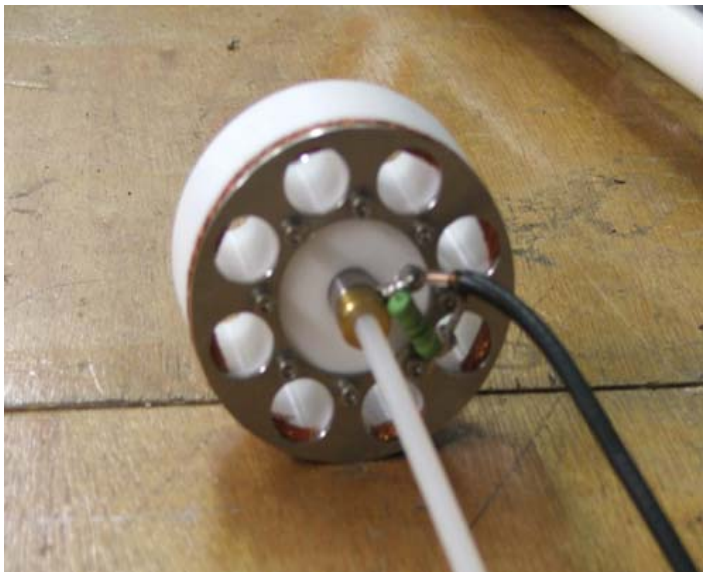

Figure 3.18: Rear face of Faraday cup showing the resistor, copper braiding and connections

3.7 Microwave Receiver Diagnostics

3.7.1 Antenna Scans

Pairs of waveguide 12 (WG12) stub receiver systems were built using single mode linearly polarised rectangular waveguide components with simple open ended waveguide apertures for 4.42GHz radiation, Figure 3.19, and were filled with lossy dielectric attenuators (section 3.7.4). These were used to measure the radiation antenna pattern emitted by the experiment in radial and azimuthal polarisations.

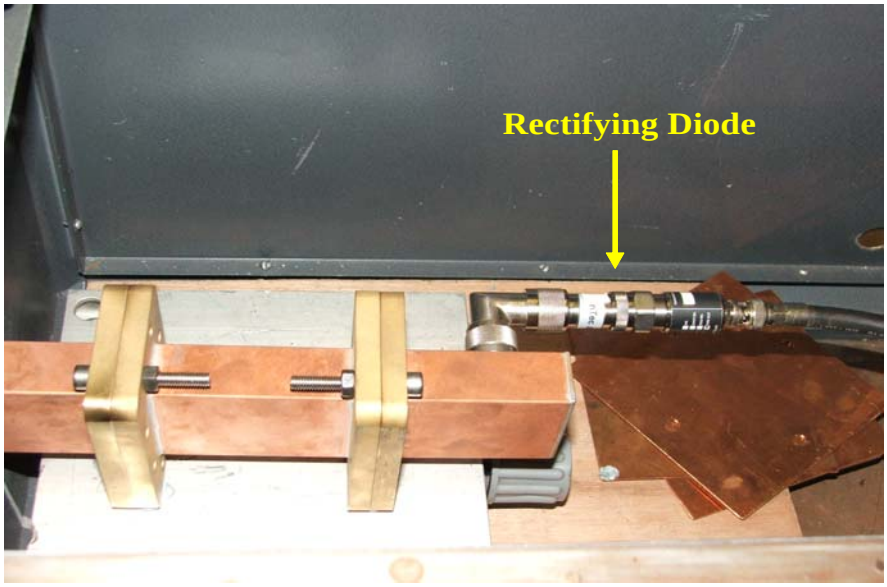

Figure 3.19: Waveguide antenna with rectifying diode

The circuit diagram in Figure 3.20 shows how the stub antennae are connected to the oscilloscope through the rectifying diodes (section 3.7.5).

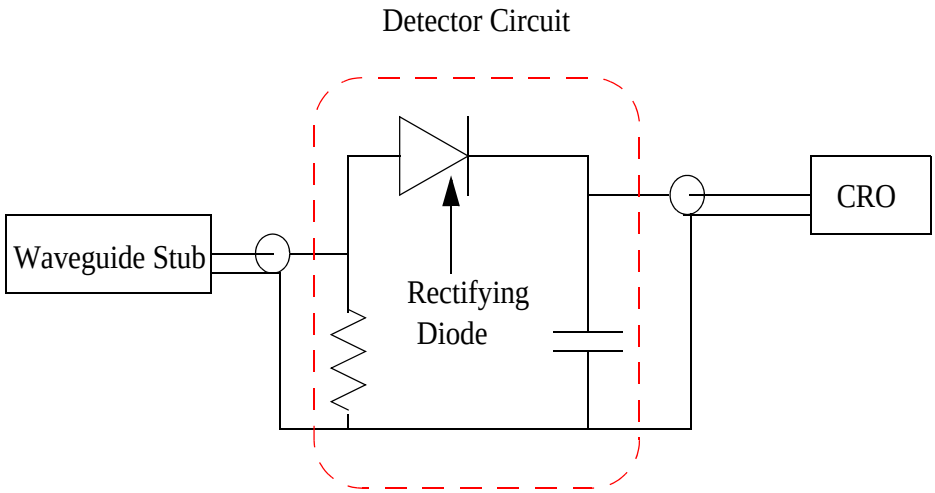

Figure 3.20: Schematic circuit diagram of rectifying diode

The two waveguide stub receiving antenna were placed in the far field region of the experiment output to capture the radiation emitted from the output window, Figure 3.21. This was carried out by collecting the power output of the system at different

angles around the cavity aperture, one antenna used to scan and one used for reference. They allowed intensity as a function of azimuthal and radial positions and polarisations to be measured depending on the orientation of the waveguide stubs at the time of measurement, Figure 3.21. Measurements were taken for azimuthal angles of up to 55°, angles greater than 55° could not be measured due to the walls of the output flange obstructing the radiation emission. The signals that were captured by the antennae were fed to calibrated rectifying diodes which enabled voltage readings to be obtained on a 1.5GHz deep memory digital oscilloscope. The readings from these measurements could then be analysed to determine the mode radiated and also the output power and efficiency of the system [Ronald et al 2008].

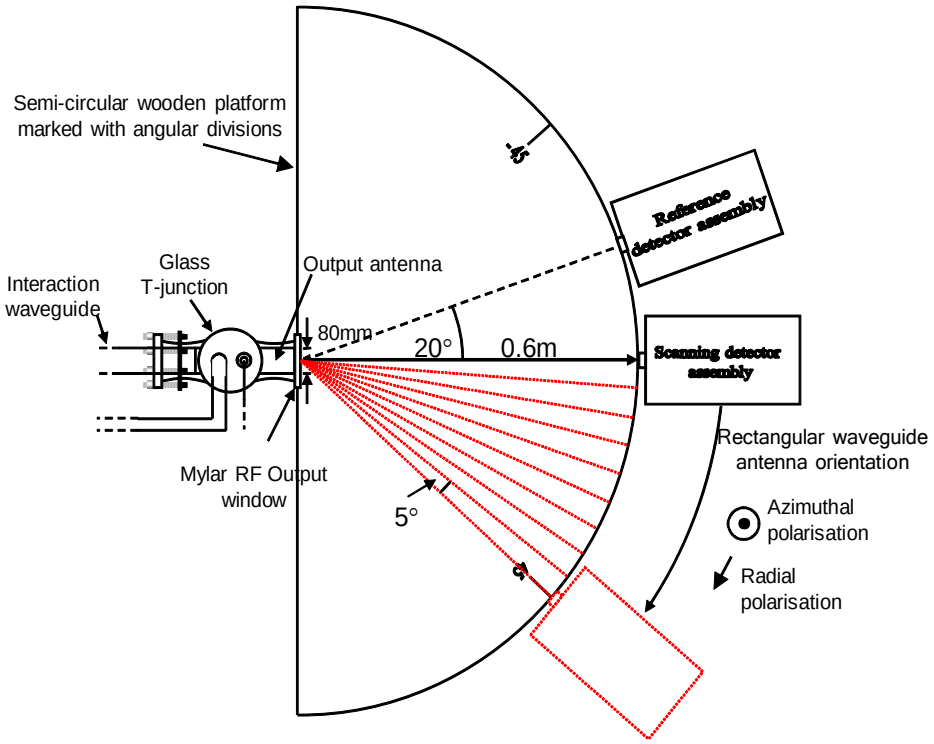

Figure 3.21: Antenna scanning apparatus

3.7.2 Spectral Measurements

To record the microwave emissions a deep memory 12GHz real time digital oscilloscope was used to capture the complete AC wave form and then perform a Fourier transform of the AC signal to yield a measurement of the wave frequency from one single experimental pulse.

3.7.3 Waveguide Adaptor/Receiving Antenna Calibration

A VNA was calibrated in waveguide 12 using first one and then the other waveguide to coaxial adaptor and using the offset short calibration method. The return loss was then measured for each waveguide-coaxial adaptor with a match on the coaxial port. An example of the resultant measurements of return loss is shown in Figure 3.22 and at the frequency of 4.42GHz this was -6dB giving a power transmission (in linear terms) of 0.75. Waveguide 12 was used due the following frequency characteristics as this was desirable for the wavelength of operation;

Cut-off frequency	f_{co} = 3.155 GHz
Frequency range	f = 3.94 – 5.99 GHz
Nominal frequency	f_n = 4.73 GHz

The waveguide to coaxial adaptors were then used to feed the RF signal to rectifiers and attenuators for the mode scan measurements.

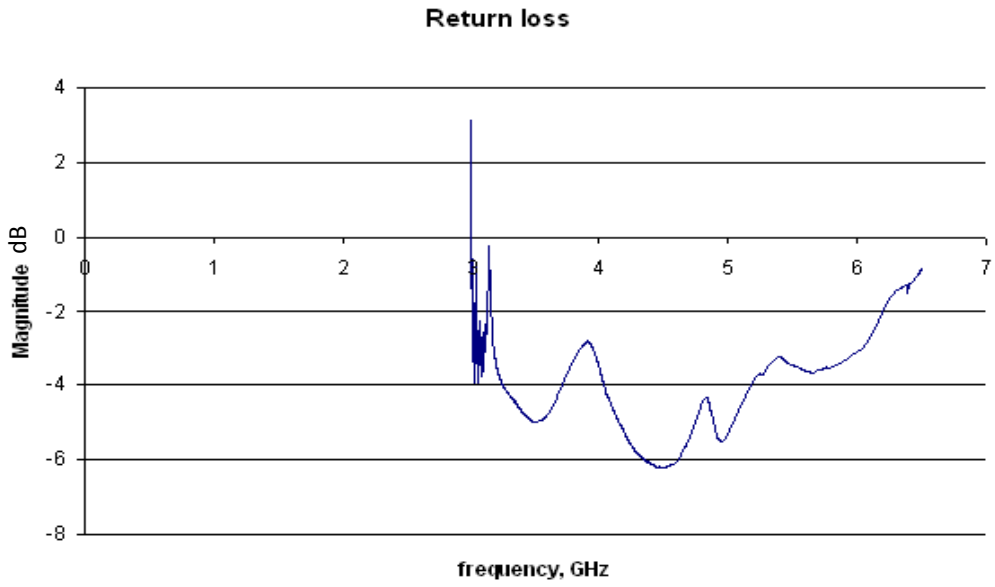

Figure 3.22: Return loss curve for WG12 to co-axial N-type WG/co-axial transition

•Microwave measurements with the Penning trap installed

When the Penning trap was inserted for plasma generation within the interaction waveguide, the value of cut-off frequency changed from 4.42GHz to 5.21GHz due to the decrease in the diameter within the trap, therefore the type of waveguide used to pick up microwave signals was changed from waveguide 12 to waveguide 14.

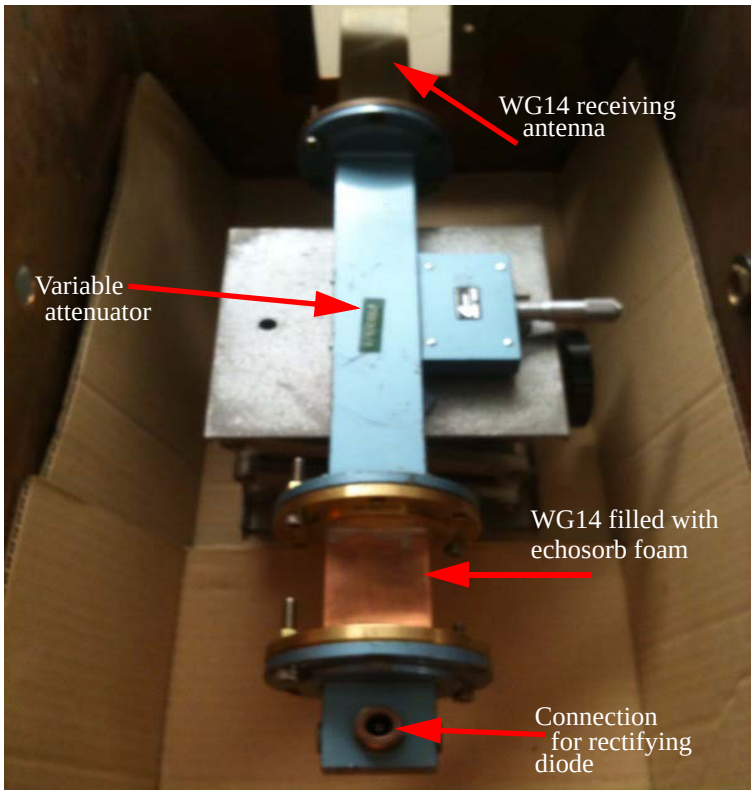

Figure 3.23: WG14 set-up showing the waveguide stubs, connection for rectifying diode, the variable attenuator, (echosorb foam inside the stub)

Calibration had to be carried out again for the new waveguide stubs to measure the attenuation of the echosorb foam, and also to document the calibration of the variable attenuator.

3.7.4 Attenuators

There are many different types of attenuator that can be used depending on what one wants to achieve and the particular circuit that one wishes to insert it into. Networks

of resistors are the standard low frequency type of attenuator. At microwave frequencies it is more common to load the transmission line with a lossy dielectric. By inserting a resistive material into an electric field, attenuation of the signal is obtained, this can be achieved by inserting a vane of lossy thin film or glass into a waveguide which can be moved from a zero electric field position, at the wall, to a maximum, in the middle, thus creating a variable attenuator, see Figure 3.23 for the attenuator used for microwave measurements with the Penning trap. Where higher precision attenuation is needed, a rotary vane attenuator can be used. If the vane is rotated from a position where it is perpendicular to the E-field of the waveguide to one where it is parallel, then the attenuation changes from zero to a maximum respectively. The foam attenuators that were used in the waveguide in this experiment are a sponge-like material loaded with a lossy powder and has the trade-name 'Echosorb'. These have an advantage over vane type attenuators in that they have comparable attenuation for harmonics.

•Echosorb Foam Calibration

The sponge attenuators that were used in the experiments add attenuation to the waveguide sections to be used in the antenna pattern measurements. By calibrating a Vector Network Analyser with an LRL technique it was possible to measure the attenuation accurately [Golio 2001]. There were two sponge pieces used, one for each waveguide receiving antenna, the calibration results were as follows:

The waveguide piece used for the scanning measurements of the mode scan had ~17dB transmission loss, and for the case of the reference waveguide piece, as shown in Figure 3.24, there was a transmission loss of ~13dB. In both cases this was measured at a frequency of 4.42GHz.

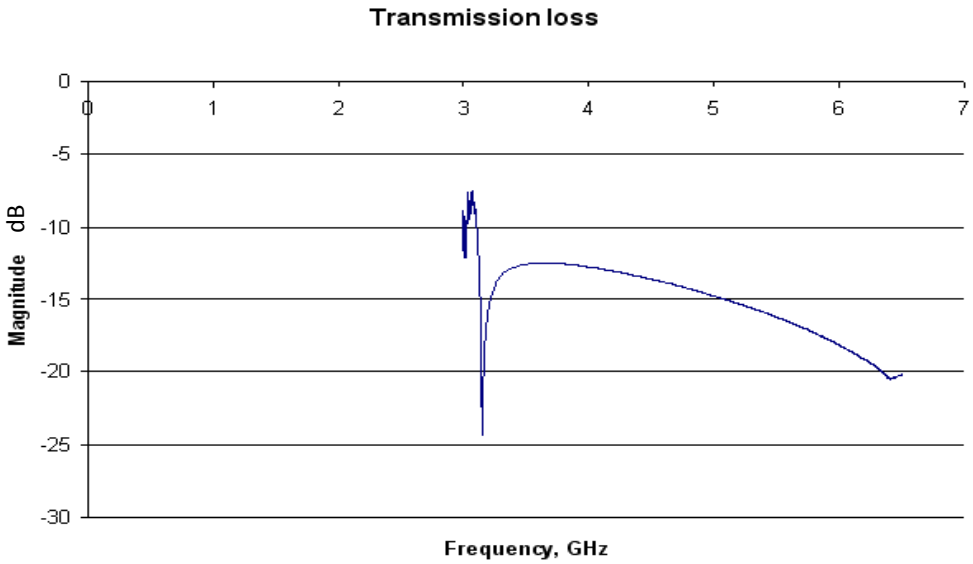

Figure 3.24: Transmission loss curves for foam attenuators

For the case where the Penning trap is installed and waveguide 14 is being used, the rectifier pick-up 'box' had a waveguide section loaded with an attenuation of ~14dB. The box used to relay the frequency of the microwave pulse had a foam attenuation of ~10dB. Both pieces were measured at 5.21GHz.

Shown in Figure 3.25 is the calibration curve for the waveguide 14 variable attenuator at 5.21GHz, showing different attenuations at different adjustable vane positions.

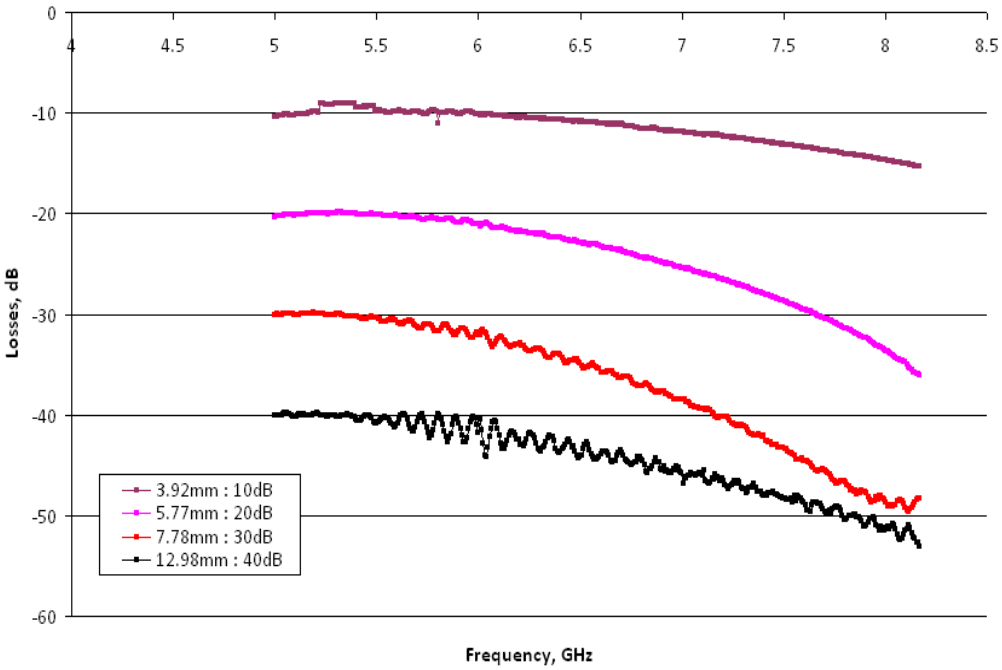

Figure 3.25: Attenuations at different vane positions of the variable attenuator at the operating frequency of 5.21GHz

3.7.5 Rectifying Diodes

Rectifying diodes, Figure 3.19, are required to allow high frequency RF signals to be measured with low bandwidth detection systems. The rectifying diodes used in this experiment were commercial devices with crystal detectors mounted inside a coaxial package. In this case the diodes used were fast gallium arsenide devices connected across the inner and outer conductors, which shorts the E-field in one direction but gives an open circuit in the other. The polarity of the signal that was obtained is dependant on the orientation of the diode and the half sine wave that was obtained was then capacitively smoothed, [Cross 1965]. By calibration of the devices output voltage into a 50Ω load against a calorimetric detector measurement of the input RF power, one can use the rectifier output voltage to determine the amplitudes and power of short duration input signals arriving at the detector input.

•Rectifier Calibration

The calibration of the rectifiers provided graphs of output voltage against input power which were fitted to an equation. The equation was used when analysing the results of the mode scan to determine the intensity of the radiation. Both of the detectors were calibrated, the one used for the scanning arm, Figure 3.26 and the one used for the reference arm, Figure 3.27, of the antenna pattern apparatus.

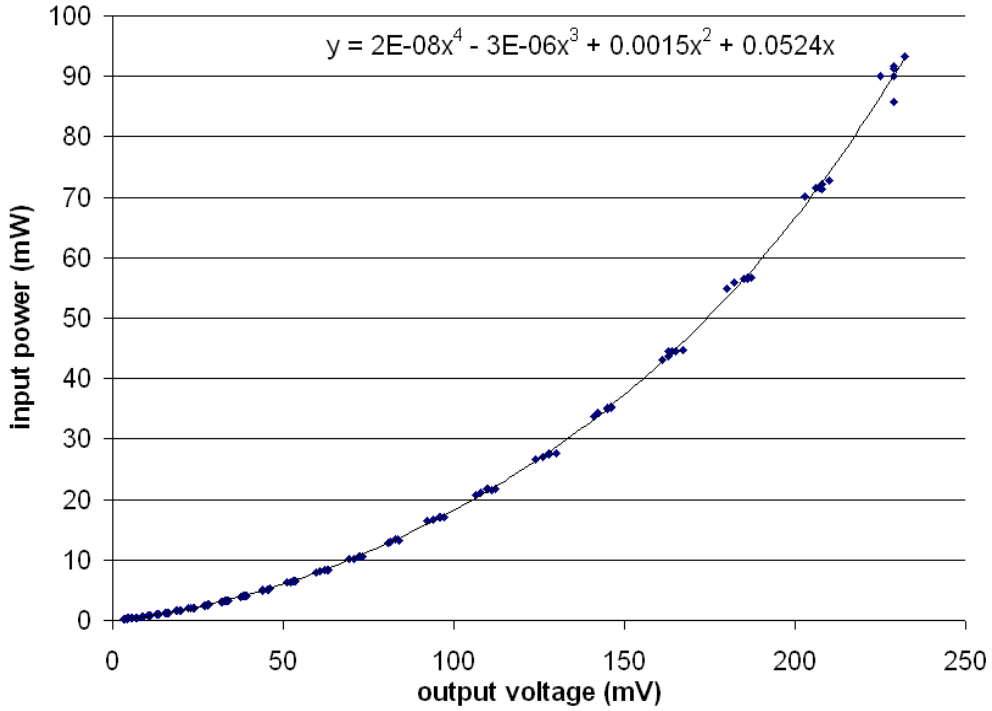

Figure 3.26: Calibration curve and fitted 4th order polynomial for the rectifier used in the scanning arm during the 4.42GHz AKR experiment with no plasma

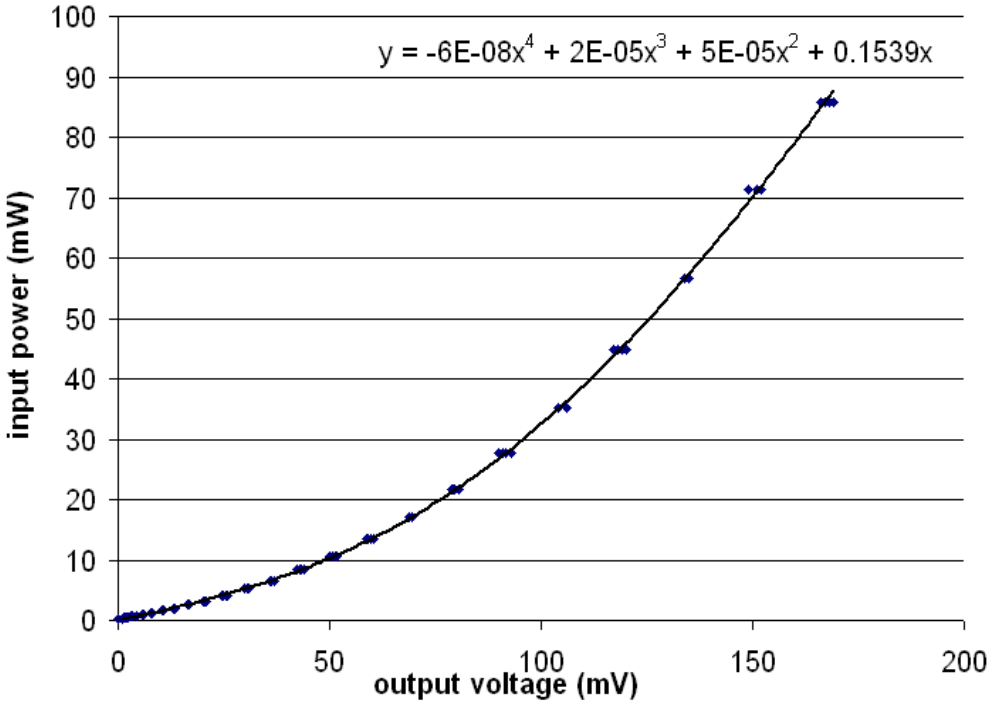

Figure 3.27: Calibration curve and fitted 4th order polynomial for the rectifier used in the reference arm during the 4.42GHz AKR experiment with no plasma

Shown in Figure 3.28 is the calibration of the Narda and HP rectifying diodes that were used for microwave measurements when the plasma trap had been installed.

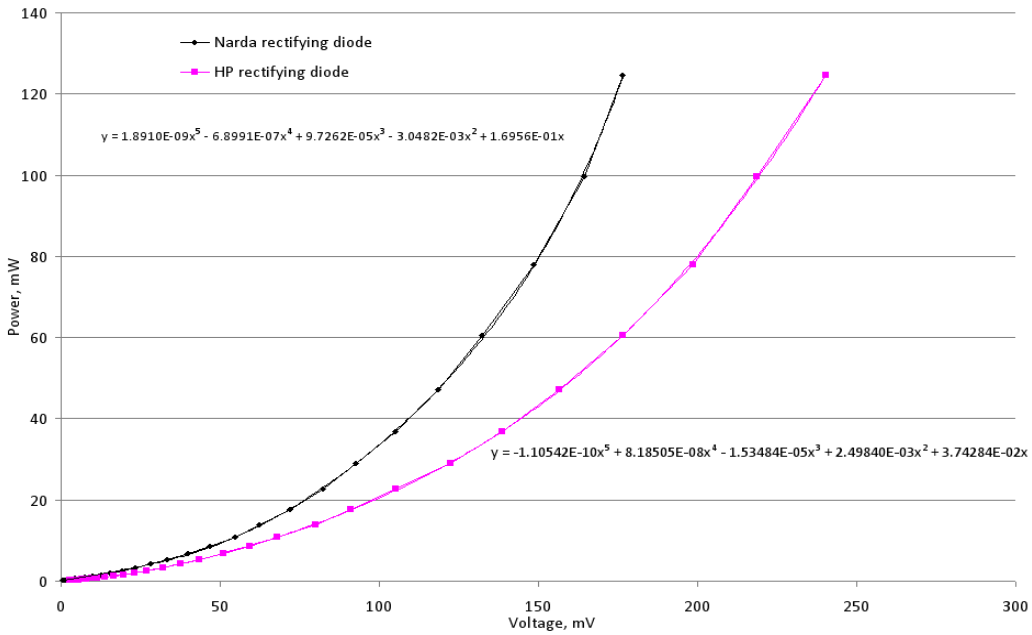

Figure 3.28: Narda and HP rectifying diode calibration used in the Penning apparatus setup, showing fitted 5th order polynomial

3.8 Plasma Generation Apparatus

3.8.1 Penning Trap Geometry

For the AKR investigations it was necessary to introduce a background plasma into the interaction region thus giving a closer approximation to the magnetospheric environment. To do this the Penning trap geometry shown in Figure 2.15 was devised and is shown below in Figure 3.29. As this new piece of apparatus will be inside the interaction waveguide, the first cathode plate must have a hole of sufficient aperture in the centre to allow the electron beam to pass through. In order to collect the microwave radiation that is generated and emitted at the exit flange the second cathode plate must be ring like, with a hole in the centre close in diameter to the trap walls, ~70mm, and ideally with a taper leading out to the waveguide walls. See Figure 3.30 for a schematic of the trap complete with dimensions.

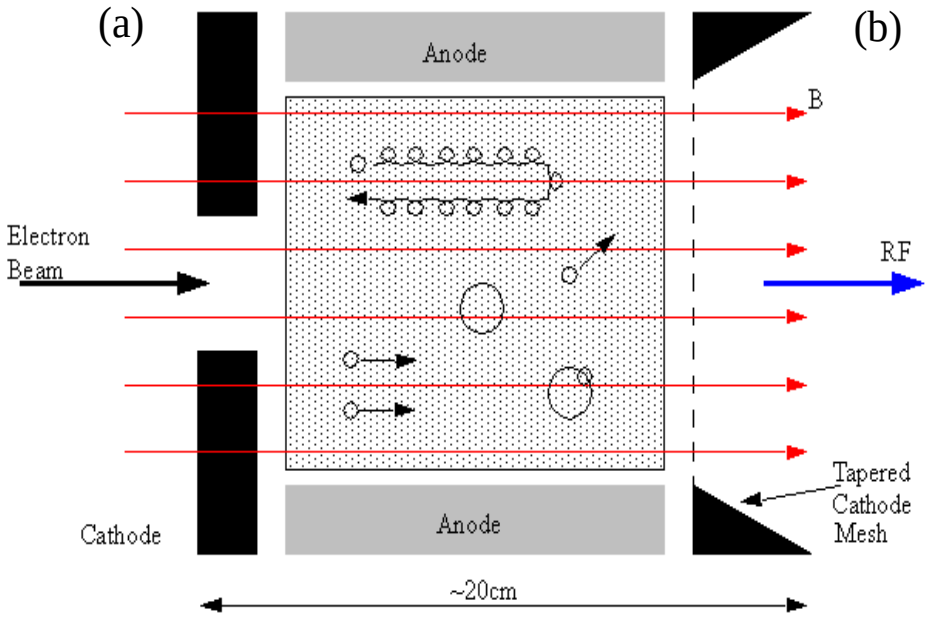

Figure 3.29: Altered geometry of Penning discharge to allow for radiation collection

At point (a) in Figure 3.29, the cathode has been opened up in the centre of the plate as discussed previously, to allow for the electron beam. This can be seen in Figure 3.30 (a) also, where it is noted that the aperture has a diameter of 40mm. At point (b) in Figure 3.29, the cathode end piece has been altered to allow the microwave radiation generated to pass through and be collected. Note how it tapers off to allow for a smoother transition to the outer diameter waveguide and hence less reflections, also seen in Figure 3.30 (b).

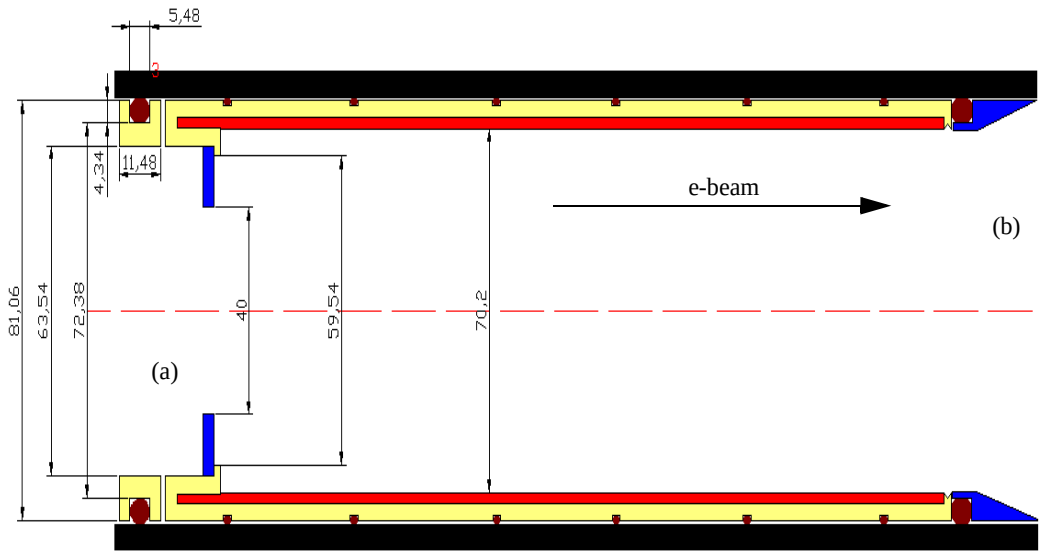

Figure 3.30: Schematic drawing of Penning trap showing the insulator walls (yellow), cathode plates (blue), cylindrical anode (red), and waveguide walls (black)

Figure 3.31, shows the position inside the interaction waveguide at which the Penning trap will be placed to allow maximum magnetic field over the length of the trap. Figure 3.32 shows a close up image of the Penning trap detailing the outer conductors, insulators and the path of the electron beam through its centre. It also shows the position of the mesh cathode with the probe connections in place, inserted into the plasma generation region within the trap. Figure 3.33 shows the schematic view of the circuitry involved. The outer walls of the Penning trap were constructed using copper, and this acted as the anode of the geometry. This was encased in a nylon jacket which acted as an insulator and prevented the copper from touching the walls of the waveguide in which it was placed. The cathodes of the trap were also constructed from copper which can be seen in Figures 3.34 and 3.35.

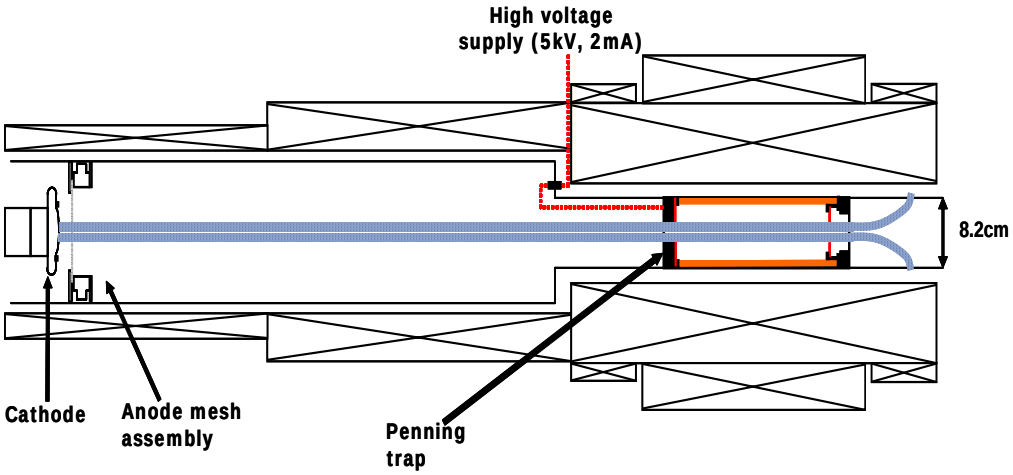

Figure 3.31: Schematic showing the position of the Penning trap within the experimental cavity

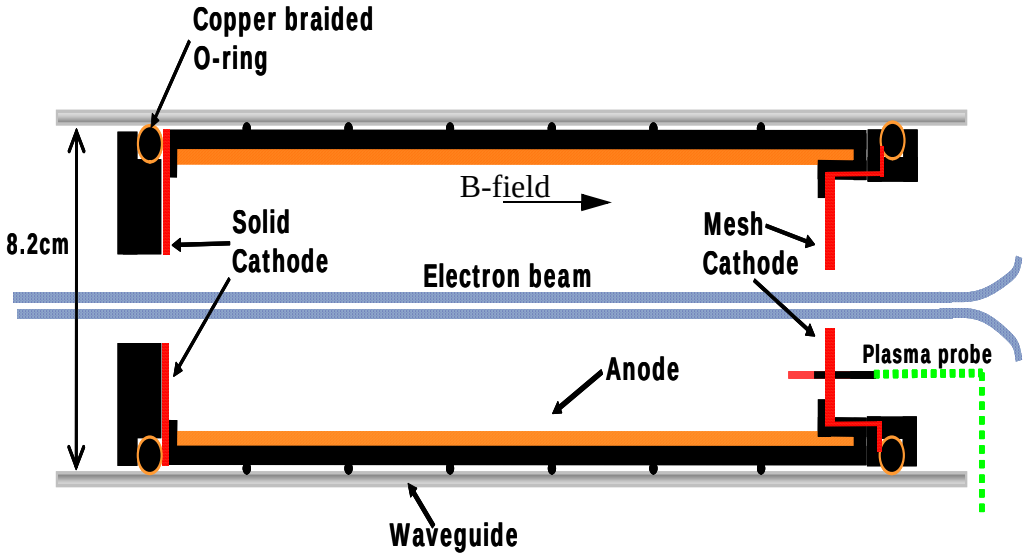

Figure 3.32: Penning trap geometry showing the cathodes, insulators, cylindrical anode, linking magnetic field, electron beam and plasma probe connection

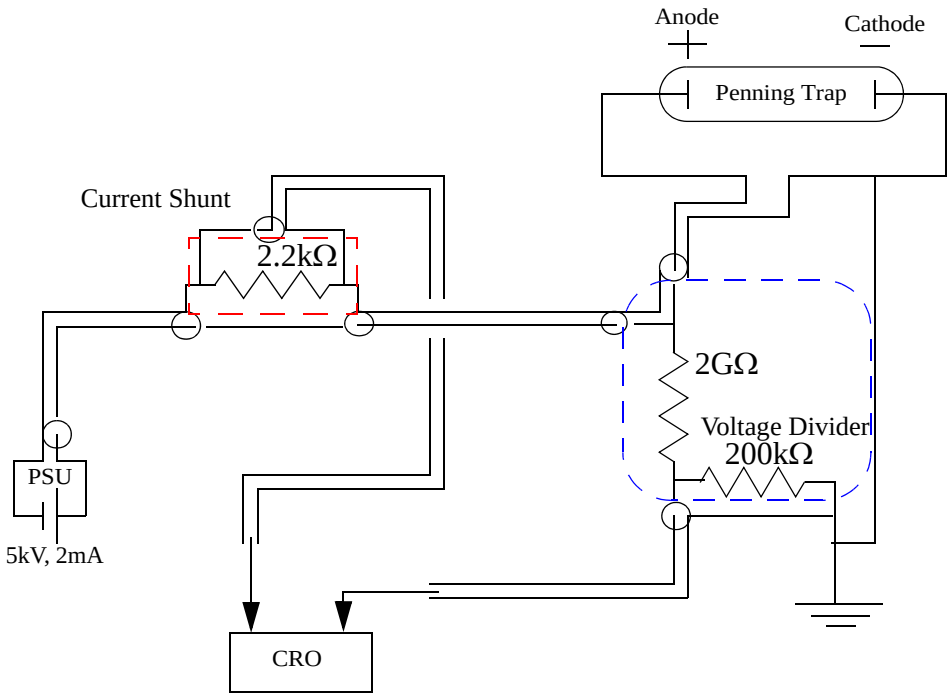

Figure 3.33: Schematic diagram of Penning trap circuit showing coaxial connections, voltage divider and current shunt

Figure 3.34: View inside the Penning trap to show the cathode at the far end of anode ‘tunnel’

A mesh was constructed as a second cathode to close off the Penning trap whilst still permitting radiation to pass through unperturbed. This was achieved using a spoke design, see Figure 3.35, which was ideal for use with the $TE_{0,m}$ modes as they have no radial E-field component to drive current on the wires.

Figure 3.35: Cathode mesh for Penning trap's radiation port, notice the radial copper spokes mounted in a metallic holder

To make the sliding electrical contact between the cathode electrodes and the waveguide walls, copper braiding over a nitrile rubber cord was used around the outer edges of the cathode electrodes, this can be seen in Figure 3.36, which also shows a clearer image of the electron beam injection end. The trap was made to be 20cm long, covering the extent of the interaction region so that the maximum magnetic field plateau coincided with this region where the plasma would be formed. The electrons that are emitted from the first cathode face, do so under Townsend's 2nd process. They are accelerated into the Penning trap along the magnetic field lines and towards the cathode at the opposite end of the trap. The cathode mesh repels the electrons and so sends them back into the trap cavity, whilst the magnetic field prevents them from drifting directly to the anode walls. The overall effect of this is that the electrons are contained in the trap making multiple 'bounces' between cathodes and colliding with

the background gas. This compensates for the weak 1st Townsend collision ionisation process by giving long electron lifetime and path length in the discharge. To apply a voltage onto the Penning trap, an HT coaxial feed-through is inserted through the vacuum vessel of the experiment and connected via HT coaxial cable to a 5kV power supply outside of the experimental bay. This can be manually controlled and the variation in Penning voltage and current measured as a function of each other.

Figure 3.36: Copper cathode face illustrating bombardment markings

3.8.2 Background Gasses

For the experiments involving the generation of plasma within the interaction cavity, a range of different gases and different pressures were investigated. The initial tests were done solely with air as the ‘foreign’ gas admitted to the vacuum chamber. Following this the gases tested were Nitrogen, Argon and Helium. To be able to bleed the gases in at a slow and controlled rate, whilst observing the rise in the vacuum pressure, a needle valve was used. This was operated simply by turning a dial on the top of the valve which allowed the gas to seep into the system and so decreasing the quality of the vacuum to a desired value by balancing the leak rate against the pump speed. The pressure was measured using ion gauges at the diode and pump ends of the experiment.

3.8.3 Plasma Probe

Having succeeded in forming the plasma within the trap, it was required that the processes occurring in the plasma were understood. It was therefore necessary to measure plasma parameters such as electron temperature and density. Langmuir type probes give a direct measurement of the local plasma density from either the electron or ion saturation currents. In this experiment, the method to measure the properties of the plasma formed within the Penning trap will be to insert a type of electrostatic probe through a nylon plate which will be placed inside the interaction waveguide just behind the cathode mesh, Figure 3.37. A length of coaxial cable was therefore stripped down to its copper wire core and used as a form of Langmuir probe, inserted into the plasma parallel to the direction of electron beam flow and magnetic field. By applying a voltage to the probe, at known values of Penning trap current and voltage, the current picked up by the probe could be measured and analysed in the form of an IV curve. By plotting the logarithm of the probe current against the probe potential the electron temperature within the plasma may be determined from its gradient, Equation 2.13.4. The disadvantage of this type of probe is local distortion of electrical properties of the plasma. Initially the probe was 10cm long (reaching halfway into the length of the Penning trap) but this caused drastic electrostatic disruptions with regards to discharge ignition and so was shortened to 2cm with the copper core exposed by 1cm. This gave rise to current collection problems across the magnetic field onto the waist of the probe rather than current solely being collected longitudinally on the end face. The protruding copper tip was therefore shortened to be flush with the nylon insulator of the coaxial cable. Any cross field current collected with this configuration is now minimised.

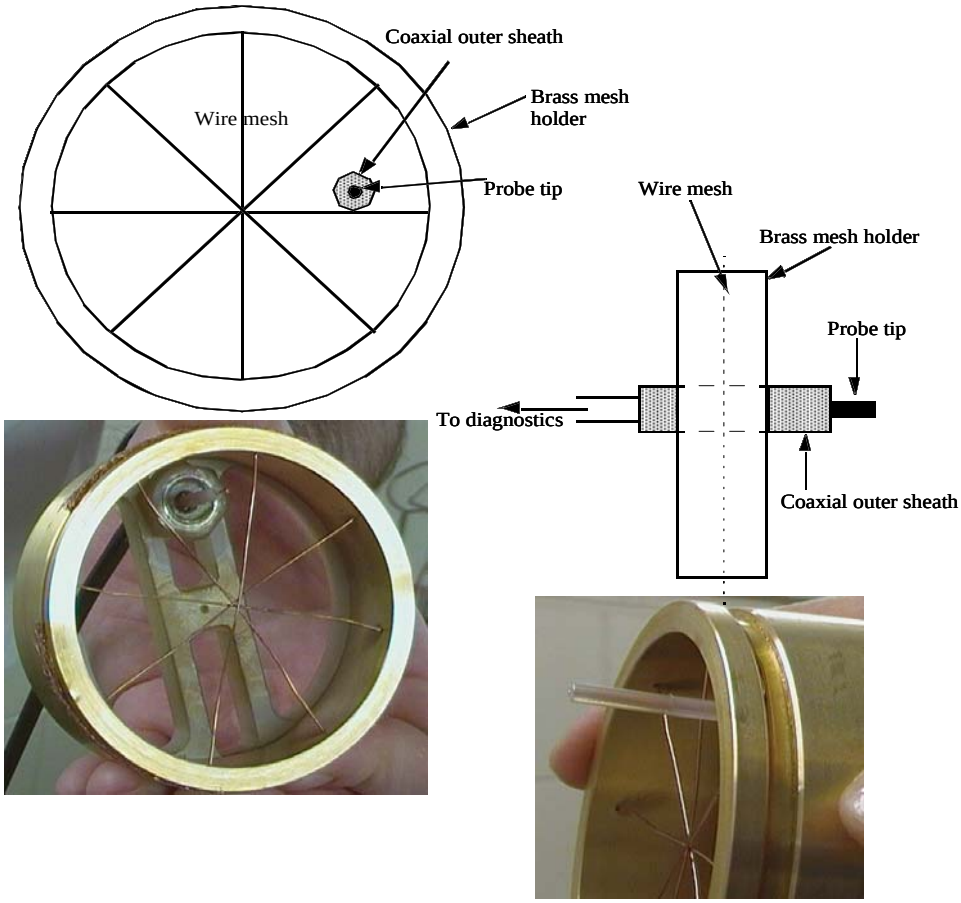

Figure 3.37: Cathode mesh with plasma probe insert showing both the cylindrical and planar probe schematically and as a component photo

This configuration allowed the probe current and voltage to be measured as the discharge current was varied. The electron temperature within the plasma was then estimated from the gradient of the logarithm of the probe current when plotted against the probe voltage, Section 2.13. The saturation currents yield an estimate for the electron number density (Equation 2.13.6) which could then be compared to the magnetospheric data. A voltage divider was placed in the connection between the oscilloscope and the plasma probe to reduce the voltage seen on the oscilloscope. This consisted initially of a 1GΩ and 10MΩ resistor giving a divider ratio of 100. This ratio was altered during the course of the experiments to 33 (using three 1GΩ resistors in parallel).

However, due to the presence of a magnetic field in these experiments, other methods to find the plasma frequency were necessary to validate the Langmuir probe measurement. Therefore the results obtained from the probe were compared to those using two different methods of calculations (which were less affected by the magnetic field) to help verify their validity. The first method was to connect the probe as a floating pick-up antenna feeding an RF spectrum analyser. This allowed the frequencies emitted by the plasma to be recorded and analysed. The probe was oriented parallel to the magnetic field within the coils and therefore was in a position to pick up oscillations along the O-mode direction. RF emission frequencies close to the plasma frequency were observed by means of this antenna configuration. These direct measurements of the plasma frequency could then be compared to the value calculated manually using the number density estimated by the probe measurements. Theory concerning the Bohm Sheath Model is shown in Section 2.13.2 providing an alternative way to get the number density and hence a value of plasma frequency. This was achieved by using the probe estimate for the electron temperature to predict the ion sheath velocity and hence the bulk ion number density from the Penning cathode current.

3.8.4 Electrical Diagnostics of the Discharge

To measure the macroscopic electrical behaviour associated with the Penning trap experiments, a LeCroy oscilloscope was used. Due to the high sensitivity and low maximum voltage of the oscilloscope, certain measures were taken to ensure accurate readings of the voltage and current from the plasma. A voltage divider was made to reduce the voltage appearing at the oscilloscope by a factor of 10,000 making accurate readings of the voltage possible, this is represented within the circuit diagram for the Penning trap in Figure 3.33. It was formed with a 2GΩ high voltage stage resistor and with a 200kΩ tap-off stage to ground across which the Penning trap voltage was measured with the oscilloscope. This voltage divider was then connected between the anode and the trap ground return.To enable an accurate current measurement to be obtained, a current shunt was constructed which measured the total current flowing through the ground sheath on the return from the Penning trap. This is also represented in Figure 3.33 where one can see the 2.2kΩ resistor.

Chapter 4 : Numerical Simulations

Chapter 4 : Numerical Simulations

4.1 Introduction

Computer simulation programmes are a valuable tool for any scientist providing helpful insights of what behaviour one may expect from an experiment. Two different primary codes were used, an analytic code Maple, and a non-linear 2D PiC code KARAT. These codes allow one to solve numerically or analytically linear and non-linear theoretical descriptions of physical systems. PiC codes enable a link between highly reduced 1D models and the physical 3D systems by allowing the physical geometry to be replicated on a grid representation. This allows solutions of problems based on solving basic physics laws (e.g. Maxwell's Equations, the continuity equation, the equation of motion, the Lorentz force equation etc.), describing the fields by interpolation between a spatially discretised mesh and the particles in merged 'super particles' instead of a very precise solution of a specialised simplified equation which is based on physical approximations. In addition to their predictive capability, multi-dimensional computer simulations may also (once benchmarked against the experiment) provide insight into difficult to measure quantities and parameters. The analytical Maple code was used to work out magnetic field configurations of the solenoids which were then programmed into KARAT along with the dimensions of the experiment. This non-linear 2D code was then used to predict the electron optics, operating frequency, non-linear dynamics, and output power of the experiment as well as illustrating the phase space evolution of the beam. Maple was also used to write a script describing the spatial and temporal growth of beam wave interactions, allowing plots of the complex roots of the wavevector to be obtained.

4.2 Linear Theory of the Cyclotron Instability

Maple is an analytic and numerical computation system that performs mathematical computations and manipulations in order to solve in principle arbitrary problems. For the purpose of this research a Maple script was written, [Chu 2004, Chu & Lin 1988, Sprangle et al 1977] to demonstrate the coupling strength, gain and growth rate of a cyclotron instability as well as indicating whether the instability will be absolute, or

convective, as a function of the waveguide dimensions, modal numbers and beam parameters allowing the impact of the electron beam configuration on the imaginary parts of the wavevector/frequency of the experiment to be investigated. It illustrates in the form of dispersion curves the beam and wave modes plus the composite 'hot' eigenwave of the coupled system, for both the unbounded and bounded cases. The codes for these two cases, (bounded and unbounded) can be seen in full in Appendices 1 and 2 respectively.

This code facilitates the analysis of different resonance conditions by simply changing magnetic field, beam current or electron beam pitch angle. The dispersion plots in Figures 4.1A to 4.6A use a method which finds only entirely real solutions of the system. Growth of wave intensity actually occurs due to the imaginary parts to the solution which occur in the 'gap' in the coupled solution shown in black in the figures. The real and imaginary parts of the complex roots of k_z are presented in Figures 4.1B and 4.2B for the unbounded case and 4.3B to 4.6B for the bounded case.

4.2.1 Unbounded Geometry

The coupled dispersion equation can be solved for discretely chosen real values of either k_z or ω to find the complex roots for the other parameter. This allows the growth rate of the instability in time or space to be understood. Figures 4.1A to 4.2A show the unbounded dispersion diagrams with varying degrees of pitch factor α=0.5 and 1.5. Geophysically reasonable parameters are used of B=12μT and I=20μA/m^2 and an accelerating voltage of 10kV. Figures 4.1B and 4.2B, show the real and imaginary parts of the complex roots of k_z over a range of real values for ω near resonance, for the case where there are no boundary conditions, i.e. no waveguide walls. It is seen from these plots how a change in the value of the pitch factor can affect the shape of the dispersion. The dispersion expression for the unbounded, free space, case is shown in Equation 4.2.1.

$$\omega^2 - k_z^2 c^2 = \frac{\omega_p^2 \left(\dfrac{\omega - k_z v_z}{\omega - k_z v_z - S\omega_c} + \dfrac{1}{2} \dfrac{k_z^2 v_\perp^2 \left(1 - \dfrac{\omega^2}{k_z^2 c^2} \right)}{(\omega - k_z v_z - S\omega_c)^2} \right)}{\gamma}$$ Equation 4.2.1

Equation 4.2.1 is a fourth order dispersion equation, meaning that at all times, there must be four roots accounted for.

Figure 4.1A shows the resonant coupling to an electron beam of 20μA/m^2 under magnetospheric parameters, with α=0.5. The blue trace represents the electron beam, the green trace is the speed of light and the black trace represents the coupled dispersion relation, Equation 4.2.1. At the points circled in pink in Figure 4.1A the beam is in resonance with the free space wave, however, in these dispersion diagrams it is only the real values that are shown, so it is not until the complex roots are solved that detail can be seen. The complex roots are shown in Figure 4.1B clarifying that the upper resonance is entirely real (i.e. stable), and the lower resonance is complex, points (i) and (ii) respectively.

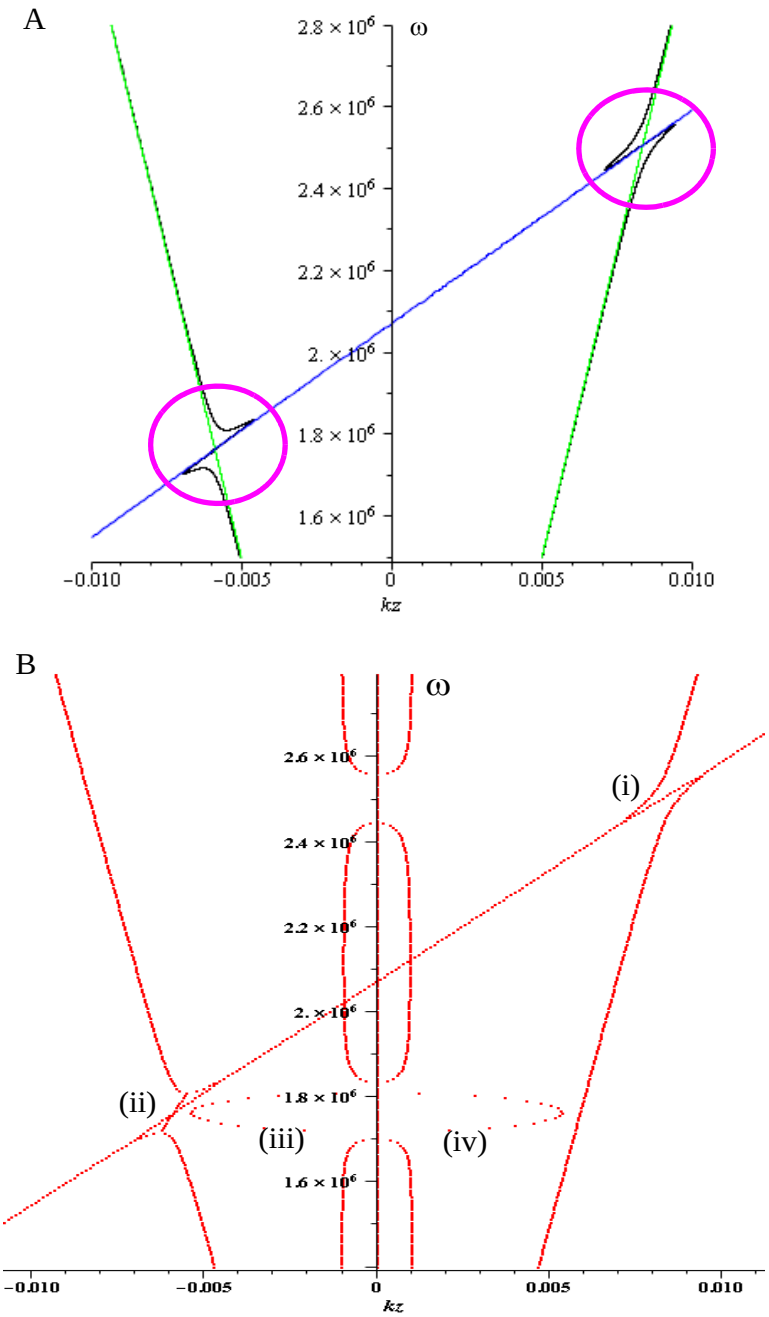

Figure 4.1: Dispersion plot for free space with current of 20μA/m^2, α=0.5, V=10kV

It is noticed in Figure 4.1B, at point (i), the similar shape to the dispersion in the plot 4.1A, and corresponds to entirely real roots of k_z for the resonant beam-wave system. (It should be noted here that the imaginary parts of the complex roots have had a x10

multiplier applied to them to make it more clear in the figure). At point (ii) where the resonance is in the negative k_z region, the real parts of the real and complex roots can be seen. At this point the fast cyclotron mode couples to the free space wave and has real and imaginary solutions. The real parts of the complex roots are at (ii) and the imaginary parts are at points (iii) and (iv). Due to the coupling with the fast cyclotron mode, the beam gives energy to the wave and its decay rate is shown at point (iii). The wave, therefore, gains energy and its growth rate is shown at point (iv). The points at which the imaginary roots of k_z go to zero are stable regimes.

As can be seen from Figure 4.2A, increasing the pitch angle to 1.5, decreases the gradient of the beam line, which is the only noticeable affect in this plot, however, referring to Figure 4.2B, there is a bigger effect occurring in relation to the complex roots.

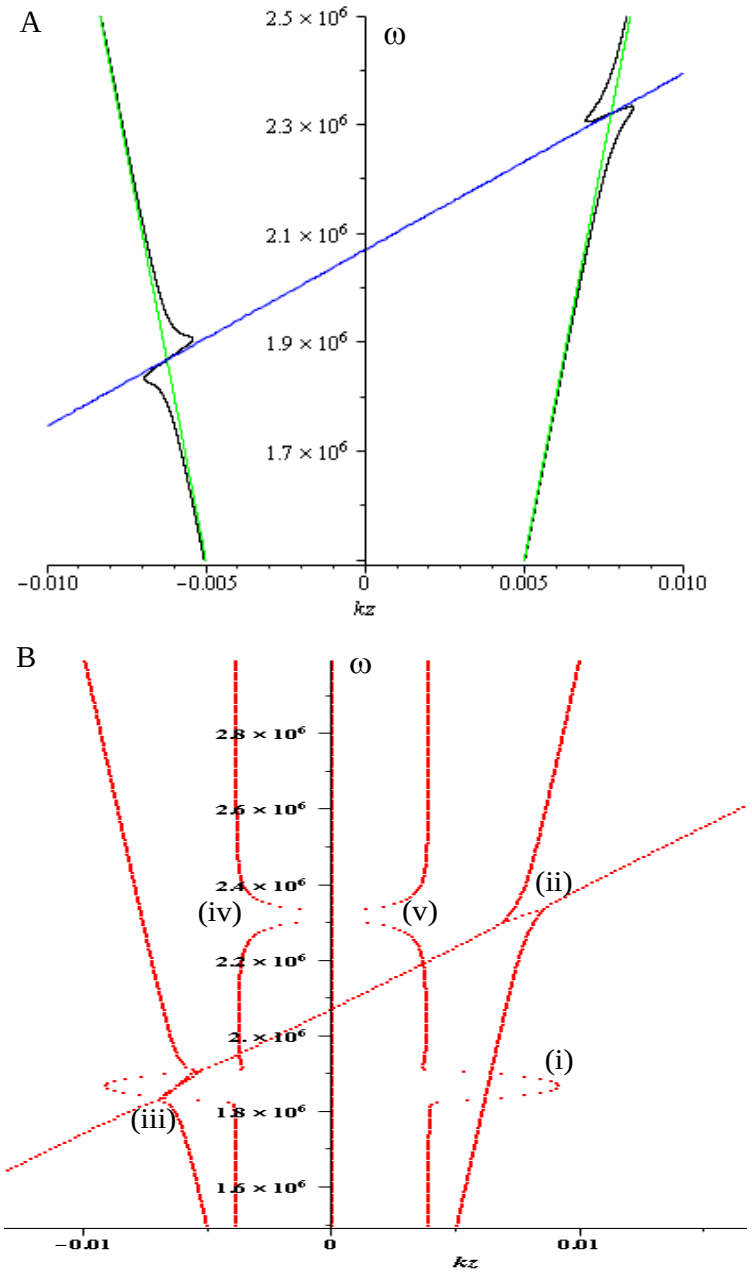

Figure 4.2: Dispersion plot for free space with current of 20μA/m^2, α=1.5, V=10kV

Figure 4.2B shows that the imaginary parts of the complex roots (which have had a x10 multiplier applied to them for clarity) have increased in value. At points (ii) and (iii) the resonance point can be seen, again with the kink in the wave trace. At point (iv) and on the opposite side to point (v), there is a stable condition where no growth

takes place, shown by the 'pinches' in towards the y-axis of the imaginary parts of the solution. Similarly referring again to point (i), there is an unstable condition where the instability is growing, shown by the bulges out to the side.

4.2.2 Bounded Geometry

Figures 4.3A to 4.6A show the dispersion plots for the case where cylindrical radiation boundaries are present. It is clear to see that increasing the pitch factor of the electrons, decreases the gradient of the electron beam line. Figures 4.3B to 4.6B show the plots of the real and imaginary parts of the complex roots in k_z, again with a cylindrical waveguide in place, giving a bounded condition, the dispersion for which is shown in Equation 4.2.2.

$$D = -C\left[\frac{(\omega - k_z v_z)T_{sm} - k_\perp v_\perp U_{sm}}{\omega - k_z v_z - S\omega_c}\right]\left[\frac{\beta_\perp^2(\omega^2 - k_z^2 c^2)H_{sm}}{(\omega - k_z v_z - S\omega_c)^2}\right] + \omega^2 - c^2(k_z^2 + k_\perp^2) \qquad \text{Equation 4.2.2}$$

Where, $C=\left(\frac{n_b e^2}{\pi r^2 m_0 \gamma K \varepsilon_0}\right)$ and $K=J_m(\mu)^2\left(\frac{1-m^2}{\mu^2}\right)$

The basic structure of Equation 4.2.2 is clearly comparable with Equation 4.2.1, however additional terms are required to express the strength of the coupling to the new non-uniform non-planar wave. The term in the red box denotes the stabilising term. The term in the blue box denotes the destabilising term which gives rise to energy exchange. Close to resonance and/or in cases of high perpendicular velocity, the destabilising term will dominate. The system becomes unstable when the destabilising term becomes big enough. It is assumed that if the beam plasma frequency is substantially less than that of the wave then the field structure of the waveguide is not strongly perturbed. T_{sm}, H_{sm} and U_{sm} are transverse coupling strength terms relating the transverse properties of the electric field and the electron beam. See Appendix 2 for expressions for T_{sm}, H_{sm} and U_{sm}.

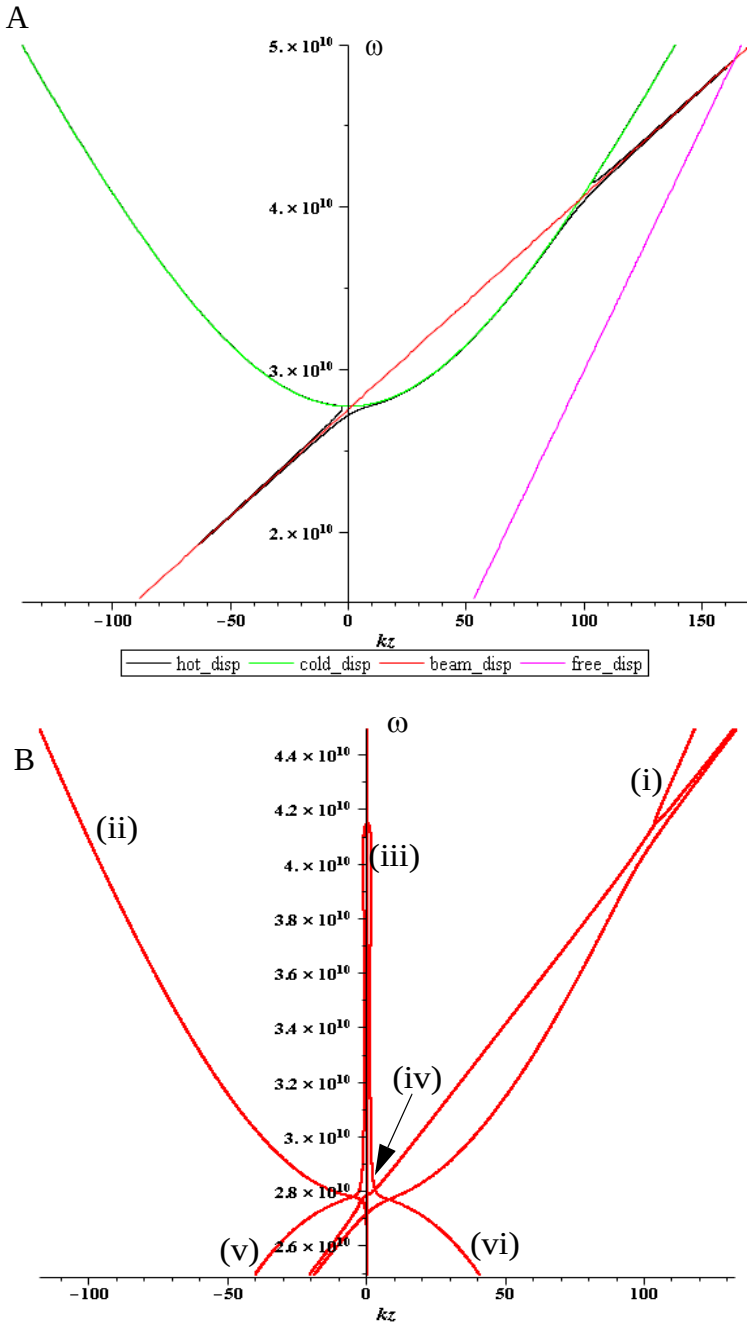

Figure 4.3: Dispersion plot for the TE_{01} mode with I=12A, α=0.5, within the boundary of a cylindrical waveguide of radius 4.14cm

Figure 4.3A shows the resonant coupling of a beam of 12A with a TE_{01} mode in a waveguide of radius 4.14cm. The waveguide mode is represented by the green trace, the beam line by the red trace, the speed of light line by the pink trace and the coupled

dispersion by the black trace. The magnetic field in this case is 0.18T suitable for near cut-off resonance with the TE_{01} mode. As is seen in this first case, with a pitch factor of 0.5, the resonance condition means the beam crosses the waveguide mode. It can be seen from Figures 4.4A and 4.5A that an increase in the pitch factor allows for a grazing resonance condition which is more beneficial for energy transfer.

In Figure 4.3B, it can be seen at point (i) that at the point of resonance there are three lines that can be distinguished, the left most line is the real forward waveguide mode, next to this is the fast cyclotron mode and beside this the slow cyclotron mode. In these cases it is the fast cyclotron mode that couples to the waveguide mode, the slow cyclotron mode stays real and does not couple. The real backward waveguide mode is seen at (ii). The imaginary part of k_z of the coupled mode may be seen from (iii) to (iv) and the second resonant point is seen at the base of the waveguide mode. The imaginary part in negative k_z, opposite point (iv) denotes the growth of the wave energy, whereas the imaginary part of k_z on the positive side, at (iv), shows decay of the beam energy. The imaginary parts can be seen to extend out to the left and right away from the ω axis, and down towards zero, indicated by points (v) and (vi). This describes evanescent decay of the wave below cut-off.

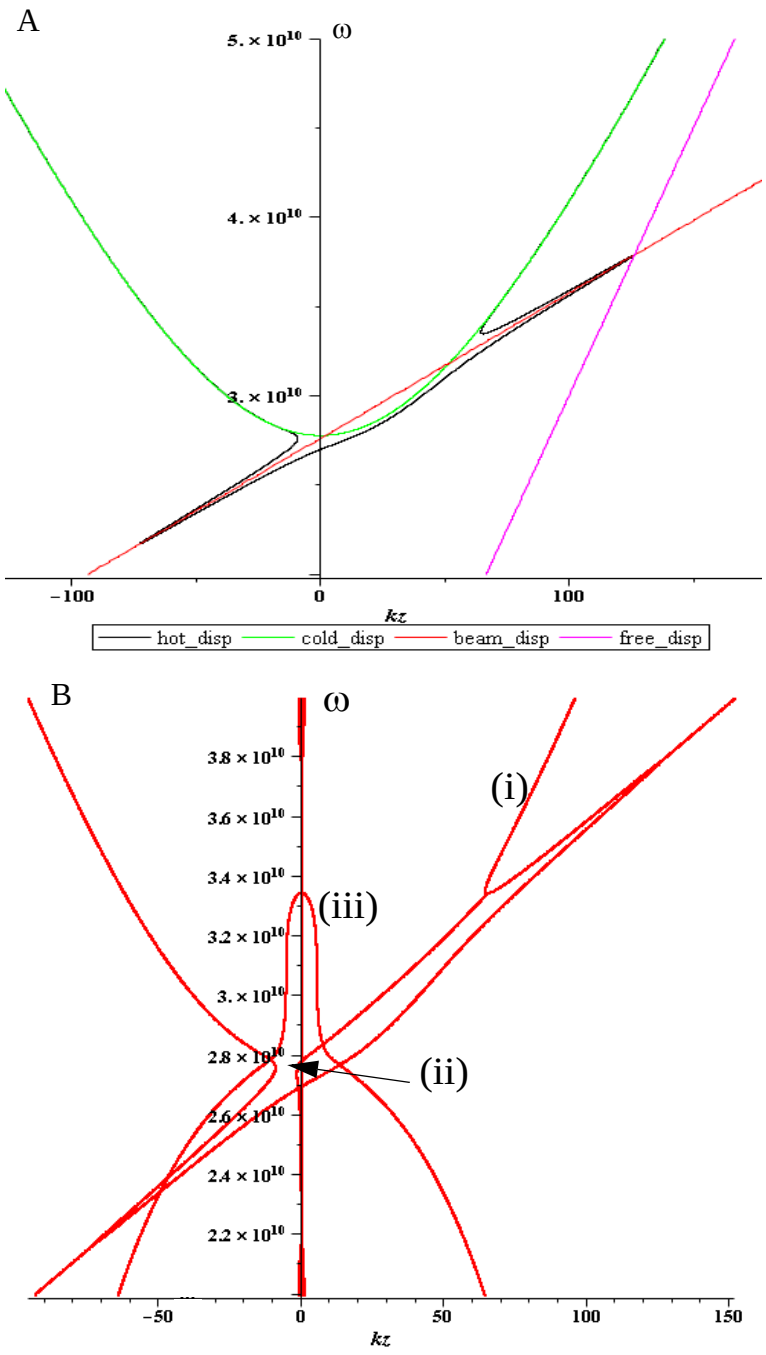

Figure 4.4: Dispersion plot for the TE_{01} mode with current of 12A, α=1.5, within the boundary of the cylindrical waveguide

Figure 4.4 show the dispersion and complex roots plots with a pitch angle of 1.5. As can be seen, with a higher pitch factor of 1.5, the upper resonance reduces in

frequency, (i), and it is clearer to see the coupling between the fast cyclotron mode of the beam and waveguide mode. There is a noteworthy effect at the lower coupling point, (ii), where there is a ‘gap’ in the plot. At this point the interaction is unstable, with no real solutions of either ω or k_z, so oscillations will occur due to an absolute instability. This may also occur at lower pitch angle of 0.5, but from the graph it is not clear to see. At point (iii) the imaginary part of the complex root has increased corresponding to a larger growth in the wave energy as it accepts the energy given up by the beam, due to resonance between the wave and the fast cyclotron beam mode. This ties in with Equation 4.2.2 whereby if the pitch angle increases then so too does $v_\perp$ and hence $\beta_\perp$. As $\beta_\perp$ appears in the ‘destabilising’ term of the dispersion equation as a squared number, this term will increase more rapidly and hence give rise to more beneficial parameters for energy transfer.

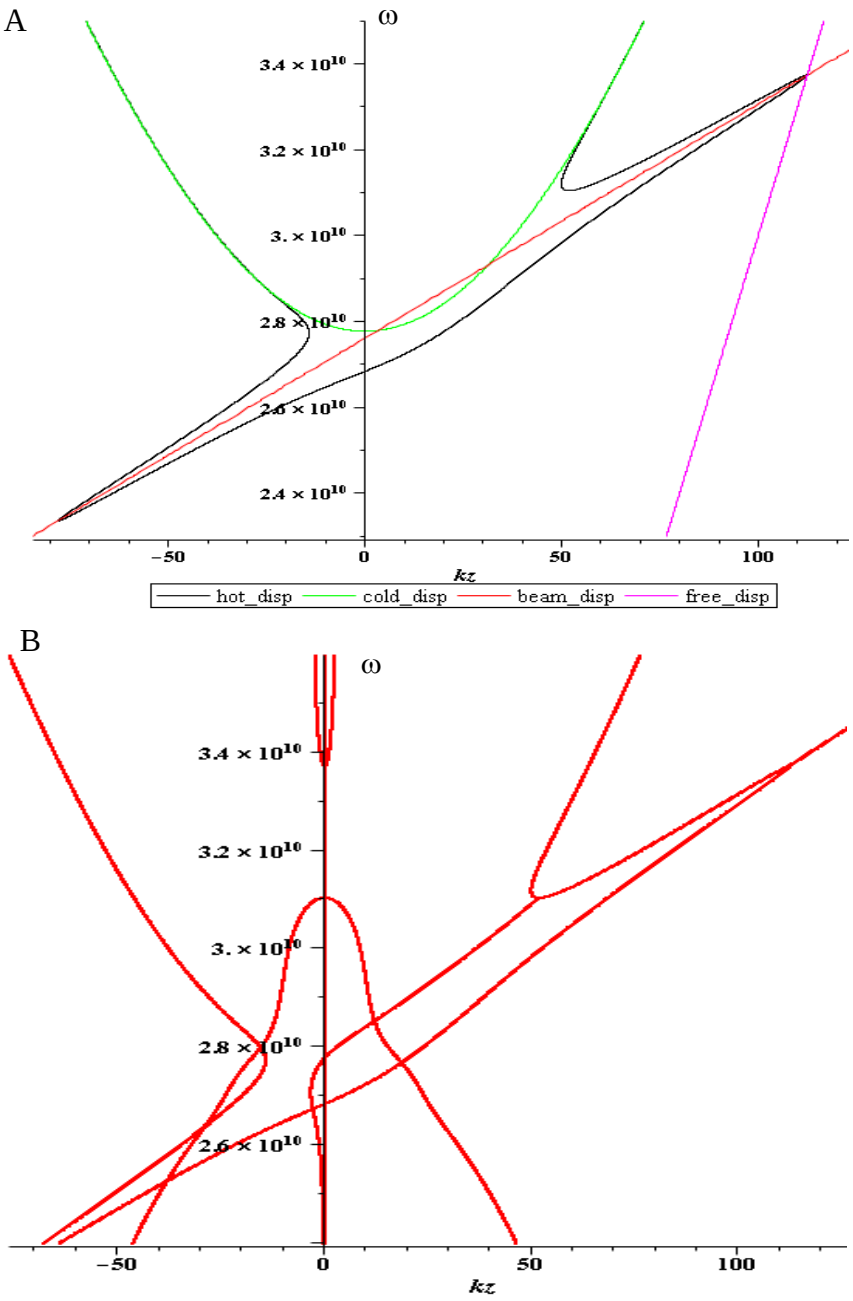

Figure 4.5: Dispersion plot for the TE_{01} mode with current of 12A, α=2.5, within the boundary of the cylindrical waveguide

Figure 4.5A shows the dispersion plot obtained with a pitch factor of 2.5 It is much easier to see in this plot of Figure 4.5B that it is the fast cyclotron beam mode that

couples to the wave. The imaginary parts of k_z have now increased even more in value, suggesting an even more substantial growth in wave energy.

Figure 4.6A shows an example of an increased current from 12A to 34A, using α=1.5, which shows more or less an identical plot to that in Figure 4.4A except that the imaginary part of k_z has again grown larger. An important thing to note about these graphs when α or I is varied, is the effect that it has on the feature in the plot in Figure 4.4 B (iii), and at the same section in Figure 4.5 and 4.6. As can be seen, increasing the value of α from 1.5 to 2.5, increases the magnitude of the imaginary component of the wave vector and hence increases the spatial growth rate. Similarly increasing the value of the beam current from 12A to 34A has a similar impact.

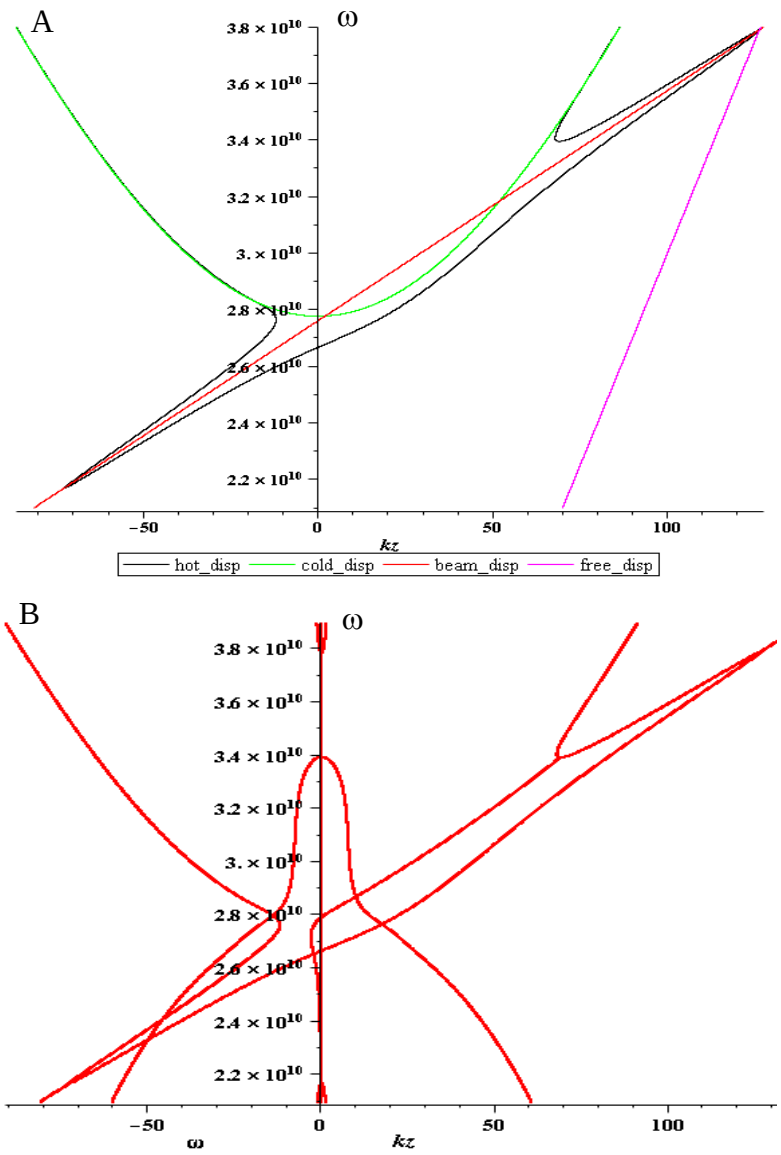

Figure 4.6: Dispersion plot for the TE_{01} mode with current of 34A, α=1.5, within the boundary of the cylindrical waveguide

The values obtained for the imaginary parts of k_z can be used in the following mathematical steps to obtain a prediction for the spatial growth profile of the system, by first considering the wave function:

$$E(z) = E_A e^{i(k_z z - \omega t)} \qquad \text{Equation 4.2.3}$$

But,

$$k_z = k_{zr} + ik_{zi}$$ Equation 4.2.4

Therefore;

$$E(z) = E_A e^{i(k_{zr}z + ik_{zi}z - \omega t)} = E_A e^{-k_{zi}z} e^{i(k_{zr}z - \omega t)}$$ Equation 4.2.5

So now, if z=L and E_A is measured at the origin, 0, one obtains:

$$E(L) = E_A e^{-k_{zi}L} e^{i(k_{zr}L - \omega t)}$$ Equation 4.2.6

Then the amplitude has grown compared to the initial value and one can write the amplitude growth as:

$$E_A(L) = E_A e^{-k_{zi}L}$$ Equation 4.2.7

Using Equations 4.2.6 and 4.2.7, the gain can be determined by substitution:

$$\text{Gain (dB)} = 10\log_{10}\left(\frac{P(L)}{P(0)}\right)$$ Equation 4.2.8

$$= 10\log_{10}\left(\frac{E_A(L)}{E_A}\right)^2$$

$$= 20\log_{10}\left(\frac{E_A e^{-k_{zi}L}}{E_A}\right)$$

$$= \frac{20\log_e(e^{-k_{zi}L})}{\log_e 10}$$

So the gain is given by the following expression;

$$G(dB) = 8.7(-k_{zi}L)$$ Equation 4.2.9

If the answer to this expression turns out to be negative, then there is attenuation, a positive answer implies gain.

The following plots, Figures 4.7 to 4.9, show 3D images of the dependence of the coupling coefficient, H_{sm}, for the TE_{01} mode on normalised control parameters p and q, and the impact of changing the harmonic number, S. Where $p = k_\perp r_c$ and $q = k_\perp r_L$, with $k_\perp$ the perpendicular component of the k-vector, r_c the guiding centre radius, and r_L the Larmor radius.

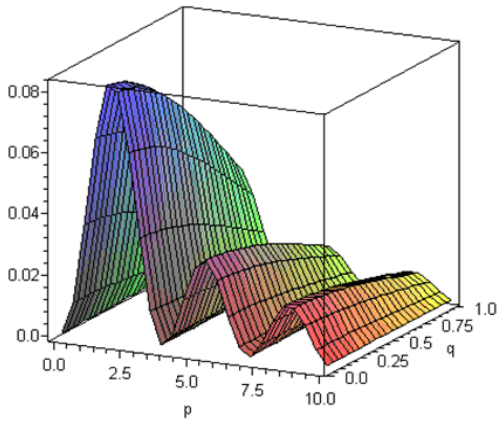

Figure 4.7: H_{sm} dependence on guide and Larmor radii at cyclotron harmonic, S=1

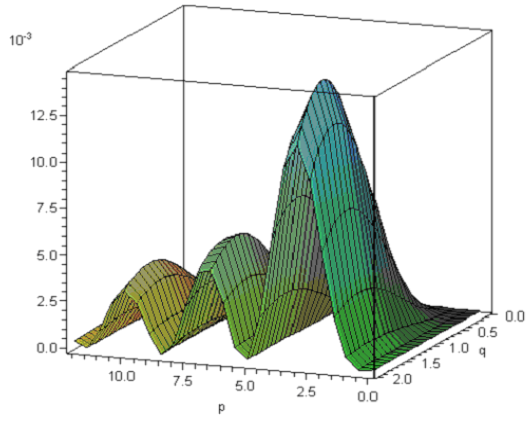

Figure 4.8: H_{sm} dependence on guide and Larmor radii at S=2

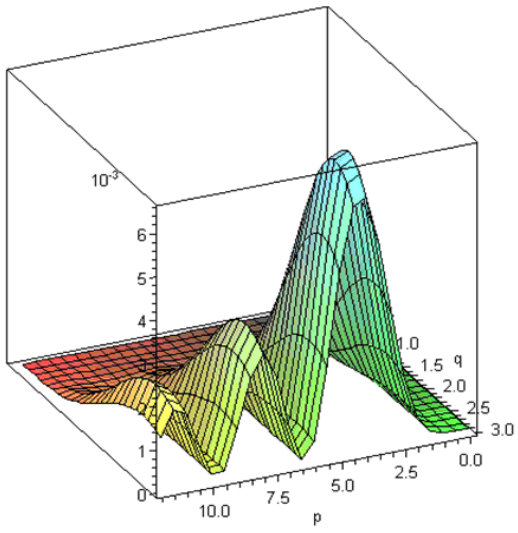

Figure 4.9: H_{sm} dependence on guide and Larmor radii at S=3

It is clear to see that as the harmonic number is increased, the maximum amplitude of the coupling coefficient decreases, (about an order of magnitude from S=1 to S=3), making the instability more difficult to excite.

4.3 Non-Linear 2D Simulations

The KARAT programme is a time dependant, fully electromagnetic, Finite Difference PiC code and was used to simulate the electron beam formation and the RF interaction. It works by solving Maxwell's equations on a grid whose dimensions are chosen to ensure that there is no dramatic variation in the fields between any two nodes, one can then determine the field experienced by any particle at any point in space by interpolation. Due to memory and time constraints, not every particle in the experiment can be simulated, therefore a merging factor is defined which collects a group of particles together into one PiC particle (by default one PiC particle contains $3x10^9$ real particles). The code then uses the Lorentz force equation, Newton's second law and the relativistic equations of motion in order to work out the trajectories of the particles. It was necessary to use this program to simulate the formation of the

velocity profile in the electron beam because in the laboratory it was impossible to reach large degrees of magnetic compressions whilst keeping the completely adiabatic conditions required for the theoretical analysis. The program was used to model a realistic compression regime and calculates the static magnetic and electric field when given appropriate information on electrode geometry, potentials and solenoid configuration. A Maple script calculates the coil configurations required for the desired experimental field profile. The rest of the experimental parameters are then programmed into the KARAT code.

4.3.1 Magnetic Field Profile Script

Before starting any simulations in the KARAT programme, one needs to be able to input the correct experimental magnetic field configurations by defining the solenoid geometry and currents. This was facilitated using a further Maple script. The Maple code does two things; It allows for the design of the solenoids and, once it has been verified against the experimental measurements of B, it allows magnetic fields to be set by predicting the current which needs to be applied to each coil. The verification of the Maple script was shown in Chapter 3 when the Hall Probe measurements were carried out, Figures 3.11 to 3.14. The script was used to set each PSU current to obtain plateau magnetic fields of B=0.18T or B=0.21T required for the two experimental configurations.

To configure the magnetic field with the Maple script, one first finds the cut-off frequency, f_c, using Equation 2.3.27, for example with an 8.28cm diameter waveguide, the cut-off frequency of the TE_{01} mode is;

TE_{01}: $f_c = 4.4194\text{GHz}$

This gave a corresponding magnetic field strength when using a rearranged version of Equation 2.2.1 to yield close to cyclotron resonance for an electron beam of energy 75kV;

TE_{01}: $B_{01}=0.1824\text{ T}$

The B-field and f_{ce} for a detuning of 1%, 2% and 3% are also required to study the strength of the RF instability. These are as follows:

1% detuning: f_{ce} = 4.375 GHz B = 0.1806 T

2% detuning: f_{ce}= 4.331 GHz B = 0.1788 T

3% detuning: f_{ce}= 4.287 GHz B = 0.1769 T

Where B here was the maximum magnetic field value over a 20cm long plateau which covered the extent of the interaction region.

With the plateau magnetic field value defined, coil parameters such as the number of turns and layers per coil, the lengths of each solenoid, currents and relative axial positions, were input into the script. A plot of the magnetic field profile, shown in Section 3.5.2, was obtained and could be fine tuned by altering the currents on each of the five coils. It was particularly important that the script allowed solenoid 4 to be altered to balance the impact of solenoid 2's fringe field in the plateau region. From these plots one obtains the mirror ratio values, taken at the cathode position, for example Figure 3.10(i) and the maximum point on the plateau, B_z/B_{z0}, Figure 3.10(ii). A detuning of 2.4% proved to work best experimentally for different values of the cathode coil and for resonance with the TE_{01} mode, where;

Solenoid 1 = 30A, 60A corresponding to cathode B-fields of 0.01T and 0.02T
Solenoid 2 = 40A
Solenoid 3 = 101.83A - plateau field of 0.18T
Solenoid 4 = 70.3A
Solenoid 5 = Solenoid 3
Solenoid 6 = 0A

Once the plot had the correct flat plateau form with the appropriate peak magnetic field, the coil configurations were written into a separate file. The file was written in a format that KARAT would be able to read and contained the parameter description of the coils. This enabled KARAT to run detailed simulations of the experiment (once the geometry of the electrodes and other characteristics had been programmed) with accurate, experimentally consistent, magnetic field profiles.

4.3.2 Electrode Configuration

Figure 4.10 shows the geometry programmed into KARAT. The dimension of the anode can was set for a radius of ~8cm as can be seen by the outer light blue line on the left of the picture. The radial decrease to the interaction waveguide of radius 4.14cm can be seen.

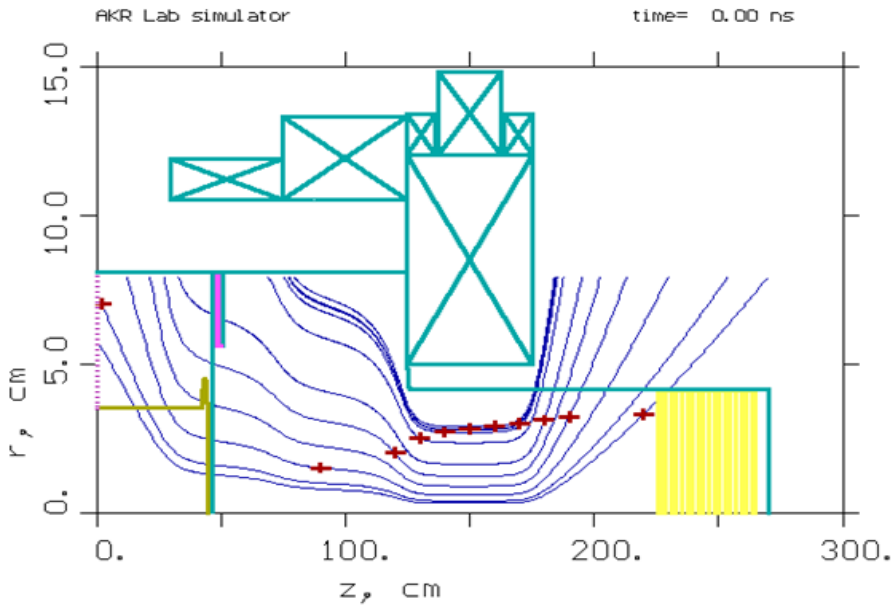

Figure 4.10: KARAT representation of simulation geometry

The solenoids are shown at the top of the picture, solenoid one situated around the electron gun region, solenoid 2 at the entrance to the interaction waveguide and solenoids three, four and five over the interaction waveguide section where the beam-wave resonance takes place. Solenoid three is the one that most critically controls the plateau of the magnetic field for that region, setting a maximum field value whilst solenoids 4 and 5 hold it steady for the 20cm of the interaction space, which is illustrated by the dark blue field lines. The electrodes were programmed to be consistent with the experiment. The cathode, visible on the left, has been given a conical shape to replicate the experimental nose cone as described in Section 3.3 and shown in Figure 3.2. However, due to the extreme foreshortening of the KARAT

graphics along the z axis, this cannot be seen in Figure 4.10. An area just at the base of the nose cone has been specified as the electron injection point to simulate the velvet emission region, this yields a hollow beam with a mean guiding centre radius ~1cm once magnetically compressed in the interaction region. A potential was set on the cathode of -75kV, with the beam current defined as a control parameter.

The anode mesh situated directly in front of the cathode face is programmed in as a foil. This allowed the user to define an equipotential surface which would appear transparent to the electrons and not hinder their motion, thus allowing an idealised representation of the experimental anode mesh. In order that the radiation emitted during the simulation was absorbed within the confines of the simulation boundaries, a ‘numerical’ absorber was placed to the far right of the interaction waveguide, effectively in the place of the output window of the experiment. Its absorbance was defined to increase progressively towards the far right of the simulated geometry.

The resolution in the simulation can be manually altered and is important as it determines the wavelength of radiation that can be simulated. It is based on an approximation of the Nyquist limit which states that there should be at least 3 resolution nodes per wavelength to be able to properly distinguish characteristics of the plots. Too few nodes can lead to numerical inaccuracy but on the other hand, if the number of nodes is too large then it can cause the simulation to run very slowly and increase the growth rate of numerical errors. In the case of these simulations it is set to be a minimum of ten nodes per wavelength. In actual fact the values most commonly used in this project were 81 nodes in the R (radial) direction and 1001 nodes in the Z (axial) direction. This gave quite a fine resolution, particularly in the radial direction, but was necessary to give a reasonable simulation of the electron gun properties. For the ~6.7cm wavelength of the radiation in this set-up, this gave ~68 nodes/wavelength in the radial direction and ~25 nodes/wavelength in the axial direction.

With the set-up and programming of the KARAT configuration script complete, simulations were undertaken investigating the impact of variables such as the injected electron current and magnetic field configuration on the power output and the

horseshoe distribution formation and evolution. The predictions from the code could be compared to experimental measurement but also gave an insight into some of the internal dynamics that could not be directly measured, i.e., the detailed evolution of the horseshoe distribution function. Evidence that it has formed can be gathered experimentally through measurements of the beam current as a function of mirror ratio. But with the 2D non-linear code, plots can be generated which clearly show the formation of the horseshoe distribution as the electron beam is travelling through the magnet system, and shows how the axial velocity component of the radiation/beam is sacrificed for increasing transverse velocity. Values of $v_{\perp}$, v_z and E_K of the electron within the distribution can be obtained at different stages of their passage through the apparatus. The computation also predicted the decay of the horseshoe distribution due to the beam-wave interaction which was something that could not be measured directly.

Other diagnostics included the measurement of I_b within the resonant cavity and measurements of E_ϕ the electrical field of the wave, the Fourier transform of E_ϕ for the spectrum of radiation, and the power in the output waveguide. By taking note of the value of I_b within the resonant cavity, the current lost through scraping or mirroring can be obtained as a reduction from the initial input current. These diagnostics played a vital role in the calculations of the electron distribution where a comparison was made between the numerical and experimental velocity distributions, see Sections 5.3 and 6.2.

4.4 Simulations of Resonance with TE_{01} Mode

The initial task for KARAT was to be able to simulate the experimental proposal before any measurements were physically taken in the laboratory. This was to aid in the prediction of results and give reassurance of the basic validity of the proposed method. The geometry was defined for the cylindrical cavity described earlier, appropriate for generation of radiation in the TE_{01} modes at 4.42GHz, and the currents on the coils defined to give a maximum magnetic field plateau of 0.18T. The resolution was initially set at quite a coarse setting, 41(R) and 501(Z) while

parameters were optimised as this decreased the run time of the simulations. Once the simulation was giving persuasive results which compared reasonably with astrophysical expectations, the resolution was changed to give a finer grid mesh at 81(R) and 1001(Z). The ultimate choice of the mesh was driven by a desire to improve accuracy of the gun calculation rather than the EM dynamics since the mesh cathode spacing is only 2cm across. This meant that for the coarse mesh there was only 12 nodes across the spacing as opposed to 25 nodes for the fine mesh. The cathode current was varied between ~10-150A with plots of beam current (in the cavity) Vs mirror ratio being compiled. This process was carried out for each of three detuning settings of 0.6%, 1.5% and 2.5% below the resonant cyclotron frequency.

The code was able to predict the mode structure, power and frequency of the emitted RF radiation.

4.4.1 Comparison of Numerical and Experimental Velocity Distributions

Measurements of the cavity beam current as a function of peak magnetic plateau allow the quantitative study of the electron distribution in velocity space. This was achieved by increasing the mirror ratio causing progressive mirroring to be obtained. These results can be compared between the experimental data and numerical predictions allowing the modification of the numerical simulation of the electron gun to achieve a comparable electron distribution function. Variations of the cathode nose cone geometry, changing the angle of the cone to regulate the simulation pitch factor, was used quasi-empirically to converge on a simulation electron beam that replicated the experimental measurements, see Section 5.3. This allowed reasonable comparisons to be drawn between the measurements of the RF instability and the numerical predictions.

4.4.2 RF Calculations

Having configured the geometry and succeeded in the generation of an experimentally consistent electron beam, the output radiation of the beam-wave resonant interaction could be computed. The predictions of the time evolution of the

electric field yielded the radiation spectrum and the spatial distribution yielded the excited mode. The phase space plots which were recorded by KARAT at discrete points along the axis of the system illustrated the formation of the horseshoe distribution as well as the process of electron bunching.

The output RF power predicted for each configuration of beam power, magnetic compression and detuning could be analysed and the values compared to the predictions of the linear theory.

4.4.3 Addition of Background Plasma

The KARAT code was altered to numerically include a Penning type trap geometry within the interaction region of the waveguide. Due to the decrease in diameter of the new interaction region, the cut-off frequency within the Penning trap differed to that of the original cylindrical waveguide. This in turn affected the resonance condition requiring an increased magnetic field plateau value;

Inside diameter of Penning trap=70.2mm
f_{co}=5.21GHz
B=0.214T

To be able to reasonably simulate the addition of a background plasma, details such as Debye length, plasma parameter and therefore the merging factor had to all be carefully considered, see Table 4.1. It is ideal to have as high a merging factor as possible as this allows the computer code to run faster and use less memory. However, increasing the value of the merging factor, increases the value of g_p, the plasma parameter. From Equation 2.6.8, it is seen that the value of g_p must be significantly lower than 1 if the plasma regime of the simulation is to be compared to the experiment (i.e. be in the weakly coupled regime). For the PiC code, a number density ~$1.12 \times 10^{13} m^{-3}$ was used corresponding to a plasma frequency of ~30MHz. This is scaled from the 9kHz plasma frequency in the auroral density cavity. The merging factor was set to 30 which gave values of g_p for the experiment and the simulation of 4.72×10^{-7} and 2.33×10^{-3} respectively, assuming the electron temperature of 10eV. It

was not possible to have a plasma frequency greater than 30MHz due to the limitations of the code, i.e. the maximum number of allowed PiC particles. The code then predicted the interactions between the ions and electrons present within the plasma and the electron beam.

Table 4.1 Comparison of PiC Code and Real Plasma Parameters

	PiC values	'Real' Values
Merging Factor = 30		
Plasma Frequency = 30MHz		
n (m^{-3})	$3.7x10^{11}$	$1.12x10^{13}$
λ_D (mm)	1.1	5.7
g_p	$2.33x10^{-3}$	$4.46x10^{-7}$

Chapter 5 : Numerical Results

Chapter 5 : Numerical Results

5.1 Introduction

Conducting numerical simulations prior to a laboratory experiment offers many advantages. Not only can it aid in the design of critical experimental components, but it also provides a database of predictions for comparison to the experimental measurements and, in this case, to magnetospheric data. The simulation code used for this study was KARAT which was configured to simulate the experimental geometry as seen earlier in Figure 3.9. It allowed predictions of the radiation frequency, the electron phase space distributions, the radiation output power and the mode pattern showing the expected resonant TE_{01} mode. This chapter will discuss the numerical predictions for beam formation, transport and mirroring Section 5.2, the analysis of the electron velocity distribution Section 5.3, the predictions of the microwave output power Section 5.4 and the simulations of the effect of the plasma on the instability Section 5.5.

5.2 Beam Transport & Mirroring Results

In this thesis the focus of numerical and experimental study was based on configurations designed to excite the TE_{01} mode within two different waveguides; the initial cylindrical waveguide with diameter 8.28cm, and the Penning interaction waveguide with diameter 7.02cm. The resonant magnetic fields for these dimensions were 0.18T and 0.21T respectively. Since the apparatus was able to obtain peak magnetic fields in excess of 0.7T, the choice of these low magnetic field regimes with low frequency resonances provided the scope to analyse the electron distribution function by the ‘mirroring’ process.

For the initial beam transport simulations the waveguide dimension was a cylindrical waveguide with a radius of 4.14cm. This would allow a beam-wave resonance at 4.42GHz to take place, near cut-off with a relatively low order TE_{01} mode. At this frequency a magnetic field of ~0.18T was necessary giving a substantial reserve

capacity of magnetic field with which the resonant electron distribution function was measured.

For reference within this chapter to multiple diagnostic points distributed along the z-axis, Figure 3.9 is repeated below in Figure 5.1. KARAT computes the magnetic field lines (shown in blue) based on the magnet coil configuration and shows a plateau region centred close to the middle of the main coil, solenoid 3. The red crosses indicate diagnostic points at which KARAT makes detailed predictions of certain physical parameters within the simulation. The cathode/electron gun is shown in dark yellow on the left hand side whilst the boundary of the anode is shown in light blue. The magnet coils are represented by the blue crossed boxes along the top of the plot surrounding the anode. As can be seen from Figure 5.1, the lengths are extremely foreshortened in the axial (z) direction compared to the radial (r) direction, meaning that although the simulation can resolve the gap between the cathode and anode mesh, this is not clearly shown on the plot.

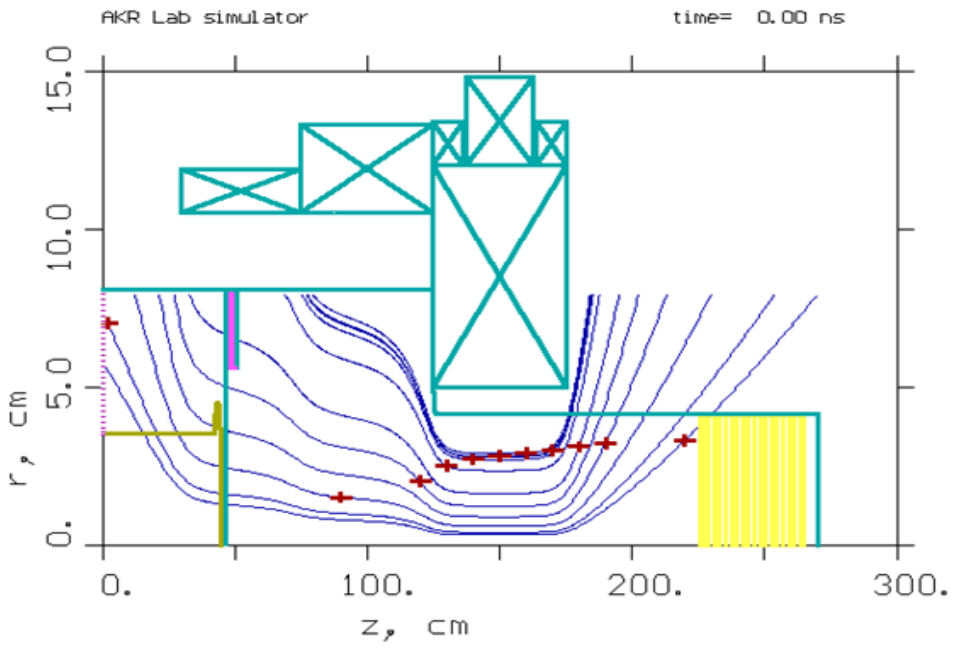

Figure 5.1: KARAT representation of the apparatus showing the magnetic field lines and the cross points along the z-axis

Figure 5.2 shows the electron beam trajectory as it passes through the system from the cathode, and into the interaction region along a region of increasing magnetic field.

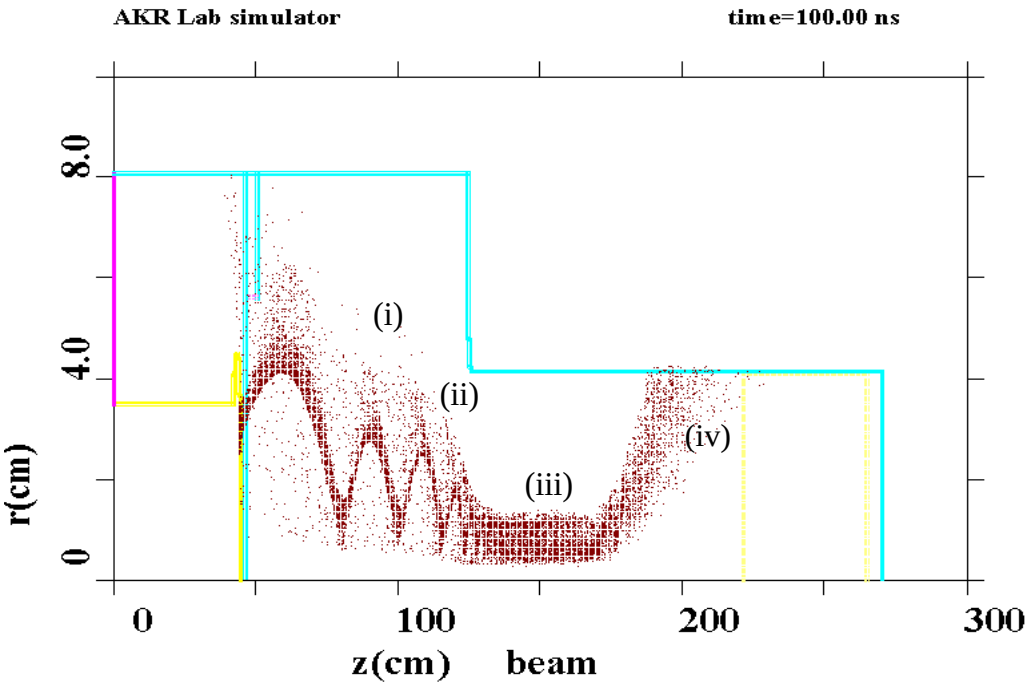

Figure 5.2: Trajectory of electron beam with magnetic compression

At point (i) in Figure 5.2 the electrons are injected into the converging magnetic field in the anode can region from the electron gun. Solenoid one controls the field in the cathode region as can be seen in Figure 3.10. This corresponds to Figure 5.3(i) where there is very little $v_\perp$ but high v_z as the formation of the horseshoe is in its early stages with a low pitch factor. At point 5.2(ii) the beam's guide and Larmor radius are decreased due to the magnetic compression taking place. The trajectory at this point is affected by solenoid two which controls the rate of magnetic compression. The magnetic compression means that there is an increase in $v_\perp$ at the cost of v_z as seen in Figure 5.3(ii). At point (iii) in Figure 5.2, where the magnetic field is at its highest point for a plateau of ~20cm, some of the higher pitch electrons are mirrored i.e. they have $v_\perp=v_{tot}$ and so acquire a negative v_z component and drift backwards towards the cathode. This can be seen in Figure 5.3(iii), and more evidently in (iv), where the tip of the horseshoe has been cut off at the axis of $v_z=0$. Figure 5.2(iv) shows the beam

expanding out after the plateau as the magnetic compression falls off. The electrons are dumped onto the waveguide side walls.

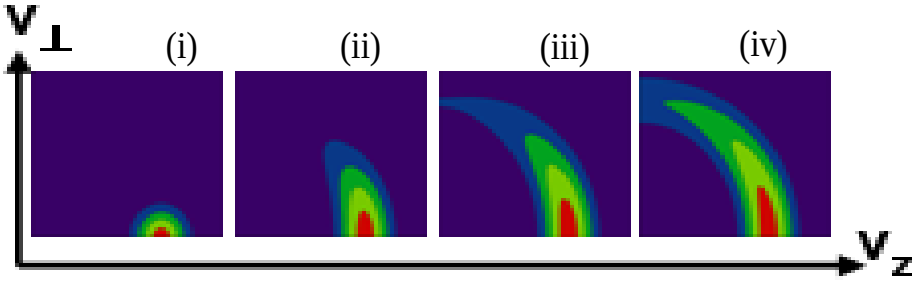

Figure 5.3: Evolution of horseshoe as magnetic flux increases, showing decreasing v_z as $v_\perp$ increases

As the axial velocity component decreases with increasing transverse velocity a horseshoe shaped electron distribution function can be seen to evolve. This is linked to the decrease in mean axial velocity with increasing mirror ratio, which in cases 5.3(iii) and (iv) leads to decreases in beam current due to mirroring. Figure 5.4 shows predicted phase space plots from a simulation by KARAT of the horseshoe distribution formation. It is similar to that shown in Figure 5.3(iii) and (iv) in that it shows the mirrored components of $v_z<0$. In this case where z=120cm, the mirrored component is that which has been reflected back from the interaction waveguide (at the point where B_z is at its maximum) and into the anode can region. The population density is seen to decrease with increasing pitch factor. Figure 5.4 corresponds to a cathode flux density of 0.01T and shows the horseshoe distribution predicted by KARAT. The point at z=120cm, which this plot refers to, is upstream from the interaction region and shows the injected electrons from the cathode at (i) with their reflected components at point (ii). Figure 5.5 shows a comparative distribution for cathode flux density of 0.02T. This figure shows a higher density of electrons at lower pitch factors (high v_z) and a greater spread in the mirrored component, due to the doubling in the beam current from 18A in Figure 5.4 to 35A.

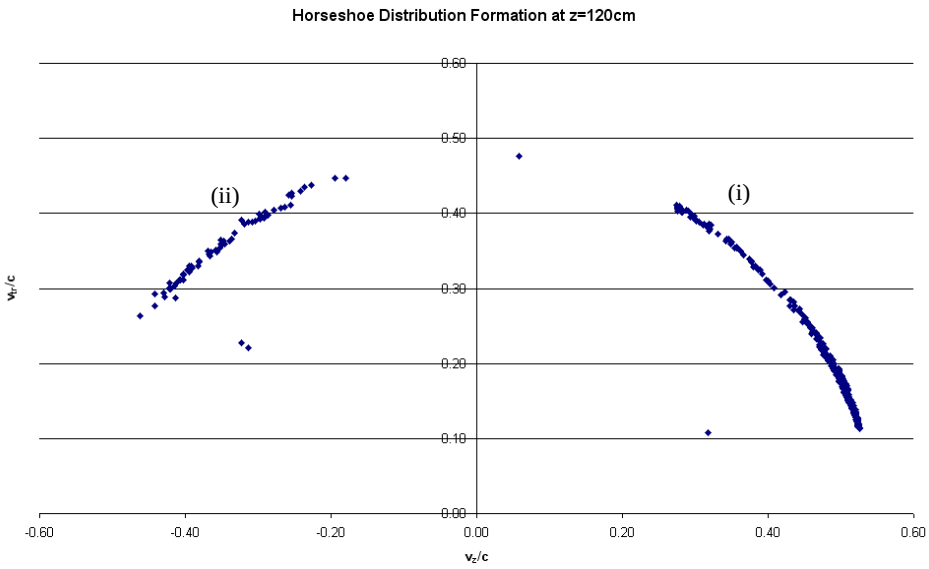

Figure 5.4: Initial trajectory of horseshoe formation, 1.5% detuning, 0.01T on the cathode, I_{beam}=18A, 120cm on z-axis

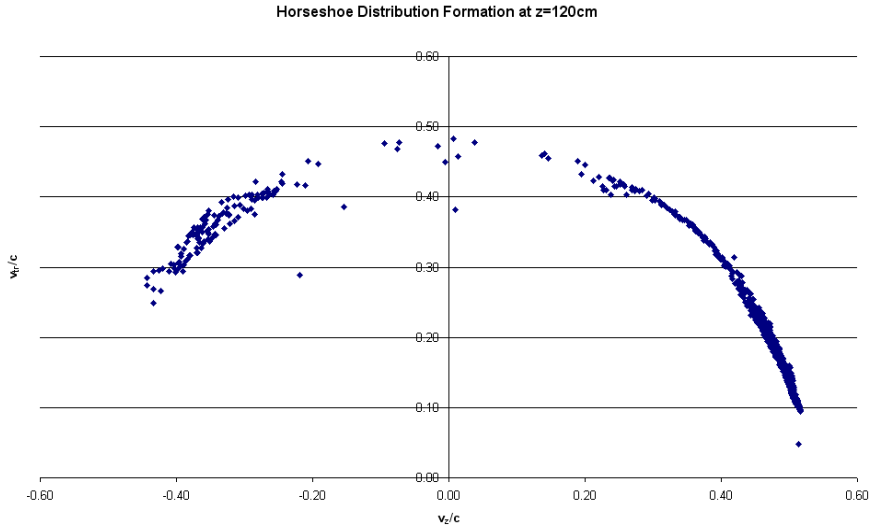

Figure 5.5: Initial trajectory of horseshoe formation, 1.5% detuning, 0.02T on the cathode, I_{beam}=35A, 120cm on z-axis

5.3 Analysis of Electron Distribution

When the beam transport experiments started in the laboratory it soon became evident that the electrons had a much higher value of perpendicular momentum than the code had predicted for the same settings of cathode and cavity magnetic fields. This meant that comparisons of the predicted RF efficiency to experimental RF efficiency were substantially different. An explanation of these differences was to look at the simulation resolution settings and simulated design of the cathode. The memory constraints of the KARAT programme on the calculation was one of the limiting factors where the resolution was concerned along with the difficulties associated with simulating the entire 3D gun region in a 2D modelling code, meant that it was not possible to fully self consistently simulate the gun geometry.

It was found that by analysing the electron beam line density distribution experimentally, that the simulations could then be improved by adjusting the simulation to match the new experimental findings. This was achieved by modifying the simulated electron gun thus varying the trajectory of the electron beam. This was possible as theories [Vorgul et al 2004, 2005, Bingham & Cairns 2000, 2002] have indicated that the critical parameter of the beam is the distribution of the electrons with high $v_{\perp}$. This meant that the properties of the electron gun could be varied until a close match between experimental and numerical beam configuration was achieved.

Figures 5.6 and 5.7 show how varying the plateau field strength has an effect on the beam current measured in the plateau region for each of the cathode field strengths. As can be seen, for both cases, as the plateau field is increased the cavity current decreases. The data from these and similar plots could then be graphed to indicate progressive mirroring with increasing plateau field (and hence mirror ratio), Figure 5.8, signified by the continually decreasing beam current.

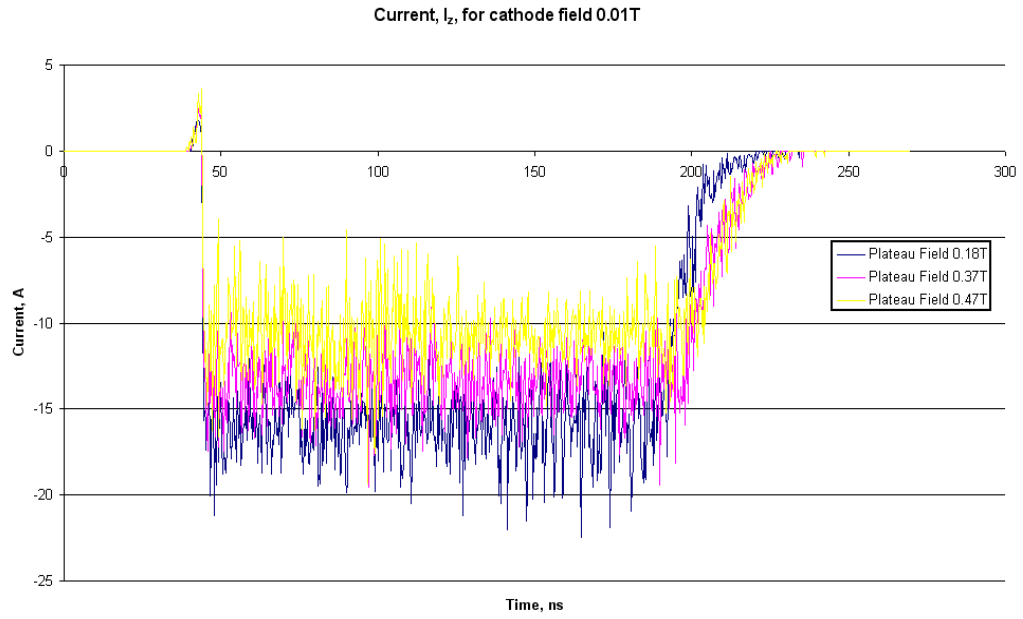

Figure 5.6: Cathode field of 0.01T showing variation in current as plateau field is altered

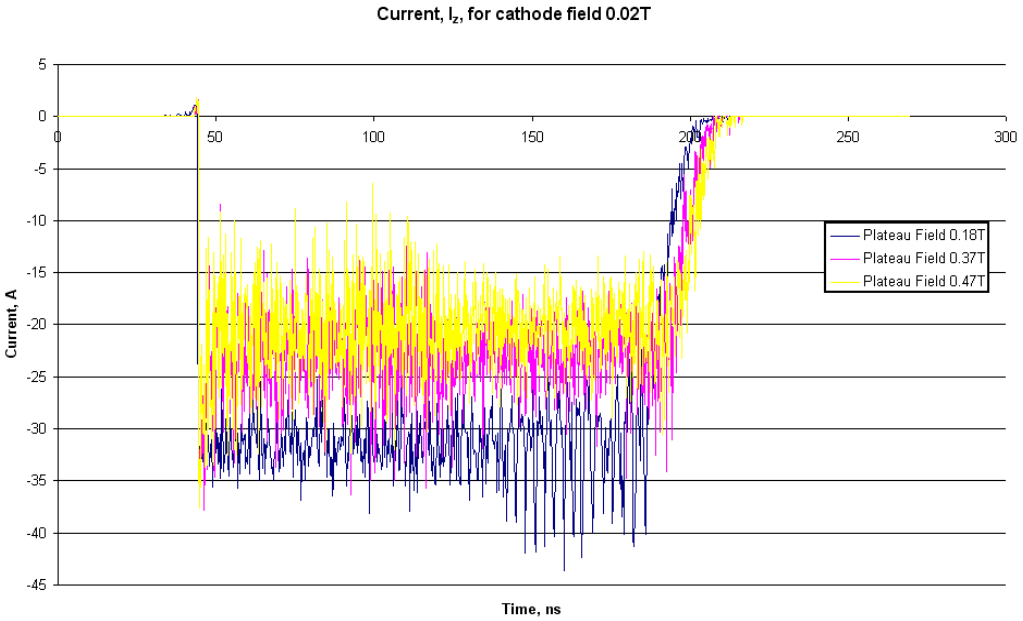

Figure 5.7: Cathode field of 0.02T showing variation in current as plateau field is altered

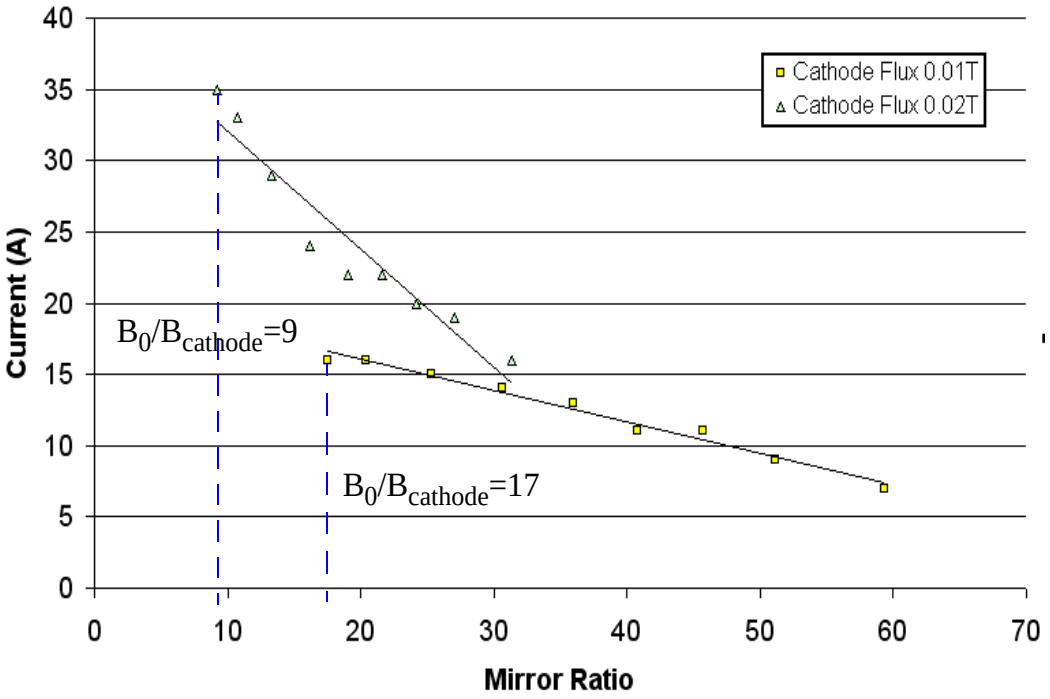

Figure 5.8: Simulated beam current in cavity Vs mirror ratio for cathode flux densities of 0.01T & 0.02T, input currents of 18A & 35A

Analysing the variation of the beam current with mirror ratio, Figure 5.8, as the plateau magnetic field, B_z, is increased from the resonant value, B_0, and relating this back to the critical value of v_z (where electrons with v_z less than v_{zcrit} will mirror), yielded the plot depicted in Figure 5.9 showing analysis of the electron distribution in velocity space as a function of the pitch angle. In Chapter 6 the experimental magnetic mirroring measurements are discussed and analysed in terms of the density of particles at certain points in the distribution. Drawing from that information in this present chapter, the details of the simulation geometry and emissivity of the electron gun were altered in a systematic process to yield a variation of electron current in the cavity with the magnetic field strength which matched experimental measurements. This enabled a much closer comparison between the predictions of the RF generation process and the laboratory measurements.

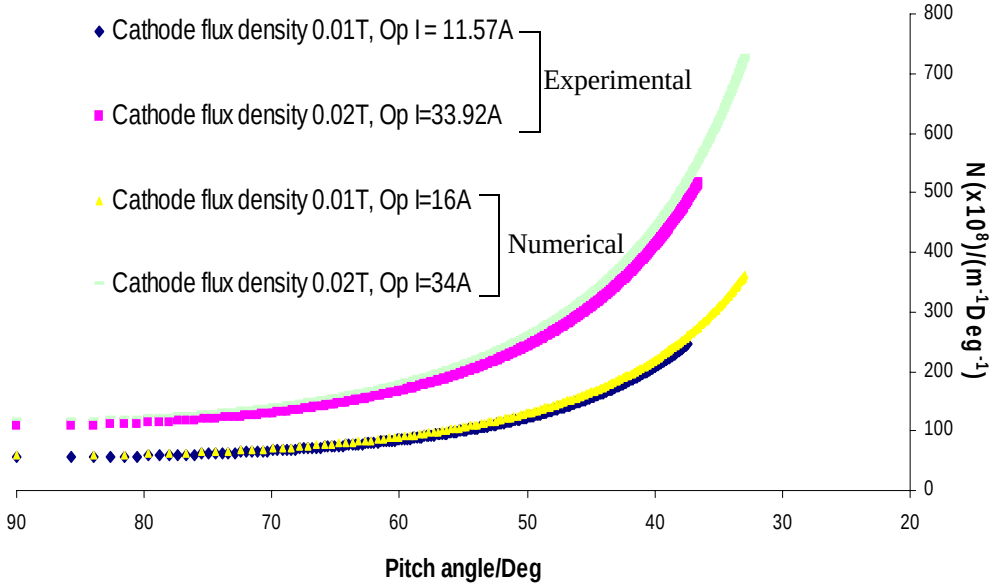

Figure 5.9: Numerically analysed electron distribution in velocity space versus pitch angle compared to experimental measurements

The electron distribution in velocity space of the electron beam formed at cathode flux densities of 0.01T and 0.02T and plateau flux density of 0.18T can be seen as a function of pitch angle in Figure 5.9, comparing the experimental data with the numerical calculations from KARAT.

5.4 RF Calculation Results

A wide range of parameters were investigated with a plateau magnetic field setting of ~0.18T, testing the impact of different detunings. The strongest resonance was numerically predicted with a detuning setting of ~1.5%. Figure 5.10 shows the expected operating frequency to be ~4.42GHz, the desired, close to cut-off, frequency value for resonance with the TE_{01} mode for a cathode flux setting of 0.01T at a detuning of 1.5% and 2.5%. In Figure 5.11 the same expected operating frequency is observed only in this case the cathode flux density is 0.02T and more prominent signs of the second harmonic are visible.

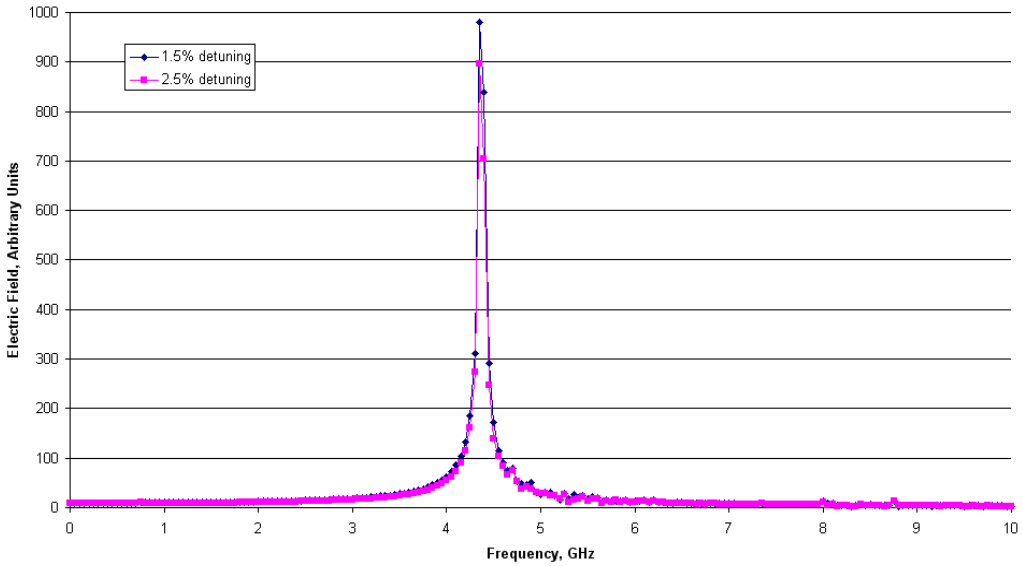

Figure 5.10: Predicted frequency of radiation with 1.5% and 2.5% detuning with 0.01T on the cathode

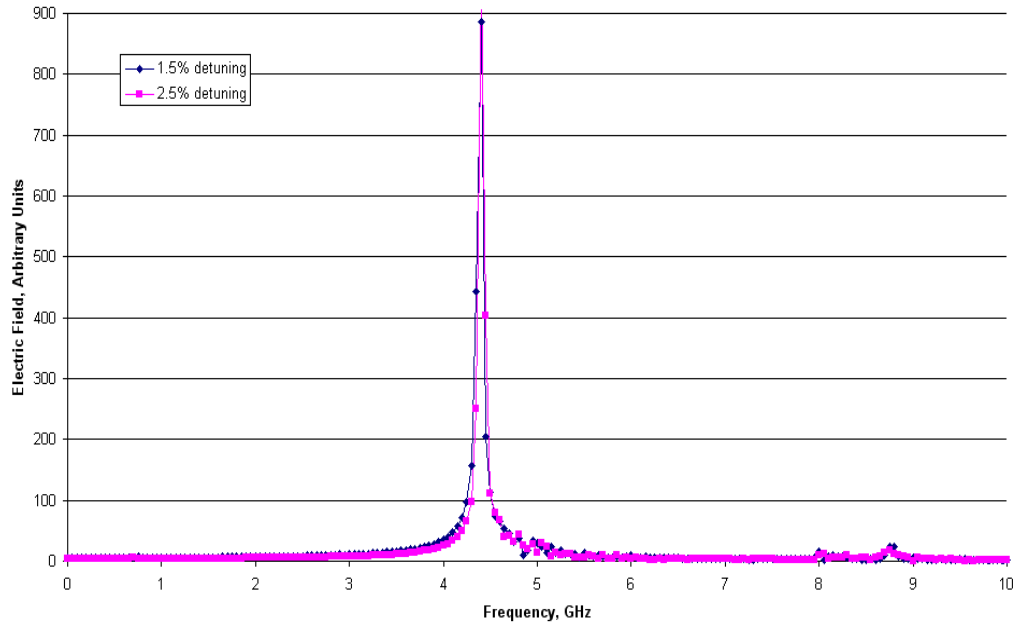

Figure 5.11: Predicted frequency of radiation with 1.5% and 2.5% detuning with 0.02T on the cathode

Figures 5.12 and 5.13 illustrate the formation and evolution of rotational electron bunching within the beam in velocity space for three different diagnostic points along the z-axis of the waveguide. These are depicted for both 0.01T and 0.02T cathode flux densities at position of z =130cm, 140cm and 190cm corresponding to electrons entering the cavity, the centre of the cavity and at the collection point respectively. Figure 5.12 shows the case for the cathode flux density of 0.01T, with 1.5% detuning. As can be seen, for the z axis positions of 130cm the electrons are formed in a circular pattern. At z=140cm although the electrons are still following broadly circular tracks in $v_{\perp}$ space the electron distribution around the path is now non-uniform which implies bunch formation. At z=190cm the size of the circular pattern has evidently reduced. This corresponds to the electrons having given up almost all of their rotational velocity as the pitch of the electrons at this point tends to zero due to 'magnetic decompression'.

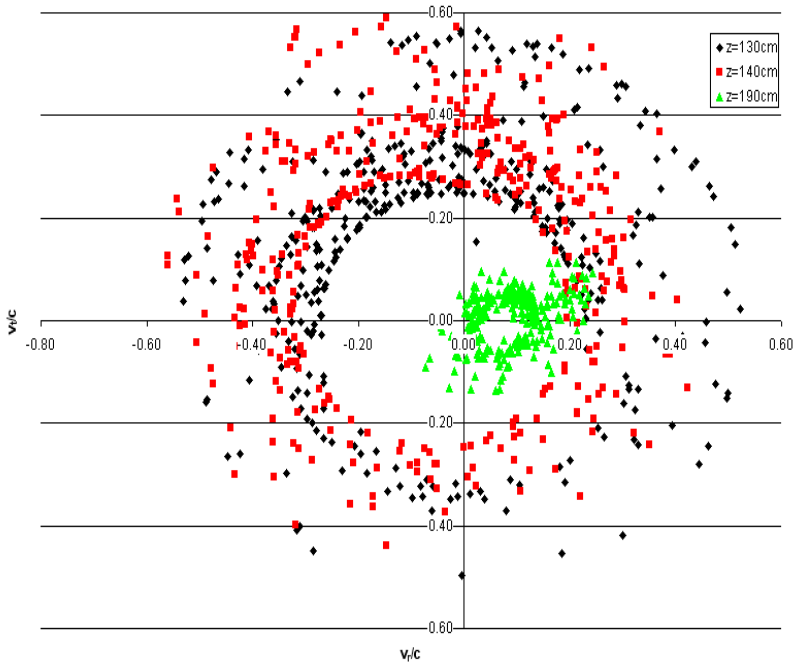

Figure 5.12: Electron bunching at z=130cm, 140cm and 190cm at 200ns into the simulation, 1.5% detuning, 0.01T on the cathode

Below in Figure 5.13, electron bunching for a cathode flux of 0.02T is predicted. In this case it is clear to see that at z=130cm i.e. at the maximum plateau magnetic field, there is strong bunching taking place. The red dots for this case clearly show the characteristic comma shape associated with CRM instability bunching mechanism.

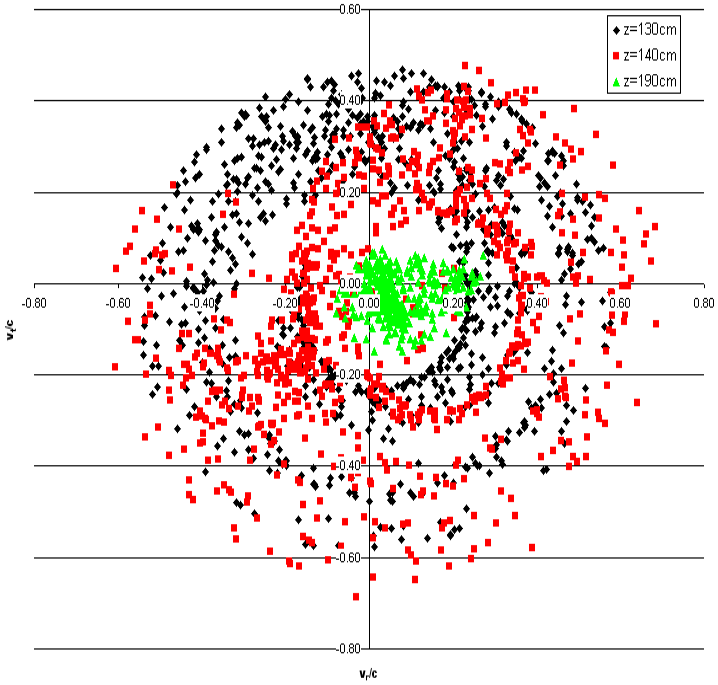

Figure 5.13: Electron bunching at z=130cm, 140cm and 190cm at 200ns into the simulation, 1.5% detuning, 0.02T on the cathode

Looking now at Figure 5.14, illustrating the horseshoe formation there is a clear line of monoenergetic electrons sitting on a sector of a circle, as was anticipated from the cathode designed for the experiment, for the initial diagnostic point at z=130cm. Moving through the system this line of electrons spreads out into a wider band in velocity phase space. The width of the band is an indication of how much energy modulation of the electrons has occurred. The electrons smear out in $v_\perp$ space and it is the excess of the electrons that move down in $v_\perp$ due to energy loss compared with those that move up in $v_\perp$ with energy gain that gives the RF output energy. Both the electron bunching and the smearing out of the horseshoe distribution are signs of the presence of a cyclotron maser instability. At z=190cm the horseshoe has lost the

majority of its rotational component, $v_{\perp}$ and has recovered some of its axial velocity, v_z, due to 'magnetic decompression'.

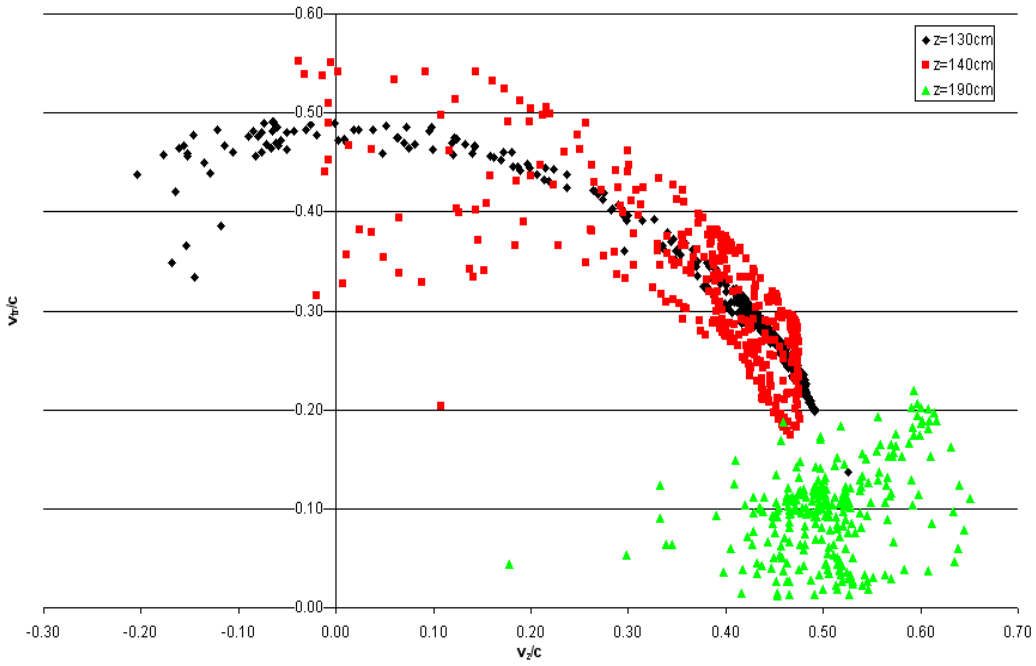

Figure 5.14: Evolution of horseshoe distribution, 1.5% detuning, 0.01T on the cathode, 130, 140 and 190cm on z-axis

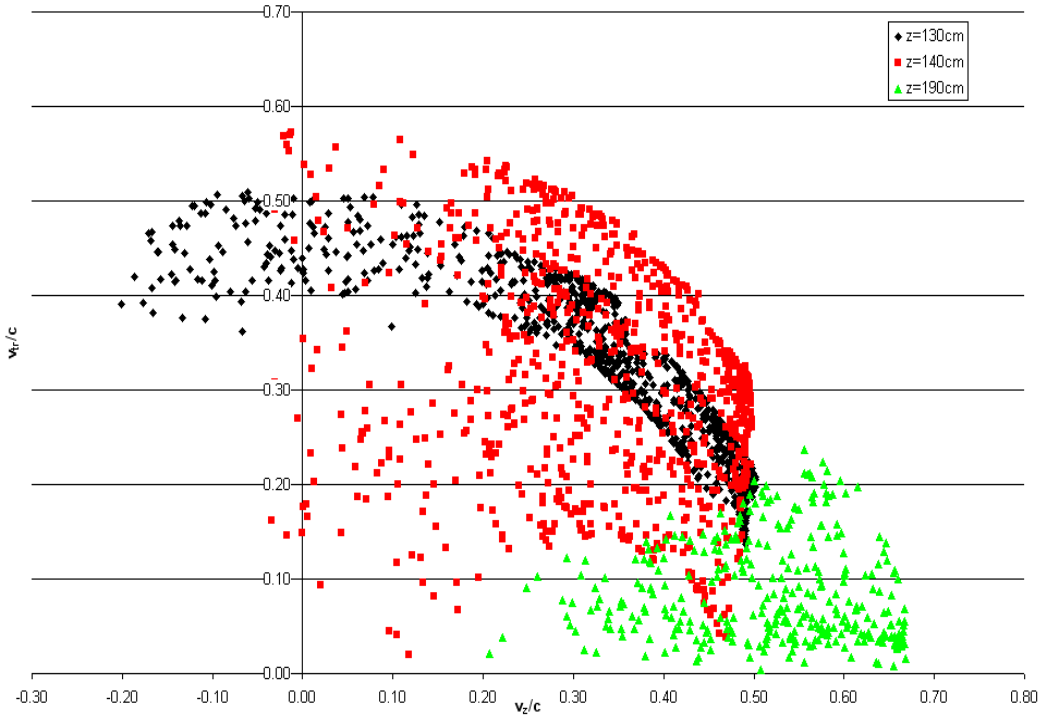

Figure 5.15: Evolution of horseshoe distribution, 1.5% detuning, 0.02T on the cathode, 130, 140 and 190cm on z-axis

The plot shown in Figure 5.15 illustrates the difference that is observed when the gun coil current is increased to 0.02T. At z=130cm the horseshoe is already more smeared out than at this stage for a cathode flux of 0.01T. This shows that with double the beam current, 35A in this case, the energy modulation of the electrons is greatly increased, leading to a higher RF output power.

The waveguide modes which give closest representation to the X-mode are the near cut-off TE modes (see discussion in Section 2.3.4). Here there is a resonance with the near cut-off TE_{01} mode, predicted in Figure 5.16 for these configurations of magnetic field, the same is also predicted in Figure 5.17 for the higher cathode flux density of 0.02T.

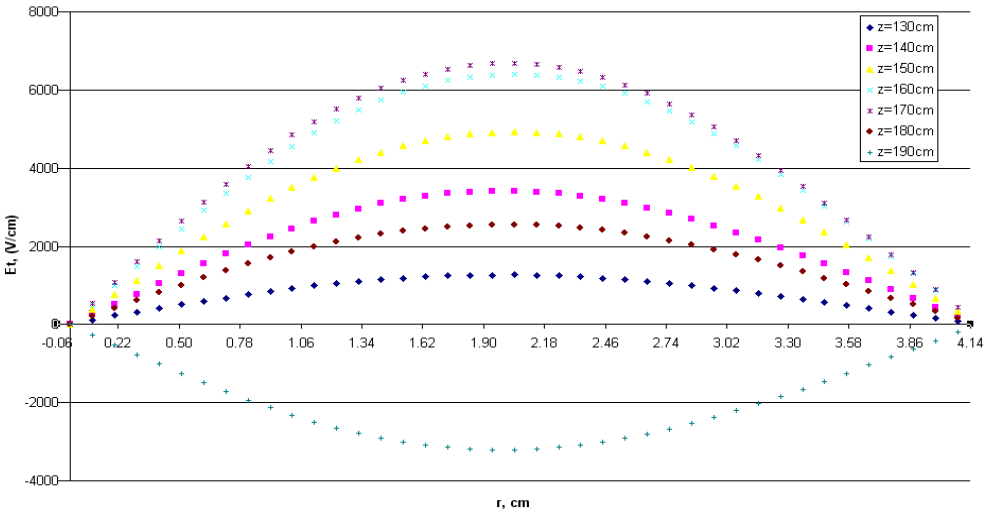

Figure 5.16: KARAT prediction of TE_{01} mode at each diagnostic point, for cathode flux 0.01T, cyclotron detuning of 1.5%

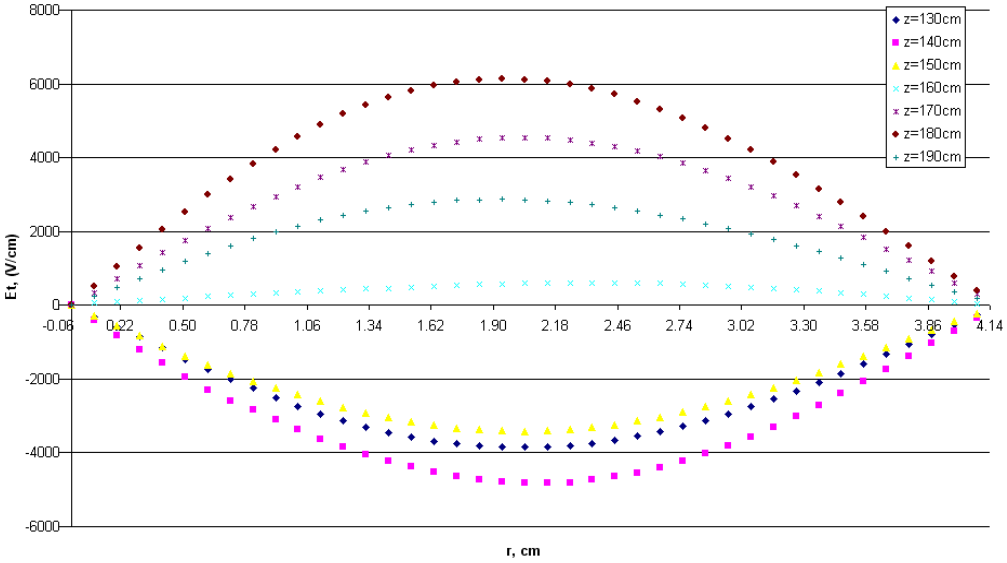

Figure 5.17: KARAT prediction of TE_{01} mode at each diagnostic point, for cathode flux 0.02T, cyclotron detuning of 1.5%

Varying the flux density of the cathode and the detuning in the cavity, plots of the Poynting flux integrated over the end of the waveguide allowed the output power of the radiation to be determined. The plots shown are displaying the 0.6%, 1.5% and 2.5% detuning, for 0.01T and 0.02T cathode flux densities. These plots are shown in Figures 5.18 and 5.19 respectively. Originally in Figure 5.18, the maximum power output of the system is ~25-30kW, with the 1.5% detuning setting giving the most stable trace. As the detuning is increased it takes longer for the power to start growing, shown clearly by the yellow trace, which does not start properly until around 120ns. This relates to the growth rate becoming weaker as the coupling becomes weaker at higher detuning settings which is consistent with Section 4.2 discussing the linear theory.

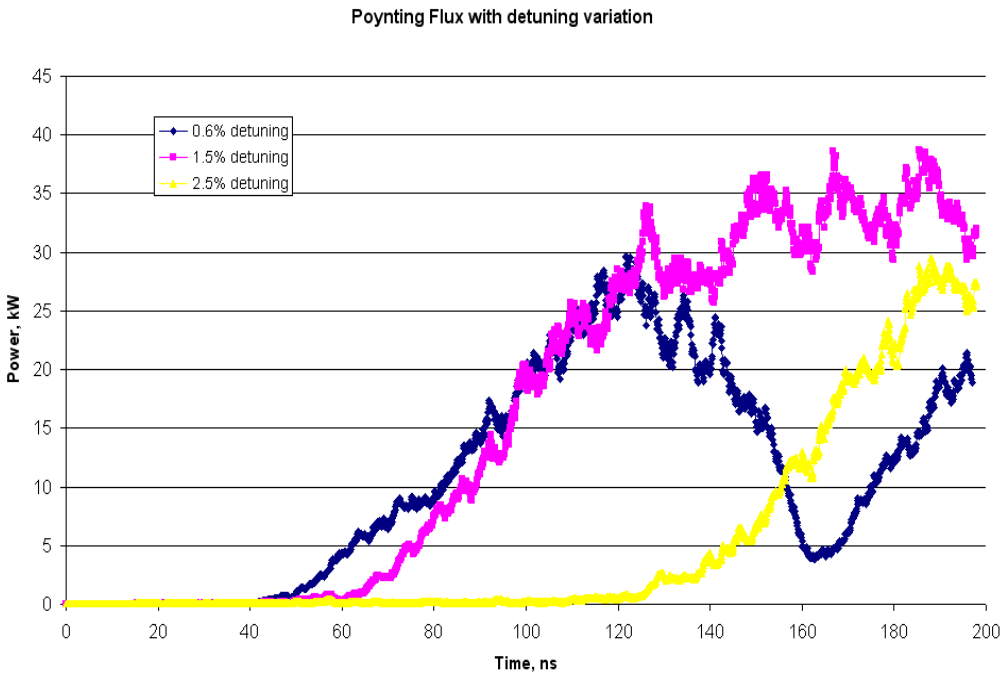

Figure 5.18: Power generated with a 0.01T cathode flux density with various detuning's

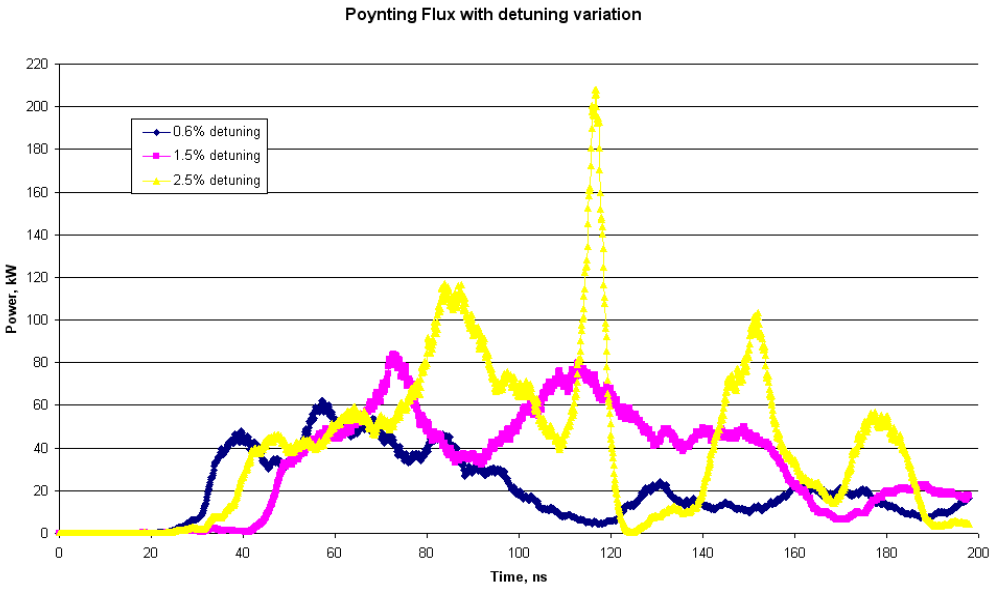

Figure 5.19: Power generated with a 0.02T cathode flux density with various detuning's

In Figure 5.19 an increase to 0.02T on the gun coil increases the power radiated due to the higher beam current. The graph appears more unstable in general now but, of the three, the 1.5% setting seems most stable and gives a maximum power of say ~50kW. In this plot the start-up times are less significantly affected by the detuning setting though it is interesting to note the speed at which the values of saturation are reached. Comparing the two plots where the current has been increased from 18A in Figure 5.18 to 35A in Figure 5.19, a stronger coupling regime has been achieved and so this leads to faster growth rate and ultimately faster saturation times. This can be seen by referring back to the plots in Section 4.2.2 relating to the complex roots of k_z.

5.5 Plasma Simulations

The dimensions of the Penning trap were input into KARAT to give a numerical representation of the experimental setup as shown in Figure 5.20. In these simulations the gun region and emission process of the electron beam is no longer simulated but instead an electron beam is injected with a predefined distribution. This was done to cut down the operation time of the code and because investigating the properties of

the gun dynamics was no longer the focus of the numerical calculations. To enable simulation of the plasma, a VOLUME was set-up in KARAT to cover the region within the Penning trap as shown in Figure 5.20 by the pink shaded rectangle. Number densities and initial temperatures are set up for the 'red' plasma ions and the 'green' plasma electrons within this volume. The merging factor of the particles is also set here, where one PiC particle contains 30 real particles (see Section 4.3).

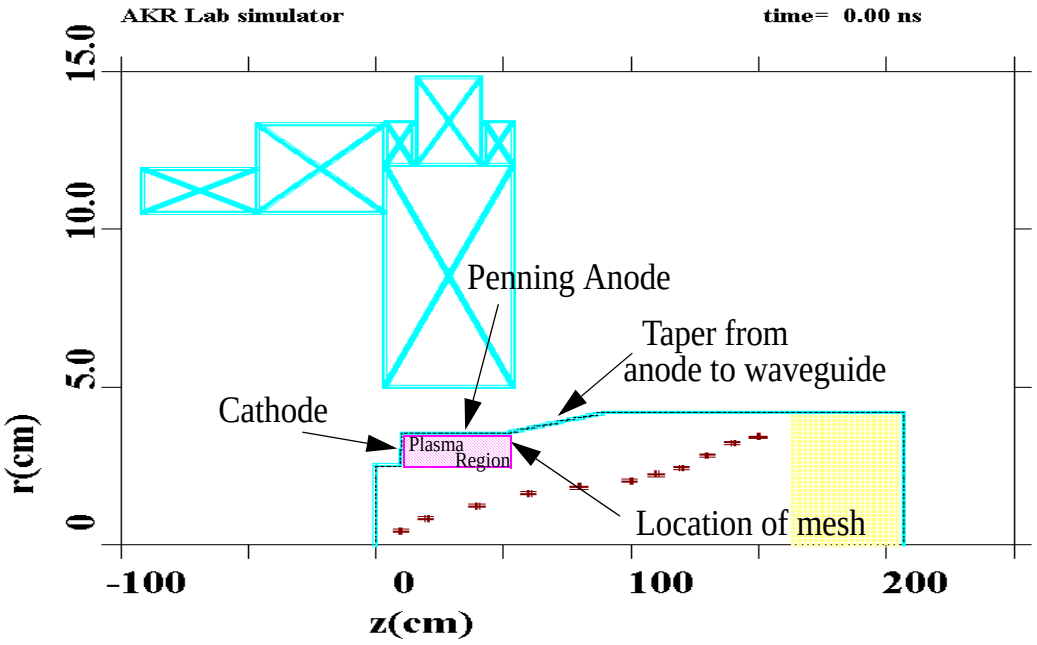

Figure 5.20: Geometry of Penning trap showing the anode outer radius representing the tapered cathode mesh support

It can be seen from this Figure 5.20 that the Penning trap has been configured with one cathode end and one open end as opposed to the two cathode trap in the laboratory setup. Simulations were then started with varying input beam currents, plasma temperature and trap geometry. For the inner dimension of the trap the new cyclotron frequency for the cut-off TE_{01} mode was 5.21GHz. Changing the temperature of the plasma electrons controlled the random motion of the plasma within the Penning region. Figure 5.21 shows the position of the plasma with an input beam current of 10A at a time of 20ns into the simulation, compared to Figure 5.22

which shows the same simulation but moved forward to 80ns. It can be seen that the plasma electrons have drifted away from the Penning cathode over time.

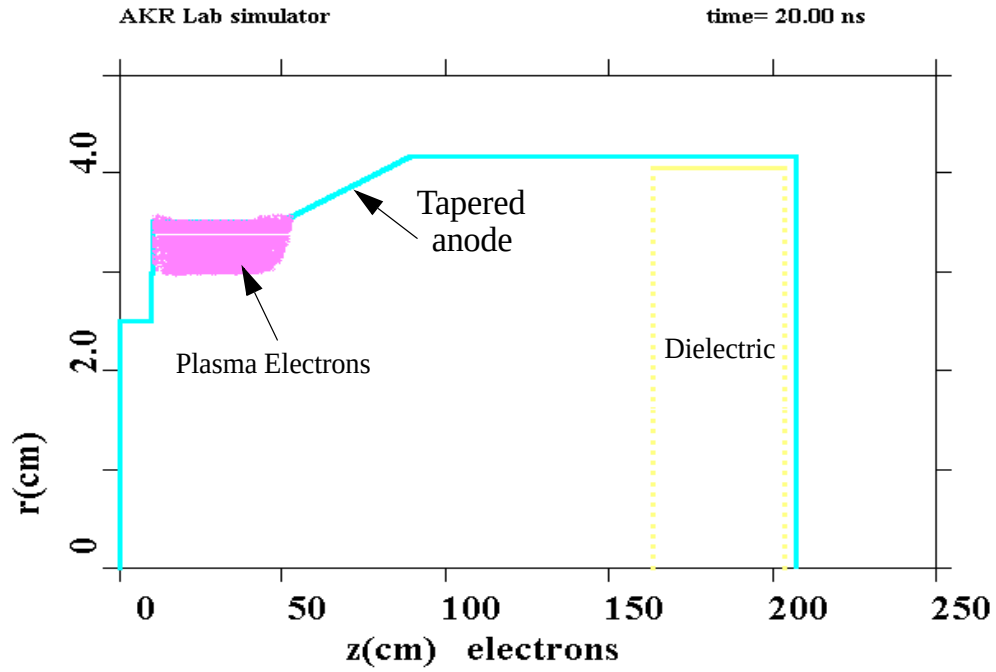

Figure 5.21: Initial position of the plasma electrons with current 10A, 20ns into the simulation time

The question arises here when viewing these plots as to why the plasma electrons appear to drift away from the injection point in the Penning trap. One speculation is that as the electron beam traverses through the trap, the sudden shock wave of the incoming electrons in the beam repels the electrons in the plasma thus pushing them away from the cathode in the positive z direction. It was seen in the simulations that when looking at the plasma ions, they appeared to drift inwards towards the electron beam trajectory as if being attracted to the beam electrons.

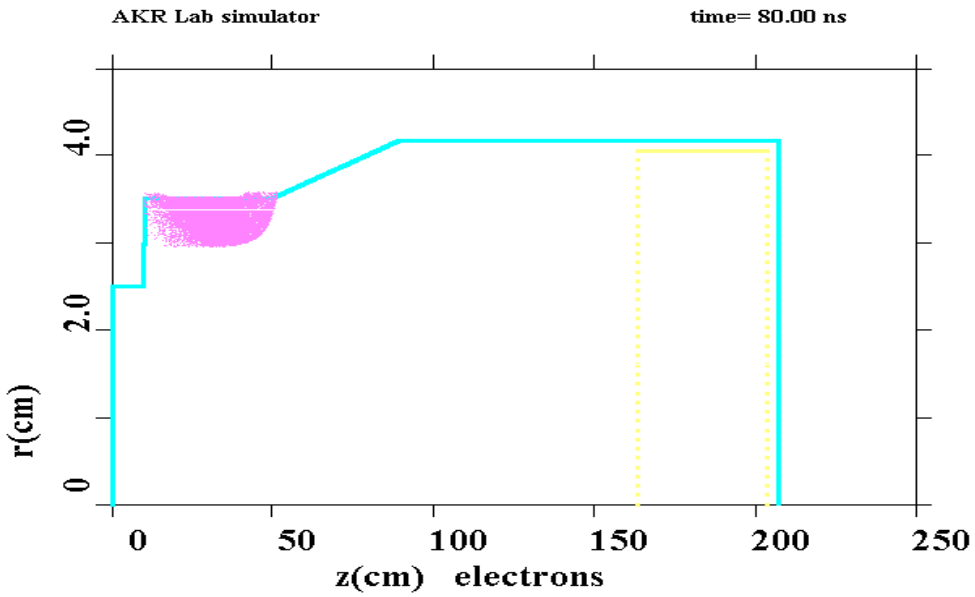

Figure 5.22: Shift in position of the plasma electrons after 80ns has passed. Notice how they are moving towards the end of the Penning region, 10A injection current.

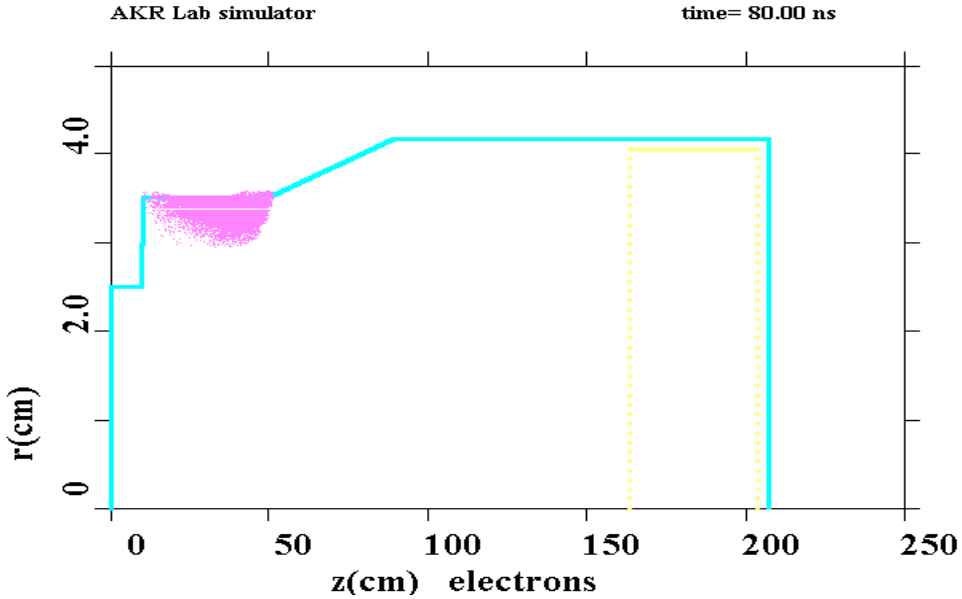

Figure 5.23: With an increase in current to 30A, the electrons have drifted at a faster rate for the same time interval of 80ns as in Figure 5.22

As the beam current increased from 10A to 30A, Figure 5.23, the rate of electron displacement increases. This would tie in with the speculation above, where having a larger current would give a larger shock wave of beam electrons entering the Penning trap and so causing the drift rate of the plasma ions and electrons to increase. Drastically increasing the magnetic field settings did not seem to have an effect on the movement of the plasma electrons within the Penning trap, implying that the motion is primarily longitudinal. The code predicted power outputs of ~20W at a very low efficiency, with an operating frequency of ~5.21GHz whilst at a plasma frequency of 30MHz. One thing to be aware of for comparison purposes later on is that the code does not simulate ‘real’ electrostatic confinement or real-time charged particle production.

Chapter 6 : Experimental Results

Chapter 6 : Experimental Results

6.1 Introduction

In conjunction with the numerical research and exploiting preliminary results from the simulations, experiments were carried out to test the predictions and allow further numerical study to take place on a more informed basis. This allowed confidence in applying the code and theory to magnetospheric situations to be improved. Section 6.2 covers the beam transport and mirroring measurements obtained by keeping the cathode magnetic flux density constant as the maximum plateau magnetic field was increased. This demonstrated the formation of the horseshoe distribution as progressive magnetic mirroring was achieved. Section 6.2 also illustrates the measurements of the diode current, voltage and beam current. In Section 6.3 an analysis of the mirroring results is presented leading to an improved understanding of the electron distribution in velocity space. The output radiation efficiency was measured as a function of the magnetic detuning, that is the percentage by which the cyclotron frequency was less than the wave frequency, discussed in Section 6.4 which also presents measurement of the operating frequency, the antenna pattern and output power, which in turn allows the efficiency of radiation to be calculated. Finally, in Section 6.5, the impact of introducing a background plasma shall be presented.

6.2 Beam Transport & Mirroring Measurements

The aim of these experiments was to study the distribution of the electron beam in velocity space thus being able to verify that the horseshoe distribution observed in the magnetosphere could be formed in the laboratory and that the energy extraction that took place could be linked to the cyclotron maser instability. Measurements of the diode voltage and current were carried out using the Rogowski coils and matching ionic shunt resistors. Figures 6.1 to 6.3 show the plots obtained from the oscilloscope relating to these measurements. Figure 6.1 shows the unprocessed measurements of the current and voltage, calibration of the electron beam diagnostics have been taken into account at this point but the diode capacitive displacement current has not. By taking measurements of the displacement current when no beam was emitted, Figure

6.2, a normalisation curve was obtained which when subtracted from Figure 6.1, allowed a fully processed plot of current and voltage to be obtained which showed true values of these measurements, Figure 6.3.

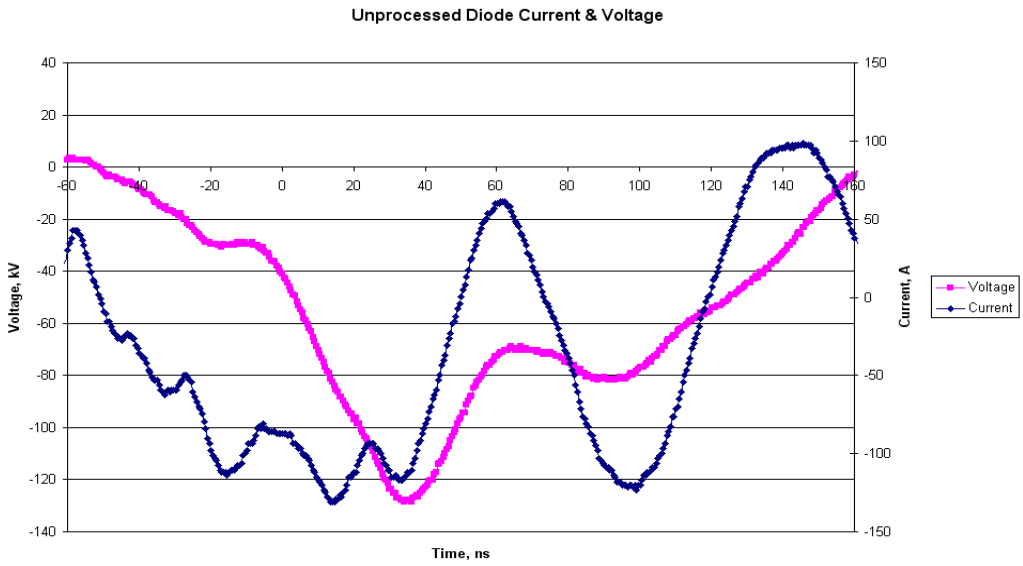

Figure 6.1: Unprocessed diode current and voltage, raw measurements obtained using the Rogowski coils and matching ionic resistor

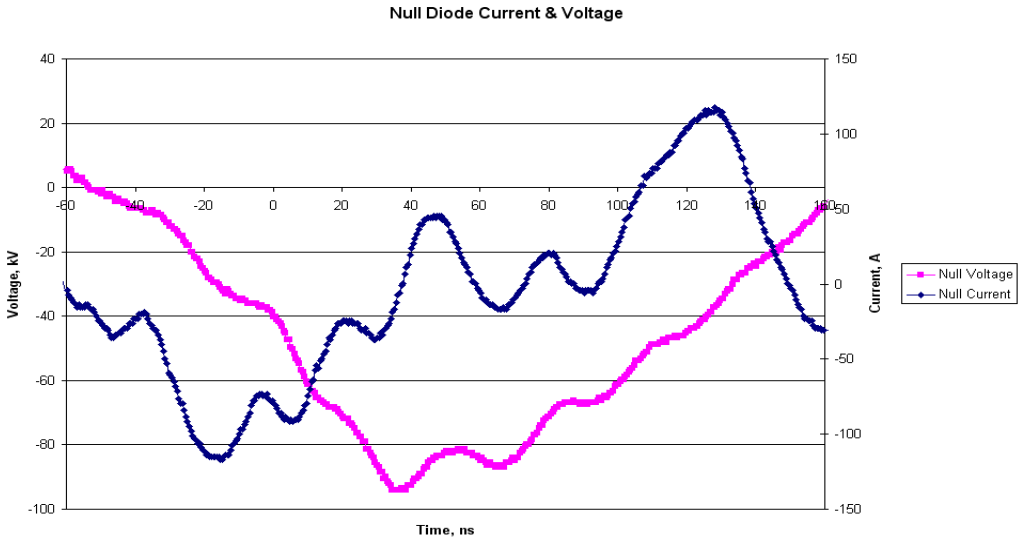

Figure 6.2: Null diode current and voltage i.e. purely displacement signal

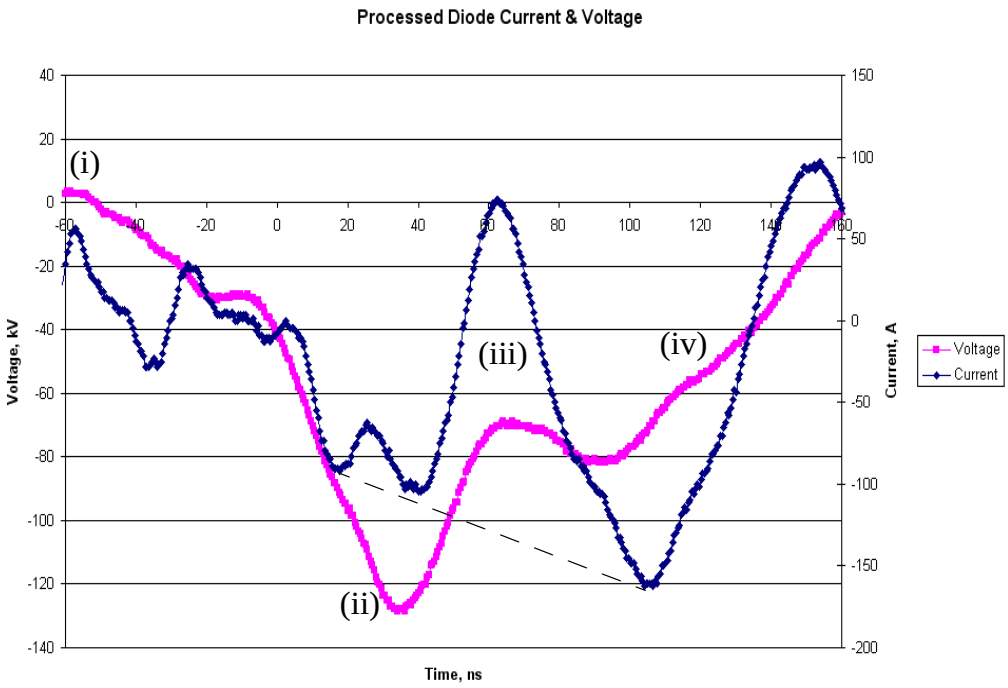

Figure 6.3: Processed diode current and voltage i.e. raw measurement of diode current/voltage minus the purely displacement effects

Prior to point (i) on Figure 6.3, the Blumlein is fully charged. At point (i) the spark gap switches and the Blumlein discharged in series to the cathode. By point (ii) the cathode ignites under explosive electron emission and the voltage sharply decreases until the cathode reaches a steady emission state at 75keV, shown by point (iii). The apparent plummet in diode current is not a 'real' representation of the emission current. It decreases here as the decreasing cathode voltage requires a capacitive increase of electron density at the anode. However, in reality the current would follow the trend of the dotted line, comparable in shape to the beam current graph in Figure 6.4. After 100ns the Blumlein is low on energy as it has almost fully discharged, therefore the voltage and current measurements fall to zero, point (iv).

Using the Faraday cup, Section 3.6.2, inserted into the interaction region of the cylindrical waveguide, the beam current at this point could be measured to determine whether magnetic mirroring of the electrons had taken place. By comparing the time

evolution of the beam current, Figure 6.4, one can see the influence of the magnetic field configuration at the electron gun. Figure 6.4 shows how the beam current is affected by an increasing value of cathode flux density, from 0.01T to 0.05T. As can be seen on the graph, an increase in this value led to a increase in the beam current collected by the cup. This noticeable increase in beam current is partly associated with improved gun performance with increasing magnetic field, i.e. increasing the cathode flux density would reduce the Larmor radii thereby achieving less 'skimming' of the outermost electrons in the trajectory, but also with reduced mirroring, as the magnetic compression at the plateau reduces.

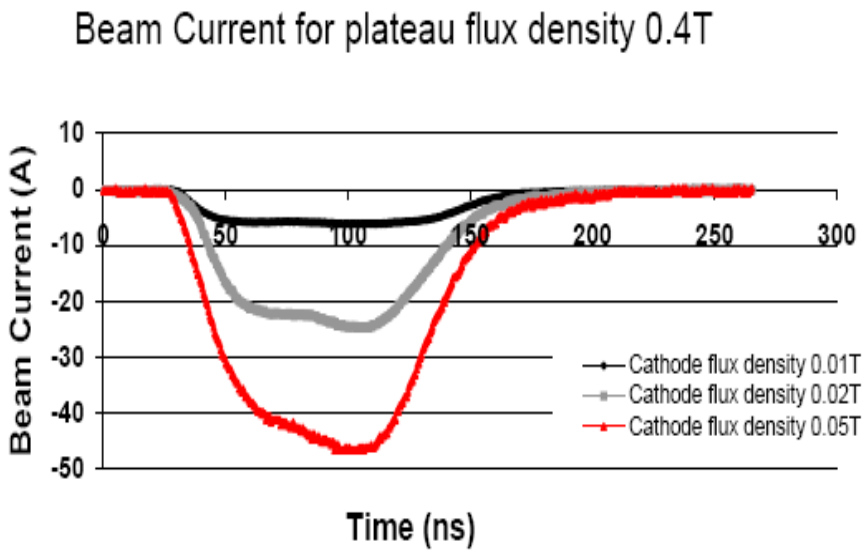

Figure 6.4: Influence of cathode magnetic flux density on electron beam current measured in the cavity for a plateau flux density of 0.4T

The measurements of the electron beam current in the cavity were normalised to the diode current, I_{beam}/I_{diode}, which can be plotted against the mirror ratio, $B_z/B_{zcathode}$, Figure 6.5. By having a set value of cathode flux density, $B_{zcathode}$, it was possible to study the influence that the plateau magnetic field, B_z, had on the cavity beam current. Continual reduction of the cavity current with increasing mirror ratio would be associated with v_z being sacrificed for an increase in $v_\perp$ since particles that have $v_\perp=v_{tot}$ will have $v_z=0$ and so will mirror, thus providing evidence of the horseshoe

distribution evolution. Figure 6.5 shows the values obtained from these measurements and, as can be seen, magnetic mirroring has taken place at each cathode flux setting, determined by the progressive loss of current with increasing mirror ratio. Four different cathode flux densities were investigated 0.01T, 0.013T, 0.02T and 0.03T with focus being placed on analysis of the 0.01T and 0.02T scenarios. The leftmost point on each of these data sets is the resonant plateau flux density of B_z~0.18T.

.

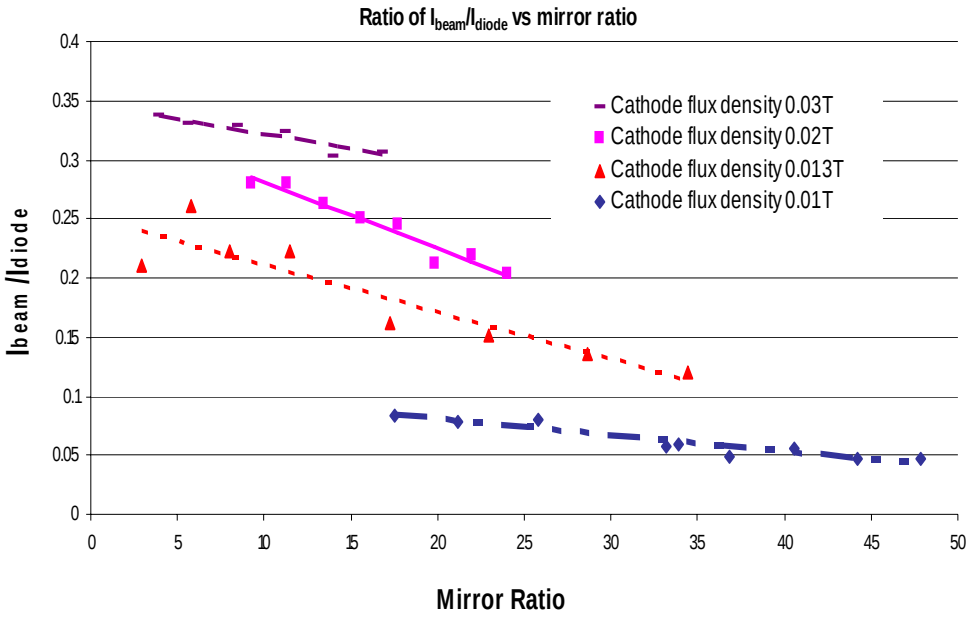

Figure 6.5: Variation of electron beam transport from accelerator to interaction space as a function of magnetic mirror ratio for four cathode magnetic flux densities

The values for the gun and plateau magnetic fields were calculated using the Maple code, see Appendix 3.

6.3 Analysis of Beam Distribution in Velocity Space

The aim of this analysis of the electron distribution in velocity space was to process the mirroring measurements to improve the understanding of how the solenoid configuration would effect the RF generation process. Analysis of Figure 6.5, as the plateau magnetic field was increased from the resonant value, and relating this back to

the critical value of v_z (where electrons with v_z less than v_{zcrit} would mirror with the appropriate magnetic field) yielded the line density of the electron beam as a function of the pitch angle. This is presented in Figure 6.6 shown for cathode flux densities of 0.01T and 0.02T and a plateau flux density of 0.18T.

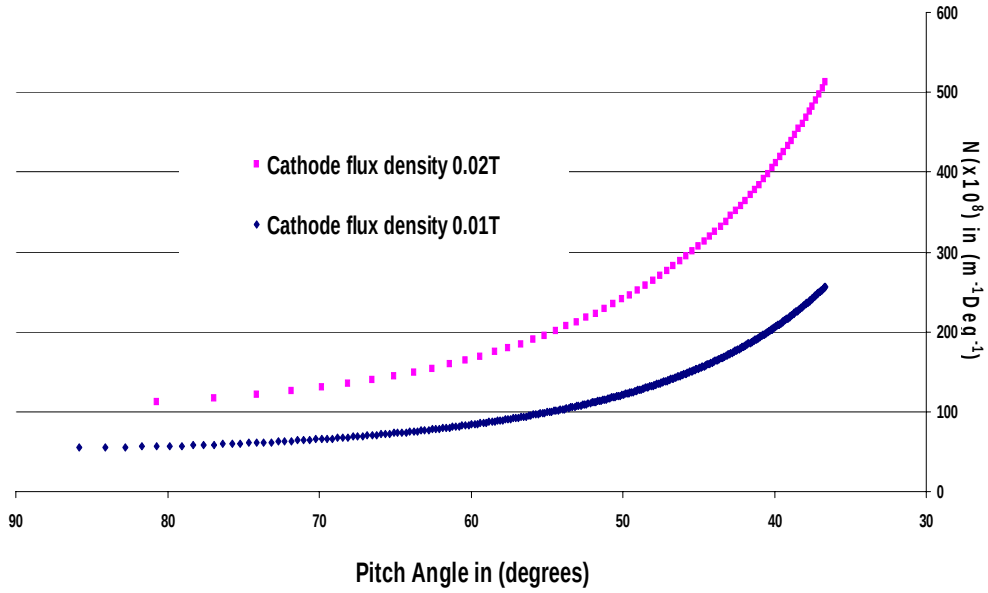

Figure 6.6: Electron distribution in velocity space for experimental values of cathode magnetic flux density

Analysis of Figures 6.5 and 6.6 demonstrates that for the lower cathode flux density of 0.01T, the electron beam had half the population at high pitch angles compared to the flux density of 0.02T. For the 0.01T case however, 2/3 of the current was associated with electrons having pitch angles greater than 37°. By studying the graph one can speculate that the higher cathode flux regime will generate more power than the lower field regime due to the doubling in electron population at high pitch angles, i.e. >37°. One may anticipate however that due to the majority of current being at low pitch angles for the higher cathode flux regime, it will have a lower efficiency of radiated power than the 0.01T regime, where most of the current lies at high pitch angles. Electrons having a pitch <37° were not measured due to apparatus limitations

as discussed in Section 3.7.1. This speculation is based on the discussion and analysis in Section 4.2.2 and Section 5.3.

6.4 Microwave Output from the Experiment

Having established that a resonance condition was satisfied and the beam-wave interaction was operating effectively, it was necessary to analyse the radiation emitted. If the frequency of the radiation could be measured, and its mode pattern established, this would allow comparisons with the radiation mode observed in the magnetosphere. The experimental microwave measurements investigated detuning settings of 1.5%, 2.5% and 3.5% with the 2.5% regime giving the highest value of radiation power. It is therefore the regime of results that will be presented in the remainder of this section.

6.4.1 Radiation Spectral Measurement

A receiving antenna was placed at the output window of the experimental apparatus allowing the radiation emitted to be collected and sent, via a single mode coaxial cable, to a 12GHz, real time, deep memory, digital oscilloscope. The AC waveform that was picked up at the receiver is shown in Figure 6.7 for a cathode flux density of 0.02T. A decrease in cathode flux density to 0.01T gave a similar AC waveform.

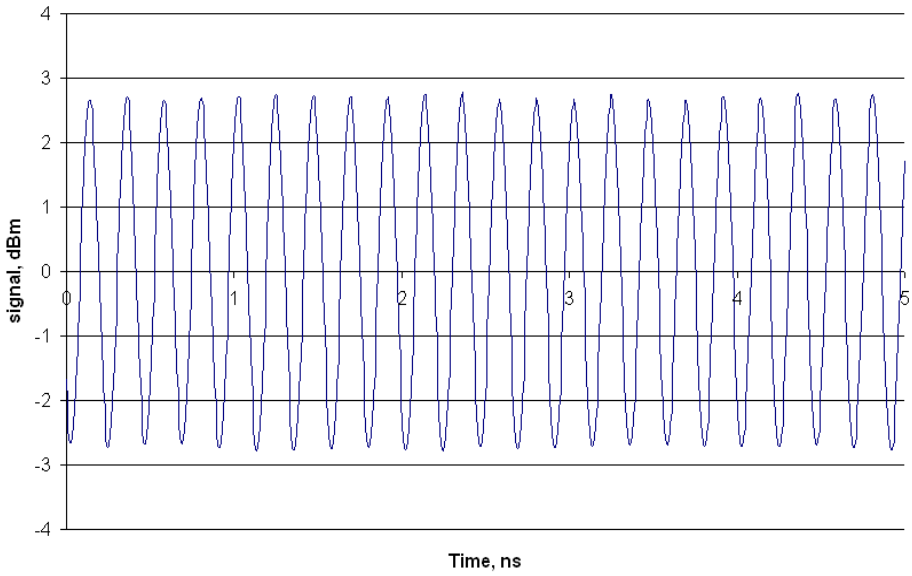

Figure 6.7: AC microwave signal for cathode flux density 0.02T

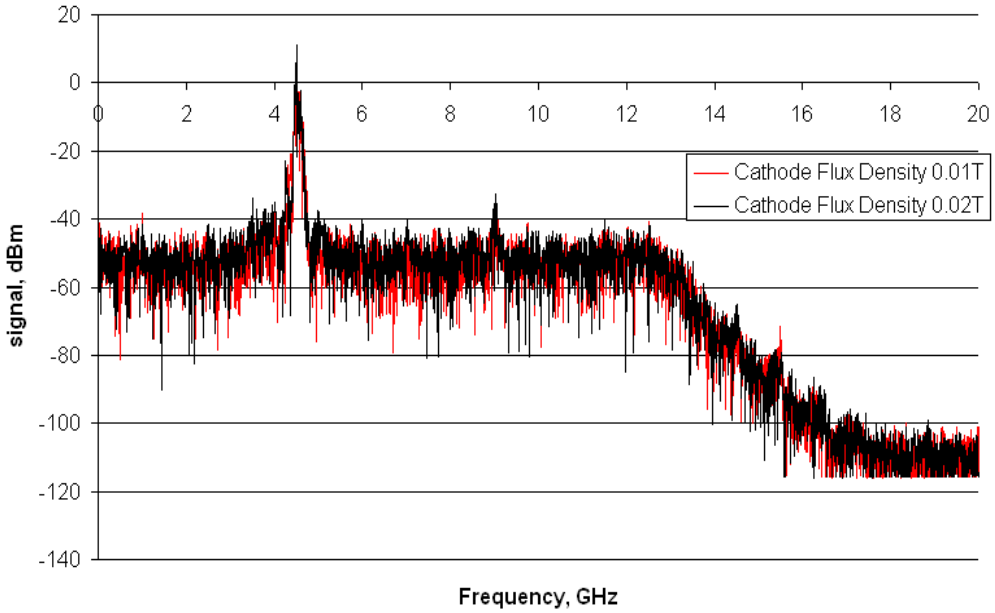

Figure 6.8: Fourier transform of the AC signal showing a comparison as cathode flux density is increased from 0.01T to 0.02T

The oscilloscope was then used to take the Fourier transform of the entire microwave pulse and allowed the spectrum of the radiation to be measured. This is shown in Figure 6.8 where the predicted operating frequency of 4.42GHz was measured for both cathode flux densities. In the case of the higher cathode flux regime, one can see signs of a second harmonic at ~9GHz.

6.4.2 Mode Pattern Measurements

The purpose of these experiments was to determine the output power and efficiency of the generated radiation. Referring to Figure 3.21, emitted radiation was collected at different angles around the output antenna of the experiment for each of the two cathode flux configurations. The orientation of the receiving scanning waveguide determined whether the radiation collected was in the azimuthal (antenna polarised perpendicular to the scanning plane) or radial (antenna polarised parallel to scanning plane) polarisation. Analysis of the measurements was carried out using the rectifier calibration equations obtained from Figures 3.26 and 3.27 to establish the power that enters the receiver aperture in mW. These values are then averaged over several pulses, to reduce and quantify the random effects, before being divided by the antenna effective cross-sectional area. This provides an estimate of the Poyntings flux as a function of the scanned angle θ, in both the radial and azimuthal polarisations. The azimuthal polarisation mode pattern is shown in Figure 6.9. In correlation with the numerical predictions, the azimuthal polarisation measurements showed a strong single peaked lobe in intensity at ~37° whilst the radial polarisation measurements showed very low intensity, therefore consistent with the expectation of the TE_{01} mode of the measured frequency radiating from an aperture of 8.28cm diameter. This provides experimental confirmation that the mode is the TE_{01} and also that the radiation polarisation and propagation direction are perpendicular to the static magnetic field. This is highly comparable to the X mode radiation observed in the magnetospheric case.

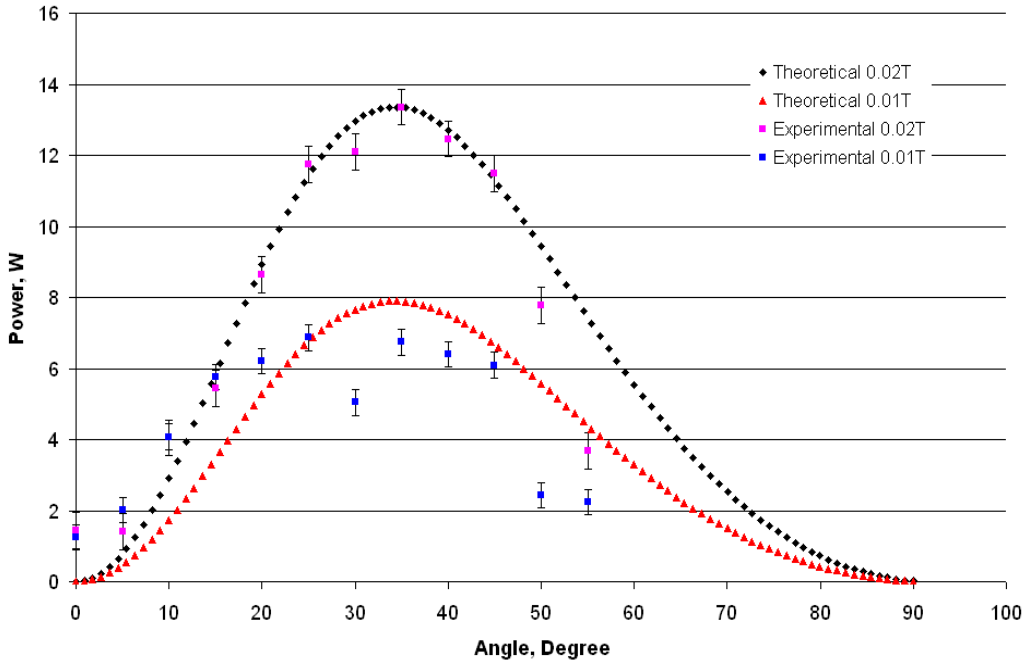

Figure 6.9: Comparison of experimentally measured and theoretically predicted mode scans for 0.01T and 0.02T cathode flux densities

Integration of each of the individual mode plots, in Figure 6.9, allowed the RF power of the system to be obtained. For the 0.01T regime 19kW was obtained by integrating the normalised theoretical pattern and 14kW by direct integration of the experimental data. For the 0.02T case the results were 34kW and 25kW respectively. Integration of the experimental antenna patterns gave lower values of power, due to interference from the vacuum flange walls meaning the maximum angle that could be experimentally measured was 0-55° as opposed to 0-90°. Integrating the normalised theoretical patterns therefore provided a more accurate estimate of output power to be obtained.

The efficiency of the system could then be estimated by taking the ratio of the RF power, stated above, to the beam power, using Equation 6.4.1:

$$\frac{\text{power(RF)}}{\text{power(beam)}} \sim \eta \qquad \text{Equation 6.4.1}$$

This means that for a beam power of ~868kW (75kV, 11.6A) for the 0.01T cathode flux regime, the efficiency is between 2% and 1.5% depending on which estimate for the RF power one uses. For the higher cathode flux regime, beam power ~2.5MW (75kV, 33.9A), the efficiency has decreased to between ~1.4% and ~1%. Referring back to Figure 6.6 it can be seen how these measurements of power and values of efficiency are consistent with the speculations that were made based on the electron distribution in velocity space, with the 0.02T regime giving higher values of power associated with the greater number of high pitch electrons but at lower efficiency, due to the much larger fraction of the beam current at low pitch angles.

6.5 Measurements of Plasma Generation Apparatus

6.5.1 Penning Trap Current-Voltage Characteristics

The Penning trap, Figure 3.32, was inserted into the interaction region of the experiment where the magnetic field would be at its maximum plateau value. A specially designed vacuum feedthrough delivered a high voltage (up to +5kV) DC signal to the anode. With the plateau magnetic field set at 0.21T for the TE_{01} resonance in the new dimensions of the interaction region, a voltage was then applied to the trap and the anode current and voltage measured. The plateau magnetic field was altered to investigate the effect this had upon the ignition, optical intensity, stability and sustained current and voltage of the discharge. The pressure dependence was also studied as was the nature of the gaseous medium, by bleeding in a range of gasses including Nitrogen, Argon and Helium. Measurements with these gases showed that Nitrogen gave very unstable results. It showed extreme bimodal behaviour where it switched between two states, either low voltage with high current or low current with high voltage, in quick succession, regardless of B-field and pressure settings. For this reason focus was placed on Argon and Helium measurements and the results are presented in the remainder of this chapter.

The initial measurements of the Penning trap I-V curves were obtained with digital voltmeters monitoring the current and voltage diagnostics and were to check that the discharge would ignite. Figure 6.10 shows data from these experiments operating

with a pressure of 10^{-5}mBar with no 'foreign' gas introduced. These preliminary results allowed one to study the ignition voltage as a function of magnetic field, pressure and gas.

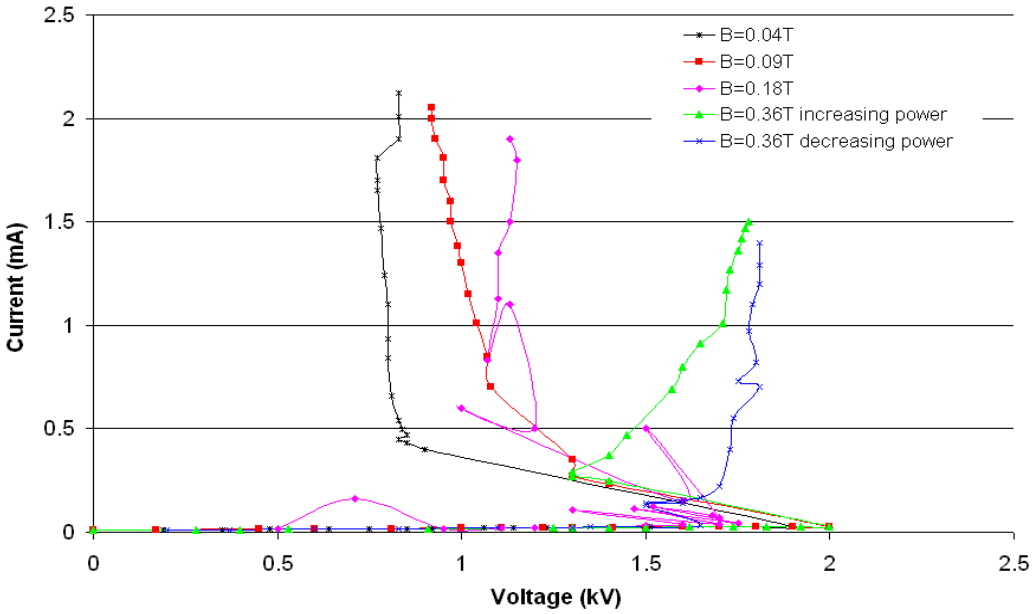

Figure 6.10: Initial Penning I-V measurements as a function of magnetic field and increasing drive power for Air at P=10^{-5}mBar

As the drive power applied to the trap was increased, the voltage measured on the output of the trap decreased as the measured current increased. The exception to this was for the cavity flux density of 0.36T where in fact the voltage measured increased with increasing current as the drive power onto the trap was increased. Study of the graph shows that in general, as the magnetic flux was increased the voltage measured across the trap also increased. To better understand the graph in Figure 6.10, one should compare it to Figure 2.14 which illustrates the regimes of gas discharge. It can be seen that in particular, the curve corresponding to B=0.04T, from Figure 6.10, correlates well with the lower part of Figure 2.14 at the point where it moves from Townsend Discharge to Normal Glow. With voltage between 1.5-2kV on the trap the discharge became self sustaining corresponding to the Townsend breakdown criterion. As is clear from Figure 6.10, once the discharge had ignited, the voltage

required to sustain the discharge fell off very sharply and then showed characteristics of two regimes. Either it showed normal resistive behaviour at high fields whereby the voltage increased with current as in the abnormal glow regime, or it showed negative dynamic resistive behaviour at low fields whereby the voltage dropped off with increasing current, like the normal glow regime.

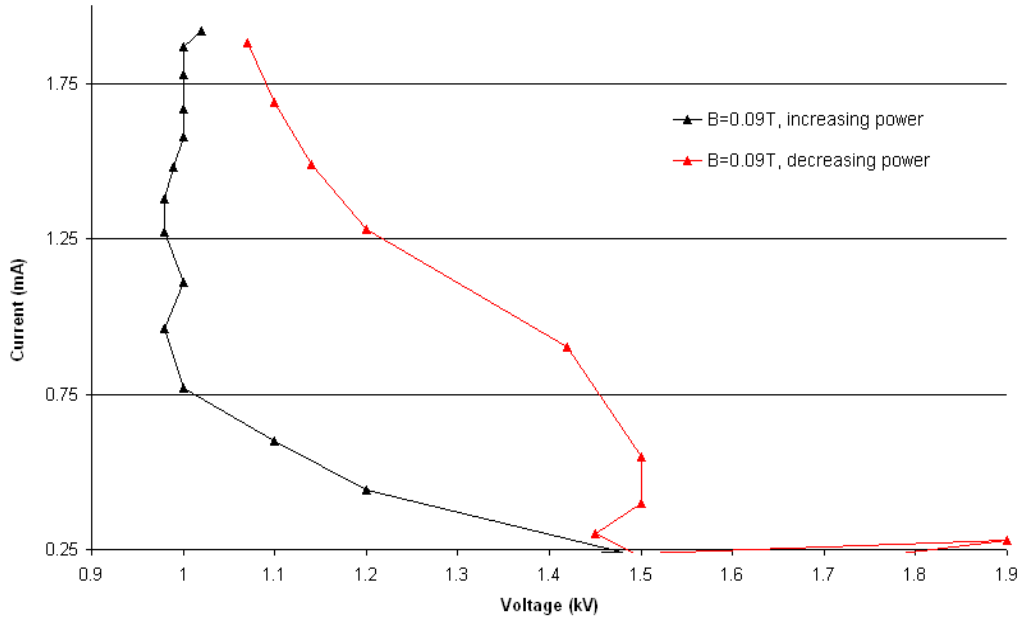

Figure 6.11: Penning trap I-V characteristic for Air at P=10^{-6}mBar, illustrating the hysteresis effect

In Figure 6.11, the pressure has been decreased from 10^{-5}mBar to 10^{-6}mBar. Comparing this graph to the same cavity flux density measurement in Figure 6.10, not much has been affected, the voltage measured still reached ~2kV before the discharge lit and still climbed to a maximum current of ~2mA. It is interesting to note here the hysteresis effect whereby it is clear that it requires a lot less voltage to sustain the discharge on the increasing stage of the cycle (black trace) than for the extinguishing stage.

6.5.2 Investigation of Discharge Parameter Space

The initial Penning trap experiments were very much trial and error with regards to the geometry of the trap and which gasses would yield a stable discharge when a

suitable magnetic field was applied. An oscilloscope was introduced to replace the digital voltmeters enabling detailed and high speed measurement of the variation of voltage and current to be obtained as the input drive power of the 5kV power supply was adjusted. A digital video camera was also set up, downstream from the electron gun, facing into the interaction region through the mylar window. This enabled observations of the discharge ignition to be recorded and viewed.

Initially, the Penning trap was constructed with two solid cathodes, one at each end of the trap, each with a 20mm hole in the centre to allow for the electron beam. This configuration was suitable for initial plasma ignition study, but further analysis investigating the impact of the plasma on radiation generation processes would have been impossible as the downstream cathode would inhibit passage of the radiation.

The solution to this problem was the addition of a cathode mesh at the far end of the trap thus allowing the plasma to be suitably electrostatically confined in the region of maximum plateau magnetic field whilst allowing for $TE_{0,n}$ mode radiation to pass through and out of the mylar exit window due to the radial spokes of the mesh being perpendicular to the E field of the mode. Experiments confirmed that the discharge ignited using this design of cathode. Although these preliminary tests did not include an electron beam it was essential that the aperture of the upstream cathode was large enough to allow for the case when an electron beam would be present. The initial aperture of 20mm was therefore increased to 40mm which, after testing, was found to have no significant impact on the ignition of the discharge. Therefore extensive experiments were conducted using this inlet aperture of 40mm and with the cathode mesh for the downstream cathode.

6.6 Analysis of Discharge Current and Voltage

6.6.1 Summary of Test Results

For the bleed gases Helium and Argon it was seen that in general the higher the pressure, the less voltage was needed to ignite and sustain the discharge. It was found

by comparing the two, Helium gave lower lighting voltages and cleaner measurements at the lower pressure of $P=1x10^{-5}$mBar whereas Argon gave its best results at a slightly higher pressure of $P=1x10^{-4}$mBar. The values obtained from the experiments for Air, Helium and Argon are presented in Tables 6.1 to 6.3 respectively, showing the pressure, cavity flux and discharge voltage and current. Figures 6.12 to 6.14 (and 6.17 to 6.19) show graphs of the voltage (blue trace) and current (green trace) measured against time and show which magnetic field setting provided the most stable results at a given pressure.

Table 6.1 Discharge Behaviour with Air

B (T)	P (mB)	Discharge	
		V (kV)	I (mA)
0.16	$5x10^{-6}$	1.6	1.5
0.21		1.8	1.25
0.27		2.1	1

As can be seen in Table 6.1, the voltage required to ignite the discharge when there was no bleed gas present, hence a maximum vacuum state, increased steadily with increasing magnetic flux whilst the associated current decreased, as can be seen looking at the graphs in Figure 6.12. The graph corresponding to 0.16T illustrates the most stable configuration which as the cavity flux increased, fluctuated between states of high V, low I and high I, low V. The bottom right graph in Figure 6.12 shows this more clearly where the image is a zoom of the ‘black boxed’ section of the 0.21T plot. This type of behaviour was also observed in the Nitrogen measurements but in that case, for all settings of magnetic flux and pressure. Notice in each of the graphs, that as the discharge ignites, there is a very sudden drop in the voltage and a sharp increase in the current.

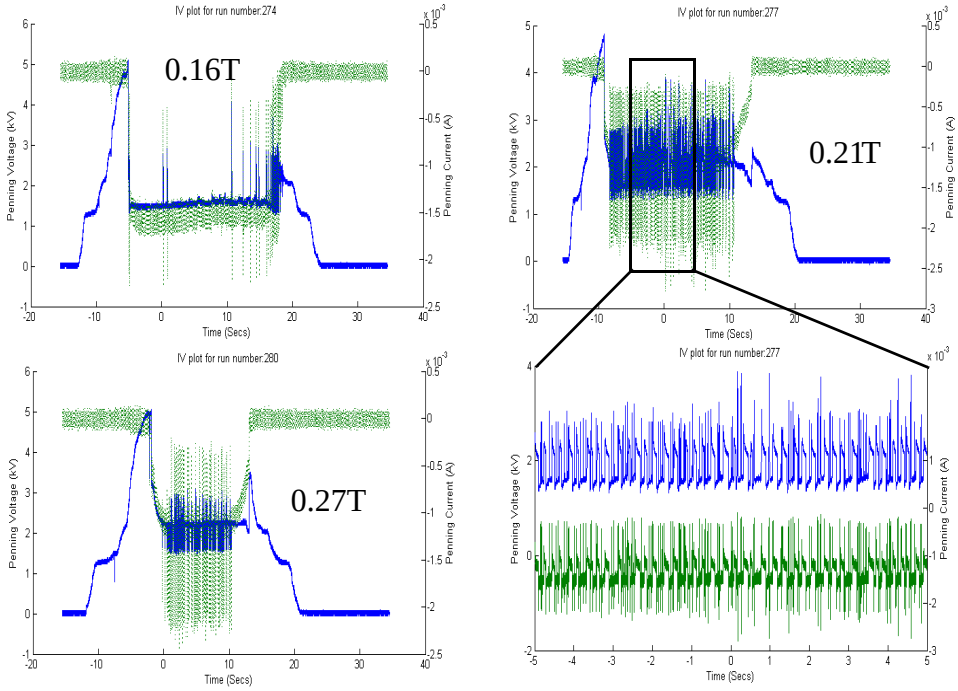

Figure 6.12: Voltage and current measurements against time for discharge ignition, P=5x10^{-6}mBar, no bleed gas present, i.e. only air as background gas

Table 6.2 Discharge Behaviour with Helium

B (T)	P (mB)	Discharge	
		V (kV)	I (mA)
0.16	1x10^{-5}	1.8	1.5
0.21		2	1.25
0.27		2.4	1.1
0.16	1x10^{-4}	1.3	1.8
0.21		1.1	1.8
0.27		1.3	1.6
0.16	5.3x10^{-4}	0.4	2.2
0.21		0.5	2.2
0.27		0.6	2.1

Table 6.2 shows results of measurements with Helium as the bleed gas. Graphs of the high-lighted section are shown in Figure 6.13. It was evident that the higher the pressure became, the less voltage was required to ignite and sustain the discharge. Focusing on the lowest pressure of $1x10^{-5}$mBar, it is seen that the voltage required for ignition increased with increasing cavity flux. This had a positive effect on the stability of the results, as can be seen in Figure 6.13. A magnetic flux of B=0.16T produced a very noisy unstable measurement compared with the relatively clean measurement shown for B=0.27T. Again, in the bottom right plot, a snapshot of the black box section for B=0.21T is shown. This highlights the improvement regarding the stability of the results compared with that in Figure 6.12. The red box highlights one of many spikes in the 0.21T plot and shows that these are regimes of bimodal behaviour.

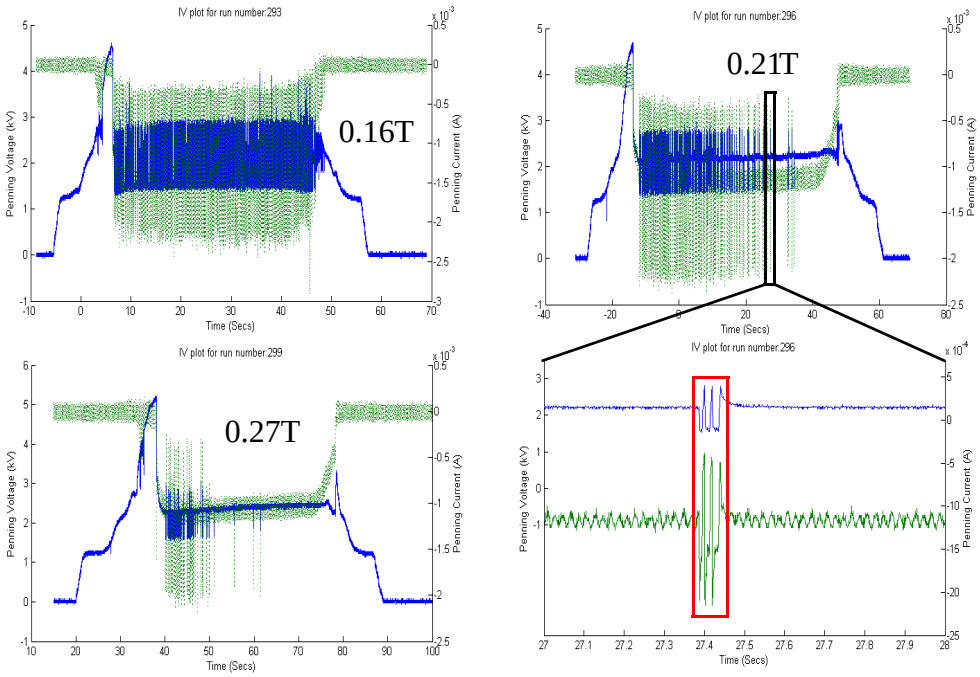

Figure 6.13: Voltage and current measurements against time for discharge ignition, P=$1x10^{-5}$mBar, using Helium as bleed gas

Table 6.3 Discharge Behaviour with Argon

B (T)	P (mB)	Discharge	
		V (kV)	I (mA)
0.16	$1x10^{-5}$	1.7	1.5
0.21		2.1	1.1
0.27		2.5	1
0.16	$1x10^{-4}$	0.7	2
0.21		0.9	1.8
0.27		1	1.7
0.16	$5.3x10^{-4}$	0.3	2.3
0.21		0.3	2.2
0.27		0.35	2.1

Table 6.3 shows the results when Argon was studied as the 'foreign' gas, graphs of the high-lighted section are shown in Figure 6.14. It was evident that at a pressure of $1x10^{-4}$mBar, Argon required less voltage to sustain the discharge than Helium and, as shown in Figure 6.14, gave the most stable measurements of voltage and current with respect to time. The three plots for each magnetic flux setting show more or less the same shape of curve with steady plateau of current and voltage. It can be seen though for B=0.16T, the voltage required to ignite the discharge was ~2.8kV whereas for B=0.21T and 0.27T the voltage required was ~3.5-4kV. Another point to discuss is that marked by the black box in the 0.21T plot. These are sections that show the ignition and end point of the discharge. These appear to be most stable at the operating condition of B=0.21T and least stable at B=0.16T, shown by the wide 'ears' in the plot, shown by the red boxes. At B=0.27T it has improved but there are signs of random unsteady spikes, again shown in the red box. The bottom right graph shows an enhanced image of the unstable 'ear' region of the 0.21T plot. These regions are due to switching between lit and extinguished states at the critical threshold of the self sustained discharge. Figure 6.14 exhibits the same characteristics as Figure 6.12 and 6.13 of a sudden voltage drop and current increase at the ignition point.

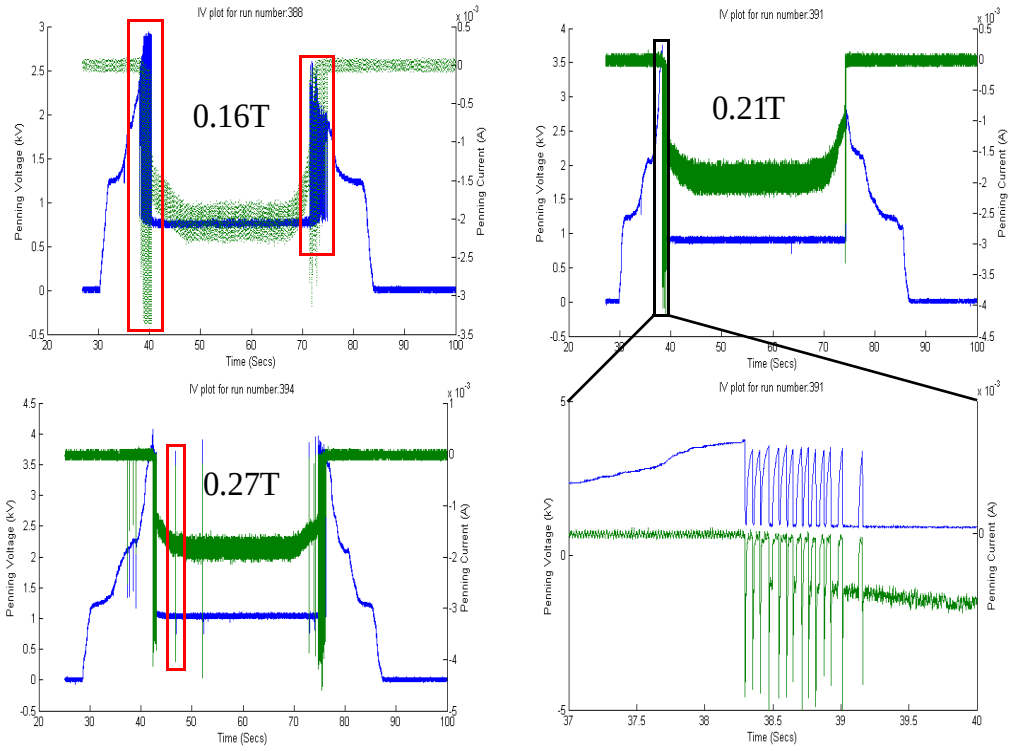

Figure 6.14: Voltage and current measurements against time for discharge ignition, P=1x10^{-4}mBar, using Argon as bleed gas

Further analysis for the Argon measurements at P=1x10^{-4}mBar, Figure 6.15 shows the relation of the Penning voltage and current as a function of each other. This is shown for the same three magnetic flux values. Focus is placed on the B=0.21T plot, corresponding to the operating cavity flux. This plot shows that initially as the voltage applied to the Penning trap was increased, the current was initially more or less zero, point (i). At the point of ignition, ~3.5kV in this case, shown at point (ii), the voltage dropped to ~0.9kV necessary to sustain the discharge and the current increased to ~1.8mA, point (iii). Point (iv) corresponds to the 'ears' of the plot in Figure 6.14, where the discharge ignites, goes out, and ignites again before either igniting and being sustained at the measured 0.9kV, or going out completely as the applied voltage to the trap is turned to zero.

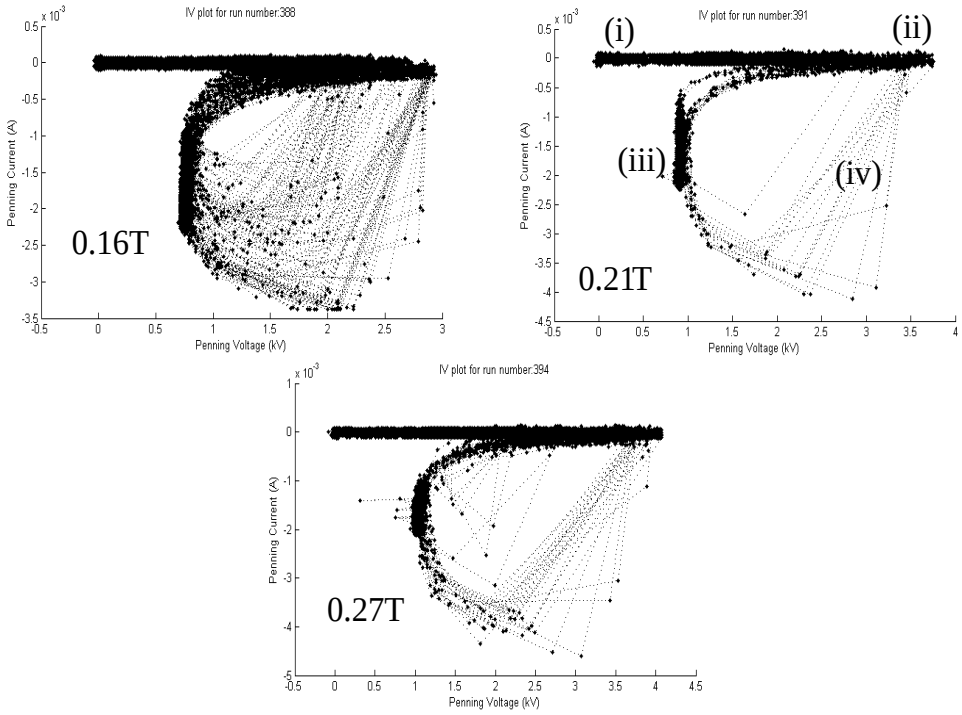

Figure 6.15: I-V characteristics of the Penning trap for Argon

The photographs in Figure 6.16 are snapshots taken from real time videos, recording the discharge ignition. The video camera in the experiment bay is connected to a television screen at the oscilloscope allowing the luminosity of the discharge to be monitored whilst measuring the voltage and current on the trap. This provided an insight into the spatial structure and temporal stability of the luminosity of the plasma throughout the voltage sweep. Figure 6.16a) shows an extremely low intensity picture taken for Argon at $1x10^{-4}$mBar with B=0.02T. Decreasing the pressure to $1x10^{-5}$mBar and increasing the cavity flux to 0.27T yielded the photo in b) which is noticeably brighter. In c), the pressure has increased yet again to $5x10^{-4}$mBar this time with B=0.16T. This photo is the most luminous of the three and was significantly more stable for the duration of the discharge ignition process.

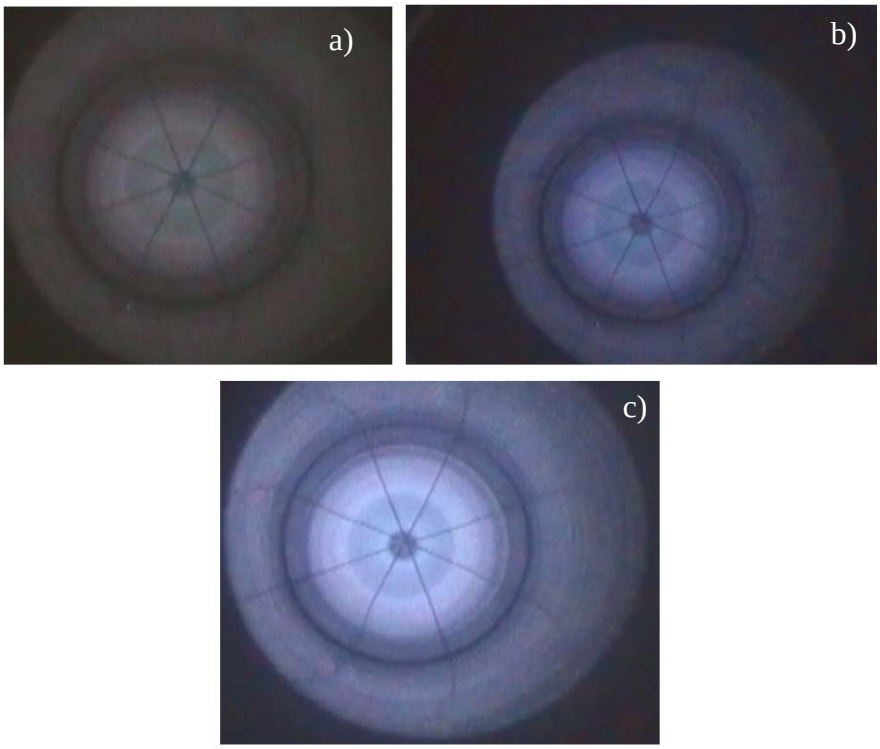

Figure 6.16: Three discharge ignition photos showing varying degrees of luminosity

6.6.2 Plasma Probe Configuration

Having established that a plasma could be ignited and sustained within the Penning trap, the next step was to find a way to measure the plasma characteristics. This was done by insertion of a co-axial type probe into the magnetic field region within the Penning trap. The probe was oriented parallel to the magnetic field of the experiment meaning in addition to collecting current under DC bias that it would also couple to the O-mode, which should show a resonance at the plasma frequency yielding the plasma density. The probe was inserted into the centre of the Penning trap magnetic field plateau and at a radial position half way out from the centre. However, when the experiments that were carried out prior to insertion of the probe were re-run with the probe in place, there were noticeable differences in the results obtained, irrespective of the gas in use. It required very much higher voltages to sustain the discharge, the discharge currents were much lower, and at the lower magnetic field settings the discharge either had very weak luminosity or the discharge would fail to ignite at all.

It was noted that as the current in the Penning trap increased the corresponding probe floating voltage decreased. The difference in the I-V characteristics induced by the addition of the probe gave sufficient evidence that the probe could not give dependable data on the required plasma parameters.

The impact of the electrostatic fields induced by the probe were investigated by modifying the voltage divider which linked the probe to the oscilloscope. Studies were based on two specific parameters, the probe load impedance and the shield potential. Four different regimes of operation were investigated and are listed below;

Regime 1) probe load impedance 1GΩ, shield potential grounded
Regime 2) probe load impedance 1GΩ, shield potential floating
Regime 3) probe load impedance 10MΩ, shield potential grounded
Regime 4) probe load impedance 10MΩ, shield potential floating

The impact on the discharge behaviour was noted in terms of the current and voltage of the discharge, the optical emissions from the discharge and the voltage and current on the probe tip. It was found that when the sheath was grounded the discharge ignited at a low voltage but had a much higher impedance compared to when the probe was not inserted. When the probe had a floating shield there was a lot of arcing occurring in the discharge and a lower luminosity than when the probe was not inserted. The main conclusions to be drawn from these four regimes of study with the ‘long’ probe was that;

1/ the discharge luminosity was always weak
2/ the discharge, when ignited, was generally always at low current and high voltage
3/ there was a lot of arcing and disruptions in the plasma
4/ the probe voltage tended to follow the anode voltage

All of these points mentioned are undesirable and all ceased to occur when the ‘long’ probe was removed. The following section presents results and analysis of these four regimes that were studied.

6.6.3 Analysis of Discharge Disruption Caused by 'Long' Probe

Tables 6.4 to 6.6 show voltage and current characteristics for Air, Helium and Argon, for the discharge ignition process but also include the plasma probe measurements. Each of the four test regimes are shown in the tables and the effect of each discussed.

Table 6.4 Discharge Behaviour of Air with 'Long' Probe

Regime	P (mB)	B (T)	Discharge		Probe	
			V (kV)	I (mA)	V (kV)	I (μA)
1	$5x10^{-6}$	0.21	3.6	0.6	2.58	2.58
2			4.7	0.25	1.54	77
3			4.2	0.4	0.38	38
4			4.8	0.2	0.47	47

Table 6.4 presents the results of measurements carried out with no bleed gas present i.e. $P=5x10^{-6}$mBar. In this case, as in Table 6.5 and 6.6, only the operating magnetic flux is shown, B=0.21T. As seen from Table 6.4, the voltage needed to ignite the discharge, Figure 6.17, was lower than before the probe insertion but the voltage needed to sustain a given discharge current was a lot higher, see Table 6.1 and Figure 6.12 for reference.

Looking at the four regimes in Table 6.1, the sustain voltage is higher when the sheath was floating than when it was grounded, shown in green. It was also higher when the probe impedance was at 10MΩ as opposed to 1GΩ, shown in blue, possibly associated with a large drain of current from the probe. This latter observation holds for Helium and Argon also.

With regards to the probe voltage, this is seen to decrease moving from Regime 1 to Regime 2, and increases when moving from Regime 3 to Regime 4. This held true regardless of gas or pressure.

Looking now at Figure 6.17, it is immediately apparent by referring to Figure 6.12, that addition of the plasma probe has had an adverse effect on the characteristics and performance of the discharge chamber. Before, when the discharge ignited, evident from a sudden rise in current, the voltage would simultaneously drop very sharply. However now, regardless of the Regime, when the discharge ignites, the voltage keeps climbing. In Regime 1 there was a second critical value where the voltage suddenly dropped slightly. The graph for Regime 1 provides the closest comparison to those in Figure 6.12 with the characteristic ‘ears’ at the ignition and final stage of operation, marked in red. However, Regimes 2 to 4 show no similarities at all. All four cases showed signs of unstable spikes due to arcing within the cavity. The red box in the plot for Regime 4 shows a point where the applied power was decreased and increased mid sweep to show that the discharge was reproducible.

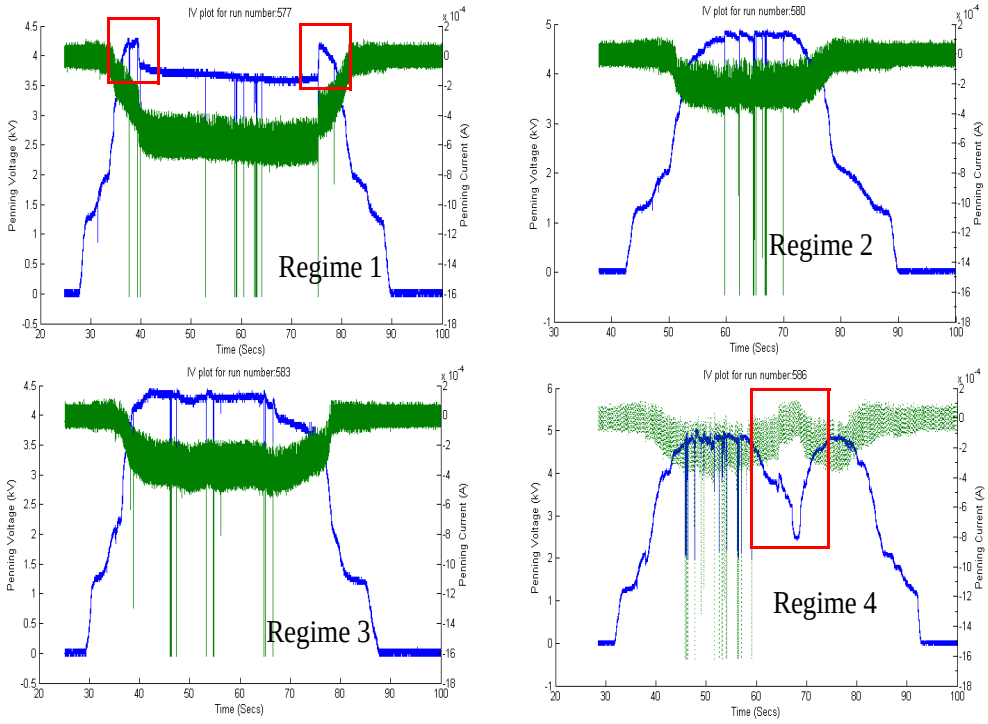

Figure 6.17: Plot corresponding to four regime measurements of Table 6.4

Table 6.5 Discharge Behaviour of Helium with 'Long' Probe

Regime	P (mB)	B (T)	Discharge		Probe	
			V (kV)	I (mA)	V (kV)	I (μA)
1	$1x10^{-5}$	0.21	3.5	0.65	2.6	2.6
2			4.9	0.2	1.49	74.6
3			4.1	0.4	0.34	34
4			4.6	0.2	0.51	51
1	$1x10^{-4}$	0.21	3.1	0.7	2.06	2.06
2			Discharge did not ignite			
3			3.1	0.75	0.5	50
4			Discharge did not ignite			
1	$5.8x10^{-4}$	0.21	2.1	1.2	1.64	1.64
2			3.3	0.4	>1	>50
3			2.4	1.1	0.59	59
4			2.9	0.4	>1	>100

Table 6.5 presents results for experiments with Helium at three different pressures. For the shaded section, refer to Table 6.2 and the top right hand graph in Figure 6.13 for comparison. As can be seen the voltage required to sustain the discharge at any given current was higher overall. Figure 6.18 shows that Regimes 1 and 3 required less voltage to ignite the discharge than prior to probe insertion, but Regimes 2 and 4 required more voltage. For $P=1x10^{-4}$mBar, Regimes 2 and 4 refused to ignite at all, both of these Regimes had the sheath floating. For $P=5.8x10^{-4}$mBar, Regimes 2 and 4, the voltage experienced by the probe exceeded 1kV and could not be measured using the installed apparatus. The closeness in the potential measured on the trap anode and the probe provide serious cause for concern. Figure 6.18 makes it clear that when the sheath is grounded, little or no arcing occurs in the trap, but as in Regimes 2 and 4, when the sheath is floating, there are unstable regions of operation with low and variable current measured.

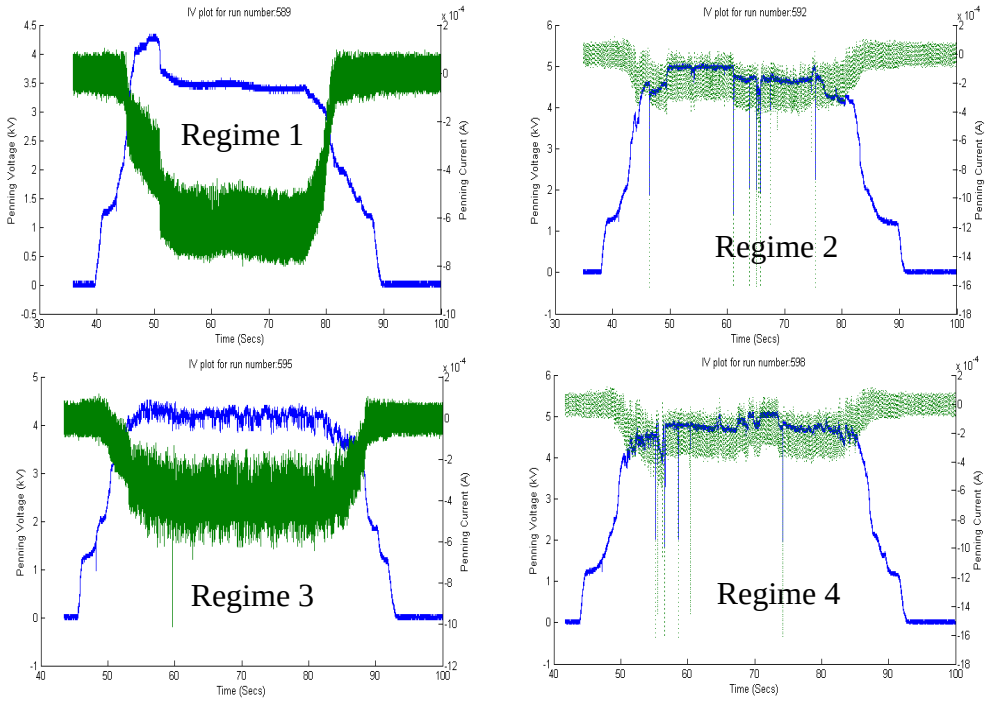

Figure 6.18: I and V against time for P=1x10^{-5}mBar corresponding to shaded area of Table 6.5

Table 6.6 Discharge Behaviour of Argon with 'Long' Probe

Regime	P (mB)	B (T)	Discharge		Probe	
			V (kV)	I (mA)	V (kV)	I (μA)
1	1x10^{-5}	0.21	3.9	0.55	2	2
2			4.9	0.2	1.6	79.8
3			4.3	0.4	0.31	30.5
4			4.8	0.2	0.63	63
1	1x10^{-4}	0.21	3.2	0.75	2	2
2			4.7	0.2	1.76	88
3			3.6	0.6	0.37	37
4			4.8	0.15	0.80	80

Table 6.6 Discharge Behaviour of Argon with 'Long' Probe

Regime	P (mB)	B (T)	Discharge		Probe	
			V (kV)	I (mA)	V (kV)	I (μA)
1	$5.8x10^{-4}$	0.21	2.3	0.75	1.74	1.74
2			4.2	0.25	>1	>50
3			3	0.8	0.62	62
4			3.8	0.25	>1	>100

The measurements given in Table 6.6 are for Argon. The time evolution of the discharge voltage and current for the shaded section with $P=1x10^{-4}$mBar is shown in Figure 6.19. In this case, referring to Table 6.3 and Figure 6.14 at B=0.21T, the voltage needed to ignite the discharge stayed around the same value of ~3.5kV regardless of regime and probe presence. Even so, the voltage needed to sustain the discharge was still far higher in Table 6.6 than Table 6.3, with poorer temporal stability of the current curves compared to the conditions prior to probe insertion. Comparing Table 6.5 to Table 6.6 for $P=1x10^{-4}$mBar, there was no signs of ignition problems using Argon as when using Helium. However, at $5.8x10^{-4}$mBar the probe voltage again exceeded 1kV in Regimes 2 and 4 and could not be measured.

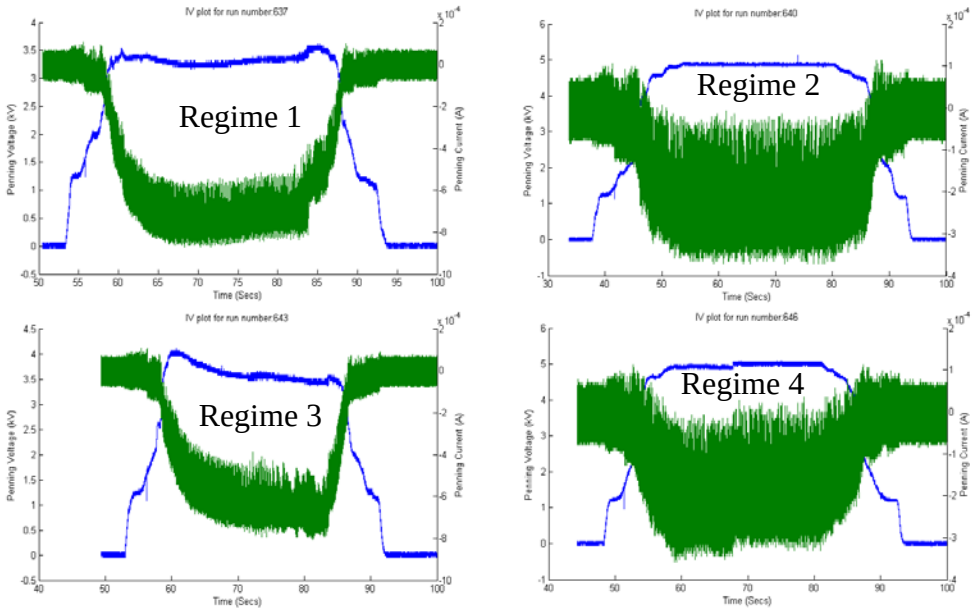

Figure 6.19: Plots of measurements from the shaded section of Table 6.6, with P=1x10^{-4}mBar

6.6.4 Analysis of Discharge with Short Probe

The probe was removed to confirm that measurements under the original configurations could be replicated. It was postulated that the long section of the probe (10cm reaching the centre of the trap) was excessively disrupting the electrostatics during the initial phase of discharge ignition.

The probe was shortened such that its 1cm tip just protruded past the face of the mesh cathode and further measurements taken. It was now possible to ignite the discharge with the probe inserted and for it to operate in a comparable mode providing the background gas pressure exceeded ~3x10^{-4}mBar. This confirmed that the previous probe length of 10cm had been having an adverse effect on the measurements. Figure 6.20 shows a photo taken of the discharge ignition with the probe inserted. The cathode mesh spokes can be seen as well as the nylon holder which supported the probe in position. The coaxial cable which connects the probe to the diagnostic apparatus is also visible.

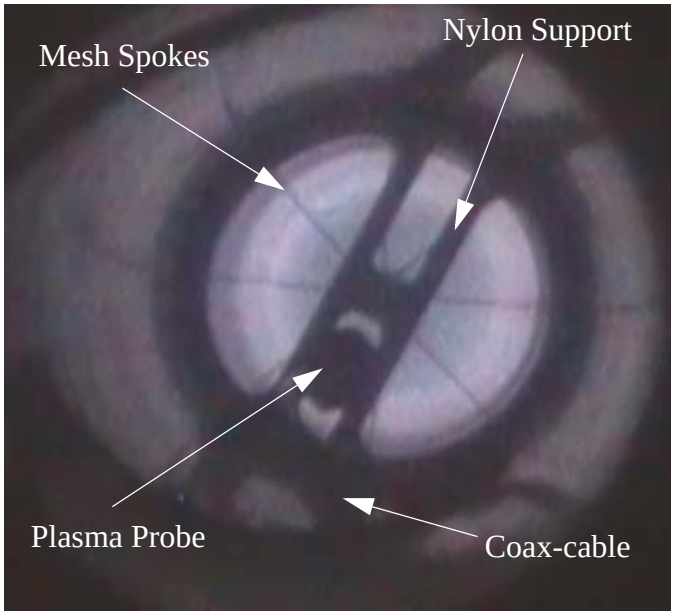

Figure 6.20: Photo of discharge ignition with probe inserted for plasma diagnostics

Satisfied that the probe was no longer severely disrupting the plasma, it could be used to characterise the plasma. The key results of interest were the electron temperature within the plasma, the plasma density and the plasma oscillation frequency. Measurements of plasma density will allow scaled comparisons to be made to the magnetospheric observations where $\frac{\omega_{ce}}{\omega_{pe}} \sim 30$. Experiments were carried out to investigate the effect that the probe voltage had on the probe current as the current in to the Penning trap was altered. The results are reported in Table 6.7 with Figure 6.21 showing the linear trend that occurs. These results are for the probe being driven positive.

Table 6.7 Discharge behaviour of Helium with 1cm probe tip

B(T)	P(mB)	Discharge		Probe tip	
		V(kV)	I(mA)	V(V)	I(μA)
0.21	$5x10^{-4}$	0.46	2.18	0	28.8
			2		27.7
			0.5		14.5
			2.18	10	31.8
			2		30.8
			0.5		16
			2.18	20	34
			2		33
			0.5		18.1
			2.18	30	36.4
			2		35.5
			0.5		19.4
			2.18	40	38.4
			2		37.4
			0.5		22
			2.18	50	41.2
			2		39.5
			0.5		22.7

The voltage to the trap was applied until the discharge was fully ignited, this gave a sustained voltage of ~0.46kV and a maximum discharge current of ~2.2mA. This behaviour was very similar to the case when the probe was not installed. At this value the current on the probe tip was at its maximum. The current applied to the discharge could then be lowered with reasonable accuracy in steps of 0.5mA allowing corresponding values of probe current to be measured, Figure 6.21. As can be seen from the table, the probe current increased with both the probe tip voltage (from 0 to

50V) and the discharge current. Figure 6.21 shows the results graphically and as can be seen, for each increase in probe voltage from 0 to 50V the probe current increased.

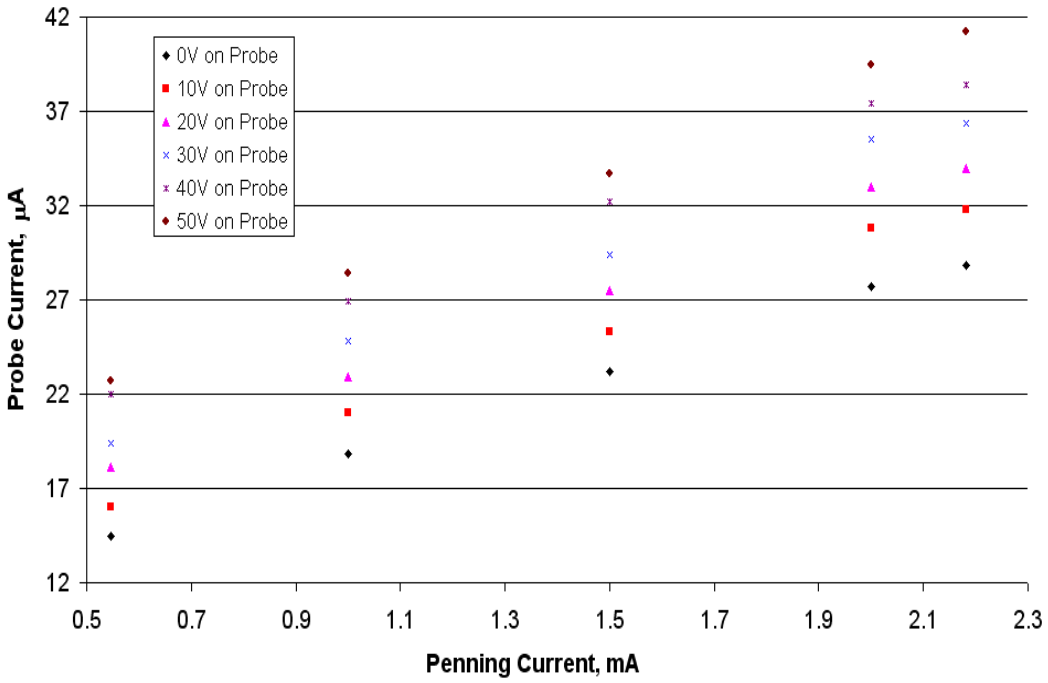

Figure 6.21: Variation of probe tip current with increasing Penning trap current for different probe potentials

A concern that arose during these measurements was that it was not clear if the current was being collected over the entire surface area of the waist of the 1cm cylindrical probe tip, or just on its circular end face. The difference in collection area impacts on the current density and therefore on the value of the electron density calculated. This was important since current flowing onto the face of the probe is parallel to the magnetic field whereas the current onto the waist of the probe would have to be across the magnetic field. Therefore, as well as carrying out experiments with the 2cm cylindrical probe length, of which 1cm was the exposed copper core, measurements were also carried out with the probe tip fully sheathed with its nylon insulator, except for the end where the probe surface is perpendicular to the magnetic field.

Figure 6.22 shows plots of current against voltage for both the 'barrel' and planar probe at the same operating conditions i.e. full discharge current (2.2mA) and a background helium gas pressure of $5x10^{-4}$mBar.

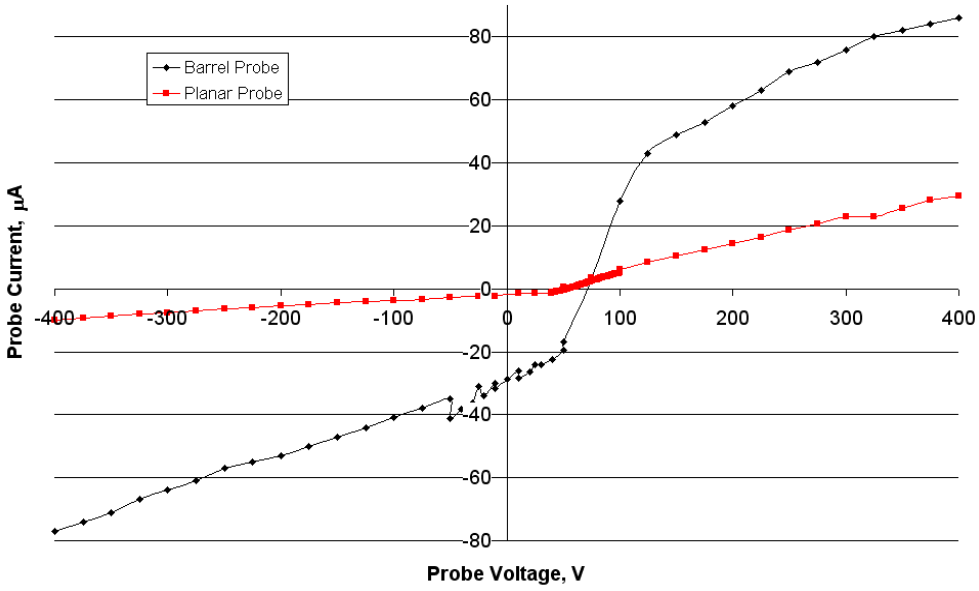

Figure 6.22: I-V characteristic plot for both the planar and cylindrical 'barrel' probe configuration

As can be seen from the plot above, as the voltage is increased from -400V to +400V (due to a more powerful voltage supply available to drive the potential on the probe), far more current was collected when the barrel probe was inserted into the trap. This meant that the whole surface area was collecting current and not just the end face perpendicular to the magnetic field. This in turn meant that it was not just the longitudinal current being collected as was preferred, but also transverse current. When the probe tip was modified so that it was fully sheathed around its circumference it could be expected that the vast majority of current collected came solely from the longitudinal direction, with much less being collected across the field lines. By sheathing the probe surface, apart from the face perpendicular to the magnetic field, the collection area was reduced by a factor of ~40. But, as can be seen in Figure 6.22, the current was only reduced by a factor of ~3. This implies that the charge motion across the field lines in the probe sheath was strongly inhibited and the

results obtained using the barrel probe questionable. Therefore the rest of the experiment was carried out with only the planar probe for more dependable results. Figure 6.23 shows the probe current density versus voltage, for different gas pressures and discharge current, now using solely the planar probe with a planar face surface area of $6.2 \times 10^{-7} m^2$. Taking the logarithm of this plot, shown in Figure 6.24, allowed the temperature of the plasma electrons to be obtained using the value of the gradient and Equation 2.13.4.

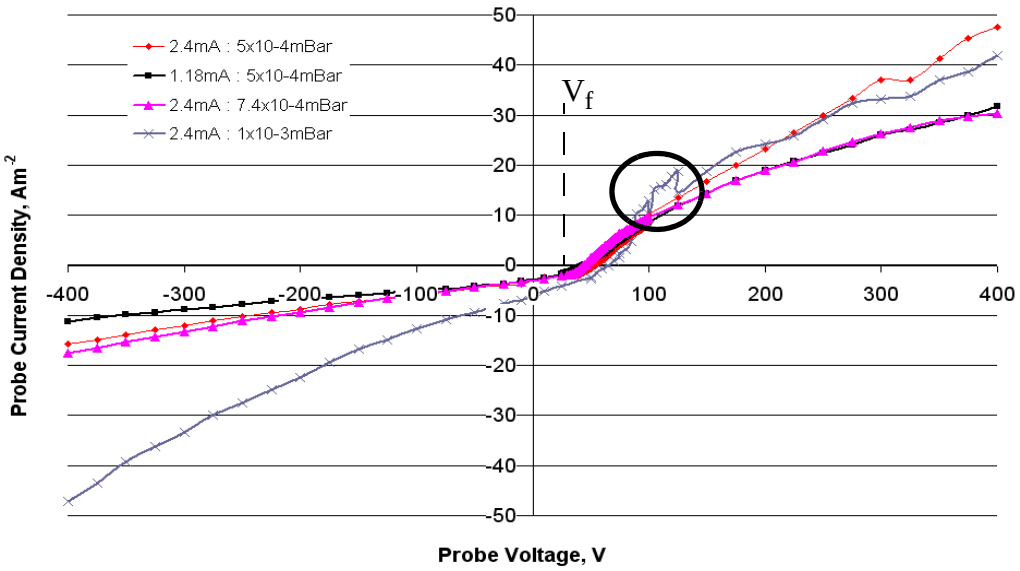

Figure 6.23: Current density versus voltage for the planar probe at different background pressures

Each of the traces shown in Figures 6.23 and 6.24 were stable except that for operating at 1×10^{-3}mBar. At this pressure the discharge became more unstable with fluctuations in the probe current density, circled in black. The area circled in green in Figure 6.24 denotes the range of points that the gradient is taken over. The maximum point on the gradient of the LogJ versus V curve in Figure 6.24 gives an estimate for V_s which can be used in Equation 2.13.7 as an alternative method to calculate the electron temperature.

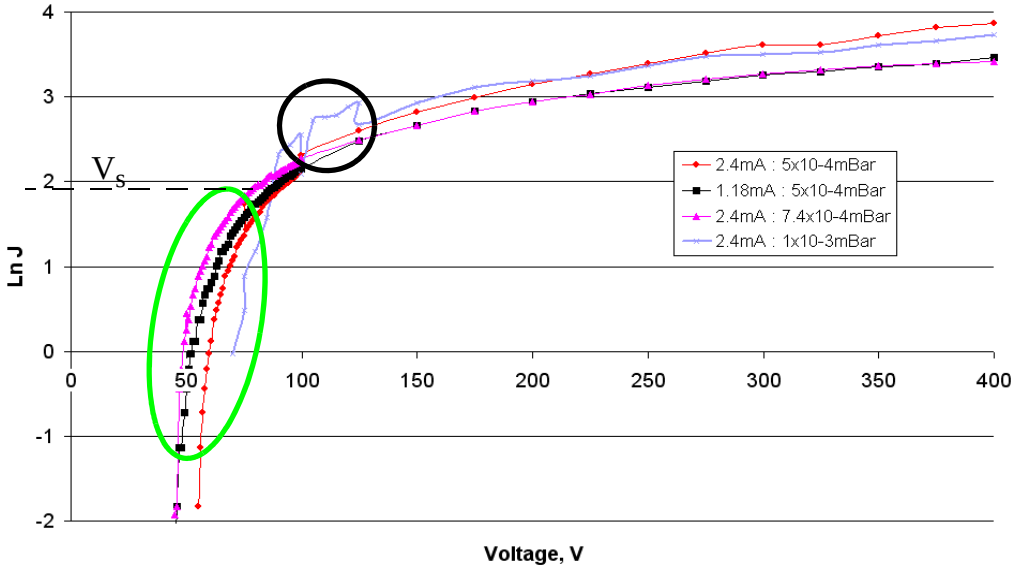

Figure 6.24: Logarithm plot of the current density allowing plasma characteristics to be obtained from equations given in Section 2.13.2

Using this estimate of electron plasma temperature, one may estimate the electron number density and plasma frequency using Figure 6.23. Estimates for J are read at the saturation point and along with Equations 2.13.5 and 2.13.6, allowed the calculation of the electron number density for each of the temperatures previously measured. The plasma frequency can then be calculated using Equation 2.6.1. These results are presented in Table 6.8 below.

Table 6.8 Plasma characteristic using planar probe

Operating condition	Electron Temperature (K)	Number Density (m^{-3})	Plasma Frequency (MHz)
1.18mA : $5x10^{-4}$mBar	$3.8x10^{4}$	$3.2x10^{14}$	161
2.4mA : $5x10^{-4}$mBar	$5.2x10^{4}$	$3.8x10^{14}$	174
2.4mA : $7.4x10^{-4}$mBar	$1.1x10^{5}$	$1.9x10^{14}$	123
2.4mA : $1x10^{-3}$mBar	$1.3x10^{5}$	$1.9x10^{14}$	124

As can be seen from Table 6.8, as the background pressure increased, so too did the electron temperature. Therefore, as is clear from Equation 2.13.6, an increase in T_e means that the value of v_{th} increases and the measurement of n_e decreases. As a check to see that these values were accurate given the limitations of probe theory in a strong magnetic field, the probe was configured in another way using a spectrum analyser, and is discussed below.

6.6.5 Spectrum Analyser Measurements

Connecting the probe as a floating pick-up antenna feeding an RF spectrum analyser yielded the graphs shown in Figures 6.25 and 6.26 showing sharp resonances (circled in blue) tuneable by the discharge current. The graph in Figure 6.25 shows measurements when at a background pressure of $7x10^{-4}$mB using helium as the 'foreign' gas. With a discharge current in the Penning trap of 0.8mA, the plasma frequency detected was ~190MHz. This corresponded to an electron number density of n_e~$4.49x10^{14}m^{-3}$. Increasing the current on the trap to 1.18mA pushed the plasma frequency up to ~240MHz corresponding to an increased electron number density of n_e~$7.16x10^{14}m^{-3}$. As the current is increased the plasma frequency increases but at the cost of the signal strength. On reaching 2.4mA at this background pressure the signal strength was very low with a plasma frequency of ~290MHz just visible before dropping to noise.

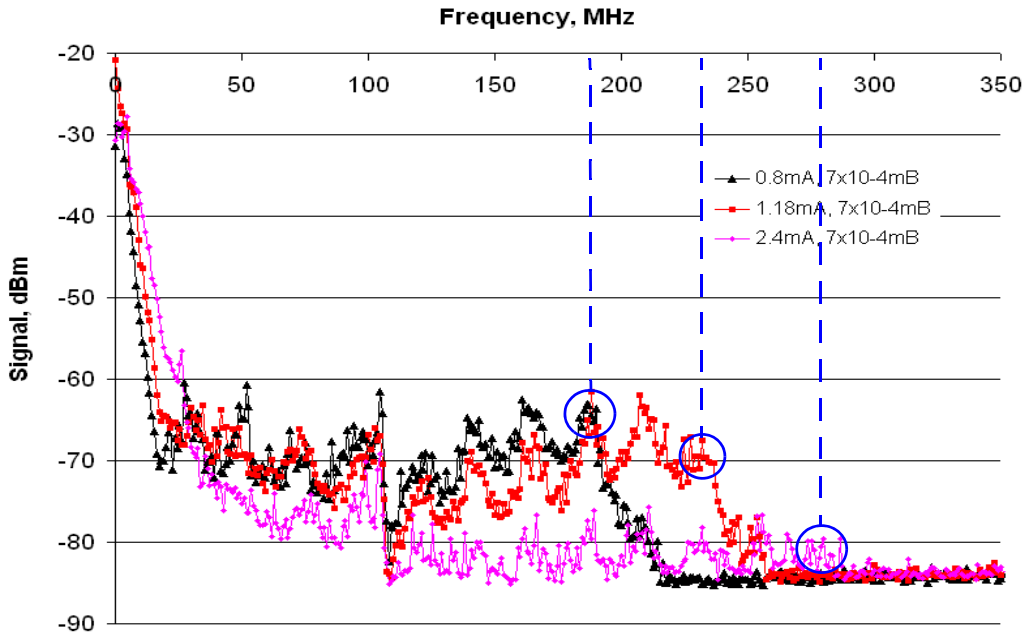

Figure 6.25: Measurements of plasma frequency using Helium at $7x10^{-4}$mB

A decrease in the background pressure to $5x10^{-4}$mB was seen to improve the signal strength of the measurements, see Figure 6.26. At this pressure, for 0.8mA on the trap a plasma frequency of ~210MHz was recorded, implying an electron number density of n_e~$5.5x10^{14}m^{-3}$. For 1.18mA the plasma frequency increased slightly to ~230MHz with n_e~$6.6x10^{14}m^{-3}$. The decreased background pressure enhanced the signal strength and allowed a clearer measurement of the plasma frequency at the highest current setting of 2.4mA. The value of plasma frequency measured in this instance was ~300MHz corresponding to an electron number density of n_e~$1.1x10^{15}m^{-3}$.

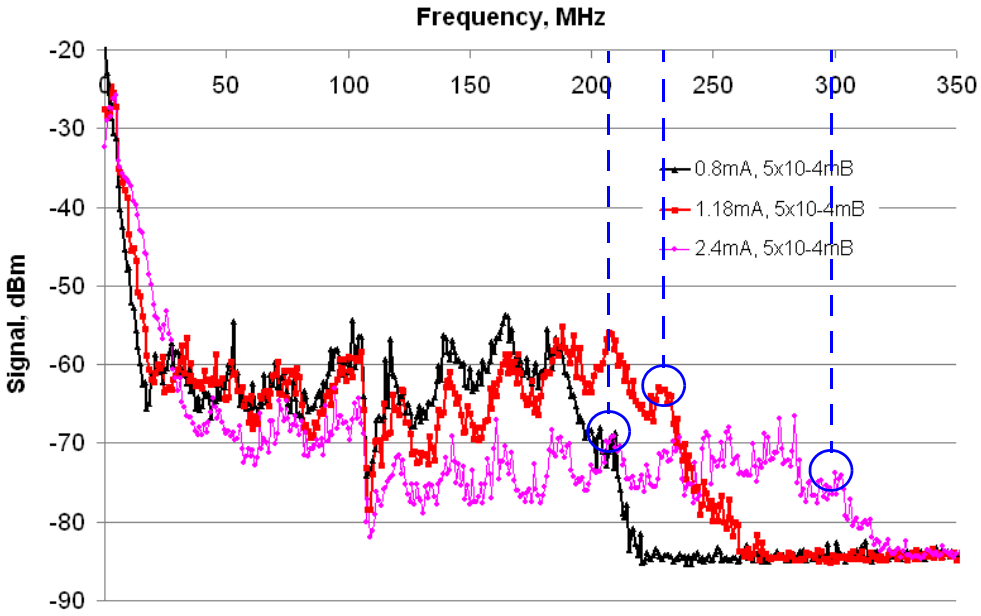

Figure 6.26: Measurements of plasma frequency using Helium at $5x10^{-4}$mB

These values obtained using the spectrum analyser compare, within a factor of two, with those obtained at the end of Section 6.6.2 using the probe IV characteristic technique and thus helping to support the measurements taking into consideration the presence of a magnetic field. Comparing these plasma frequencies to the cyclotron frequency within the Penning trap of 5.21GHz, it is seen that the ratio ω_{ce}/ω_{pe}~20.

6.6.6 Bohm Criterion Analysis of Discharge Current

Using Bohm sheath theory provides another method of estimating the number density of the electrons within the plasma. Using the probe estimate of T_e for the case where the discharge current is 2.4mA and the background pressure with helium is $5x10^{-4}$mBar, one has an electron temperature of $5.2x10^{4}$K. This can be inserted into Equation 2.13.8 which gives a value of the ion sheath velocity, $v_{sh}=10.4x10^{3}ms^{-1}$. This is then substituted into Equation 2.13.9, where the area of the cathode surface face is ~$0.0016m^2$ and the value used for I_c is 2.4mA. This gives a value for the ion number density of, $n_i=9.02x10^{14}m^{-3}$. As can be seen looking back to Table 6.8, this result is broadly comparable to that calculated for the electron number density,

n_e=3.8x10^{14}m^{-3}, obtained from probe theory and very close to the estimate of n_e=1.1x10^{15}m^{-3} from the spectrum analyser measurements. This was the third and final method of estimating the plasma density. The results are within a factor of three of each other giving confidence in the plasma frequency to within a factor of 1.7. Critically the plasma frequency can be set to be ~f_{ce}/20, comparable to the magnetospheric ratio.

It should be noted that there is a possible downside uncertainty of ~20% to be associated with these estimates of plasma frequency obtained using Bohm theory at a Penning potential of ~500V. This is due to the fact that the ion current estimated for use in the plasma frequency calculation may be an overestimate due to secondary emission of electrons. Typical secondary emission coefficients (second Townsend coefficients) for discharges of comparable voltage are up to 0.5, suggesting the ion current is on the order of 0.67 lower than the cathode current [von Engel 1994, Huddlestone & Leonard 1965, Healea & Houtermans 1940, Rostagni 1937, Hill et al 1939, Bohm & Perrin 1992]. Unfortunately these sources do not specifically quote data for helium ions on a copper cathode.

6.7 Microwave Generation with Background Plasma

6.7.1 Beam Current Measurements

As a precursor to the microwave resonance measurements it was necessary to carry out beam current measurements with the Penning trap installed in the experiment. This would ensure that the beam transport was not affected by the modified system. The Faraday cup was therefore placed into the interaction waveguide, replacing the cathode mesh of the trap. Different Blumlein charging voltages and cathode-anode gap spacings were iteratively used to find the optimum operating regime. Initially the anode-cathode gap spacing was set to 1cm. This was half the spacing that was used in the original AKR setup and allowed a lower charging voltage to be applied.

Figure 6.27 shows the independence of the beam current from the gas pressure demonstrating that the system remains collisionless. Any changes in the microwave

measurements would therefore be solely due to the electromagnetic coupling to the plasma and not scattering of the beam on the gas. As well as determining that the beam properties were not affected by the change in pressure, this experiment also determined that the electron gun was able to hold a high enough accelerating voltage without arcing in these conditions.

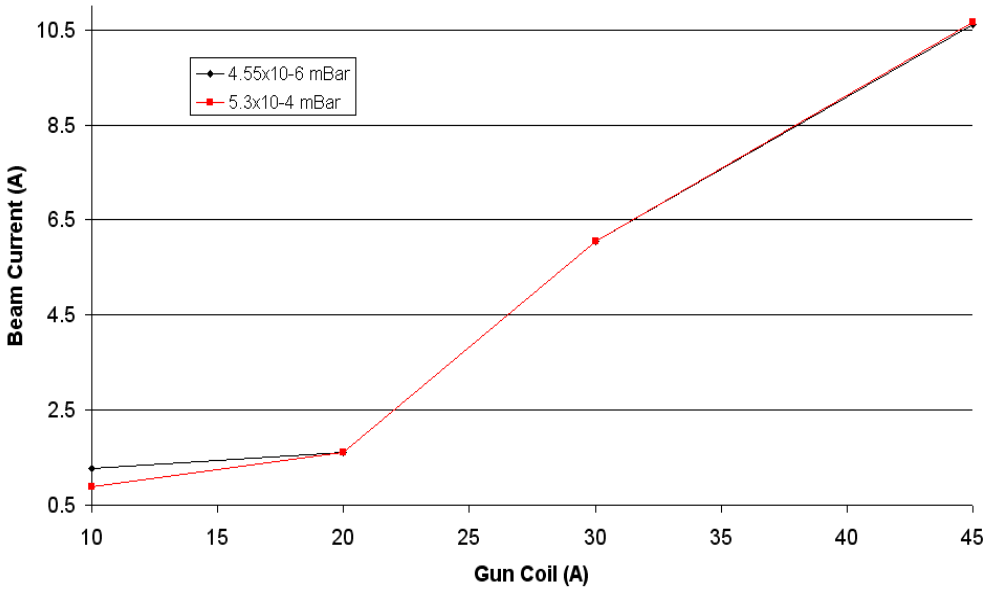

Figure 6.27: Differences in I_{beam} as pressure increases from 10^{-6}mBar to 10^{-4}mBar, V_{ch}=21.2kV

Tuning the charging voltage, gun magnetic field and anode-cathode gap showed that a charging voltage of 50kV with a cathode-anode gap spacing of 1.5cm, gave a good overall operating regime for the electron gun. The rest of the experimental results presented use these parameters. The diode current and voltage pulses for 50kV charging potential were very reproducible from pulse to pulse and can be seen in Figure 6.28. As shown the diode current was ~190A with a diode voltage ~75kV. The beam current pulse measured by the oscilloscope is shown in Figure 6.29 and as can be seen is ~60A. The variation of beam current with magnetic field for this regime is presented in Figure 6.30 and shows progressive mirroring as the magnetic field was increased, thus still demonstrating a horseshoe shape distribution of the electrons, even with the added geometry of the Penning trap.

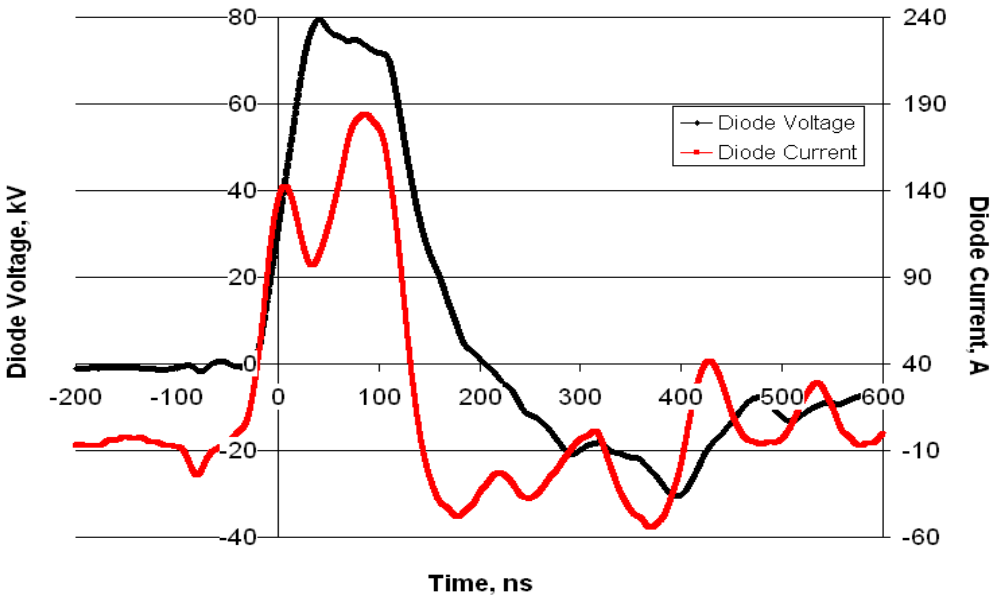

Figure 6.28: For 50kV charging potential there was, at optimum condition, ~75kV diode voltage and ~190A diode current

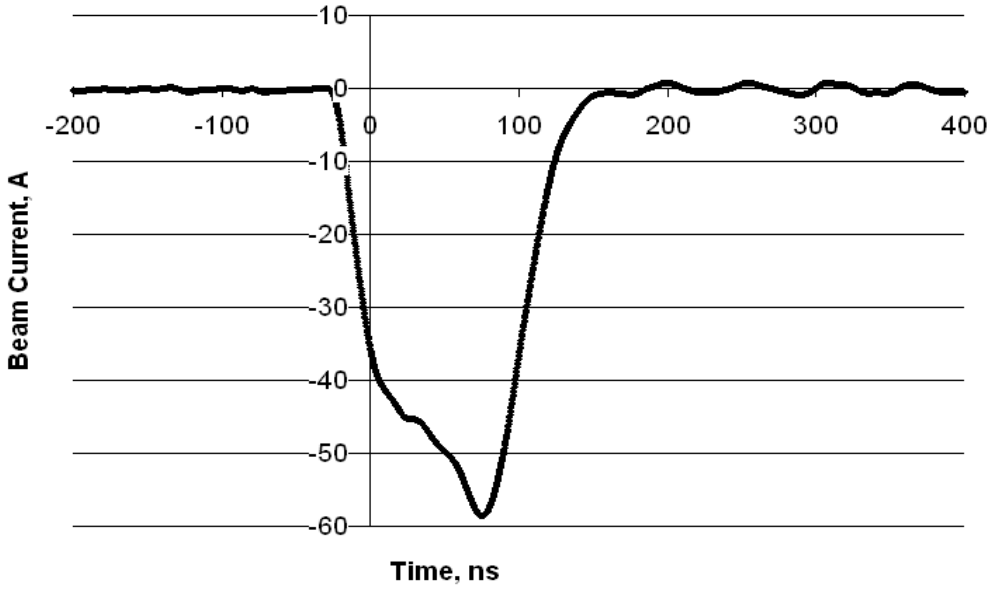

Figure 6.29: Beam current of ~60A for 50kV charging potential

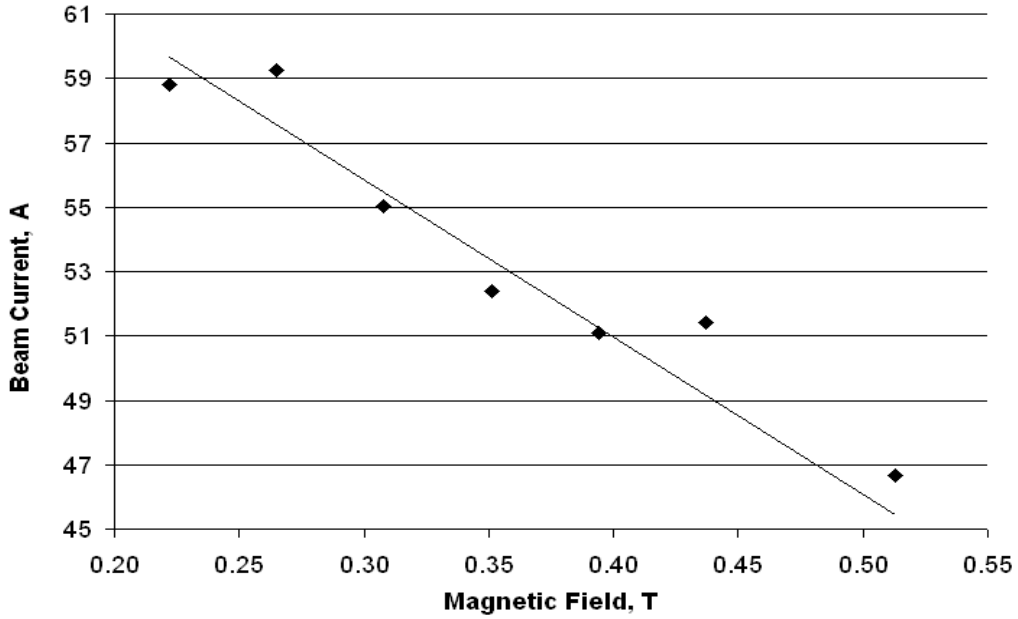

Figure 6.30: Beam current measured at P=5x10^{-4}mBar, for B-fields increasing from 0.21T, with a charging voltage of 50kV

This optimised operating regime and the demonstration of progressive mirroring in the beam current (implying the formation of a horseshoe velocity distribution) provided a basis for RF generation experiments.

6.7.2 Microwave Measurements

As mentioned in Chapter 3, the cut-off frequency of the Penning trap is 5.21GHz. This meant that the detection apparatus was based on waveguide 14 components. The calibration of the components is discussed in Sections 3.7.3 and 3.7.4 with Figure 3.23 showing the inside of the receiver box with the variable attenuator in place.

It was necessary to tune to locate the optimum settings for microwave generation by means of a magnetic field sweep presented in Figure 6.31 comparing microwave power coupled into the detection waveguide at each magnetic field setting.

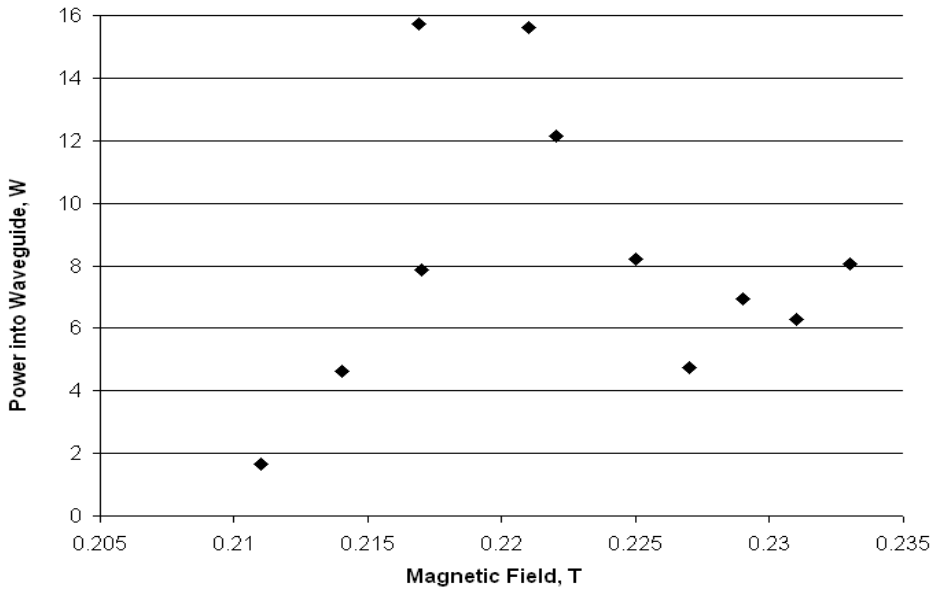

Figure 6.31: Magnetic field sweep illustrating the effect of detuning on the power received into the waveguide, optimised at 0.222T

The graph shows that the strongest microwaves pulse signals were measured at magnetic fields in the range of 0.217T to 0.221T. The tuning was carried out to maximise the pulse amplitude and width therefore leading to optimum pulse energy. Figures 6.32 and 6.33 show how critical the tuning is showing a short, low energy pulse at a slightly non-optimal magnetic field, ~0.217T, compared to a wide, high energy pulse, at magnetic field of 0.22T.

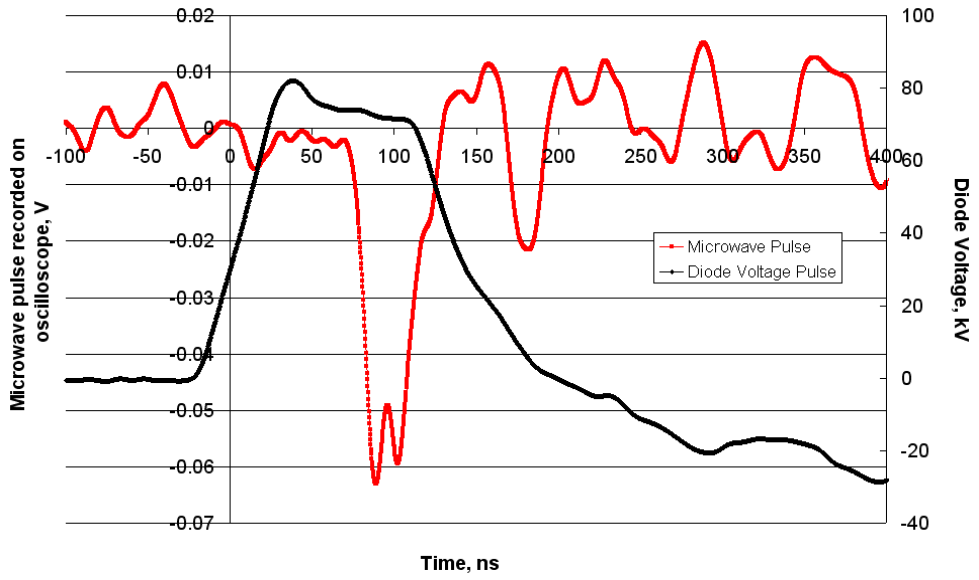

Figure 6.32: Microwave pulse sitting to the edge of the diode voltage pulse and of short duration

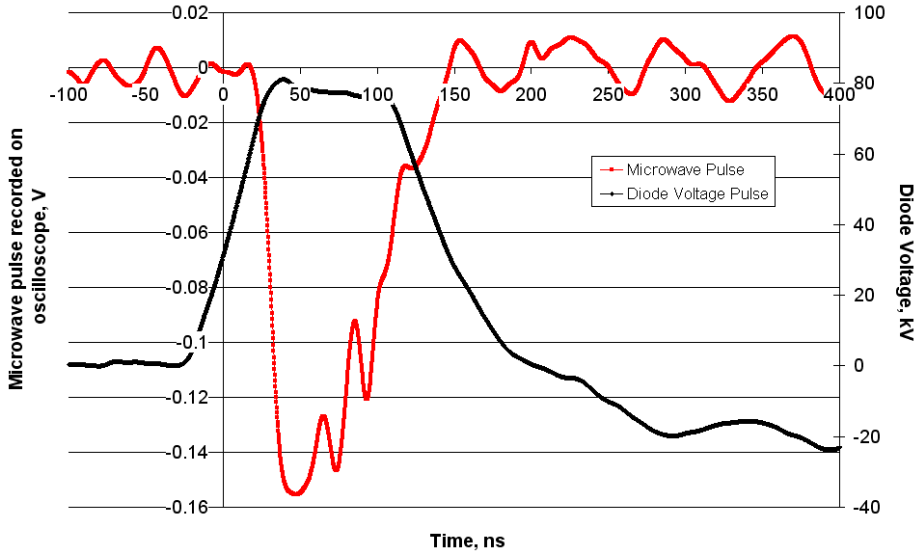

Figure 6.33: Optimum microwave pulse shape, showing the optimised pulse duration across the width of the diode voltage pulse

From this analysis it was decided to operate the experiment working at one magnetic field setting of 0.222T. It was noticed that on occasion, no microwave pulse was observed on firing the electron gun. Table 6.9 shows the statistics of this effect and the power detected as a function of the plasma frequency.

Table 6.9 Average Power Detected at B=0.222T

Plasma Frequency (MHz)	Average Power Detected (W)	Statistical Occurrence of Microwaves (%)
0	12.2	95
240	3.3	10
300	0.8	3

This data shows that increasing the plasma density reduces sharply the fraction of electron beam pulses that yielded microwave output signals and the radiation production efficiency. With a plasma frequency of 300MHz the microwave signals are generated only three pulses in ten. The radiated power has decreased by a factor of 15, from 12.2W to 0.8W.

Figure 6.34 shows three microwave pulses that were detected at a distance of 1m from the output of the experiment. In this case the magnetic field has been altered slightly (0.229T) to show the impact it has on the microwave power and generation statistics. The results for this are presented in Table 6.10 with a plot in Figure 6.34 for illustration.

Table 6.10 Average Power Detected at B=0.229T

Plasma Frequency (MHz)	Average Power Detected (W)	Statistical Occurrence of Microwaves (%)
0	7.6	100
240	4.8	50
300	1.8	70

As can clearly be seen from Table 6.10, the average power detected from the experiment at these settings reduces, from a maximum of 7.6W to around 1.8W, as the plasma frequency increases from 0-300MHz. The probability of generating a microwave signal has improved significantly for the 300MHz plasma frequency setting than when operating with B=0.222T. The overall decrease in average microwave power is now about a factor of 4, so the effect of the plasma has not been as drastic in this case, where ω_{ce} has been increased by ~3%.

Figure 6.34 shows the microwave power obtained in a single shot for the three different plasma frequencies, at B=0.229T. This is to illustrate the time evolution of the microwave pulse and the effect the plasma had on its amplitude. As is shown, the power decreased from ~7.2W to 1.8W as the plasma frequency increased.

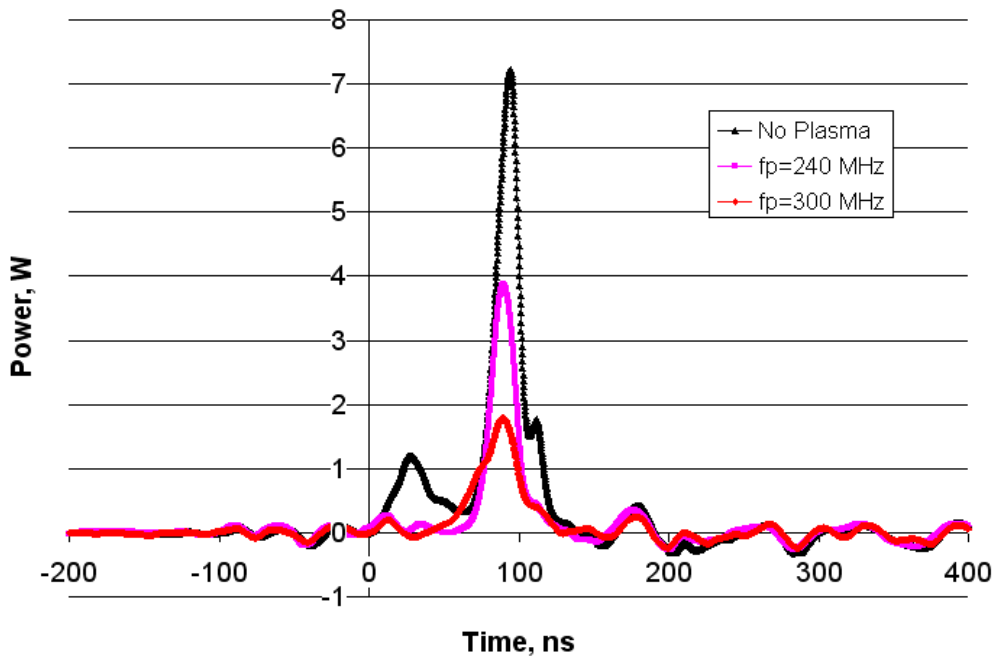

Figure 6.34: Microwave pulse power into waveguide with B=0.229T, corresponding to Table 6.10

The frequency of the emission was determined by use of a real time 12GHz oscilloscope. This captured the AC waveform on which the oscilloscope performed an FFT, giving the results plotted in Figure 6.35. The graph shows that there was little change in the value of the emission frequency, which sits at ~5.4GHz, with the addition of the plasma.

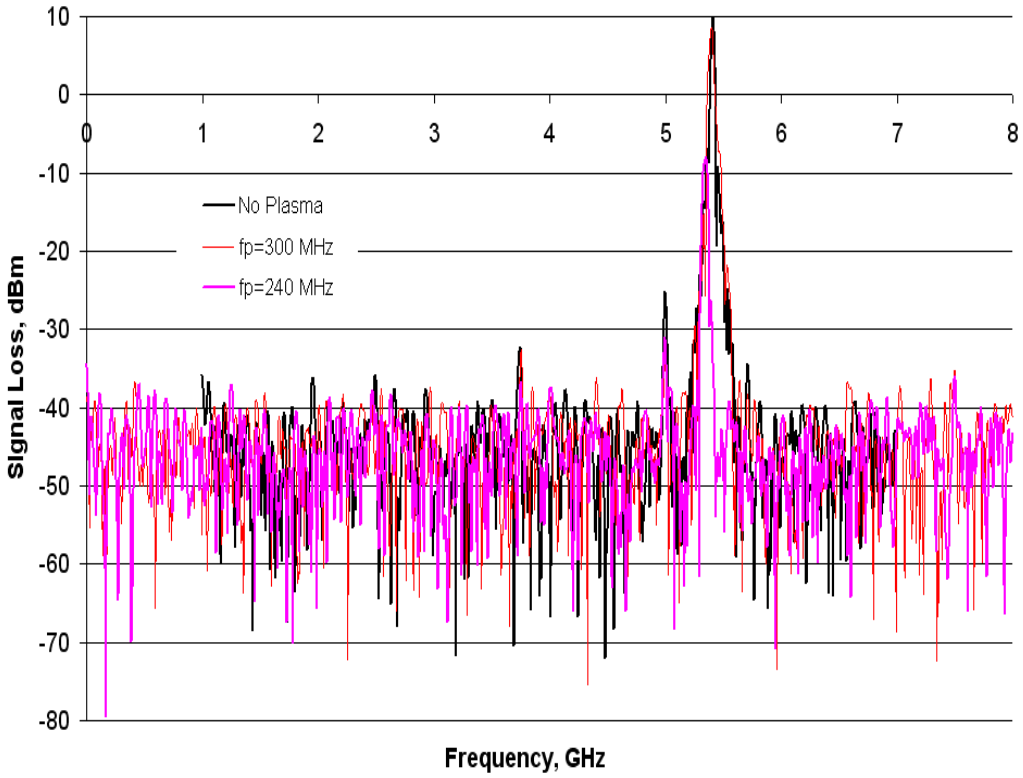

Figure 6.35: Microwave pulse spectra measurements with and without background plasma

The final part of the experiment was to obtain the mode pattern to determine the modes that were excited and hence the radiation polarisations and propagation angles. Integration of the mode pattern would determine the power of the emitted radiation. The antenna pattern was measured by taking measurements at 5° intervals, from 0° directly in from of the output window to ~55° out to the side.

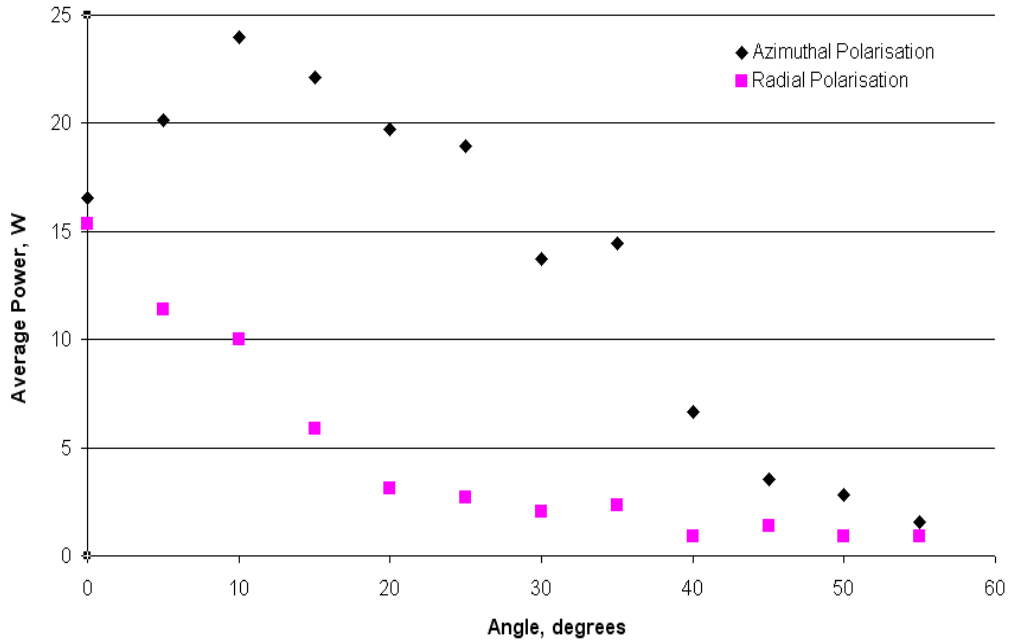

Figure 6.36: Mode patterns from having the receiving waveguide positioned azimuthally and radially with respect to the scanning plane

As can be seen from Figure 6.36, the mode patterns obtained do not match the TE_{01} mode as clearly as previously measured in the original apparatus. However with the design of the Penning cathode mesh, and the dimensions of the Penning trap, it can only be the TE_{01} mode that is generated and emitted at the frequency measured. The peak microwave power measurements were obtained at 0° with the receiving waveguide in the radial polarisation and 10° when in the azimuthal polarisation. Integrating the power density over the area that the scanning detector mapped resulted in a maximum total RF power output of 62.6kW. With a beam power ~4.2MW this gave an efficiency of emission ~1.5%.

Chapter 7 : Discussion and Conclusions

Chapter 7 : Discussion, Conclusions & Future Work

7.1 Overview

The aim of this project was to provide experimental measurements to support the development of the theoretical understanding of the production of Auroral Kilometric Radiation (AKR), providing a reference point for validation of numerical simulations which can then be used to study the magnetospheric dynamics. Two key objectives of this investigation were to 1) Investigate whether there was sufficient free energy in the electron distribution available to produce radiation with an efficiency of emission ~1-2% as is measured in the magnetosphere and 2) Study the effect that a background plasma would have on cyclotron radiation emission processes.

A scaled laboratory experiment was constructed to replicate major aspects of the configuration of the auroral density cavity found at the Earth's polar magnetosphere where (AKR) emission is observed. A system of magnet solenoids was built to encapsulate an evacuated waveguide in order to magnetically compress an electron beam as it leaves the cathode and traverses through the apparatus. This replicated the region of increasing magnetic field that the electron beam experiences as it descends towards the Earth's ionosphere. Cyclotron frequencies of 4.42GHz and 5.21GHz were used, close to cut-off for the TE_{01} mode of the interaction waveguides of diameter 8.28cm and 7.02cm respectively, with an interaction region ~20cm in length. These were scaled from the 300kHz magnetospheric cyclotron frequency, by increasing the magnetic field, and the auroral density cavity dimension of ~9500km. The energy of the electron beam was measured as were its current (in the interaction waveguide) and its electron distribution in velocity space demonstrating the formation of the horseshoe distribution function. It is thought that the horseshoe distribution observed by satellites in the magnetosphere is unstable to the cyclotron resonance maser (CRM) instability and that this mechanism is the cause of the radio-wave emission. The experimental and numerical studies undertaken in this work corroborate this postulation. Addition of a thermal background plasma into the experimental apparatus by means of a Penning trap allowed the experiment to more closely reproduce the

environment found by satellites in the magnetosphere. Values of discharge voltage and current for varying degrees of pressure, magnetic field and bleed gas were investigated. To diagnose the plasma properties a plasma probe was designed and inserted into the Penning trap. This allowed the plasma parameters to be studied as a function of gas type and background gas pressure. The effect of the presence of the tenuous plasma on the strength and spectra of the emitted radiation was studied. In the magnetosphere, the electron density within the auroral density cavity is ~1cm^{-3} with estimates of the plasma frequency, f_p~9kHz, a factor of 30 less than the cyclotron frequency. In the experiment f_c=5.21GHz and f_{pe}~160-300MHz.

Conclusions from the numerical and experimental measurements are summarised in the following sections, 7.2 and 7.3. Comparisons are made between the numerical predictions (Chapter 4 and 5) and experimental measurements (Chapter 6) in Section 7.4.1. Final comparisons can then be made to magnetospheric data, Section 7.4.2. Finally, ideas and directions for future work will be outlined.

7.2 Review of Numerical Predictions

The numerical simulations aided the design of the apparatus whilst providing predictions of the experimental performance and insight into certain parameters which could not be directly experimentally measured. KARAT allowed predictions to be made of the electron beam transport and distribution characteristics in velocity space. The simulated electron trajectory, as it leaves the cathode and is magnetically compressed, can be seen in Figure 5.2, allowing the experimental geometry to be designed and optimised. Predictions of electron beam current in the cavity showed that it decreased with increasing plateau flux density, Figures 5.6 and 5.7. The predictions of the transverse velocity distribution showed that electron bunching occurred, Figures 5.12 and 5.13, and showed the loss of rotational velocity as radiation was emitted showing presence of the CRM instability. Stronger bunching was evident at cathode flux densities of 0.02T than 0.01T. The horseshoe distribution plots, Figures 5.14 and 5.15, showed that the electron distribution in velocity space

was, as predicted by theory, unstable to an electron cyclotron resonance maser type of instability evident from the smearing of the horseshoe distribution in $v_\perp/v_z$ space, as radiation was emitted, Figure 5.15. RF emission predictions were also obtained using this code. The simulation predicted the operating frequency to be 4.42GHz, Figures 5.10 and 5.11, consistent with the dimensions (and cut-off frequency) of the interaction waveguide and the scaling of the magnetospheric cyclotron frequency to dimensions that the laboratory could accommodate. The waveguide mode of operation with which the beam was at resonance was the near cut-off TE_{01} mode. The simulations confirmed the excitation of this mode, Figures 5.16 and 5.17. Maximum radiation power predicted by KARAT was ~20kW for a cathode flux density of 0.01T and ~50kW for 0.02T, corresponding to efficiencies of emission ~2%. The electron distribution in velocity space, Figure 5.9, was matched to experimental data, discussed in Section 7.4, to allow comparison between numerical predictions and experimental measurements of the radiation generation.

A linear theory analysis describing the growth and decay properties of the beam-wave resonance was undertaken. This allowed growth rate and stability to be assessed by plotting the real and imaginary parts of the complex roots of k_z. Resonance between the waveguide mode and the fast cyclotron mode of the beam was shown to exhibit stronger growth as the current and the pitch angle increased hence one may compare Figures 5.18 and 5.19. Doubling the cathode flux density from 0.01T to 0.02T doubled the number of electrons at high pitch angles (>35°). This leads to a higher growth rate and a higher output power as predicted by the simulations.

KARAT was used to simulate the Penning trap numerically allowing predictions of the effect of the plasma on the electron beam as it passed through the interaction cavity, and vice versa. Preliminary simulations show that when the electron beam enters the Penning trap the plasma electrons are displaced from the gun end of the trap. With an increase in the electron beam current, the plasma electrons were displaced at a faster rate. The ions on the other hand, drift radially inwards towards the electron beam. This is seen in Figures 5.21 to 5.23. The KARAT calculations predicted very little power output with a very noisy spectrum (close to the cyclotron

frequency of 5.21GHz) at a plasma frequency ~30MHz. This appeared to be incoherent emission from the electron beam.

7.3 Review of Experimental Measurements

Chapter 6 described experimental results obtained from the scaled AKR apparatus. The first set of experiments yielded the beam transport measurements demonstrating the beam current could be controlled as a function of magnetic compression for different cathode flux densities. It was found that mirroring occurred since the collected beam current decreased with increasing magnetic compression. This suggested that the horseshoe distribution was evolving with increasing mirror ratio (as predicted numerically), illustrated by Figures 6.5 and 6.6. Figure 6.6 illustrates the electron distribution in velocity space and showed that there were more electrons at high pitch angles with a cathode flux density of 0.02T than at 0.01T, thus one would expect higher RF power output at the higher magnetic field. However, doubling the cathode flux density much more than doubles the total current and therefore there are many more electrons at low pitch angles <35°. This could reduce the wave production efficiency.

Microwave radiation measurements were carried out allowing operating frequency, spectral content and power of the emitted radiation to be determined. Magnetospherically the radiation has been observed to be polarised in the X mode which shares similar properties to TE_{01} modes close to cut-off, both propagating and polarised perpendicular to the magnetic field. Fourier transform of the output wave signal showed a frequency peak at 4.42GHz, close to cut-off for the TE_{01} mode, which was confirmed as the mode of resonance, Figure 6.9, by the antenna scan measurements in the far field of the experimental output window. Integration of these plots led to values of the radiated power being obtained with maximum power achieved experimentally at ~19kW for a cathode flux density of 0.01T and ~35kW for 0.02T. These powers corresponded to efficiencies of emission of ~2% and 1.4% respectively. This was consistent with expectations based on the measurements of the

electron beam distribution and showed that there was sufficient free energy available to obtain these efficiencies of emission as in the magnetospheric case.

A Penning type trap was designed and inserted into the interaction waveguide and a gas discharge formed to represent the low temperature magnetospheric background plasma. The reduced dimensions of the trap mean an operating frequency of 5.21GHz, close to cut-off for the TE_{01} mode. Experiments showed that the discharge could be ignited at varying gas pressures, magnetic fields and using different bleed gases. Voltage and current measurements of the trap were recorded for Argon and Helium as the 'foreign' gas. Nitrogen was not investigated in detail as it gave very unstable results. It was found that Helium discharges were most stable at a pressure of $1x10^{-5}$mBar, whereas Argon yielded the most stable discharge at $1x10^{-4}$mBar. With Helium, of the three magnetic fields studied, it was clear that as the magnetic field increased, the stability of the discharge improved, see Figure 6.13.

A probe was inserted into the plasma region to allow measurement of the plasma frequency, temperature and electron density. Although the most stable discharge results were obtained with Argon at $1x10^{-4}$mBar, as soon as the probe was inserted into the Penning trap, the discharge dynamics changed drastically. This was due to the probe disrupting the electrostatics during the discharge ignition and so the initial 10cm long probe was reduced to a 1cm cylindrical 'barrel' probe. The operating conditions with the probe in place also needed to change as it was only when using Helium at $>1x10^{-4}$mBar that the external IV characteristics were independent of the probe. Therefore these conditions with the short probe were adopted for the experiments investigating the impact of the background plasma on the wave production. The idea of inserting the probe in the manner shown in Figure 3.32, i.e. parallel to the static magnetic field, was to facilitate measurements of O-mode oscillations and to pick up longitudinal currents (aligned with the magnetic field). With the cylindrical probe it became obvious that it was picking up substantial current drawn across the magnetic field lines which is not consistent with the assumptions of conventional probe theory. The probe tip was modified to be sheathed entirely in Nylon except for the end tip which is perpendicular to the magnetic field. Figure 6.22

shows the obvious difference in current collection between the two probe geometries. With this more analytically appropriate probe geometry and suitable operating conditions, probe IV characteristics were measured as a function of discharge current and background gas pressures, values of T_e, n_e and f_p were obtained, Table 6.8.

The IV measurements from the probe allowed values of electron temperature to be obtained ~10^4K relating to a plasma frequency of ~161-174MHz, whilst using Helium as the bleed gas at a pressure of $5x10^{-4}$mBar. It was seen that the plasma frequency could be controlled by variation of the discharge current. As this experiment has a very strong magnetic field, probe theory may be inaccurate and so the Bohm sheath model was used as an alternative method to calculate the plasma frequency based on the ion current on the cathode of the discharge chamber. This gave f_p~245MHz but one should remember as can be seen from Equation 2.13.8, that this model still relies on the value of electron temperature which was obtained through the Langmuir probe theory method, Figures 6.23 and 6.24. Even so, comparison of the plasma frequencies obtained using these two methods are consistent to within a factor of two. A third method implemented was to use the probe as a direct AC pick-up antenna thereby picking up signals from within the plasma and therefore not relying on probe or Bohm theory. This showed values of f_p~200-300MHz which is very comparable to the DC measurements. Hence, a plasma could be experimentally generated and measured to have a plasma frequency ~ $\frac{1}{20}$ cyclotron frequency.

With the plasma characterised, microwave measurements were then carried out to determine what effects the plasma might have on the RF generation process. Magnetic field sweeps allowed the sensitivity of the instability to the magnetic detuning to be measured, adding to the plasma characteristics for comparison to magnetospheric results. Figure 6.31 showed that the optimum power into the waveguide was obtained using a magnetic field setting of 0.22T. Using this magnetic field, the effect of varying the plasma density was investigated. Table 6.9 showed that as the plasma density was increased from 0-300MHz, the generation of microwave signals became increasingly more sporadic. Furthermore the efficiency of the wave production decreased by a factor of 18, from around 1.5% to 0.08%, as the plasma frequency increased to

300MHz. Table 6.10 shows data for average power when at a magnetic field of 0.229T, with Figure 6.34 showing the temporal evolution of individual microwave pulses.

7.4 Discussion

7.4.1 Comparisons between Numerical Predictions and Experimental Measurements

The numerical computations and the experiment both showed formation of the horseshoe distribution of the electrons. This was shown in the velocity space plots in Section 5.4 and by experimental measurement of beam current with increasing magnetic mirror ratio, Section 6.2.

Using a set of experimental results investigating the electron velocity space distribution in the cavity, the simulations were revised to achieve a similar electron distribution. The numerically simulated gun geometry was fine tuned to change the pitch of the electrons as they are emitted from the cathode. This enabled a match to the experimentally measured electron distribution, allowing for meaningful comparisons of the non-linear dynamics. The values in Table 7.1 gives a summary of the predictions from the code and are results taken from analysis of Figures 5.8 and 5.9. They are compared to experimental results with matching number density of high pitch electrons (Figure 5.9). The table shows that for the lower cathode flux density of 0.01T a beam current of 16A gave microwave output power of 20kW, whilst at the higher cathode flux density 0.02T a power of 50kW was predicted at a beam current of 34A. The predicted power output plots can be seen in Figures 5.18 and 5.19. This doubling in predicted output power can be linked, in Figure 5.9, to the fact that there are double the number of high pitch electrons present for the higher cathode flux density of 0.02T than there was for 0.01T. However, at B=0.02T, the majority of the experimental electron beam current was associated with the low pitch (<35°) electrons which were not involved with the energy transfer process. This meant that the experimental measurement of the efficiency of radiated power was lower than with B=0.01T where the majority of current lies at high pitch angles, (>35°).

Table 7.1 Comparisons of the peak RF generation efficiencies for varying cathode flux density

	Experimental		Numerical	
Magnetic Flux	0.01T	0.02T	0.01T	0.02T
I_{cavity} (A)	11.6	33.9	16	34
P_{out} (kW)	19	35	20	50
η (%)	~2	~1.4	~2	~2

To represent the Penning trap in the simulation, the geometry of the interaction waveguide was altered and the KARAT program reconfigured to allow for a PiC plasma to be present in the main 'volume'. An electron beam was then injected in and through the plasma containing region and the effects noted and analysed. It was seen (Figures 5.21 to 5.23) that as time evolved, the plasma electrons drifted away from the cathode face, at the insertion end of the Penning trap, towards the tapered cathode at the exit of the trap. The plasma ions, in red, drifted radially inwards towards the electron beam as time progressed, showing possible charge attraction. KARAT predicted very little output power with very low efficiencies working with a plasma frequency of 30MHz. In contrast, the experimental measurements of the wave production efficiency dropped from ~1% to ~0.1% at a plasma frequency of 300MHz.

7.4.2 Comparisons of Measured Data and Simulations to Magnetospheric Observations

The fact that the close to cut-off TE_{01} mode was generated at the cyclotron frequency in conjunction with progressive magnetic mirroring, implied the operation of the CRM instability in an electron beam with a horseshoe distribution in velocity space. The near cut-off TE_{01} mode predicted numerically and measured experimentally was polarised and propagating perpendicular to the z-axis magnetic field direction. This was therefore comparable to the radiation measured in the magnetosphere which was found to be polarised in the extraordinary (X) mode, and has the same propagation and polarisation characteristics, oriented and travelling perpendicular to the static

magnetic field. This strongly supports the postulated theory that the radiation observed by satellites is produced from a horseshoe distribution function which is unstable to the CRM instability process.

The power of emitted radiation in the experiment and in the code ranged from ~19-50kW corresponding to efficiencies of 1-2%. The radiation spectrum was centred at 4.42GHz. This corresponds well with the electron cyclotron frequency. Taking into consideration the scaling associated with the laboratory dimensions, these are comparable to the GW powers that have been recorded in the magnetosphere, also with radiation efficiencies ~1% and with spectra regulated by the cyclotron frequency (~300kHz).

To further enhance the comparisons between the experimental measurements and the magnetospheric observations, a background plasma was introduced by means of a Penning trap installation. Measurements with the Penning trap installed gave operating frequencies close to cut-off for the TE_{01} mode of 5.21GHz, and plasma frequencies on the order of 161-300MHz. This gives a ratio of $\frac{\omega_{ce}}{\omega_p} \sim 17 - 32$. In the auroral density cavity with an electron number density ~1cm^{-3} and radiation emission frequencies ~300kHz, this gives a plasma frequency ~9kHz which leads to a ratio of $\frac{\omega_{ce}}{\omega_p} \sim 33$. It can be seen therefore how comparable the experimental conditions are to those observed magnetospherically. The impact of the plasma however reduced the radiation generation efficiency significantly in the laboratory, from ~1.5% to ~0.1%.

7.5 Future Work

When a background plasma was generated in the experiment it was seen that the statistical nature of the radiation generation was drastically affected. Therefore, to further complete this study, the most immediate requirement for future work will be to carry out an investigation on this observation. It may be the case that there are competing modes during the radiation generation process and identification of this mode is of interest.

For the future development of this experiment, more in depth plasma characteristics will be studied by further investigation with plasma probes. Probe behaviour under magnetised conditions is currently a major field of investigation (Zimmermann et al.) and scope exists for this project to contribute fundamentally to this work and to benefit from the research. With the existing AKR magnet coil apparatus and the Penning trap, there is the potential to study higher plasma densities. The trap may also be lengthened from its current 20cm length, thus providing a larger plasma generation region. This may mean reconfiguring the magnet coils so as to allow for a longer maximum plateau region from the main coil to cover the extent of the trap region. This may reveal slower growing instabilities and allow operation at lower plasma density.

At the moment the radiation is generated in the TE_{0m} mode, close to cut-off for the waveguide dimensions. While this mode is comparable to properties of the X-mode measured in magnetospheric observations, it would be a step forward to allow direct egress of the X-mode in the laboratory. Therefore it is proposed that the transverse radiation boundaries be removed from the experiment.

Separately, with the transverse boundaries still intact, the cathode mesh of the Penning trap will be removed to allow for R-mode instabilities to be studied. It was found during the preliminary work on the discharge ignition experiments that the Penning trap was capable of igniting with only the gun end cathode plate and so removal of the mesh will be possible. With the cathode mesh removed the plasma will be more ‘freely’ able to drift out of the trap and therefore out of the maximum plateau magnetic field region. This would have to be studied closely for adverse affects, i.e. undesired resonance conditions in the profiled magnetic field. Being able to carry out this experiment successfully might allow the study of the generation of R-mode radiation relevant to the Chorus phenomenon which occurs along the magnetic field lines at the Earth’s equatorial regions.

Significant apparatus modification will later allow for investigation of important fusion relevant instabilities such as the anomalous Doppler resonance (currently a

topic of theoretical and numerical investigation with our collaborators at the University of St. Andrews), the two stream instability and also the filamentation instability.

The numerical codes must also be improved regarding the modelling of the electron gun to provide a closer comparison to the electron beam transport measurements obtained experimentally. Improvements must also be made to the way KARAT models a plasma in a confined region to provide a comparison to the experimental measurements obtained with the Penning trap. Given the difficult scaling of the plasma parameter with particle agglomeration, it is likely that a highly parallel code should be adopted to cope with the size of the numerical problem. However recent work I have undertaken involving similar simulations have shown that the merging factor does not seriously compromise the accuracy of the simulations as had previously been thought. This makes such simulations more realisable.

3D numerical codes are being developed to investigate second harmonic modes [Gillespie et al 2008] and coupling to non-azisymmetric radiation modes - these will be critical to the investigation of the anomalous Doppler instability and the Chorus effect.

References

Allen J.E. and Phelps A.D.R., 1977, ‘Waves and microinstabilities in plasmas-linear effects’, Rep. Prog. Phys., **40**, pp1305-1368

Bell T.F and Buneman O., 1964, ‘Plasma instability in the whistler mode caused by a gyrating electron stream’, Physical Review, **133**, pp1300-1302

Benediktov E.A., Getmantsev G.G., Sazonov Yu.A. and Tarasov A.F., 1965,’Preliminary results of measurements of the intensity of the distributed cosmic radio emission in the 725 and 1525 KC frequencies on the satellite “electron 2”’, Cosm. Res., **3**, pp614-617

Benson R.F., 1985, ‘Auroral kilometric radiation: wave modes, harmonics and source region electron density structures’, Journal of Geophysical Research - Space Physics, **90**, pp2753-2784

Benson R.F. and Calvert W., 1979, ‘ISIS 1 observations at the source of auroral kilometric radiation’, **6**, pp479-482

Bingham R. and Cairns R.A., 2000, 'Generation of Auroral kilometric radiation by electron horseshoe distributions', Physics of Plasmas, **7**, pp3089-3092

Bingham R. and Cairns R.A., 2002, 'A New Cyclotron Maser Radiation Mechanism in Space Plasmas', Physica Scripta, **T98**, pp160-162

Bingham R., Kellett B.J., Cairns R.A., Dendy R.O. and Shukla P.K., 1999, 'Wave generation by ion horseshoe distributions on auroral field lines', Geophysical Research Letters, **26**, pp2713-2716

Bingham R., Cairns R.A. and Kellett B.J., 2001, 'Coherent cyclotron maser radiation from UV Ceti', A&A, **370**, pp1000-1003

Bingham R., Kellett B.J., Cairns R.A., Vorgul I., Phelps A.D.R., Ronald K. and Speirs D.C, 2004, ‘Cyclotron maser radiation in space and laboratory plasmas’, contribution to plasma physics, **44**, pp382-387

Bohm C. and Perrin J., 1993, ‘Retarding-field analyser for measurements of ion energy distributions and secondary electron emission coefficients in low-pressure radio frequency discharges’, Review of Scientific Instruments, **64**, pp31-43

Boyd T. J. M. and Sanderson J. J., 1969, ‘Plasma Dynamics’, Thomas Nelson & Sons

Boyd T.J.M. and Sanderson J.J., 2003, ‘The Physics of Plasmas’, Cambridge University Press

Bratman V.L., Cross A.W., Denisov G.G., He W., Phelps A.D.R, Ronald K., Samsonov S.V., Whyte C.G. and Young A.R., 2000, 'High-gain wide-band gyrotron travelling wave amplifier with a helically corrugated waveguide', Phys Rev Lett, **84**, pp2746-2749

Burinskaya T.M. and Rauch J.L., 2007, ‘Waveguide regime of cyclotron maser instability in plasma regions of depressed density’, Plasma Physics Reports, **33**, pp28-37

Cairns R.A., Speirs D.C., Ronald K., Vorgul I., Kellett B.J., Phelps A.D.R. and Bingham R., 2005, ‘A cyclotron maser instability with application to space and laboratory plasmas’, Physica Scripta, **T116**, pp23-26

Calvert W., 1981, ‘The Auroral Density Cavity’, Geophysical Research Letters, **8**, pp919-921

Calvert W., 1982, ‘A feedback model for the source of auroral kilometric radiation’, Journal of Geophysical Research-Space Physics, **87**, pp8199-8214

Carlson C.W., Pfaff R.F. and Watzin J.G., 1998, ‘The Fast auroral snapshot (FAST) mission’, Geophysical Research Letters, **25**, pp2013-2016

Chambers A., Fitch R.K. and Halliday B.S., 1998, ‘Basic Vacuum Technology’, 2nd Ed, IoP Publishing

Chapman B., 1980, ‘Glow Discharge Processes-sputtering and plasma etching’, John Wiley & Sons

Chen F.F., 1974, ‘Introduction to Plasmas Physics and Controlled Fusion’, Vol. **1**, 2nd Ed, Plenum Press

Chu K.R., 1978, ‘Theory of electron cyclotron maser interaction in a cavity at the harmonic frequencies’, Physics of Fluids, **21**, pp2354-2364

Chu K.R., 2004, ‘The electron cyclotron maser’, Reviews of Modern Physics, **76**, pp489-540

Chu K.R. and Lin A.T., 1988, ‘Gain and Bandwidth of the Gyro-TWT and CARM Amplifiers’, IEEE transactions on plasma science, **16**, pp90-104

Collin R.E., 2001, 'Foundations for Microwave Engineering' 2nd Ed., John Wiley & Sons

Cooke S.J., Cross A.W., He W. and Phelps A.D.R, 1996, ‘Experimental operation of a cyclotron autoresonance maser oscillator at the second harmonic’, Phys. Rev. Lett., **77**, pp4836-4839

Cross A.W., 1965, 'Experimental Microwaves' W.H. Sanders

Cross A.W., Spark S.N. and Phelps A.D.R., 1995, ‘Gyrotron experiments using cavities of different ohmic-Q’, Int. J. Electronics, **79**, pp481-493

Delory G.T., Ergun R.E., Carlson C.W., Muschietti L., Chaston C.C., Peria W. and McFadden J.P., 1998, 'FAST observations of electron distributions within AKR source regions', Geophysical Research Letters, **25**, no 12, pp2069-2072

Denisov G.G., Bratman V.L., Cross A.W., He W., Phelps A.D.R., Ronald K., Samsonov S.V. and Whyte C.G., 1998, 'Gyrotron travelling wave amplifier with a helical interaction waveguide', Phys. Rev. Lett., **81**, pp5680-5683

Diver D.A., 2001, 'A Plasma Formulary for Physics, Technology, and Astrophysics', WILEY-VCH

Dunckel N., Ficklin B., Rorden L. and Helliwel R.A., 1970, 'Low-frequency noise observed in distant magnetosphere with ogo-1', Journal of Geophysical Research, **75**, pp1854-1863

Ergun R.E., Carlson C.W., McFadden J.P., Mozer F.S., Delory G.T., Peria W., Chaston C.C., Temerin M., Elphic R., Strangeway R., Pfaff R., Cattell C.A., Klumpar D., Shelly E., Peterson W., Moebius E. and Kistler L., 1998, 'FAST satellite wave observations in the AKR source region', Geophysical Research Letters, **25**, 2061-2064

Ergun R.E., Carlson C.W., McFadden J.P., Delory G.T., Strangeway R.J. and Pritchett P.L., 2000, 'Electron-cyclotron maser driven by charged-particle acceleration from magnetic field-aligned electric fields', The Astrophysical Journal, **538**, pp456-466

Flyagin V.A., Gapanov A.V., Petelin M.I. and Yulpatov V.K., 1977, 'The Gyrotron', IEEE Transactions on microwave theory and techniques, **MTT 25**, pp514-521

Garven M., Spark S.N., Cross A.W., Cooke S.J. and Phelps A.D.R., 1996, 'Gyrotron Experiments Employing a Field Emission Array Cathode', Phys Review Letters, **77**, pp2320-2323

Gillespie K.M., Speirs D.C., Ronald K., McConville S.L., Phelps A.D.R., Bingham R., Cross A.W., Robertson C.W., Whyte C.G., He W., Vorgul I., Cairns R.A. and Kellett B.J., 2008, '3D PiC code simulations for a laboratory experimental investigation of Auroral Kilometric Radiation mechanisms', Plasma Physics and Controlled Fusion, 50, pp1-11

Gilmour A.S. (Jnr.), 1986, 'Microwave Tubes', Artech House

Ginzburg N.S., Peskov N. Yu., Phelps A.D.R., Cross A.W., He W. and Winning P., 1996, 'Theoretical and experimental studies of a Ka-band free electron laser with a guide magnetic field', Digest of the 23rd Annual Plasma Physics Conference (IoP) Crieff (Scotland), pp17

Golio M., (Ed), 2001, 'The RF and Microwave Handbook' CRC Press

Granatstein V.L. and Alexeff I., (Eds), 1987, 'High-Power Microwave Sources', Artech House

Green J.L., Gurnett D.A. and Shawhan S.D., 1977, 'The angular distribution of auroral kilometric radiation', Journal of Geophysical Research, **82**, pp1825-1838

Gurnett D.A., 1974, 'Earth as a radio-source - terrestrial kilometric radiation', Journal of Geophysical Research, **79**, pp4227-4238

Gurnett D.A. and Green J.L., 1978, 'Polarization and origin of auroral kilometric radiation', Journal of Geophysical Research, **83**, pp689-696

Healea M. and Houtermans C., 1940, 'The Relative Secondary Electron Emission due to He, Ne and A Ions Bombarding a Hot Nickel Target', Physical Review, **58**, pp608-610

Hill A.G., Buechner W.W., Clark J.S. and Fisk J.B., 1939, ‘The Emission of Secondary Electrons Under High Energy Positive Ion Bombardment’, Physical Review, **55**, pp463-470

Howatson A.M., ‘An introduction to gas discharges’, 2nd Ed, 1976, Pergamon Press

Huddlestone R.H. and Leonard S.L., ‘Plasma Diagnostic Techniques’, 1965, Academic Press

Humphries A.Jr., ‘Charged Particle Beams’, 1990, John Wiley and Sons

Kaiser M.L., Alexander J.K., Riddle A.C., Pearce J.B and Warwick J.W, 1978, ‘Direct measurements by voyager 1 and voyager 2 of polarisation of terrestrial kilometric radiation’, Geophysical Research Letters, **5**, pp857-860

Kellett B.J., Graffagnino V.T., Bingham R., Muxlow T.W.B. and Gunn A.G., 2007, ‘CU Virginis - The first stellar pulsar’, arXiv: astro-ph/0701214

Koch R., 2006, ‘Wave particle interactions in plasmas’, Plasma Physics and Controlled Fusion, **48**, pp229-345

Konoplev I.V and Phelps A.D.R., 2000, ‘High-gain compton free electron laser driven by pre-bunched electrons’, Physics of Plasmas, **7**, pp4280-4290

Kukreja V., 2005, 'Field-Emission Properties in the ERL-Electron Source', pp1-11

Latham R.V., 1983, 'Prebreakdown Electron Emission', IEEE Trans. on Electrical Insulation, EI-18, pp194-203

Lawson J.D., 1988, ‘The Physics of charged-particle beams’, 2nd Ed, Clarendon Press

Llewellyn-Jones F., 1957, ‘Ionization and Breakdown in Gases’, Chapman & Hall Ltd.

Lorrain P., Corson D.P. and Lorrain F., 1988, 'Electromagnetic Fields and Waves', Freeman

Louarn P., Roux A., de Feraudy H. and Le Queau D., 1990, ‘Trapped electrons as a free energy source for the auroral kilometric radiation’, Journal of geophysical research, **95**, pp5983-5995

Mandl F., 1988, 'Statistical Physics', 2nd Ed, Wiley

McConville S.L., Speirs D.C., Ronald K., Phelps A.D.R., Cross A.W., Bingham R., Robertson C.W., Whyte C.G., He W., Gillespie K.M., Vorgul I., Cairns R.A. and Kellett B.J., 2008, ‘Demonstration of auroral radio emission mechanisms by laboratory experiment’, Plasma Physics and Controlled Fusion, **50**

Mellott M.M., Huff R.L. and Gurnett D.A., 1986, ‘DE-1 observations of harmonic auroral kilometric radiation’, Journal of geophysical research-space physics, **91**, pp3732-3738

Melrose D.B and Dulk G.A., 1982, ‘Electron cyclotron masers as the source of certain solar and stellar radio-bursts’, Astrophysical Journal, **259**, pp844-858

Mesyats G.A. and Proskurovsky D.I., 1989, 'Pulsed Electrical Discharge in Vacuum', Springer-Verlag

Miller R.B., 1998, ‘Mechanism of explosive electron emission for dielectric fibre (velvet) cathodes’, Journal of applied physics, **84**, pp3880-3889

Mutel R.L., Gurnett D.A. and Christopher I.W., 2004, ‘Spatial and temporal properties of AKR burst emission derived from Cluster WBD VLBI studies’ Annales Geophysicae, **22**, pp2625-2632

Nusinovich G.S., 2004, 'Introduction to the physics of Gyrotrons', John Hopkins University Press

Perraut S., de Feraudy H., Roux A., Decreau P.M.E, Paris J. and Matson L., 1990, ‘Density measurements in key regions of the Earth’s magnetosphere: cusp auroral region’, Journal of Geophysical Research, **95**, pp5997-6014

Petelin M.I., 1993, ‘Physics of advanced gyrotrons’, Plasma Physics and Controlled Fusion, **35**, pp343-351

Petelin M.I., 1999, ‘One century of cyclotron radiation’, IEEE transactions on plasma science, **27**, pp294-302

Pozar D.M., 1998, 'Microwave Engineering' 2nd Ed., John Wiley & Sons

Pritchett P.L. and Strangeway R.J., 1985, ‘A simulation study of kilometric radiation generation along an auroral field line’, Journal of Geophysical Research - Space Physics, **90**, pp9650-9662

Pritchett P.L., Strangeway R.J., Carlson C.W., Ergun R.E., McFadden J.P. and Delory G.T., 1999, Free energy sources and frequency bandwidth for the auroral kilometric radiation', Journal of Geophysical Research, **104**, pp10,317-10,326

Pritchett P.L., Strangeway R.J., Ergun R.E. and Carlson C.W., 2002, 'Generation and propagation of cyclotron maser emissions in the finite auroral kilometric radiation source cavity', Journal of Geophysical Research, **107**, pp13.1 - 13.17

Radmanesh M.M., 2001, 'Radio Frequency and Microwave Electronics Illustrated', Prentice Hall

Ronald K., 1996, Ph.D. Thesis, University of Strathclyde

Ronald K., Cross A.W., Phelps A.D.R., He W., Yin H. and Spark S.N., 1998, ‘Explosive cathode gyrotron experiments’, IEEE Trans. on Plasma Science, PS-26, pp375-382

Ronald K., McConville S.L., Speirs D.C., Phelps A.D.R., Robertson C.W., Whyte C.G., He W., Gillespie K.M., Cross A.W. and Bingham R., 2008, ‘Electron beam measurements for a laboratory simulation of auroral kilometric radiation’, Plasma Sources Science and Technology, **17**, pp1-8

Rostagni A., 1938, ‘On the Sensitivity of the Balanced Space Charge Method for Detecting Ionization of Gases by Collision of Ions and Atoms’, Physical Review, **53**, pp729-731

Roux A., Hilgers A., de Feraudy H., le Queau D., Louard P., Perraut S., Bahnsen A., Jespersen M., Ungstrup E. and Andre M., 1993, 'Auroral Kilometric Radiation sources: In Situ and Remote Observations From Viking', Journal of Geophysical Research, **98**, pp11,657-11,600

Sander K.F., 1987, 'Microwave Components and Systems', Addison-Wesley Publishing Company

Shawhan S.D and Gurnett D.A., 1982, ‘Polarization measurements of auroral kilometric radiation by dynamics explorer-1’, Geophysical Research Letters, **9**, pp913-916

Shiffler D.A., Ruebush M., Zagar D., LaCour M., Golby K., Clark M.C., Haworth M.D. and Umstattd R., 2002, ‘Emission Uniformity and Emittance of Explosive Field-Emission Cathodes’, IEEE Trans. on Plas. Sci, Vol.**30**, No.4, pp1592-1596

Somerville I.C., MacGregor S.J. and Farish O., 1990, 'An efficient stacked-Blumlein HV pulse generator', Meas. Sci. Technol., **1**, pp865-868

Speirs D.C., Vorgul I., Ronald K., Bingham R., Cairns R.A., Phelps A.D.R., Kellett B.J., Cross A.W., Whyte C.G and Robertson C., 2005, ‘A laboratory experiment to investigate auroral kilometric radiation emission mechanisms’, Journal of plasma physics, **71**, pp665-674

Speirs D.C., McConville S.L., Gillespie K.M., Ronald K., Phelps A.D.R., Cross A.W., Bingham R., Robertson C.W., Whyte C.G., Vorgul I., Cairns R.A. and Kellett B.J., 2008, ‘Numerical simulation of auroral cyclotron maser processes’, Plasma Physics and Controlled Fusion, **50**, pp1-15

Sprangle P. and Drobot A.T., 1977, 'The linear and self-consistent nonlinear theory of the electron cyclotron maser instability', IEEE trans. on microwave theory and techniques, vol. MTT-**25**, no.6

Sprangle P., Granatstein V.L. and Drobot A., 1977, ‘The electron cyclotron maser instability’, Journal de Physique, **12**, No. 38, pp135-152

Stix T.H., 1992, 'Waves in Plasmas', American Institute of Physics

Strangeway R.J., Kepkp L., Elphic R.C., Carlson C.W., Ergun R.E., McFadden J.P., Peria W.J., Delory G.T., Chaston C.C., Temerin M., Cattell C.A., Mobius E., Kistler L.M., Klumpar D.M., Peterson W.K., Shelley E.G and Pfaff R.F., 1998, ‘Fast observations of the VLF waves in the auroral zone: evidence of very low plasma densities’, Geophysical Review Letters, **25**, pp2065-2068

Twiss R.Q., 1985, ‘Radiation transfer and the possibility of negative absorption in radio astronomy’, Australian Journal of Physics, 11, pp564-579

Ungstrup E., Bahnsen A., Wong H.K., Andre M and Matson L., 1990, ‘Energy source and generation mechanism for auroral kilometric radiation’, Journal of Geophysical Research, **95**, pp5973-5981

von Engel A., 1983, ‘Electric Plasmas: Their Nature and Uses’, Taylor & Francis Ltd.

von Engel A., 1994, ‘Ionized gases’, American Institute of Physics

Vorgul I., Ronald K., Speirs D.C., Bingham R., Cairns R.A. and Phelps A.D.R., 2004, ‘Analysis of a cyclotron maser instability with application to space and laboratory plasmas’, 31st EPS Conference on Plasma Physics, **28G**, pp1-4

Vorgul I., Cairns R.A and Bingham R., 2005, ‘Analysis of a cyclotron maser instability in cylindrical geometry’, Physics of Plasmas, **12**, pp1-8

Woan G., 2000, 'The Cambridge Handbook of Physics Formulas' Cambridge University Press

Wu C.S. and Lee L.C., 1979, 'A theory of the terrestrial kilometric radiation', The Astrophysical Journal, **230**, pp621-626

Yin H., He W., Robb G.R.M., Phelps A.D.R., Ronald K. and Cross A.W., 1999, ‘Coherent microwave generation from a pseudospark cathode Cherenkov maser’, Phys. Rev. ST accel. Beams, 020701

Zarka P., Treumann R.A., Ryabov B.P. and Ryabov V.B., 2001, ‘Magnetically-driven planetary radio emissions and application to extrasolar planets’, Astrophysics and Space Science, **277**, pp293-300

Zimmermann T.M.G., Coppins M. and Allen J.E., 2009, ‘The effect of a magnetic field on a cylindrical object in a plasma’, Physics of Plasmas, **16**

Appendix 1 - Bounded Script

Sandra McConville - 1st March '07

This script will evaluate gain for our system using equations from Chu [K. R. Chu, 1988, "Gain and Bandwidth of the Gyro-TWT and CARM Amplifiers", IEEE trans on plas sci, vol 16, no2, pp90-104] all variables in SI units.

n in this case is the linear density, so in actual fact nb=n*A=I/Vz

```
> restart;

  hot_disp:=(-coupling)*(((((omega-kz*vz)*Tsm)-((kperp*vperp)*
  Usm))/((omega-kz*vz)-(s*omegac)))-(((betaperp^2*(omega^2-
  kz^2*c^2)*Hsm)/((omega-kz*vz)-(s*omegac))^2)))+(omega^2-c^2*
  (kz^2+kperp^2));
```

This section will deal with the expressions for the Bessel functions, f is the undifferentiated Bessel, g is the first dervative, h is the second derivative.

```
> f:=BesselJ(s,q); f1:=BesselJ(s-m,p); f2:=BesselJ(s1,q);
  f3:=BesselJ(s1-m,p); f4:=BesselJ(s2,q); f5:=BesselJ(s2-m,p)
  ;
  g:=diff(f,q); g1:=diff(f1,p);
  h:=diff(g,q); h1:=diff(g1,p);

  Hsm:=((f1)^2)*g^2;
  Tsm:=2*Hsm+(q*g)*((2*(f1^2)*h)-f*(((1/p)*f1*g1)+g1^2+f1*h1)
  );
  Usm:=(-0.5*q*g)*(f2*(((f3)^2)-((f1)^2))+(f4*((f5^2)-(f1^2))
  ));

  coupling:=(nb*e^2)/(Pi*r^2*mo*gam*K*epsi0):

  K:=((BesselJ(m,mu))^2)*(1-m^2/mu^2):
```

The following section will define variable needed for the equations. To get Hsm and Tsm and Usm for the equation we need to define and evaluate the Bessel functions as above.

```
> freq:=4.42e9; c:=3e8; r:=.0414; m:=0; mu:=3.832; mo:=
  9.11e-31; e:=1.602e-19; beamvolt:=75e3; B:=0.18; curr:=34;
  alpha:=1.5; epsi0:=8.854e-12; rc:=0.01;
```

The following bits of code define expressions for further variables using those defined above.

```
> nb:=curr/(e*vz); omegap:=((nb*e^2)/(mo*epsi0))^0.5; gam:= 1+(
  (e*beamvolt)/(mo*c^2)); v:=c*(1-1/gam^2)^0.5; vz:=v/(
  (alpha^2+1)^0.5); vperp:=alpha*vz; kperp:=mu/r; omegac:=(e*B)
  /(gam*mo); betaperp:=vperp/c; rL:=(gam*mo*vperp)/(e*B); s:=1;
  s1:=s-1; s2:=s+1; p:=kperp*rc; q:=kperp*rL;
```

The next line of code is to try and plot kz against omega.

```
> free_disp:=omega-c*kz;
  cold_disp:=omega-c*(kperp^2+kz^2)^0.5;
  beam_disp:=omega-s*omegac-kz*vz;

  Tsm;
  coupling;
  evalf(coupling);
  K;

  with(plots):
  implicitplot([hot_disp, cold_disp, beam_disp, free_disp], kz=
  -150..150, omega=2.1e10..3.8e10, title="Dispersion for Gain",
  color=[black, green, red, magenta], labels=[kz,'omega'],
  legend=["hot_disp", "cold_disp", "beam_disp", "free_disp"],
  numpoints=200000,titlefont=[TIMES, BOLD, 12], font=[TIMES,
  BOLD, 10], labelfont=[TIMES, BOLD, 12]);
```

```
> omegamin:=2.1e10; omegamax:=3.9e10; resomega:=1200;
  kzmin:=-1500; kzmax:=1500; reskz:=120;

  stepomega:=(omegamax-omegamin)/(resomega);
  stepkz:=(kzmax-kzmin)/(reskz-1);

  dispomega:=Array(1..resomega, 1..5);
  dispkz:=Array(1..reskz, 1..5);

  curve:=(hot_disp)*((omega-kz*vz)-(s*omegac))^2;
  curve2:=simplify(curve):
  simplify(curve):
```

The next expression is the equation from Chu, using the values and expressions coded above.

```
> counter:=1;
```

```
for omega from omegamin by stepomega to omegamax do
'omega'=omega;
fsolve(curve2,kz,complex);
answer:=%:
dispomega[counter,1]:=answer[1]; dispomega[counter,2]:=answer
[2]; dispomega[counter,3]:=answer[3]; dispomega[counter,4]:=
answer[4]; dispomega[counter,5]:=omega:
counter:=counter+1;
end do:

with(plots):

pointsRe:=seq([Re(dispomega[counters,1]),dispomega[counters,
5]],counters=1..resomega), seq([Re(dispomega[counters,2]),
dispomega[counters,5]],counters=1..resomega), seq([Re
(dispomega[counters,3]),dispomega[counters,5]],counters=1..
resomega), seq([Re(dispomega[counters,4]),dispomega[counters,
5]],counters=1..resomega):

pointsIm:=seq([1*Im(dispomega[counters,1]),dispomega
[counters,5]],counters=1..resomega), seq([1*Im(dispomega
[counters,2]),dispomega[counters,5]],counters=1..resomega),
seq([1*Im(dispomega[counters,3]),dispomega[counters,5]],
counters=1..resomega), seq([1*Im(dispomega[counters,4]),
dispomega[counters,5]],counters=1..resomega):

points:={pointsRe, pointsIm}:

pointplot(points, color=red, symbol=point, labels=[kz,
'omega'], title="Real and Imaginary roots of kz" ,titlefont=
[TIMES, BOLD, 12], font=[TIMES, BOLD, 10], labelfont=[TIMES,
BOLD, 12]);



> unassign('omega');

counters:=1;

for kz from kzmin by stepkz to kzmax do
'kz'=kz;
fsolve(curve2,omega,complex);
```

```
answer:=%:
dispkz[counters,1]:=answer[1]: dispkz[counters,2]:=answer[2]:
dispkz[counters,3]:=answer[3]: dispkz[counters,4]:=answer[4]:
dispkz[counters,5]:=kz:
counters:=counters+1;
end do:

with(plots):

pointsRe:=seq([dispkz[counters,5], Re(dispkz[counters,1])],
counters=1..reskz), seq([dispkz[counters,5], Re(dispkz
[counters,2])],counters=1..reskz), seq([dispkz[counters,5],
Re(dispkz[counters,3])],counters=1..reskz), seq([dispkz
[counters,5], Re(dispkz[counters,4])],counters=1..reskz):

pointsIm:=seq([dispkz[counters,5], Im(dispkz[counters,1])],
counters=1..reskz), seq([dispkz[counters,5], Im(dispkz
[counters,2])],counters=1..reskz), seq([dispkz[counters,5],
Im(dispkz[counters,3])],counters=1..reskz), seq([dispkz
[counters,5], Im(dispkz[counters,4])],counters=1..reskz):

points:={pointsRe, pointsIm}:

pointplot(points, color=red, symbol=point, labels=['kz',
omega], title="Real and Complex roots of omega", titlefont=
[TIMES, BOLD, 12], font=[TIMES, BOLD, 10], labelfont=[TIMES,
BOLD, 12]);
```

```
> unassign('p'); unassign('q'); unassign('s'); unassign('m');
  s:=1;
  m:=0;
  plot3d(Hsm,p=0..10,q=0..1);
```

```
> unassign('p'); unassign('q');unassign('s');
  s:=2;
  plot3d(Hsm,p=0..12,q=0..2);
```

```
> unassign('p'); unassign('q');unassign('s');
  s:=3;
  plot3d(Hsm,p=0..12,q=0..3);
```

```
> unassign('p'); unassign('q');unassign('s');
  s:=4;
```

Appendix 2 - Unbounded Script

Sandra McConville - 1st March '07

This code is to plot the free dispersion of a waveguide, using an example from the Sprangle & Drobot paper.

```
> restart;
```

The free dispersion expression will be given below before any variables are introduced to make sure that it is written correctly.

```
> hot_disp:=(omegap^2/gam)*(((omega-kz*vz)/((omega-kz*vz)-(s*
  omegac)))+(((kz^2*vperp^2*(1-omega^2/(kz^2*c^2)))/(2*((omega-
  kz*vz)-(s*omegac))^2))))-omega^2+kz^2*c^2;
  free_disp:=omega^2-c^2*kz^2;
  beam_disp:=omega-s*omegac-kz*vz;
```

The follwing section defines the set variables needed to compute the above expression.

```
> c:=3e8; e:=1.602e-19; mo:=9.11e-31; epsi0:=8.854e-12; r:=
  .0115;
```

This section deals with variables which may, throughout the experiment, be varied.

```
> beamvolt:=10e3; B:=12e-6; curr:=20e-6; alpha:=0.5; mu:=3.832;
  s:=1;
```

This setion deals with smaller expressions needed to obtain more variables required to get the free dispersion.

```
> gam:= 1+((e*beamvolt)/(mo*c^2)); v:=c*(1-1/gam^2)^0.5; vz:=v/
  ((alpha^2+1)^0.5); vperp:=alpha*vz; omegac:=(e*B)/(gam*mo);
  betaperp:=vperp/c; nb:=curr/(e*vz); omegap:=((nb*e^2)/(mo*
  epsi0))^0.5;
```

Now to plot the free space coupled mode dispersion

```
> free_disp;hot_disp;beam_disp;

  with(plots):
  implicitplot([hot_disp, free_disp, beam_disp], kz=-0.01.
  .0.01, omega=1.5e6..2.8e6, color=[black, green, blue],
  numpoints=2000000);
```

Now to get the Re and Im roots of this dispersion

```
> omegamin:=1.4e6; omegamax:=2.4e6; resomega:=240;
  kzmin:=-300; kzmax:=300; reskz:=120;

  stepomega:=(omegamax-omegamin)/(resomega);
```

```
stepkz:=(kzmax-kzmin)/(reskz);

dispomega:=Array(1..resomega, 1..5);
dispkz:=Array(1..reskz, 1..5);

curve:=(hot_disp)*((omega-kz*vz)-(s*omegac))^2;
curve2:=simplify(curve):
simplify(curve):

> counter:=1;

for omega from omegamin by stepomega to omegamax do
'omega'=omega;
fsolve(curve2,kz,complex);
answer:=%:
for counter2 from 1 by 1 to 4 do
dispomega[counter, counter2]:=answer[counter2]
end do;
dispomega[counter,5]:=omega:
counter:=counter+1;
end do:

with(plots):

pointsRe:=seq([Re(dispomega[counters,1]),dispomega[counters,
5]],counters=1..resomega), seq([Re(dispomega[counters,2]),
dispomega[counters,5]],counters=1..resomega), seq([Re
(dispomega[counters,3]),dispomega[counters,5]],counters=1..
resomega), seq([Re(dispomega[counters,4]),dispomega[counters,
5]],counters=1..resomega):

pointsIm:=seq([10*Im(dispomega[counters,1]),dispomega
[counters,5]],counters=1..resomega), seq([10*Im(dispomega
[counters,2]),dispomega[counters,5]],counters=1..resomega),
seq([10*Im(dispomega[counters,3]),dispomega[counters,5]],
counters=1..resomega), seq([10*Im(dispomega[counters,4]),
dispomega[counters,5]],counters=1..resomega):

points:={pointsRe, pointsIm}:

pointplot(points, color=red, symbol=point, labels=[kz,
'omega'], title="Real and Imaginary roots of kz" ,titlefont=
```

```
  [TIMES, BOLD, 12], font=[TIMES, BOLD, 10], labelfont=[TIMES,
  BOLD, 12]);

> unassign('omega');

  counters:=1;

  for kz from kzmin by stepkz to kzmax do
  'kz'=kz;
  fsolve(curve2,omega,complex);
  answer:=%:
  dispkz[counters,1]:=answer[1]: dispkz[counters,2]:=answer[2]:
  dispkz[counters,3]:=answer[3]: dispkz[counters,4]:=answer[4]:
  dispkz[counters,5]:=kz:
  counters:=counters+1;
  end do:

  with(plots):

  pointsRe:=seq([dispkz[counters,5], Re(dispkz[counters,1])],
  counters=1..reskz), seq([dispkz[counters,5], Re(dispkz
  [counters,2])],counters=1..reskz), seq([dispkz[counters,5],
  Re(dispkz[counters,3])],counters=1..reskz), seq([dispkz
  [counters,5], Re(dispkz[counters,4])],counters=1..reskz):

  pointsIm:=seq([dispkz[counters,5], Im(dispkz[counters,1])],
  counters=1..reskz), seq([dispkz[counters,5], Im(dispkz
  [counters,2])],counters=1..reskz), seq([dispkz[counters,5],
  Im(dispkz[counters,3])],counters=1..reskz), seq([dispkz
  [counters,5], Im(dispkz[counters,4])],counters=1..reskz):

  points:={pointsRe, pointsIm}:

  pointplot(points, color=red, symbol=point, labels=['kz',
  omega], title="Real and Complex roots of omega", titlefont=
  [TIMES, BOLD, 12], font=[TIMES, BOLD, 10], labelfont=[TIMES,
  BOLD, 12]);
```

Appendix 3 - Magnetic Field Configuration Script

Sandra McConville - 26-9-9

This script is used to calculate and plot the resultant axial magnetic field due to a set of finite coils. The coils are unlimited in number and are specified in terms of their geometries, currents and relative axial positions. The script is very useful for the purpose of tuning for a specific magnetic field profile in experiment. * It can also generate a space delimited data file of the axial magnetic field profile for importation into PIC code modelling packages such as KARAT or Magic ----------*In the process of being added*
First the script parameters are cleared / initialised :-

```
> restart;
```

The properties and positions of each individual solenoid are now consecutively specified. A unique numerical index is used to identify parameters associated with a specific solenoid. Solenoid 1 is set

Solenoid 1

```
> A1:=40;N1:=143;M1:=N1;L1:=0.5;dz1:=1;LA1:=4;Ri1:=0.105;Ro1:=
  (Ri1+LA1/M1);R1:=(Ri1+Ro1)/2;
```

Solenoid 2

```
> A2:=30;N2:=143;M2:=N2;L2:=0.45;dz2:=dz1-L1/2-L2/2;LA2:=2;Ri2:=
  0.105;Ro2:=(Ri2+LA2/M2);R2:=(Ri2+Ro2)/2;
```

Solenoid 3

```
> A3:=210;N3:=143;M3:=N3;L3:=0.5;dz3:=dz1+L1/2+L3/2;LA3:=10;Ri3:=
  0.05;Ro3:=(Ri3+LA3/M3);R3:=(Ri3+Ro3)/2;
```

Solenoids 4 and 5, shimming solenoids to extend the flat central field portion of the main solenoid 3, Solenoid 6, mirroring solnoid for diagnostics,

```
> A4:=160;N4:=143;M4:=N4;L4:=0.11;dz4:=dz1+L1/2+L4/2;LA4:=2;Ri4:=
  Ro3;Ro4:=(Ri4+LA4/M4);R4:=(Ri4+Ro4)/2;A5:=A3;N5:=N4;M5:=N5;L5:=
  L4;dz5:=dz1+L1/2+L3-L5/2;LA5:=2;Ri5:=Ro3;Ro5:=(Ri5+LA5/M5);R5:=
  (Ri5+Ro5)/2;A6:=0;N6:=N4;M6:=N5;L6:=0.25;dz6:=dz3;LA6:=4;Ri6:=
  Ro3;Ro6:=(Ri6+LA6/M6);R6:=(Ri6+Ro6)/2;
> b:=(mu*A*N/2)*(((L/2-(l-dz))/sqrt(R^2+(L/2-(l-dz))^2))-((-L/2-
  (l-dz))/sqrt(R^2+(-L/2-(l-dz))^2)));
> B:=M*integrate(b,R=Ri..Ro);
> mu:=Pi*4E-7;
  B1:=eval(B,[A=A1,N=N1,M=M1,L=L1,dz=dz1,LA=LA1,Ri=Ri1,Ro=Ro1,R=
  R1]);
> lim1:=-L1/2+dz1;lim2:=L1/2+dz1;
  plot(B1,l=lim1..lim2);

> B2:=eval(B,[A=A2,N=N2,M=M2,L=L2,dz=dz2,LA=LA2,Ri=Ri2,Ro=Ro2,R=
  R2]);
> lim3:=-L2/2+dz2;lim4:=L2/2+dz2;
  plot(B2,l=lim3..lim4);
```

```
> B3:=eval(B,[A=A3,N=N3,M=M3,L=L3,dz=dz3,LA=LA3,Ri=Ri3,Ro=Ro3,R=
  R3]);
> B4:=eval(B,[A=A4,N=N4,M=M4,L=L4,dz=dz4,LA=LA4,Ri=Ri4,Ro=Ro4,R=
  R4]);
> B5:=eval(B,[A=A5,N=N5,M=M5,L=L5,dz=dz5,LA=LA5,Ri=Ri5,Ro=Ro5,R=
  R5]);
> B6:=eval(B,[A=A6,N=N6,M=M6,L=L6,dz=dz6,LA=LA6,Ri=Ri6,Ro=Ro6,R=
  R6]);
> lim5:=-L3/2+dz3;lim6:=L3/2+dz3;
  plot(B3+B4+B5,l=lim5..lim6);

> lim5:=-L3/2+dz3;lim6:=L3/2+dz3;
  plot(B3+B4+B5+B6,l=lim5..lim6);

> Btot:=B1+B2+B3+B4+B5+B6;
> plot(Btot,l=0..lim6);fieldmax:=eval(Btot,l=1.5);evalf(fieldmax);
  gunfield:=eval(Btot, l=0.43);evalf(gunfield);evalf
  (fieldmax/gunfield);
```

Work out limiting Larmor step and radius as a function of z from Btot and the electron energy (V), assume alpha is zero for Larmor step and infintie for Larmor radius

```
> ce:=1.6E-19;me:=9.11E-31;cl:=3E8;V:=100000;gmma:=1+ce*V/(me*
  cl^2);ve:=cl*sqrt((1-1/gmma^2));freq:=ce*Btot/(2*3.1416*gmma*me)
  ;Lz:=ve/freq;Lr:=ve/(2*3.1416*freq);plot([Lz,Lr],l=lim3..lim6,
  color=[red,green]);plot((diff(Btot,l))*(Lz/Btot),l=lim3..lim6);
```

Write out the data for Bz on axis to a file called Bz for Karat and or Magic, file format is [axial location/cm,field/G]

```
> stepno:=1;steps:=87;minz:=0;maxz:=2.8;stepsize:=(maxz-minz)
  /steps;
  fopen("C:/Documents and Settings/Sandra
  McConville/Desktop/maple/BWO and KARAT/Bz",WRITE,TEXT);
  printlevel:=0;
  for step from minz by stepsize to maxz do
  fprintf("C:/Documents and Settings/Sandra
  McConville/Desktop/maple/BWO and KARAT/Bz","%d\t%f\t%f\n",
  stepno,evalf(step*100),eval(10000*Btot,l=step));
  stepno:=stepno+1;
  end do;
  fprintf("C:/Documents and Settings/Sandra
  McConville/Desktop/maple/BWO and KARAT/Bz","%d\t%d\t%f\n",
  stepno,-999,0);fclose("C:/Documents and Settings/Sandra
  McConville/Desktop/maple/BWO and KARAT/Bz");printlevel:=1;
```

Solenoid 1

```
> R:=R1*100;Z:=dz1*100;dR:=LA1*0.007*100;dZ:=L1*100;N:=L1/0.007;
  A:=LA1*A1;
```

Solenoid 2

```
> R:=R2*100;Z:=dz2*100;dR:=LA2*0.007*100;dZ:=L2*100;N:=L2/0.007;
  A:=LA2*A2;
```

Solenoid 3

```
> R:=R3*100;Z:=dz3*100;dR:=LA3*0.007*100;dZ:=L3*100;N:=L3/0.007;
  A:=LA3*A3;
```

Solenoid 4

```
> R:=R4*100;Z:=dz4*100;dR:=LA4*0.007*100;dZ:=L4*100;N:=L4/0.007;
  A:=LA4*A4;
```

Solenoid 5

```
> R:=R5*100;Z:=dz5*100;dR:=LA5*0.007*100;dZ:=L5*100;N:=L5/0.007;
  A:=LA5*A5;
```

Solenoid 6

```
> R:=R6*100;Z:=dz6*100;dR:=LA6*0.007*100;dZ:=L6*100;N:=L6/0.007;
  A:=LA6*A6;
```

Solenoid1- Solenoid6

```
> counter1:=1;
  print (solenoid, counter1);
  R:=R1*100;Z:=dz1*100;dR:=LA1*0.007*100;dZ:=L1;N:=L1/0.007;A:=
  LA1*A1;
  counter1:=counter1+1;
  print (solenoid, counter1);R:=R2*100;Z:=dz2*100;dR:=LA2*0.007*
  100;dZ:=L2;N:=L2/0.007;A:=LA2*A2;
  counter1:=counter1+1;
  print (solenoid, counter1);R:=R3*100;Z:=dz3*100;dR:=LA3*0.007*
  100;dZ:=L3;N:=L3/0.007;A:=LA3*A3;
  counter1:=counter1+1;
  print (solenoid, counter1);R:=R4*100;Z:=dz4*100;dR:=LA4*0.007*
  100;dZ:=L4;N:=L4/0.007;A:=LA4*A4;
  counter1:=counter1+1;
  print (solenoid, counter1);R:=R5*100;Z:=dz5*100;dR:=LA5*0.007*
  100;dZ:=L5;N:=L5/0.007;A:=LA5*A5;
  counter1:=counter1+1;
  print (solenoid, counter1);R:=R6*100;Z:=dz6*100;dR:=LA6*0.007*
  100;dZ:=L6;N:=L6/0.007;A:=LA6*A6;
> stepno:=1;steps:=6;minz:=1;maxz:=6;stepsize:=(maxz-minz)/steps;
  fopen("C:/Documents and Settings/Sandra
  McConville/Desktop/maple/BWO and KARAT/Solenoid",WRITE,TEXT);
  printlevel:=0;
  counter1:=1;
```

```
print (solenoid, counter1);
R:=R1*100;Z:=dz1*100;dR:=LA1*0.007*100;dZ:=L1*100;N:=trunc
(L1/0.007);A:=LA1*A1;
fprintf("C:/Documents and Settings/Sandra
McConville/Desktop/maple/BWO and KARAT/Solenoid",
"%d\t%f\t%f\t%f\t%f\t%f\t%f\n",stepno, R, Z, dR, dZ, N, A, l=
step);
stepno:=stepno+1;
counter1:=counter1+1;
print (solenoid, counter1);R:=R2*100;Z:=dz2*100;dR:=LA2*0.007*
100;dZ:=L2*100;N:=trunc(L2/0.007);A:=LA2*A2;
fprintf("C:/Documents and Settings/Sandra
McConville/Desktop/maple/BWO and KARAT/Solenoid",
"%d\t%f\t%f\t%f\t%f\t%f\t%f\n",stepno, R, Z, dR, dZ, N, A, l=
step);
stepno:=stepno+1;
counter1:=counter1+1;
print (solenoid, counter1);R:=R3*100;Z:=dz3*100;dR:=LA3*0.007*
100;dZ:=L3*100;N:=trunc(L3/0.007);A:=LA3*A3;
fprintf("C:/Documents and Settings/Sandra
McConville/Desktop/maple/BWO and KARAT/Solenoid",
"%d\t%f\t%f\t%f\t%f\t%f\t%f\n",stepno, R, Z, dR, dZ, N, A, l=
step);
stepno:=stepno+1;
counter1:=counter1+1;
print (solenoid, counter1);R:=R4*100;Z:=dz4*100;dR:=LA4*0.007*
100;dZ:=L4*100;N:=trunc(L4/0.007);A:=LA4*A4;
fprintf("C:/Documents and Settings/Sandra
McConville/Desktop/maple/BWO and KARAT/Solenoid",
"%d\t%f\t%f\t%f\t%f\t%f\t%f\n",stepno, R, Z, dR, dZ, N, A, l=
step);
stepno:=stepno+1;
counter1:=counter1+1;
print (solenoid, counter1);R:=R5*100;Z:=dz5*100;dR:=LA5*0.007*
100;dZ:=L5*100;N:=trunc(L5/0.007);A:=LA5*A5;
fprintf("C:/Documents and Settings/Sandra
McConville/Desktop/maple/BWO and KARAT/Solenoid",
"%d\t%f\t%f\t%f\t%f\t%f\t%f\n",stepno, R, Z, dR, dZ, N, A, l=
step);
stepno:=stepno+1;
counter1:=counter1+1;
print (solenoid, counter1);R:=R6*100;Z:=dz6*100;dR:=LA6*0.007*
```

```
100;dZ:=L6*100;N:=trunc(L6/0.007);A:=LA6*A6;
fprintf("C:/Documents and Settings/Sandra
McConville/Desktop/maple/BWO and KARAT/Solenoid",
"%d\t%f\t%f\t%f\t%f\t%f\t%f\n",stepno, R, Z, dR, dZ, N, A, l=
step);
stepno:=stepno+1;
fprintf("C:/Documents and Settings/Sandra
McConville/Desktop/maple/BWO and KARAT/Solenoid","%d\t%d\t%f\n",
stepno,-999,0);fclose("C:/Documents and Settings/Sandra
McConville/Desktop/maple/BWO and KARAT/Solenoid");printlevel:=1;
```

Solenoid 2

```
> totallength2:=0;
for counter2 from 1 by 1 to LA2 do
print (layer_sol2,counter2);
wirelength2:=L2*N2*(2*Pi*(Ri2+((counter2-1)*(1/M2))+(1/(2*M2))))
;
numwires2:=wirelength2/25;
print (number_of_wires, evalf(numwires2));
totallength2:=totallength2+wirelength2;
end do;
```

Solenoid 3

```
> totallength3:=0;
for counter3 from 1 by 1 to LA3 do
print (layer_sol3,counter3);
wirelength3:=L3*N3*(2*Pi*(Ri3+((counter3-1)*(1/M3))+(1/(2*M3))))
;
numwires3:=wirelength3/27;
print (number_of_wires, evalf(numwires3));
totallength3:=totallength3+wirelength3;
end do;
```

Solenoid 4

```
> totallength4:=0;
for counter4 from 1 by 1 to LA4 do
print (layer_sol4,counter4);
wirelength4:=L4*N4*(2*Pi*(Ri4+((counter4-1)*(1/M4))+(1/(2*M4))))
;
numwires4:=wirelength4/27;
print (number_of_wires, evalf(numwires4));
totallength4:=totallength4+wirelength4;
end do;
```

Solenoid 5

```
> totallength5:=0;
```

```
for counter5 from 1 by 1 to LA5 do
print (layer_sol5,counter5);
wirelength5:=L5*N5*(2*Pi*(Ri5+((counter5-1)*(1/M5))+(1/(2*M5))))
;
numwires5:=wirelength5/27;
print (number_of_wires, evalf(numwires5));
totallength5:=totallength5+wirelength5;
end do;
```

Solenoid 6

```
> totallength6:=0;
for counter1 from 1 by 1 to LA1 do
print (layer_sol6,counter1);
wirelength1:=L6*N6*(2*Pi*(Ri6+((counter1-1)*(1/M6))+(1/(2*M6))))
;
numwires1:=wirelength1/10;
print (number_of_wires, evalf(numwires1));
totallength6:=totallength6+wirelength1;
end do;
```

Net small-bore conductor length required

```
> multisolenoid_conductor_length:=totallength1+totallength2+
totallength3+totallength4+totallength5+totallength6;
```

Power dissipation

Common Parameters

```
> Rwi:=0.00125;Rwo:=0.0026;
```

Solenoid 1

```
> totalresistanceA1:=evalf(totallength1*0.0313/28.6);
totalresistanceA1HOT:=evalf(totallength1*0.0363/28.6);
totalresistanceB1:=(1.724E-8)*totallength1/(Pi*(Rwo^2-Rwi^2));
totalresistanceB1HOT:=(1.16*1.724E-8)*totallength1/(Pi*(Rwo^2-
Rwi^2));drivevoltageA1:=evalf(totalresistanceA1*A1);
drivevoltageA1HOT:=evalf(totalresistanceA1HOT*A1);
drivevoltageB1:=evalf(totalresistanceB1*A1);drivevoltageB1HOT:=
evalf(totalresistanceB1HOT*A1);totalpowerA1:=drivevoltageA1*A1;
totalpowerA1HOT:=drivevoltageA1HOT*A1;totalpowerB1:=
drivevoltageB1*A1;totalpowerB1HOT:=drivevoltageB1HOT*A1;
Vol_sol1:=totallength1*Pi*(Rwo^2-Rwi^2);totalweight_sol1:=evalf
(8.89E3*evalf(Vol_sol1));
```

Solenoid 2

```
> totalresistanceA2:=evalf(totallength2*0.0313/28.6);
totalresistanceA2HOT:=evalf(totallength2*0.0363/28.6);
totalresistanceB2:=(1.724E-8)*totallength2/(Pi*(Rwo^2-Rwi^2));
```

```
totalresistanceB2HOT:=(1.16*1.724E-8)*totallength2/(Pi*(Rwo^2-
Rwi^2));drivevoltageA2:=evalf(totalresistanceA2*A2);
drivevoltageA2HOT:=evalf(totalresistanceA2HOT*A2);
drivevoltageB2:=evalf(totalresistanceB2*A2);drivevoltageB2HOT:=
evalf(totalresistanceB2HOT*A2);totalpowerA2:=drivevoltageA2*A2;
totalpowerA2HOT:=drivevoltageA2HOT*A2;totalpowerB2:=
drivevoltageB2*A2;totalpowerB2HOT:=drivevoltageB2HOT*A2;
Vol_sol2:=totallength2*Pi*(Rwo^2-Rwi^2);totalweight_sol2:=evalf
(8.89E3*evalf(Vol_sol2));
```

Solenoid 3

```
> totalresistanceA3:=evalf(totallength3*0.0313/28.6);
totalresistanceA3HOT:=evalf(totallength3*0.0363/28.6);
totalresistanceB3:=(1.724E-8)*totallength3/(Pi*(Rwo^2-Rwi^2));
totalresistanceB3HOT:=(1.16*1.724E-8)*totallength3/(Pi*(Rwo^2-
Rwi^2));drivevoltageA3:=evalf(totalresistanceA3*A3);
drivevoltageA3HOT:=evalf(totalresistanceA3HOT*A3);
drivevoltageB3:=evalf(totalresistanceB3*A3);drivevoltageB3HOT:=
evalf(totalresistanceB3HOT*A3);totalpowerA3:=drivevoltageA3*A3;
totalpowerA3HOT:=drivevoltageA3HOT*A3;totalpowerB3:=
drivevoltageB3*A3;totalpowerB3HOT:=drivevoltageB3HOT*A3;
Vol_sol3:=totallength3*Pi*(Rwo^2-Rwi^2);totalweight_sol3:=evalf
(8.89E3*evalf(Vol_sol3));
```

Solenoid 4

```
> totalresistanceA4:=evalf(totallength4*0.0313/28.6);
totalresistanceA4HOT:=evalf(totallength4*0.0363/28.6);
totalresistanceB4:=(1.724E-8)*totallength4/(Pi*(Rwo^2-Rwi^2));
totalresistanceB4HOT:=(1.16*1.724E-8)*totallength4/(Pi*(Rwo^2-
Rwi^2));drivevoltageA4:=evalf(totalresistanceA4*A4);
drivevoltageA4HOT:=evalf(totalresistanceA4HOT*A4);
drivevoltageB4:=evalf(totalresistanceB4*A4);drivevoltageB4HOT:=
evalf(totalresistanceB4HOT*A4);totalpowerA4:=drivevoltageA4*A4;
totalpowerA4HOT:=drivevoltageA4HOT*A4;totalpowerB4:=
drivevoltageB4*A4;totalpowerB4HOT:=drivevoltageB4HOT*A4;
Vol_sol4:=totallength4*Pi*(Rwo^2-Rwi^2);totalweight_sol4:=evalf
(8.89E3*evalf(Vol_sol4));
```

Solenoid 5

```
> totalresistanceA5:=evalf(totallength5*0.0313/28.6);
totalresistanceA5HOT:=evalf(totallength5*0.0363/28.6);
totalresistanceB5:=(1.724E-8)*totallength5/(Pi*(Rwo^2-Rwi^2));
totalresistanceB5HOT:=(1.16*1.724E-8)*totallength5/(Pi*(Rwo^2-
Rwi^2));drivevoltageA5:=evalf(totalresistanceA5*A5);
drivevoltageA5HOT:=evalf(totalresistanceA5HOT*A5);
```

```
drivevoltageB5:=evalf(totalresistanceB5*A5);drivevoltageB5HOT:=
evalf(totalresistanceB5HOT*A5);totalpowerA5:=drivevoltageA5*A5;
totalpowerA5HOT:=drivevoltageA5HOT*A5;totalpowerB5:=
drivevoltageB5*A5;totalpowerB5HOT:=drivevoltageB5HOT*A5;
Vol_sol5:=totallength5*Pi*(Rwo^2-Rwi^2);totalweight_sol5:=evalf
(8.89E3*evalf(Vol_sol5));
```

Solenoid 6

```
> totalresistanceA6:=evalf(totallength6*0.0313/28.6);
totalresistanceA6HOT:=evalf(totallength6*0.0363/28.6);
totalresistanceB6:=(1.724E-8)*totallength6/(Pi*(Rwo^2-Rwi^2));
totalresistanceB6HOT:=(1.16*1.724E-8)*totallength6/(Pi*(Rwo^2-
Rwi^2));drivevoltageA6:=evalf(totalresistanceA6*A6);
drivevoltageA6HOT:=evalf(totalresistanceA6HOT*A6);
drivevoltageB6:=evalf(totalresistanceB6*A6);drivevoltageB6HOT:=
evalf(totalresistanceB6HOT*A6);totalpowerA6:=drivevoltageA6*A6;
totalpowerA6HOT:=drivevoltageA6HOT*A6;totalpowerB6:=
drivevoltageB6*A6;totalpowerB6HOT:=drivevoltageB6HOT*A6;
Vol_sol6:=totallength6*Pi*(Rwo^2-Rwi^2);totalweight_sol6:=evalf
(8.89E3*evalf(Vol_sol6));
```

Net Power dissipation in solenoid configuration

Using Experimentally measured resistance:-

```
> Net_powerA:=totalpowerA1+totalpowerA2+totalpowerA3+totalpowerA4+
totalpowerA5+totalpowerA6;
Net_powerA_HOT:=totalpowerA1HOT+totalpowerA2HOT+totalpowerA3HOT+
totalpowerA4HOT+totalpowerA5HOT+totalpowerA6HOT;
```

Using standard commercial OFC resistance:-

```
> Net_powerB:=totalpowerB1+totalpowerB2+totalpowerB3+totalpowerB4+
totalpowerB5+totalpowerA6;
Net_powerB_HOT:=totalpowerB1HOT+totalpowerB2HOT+totalpowerB3HOT+
totalpowerB4HOT+totalpowerB5HOT+totalpowerA6HOT;
```

Net mass of copper in solenoid system

```
> Totalweight_allsol:=totalweight_sol1+totalweight_sol2+
totalweight_sol3+totalweight_sol4+totalweight_sol5+
totalweight_sol6;
totallength:=totallength1+totallength2+totallength3+
totallength4+totallength5+totallength6;

>
```

Appendix 4 - Published Papers

IOP Publishing Plasma Physics and Controlled Fusion

Plasma Phys. Control. Fusion **50** (2008) 074010 (13pp) doi:10.1088/0741-3335/50/7/074010

Demonstration of auroral radio emission mechanisms by laboratory experiment

S L McConville[1], D C Speirs[1], K Ronald[1], A D R Phelps[1], A W Cross[1], R Bingham[1,3], C W Robertson[1], C G Whyte[1], W He[1], K M Gillespie[1], I Vorgul[2], R A Cairns[2] and B J Kellett[3]

[1] SUPA Department of Physics, University of Strathclyde, G4 0NG, Scotland, UK
[2] School of Mathematics and Statistics, University of St. Andrews, KY16 9SS, Scotland, UK
[3] Space Physics Division, STFC, Rutherford Appleton Laboratory, OX11 0QX, England, UK

E-mail: sandra.l.mcconville@strath.ac.uk

Received 26 October 2007, in final form 4 February 2008
Published 3 June 2008
Online at stacks.iop.org/PPCF/50/074010

Abstract

Auroral kilometric radiation occurs in regions of depleted plasma density in the polar magnetosphere. These emissions are close to the electron cyclotron frequency and appear to be connected to the formation of high pitch angle electron populations due to the conservation of the magnetic moment. This results in a horseshoe type distribution function being formed in velocity space where electrons are magnetically compressed as they descend towards the Earth's atmosphere. Satellites have observed that radio emissions occur in conjunction with the formation of this distribution and show the radiation to have propagation and polarization characteristics of the extraordinary (X-mode) plasma mode with emission efficiency observed at ∼1–2%. To investigate this phenomenon a laboratory experiment, scaled to microwave frequencies and lab dimensions by increasing the cyclotron frequency, was constructed whereby an electron beam propagated through a region of increasing magnetic field created by five independently variable solenoids. Results are presented for two experimental regimes of resonant coupling, 11.7 and 4.42 GHz, achieved by varying the peak magnetic field. Measurements of the experimental radiation frequency, power and efficiency were undertaken as a function of the magnetic compression. Results showed the radiation to be polarized in the near cut-off transverse electric radiation modes, with efficiency of emission ∼1–2%, peak power outputs of ∼19–30 kW and frequency close to the cyclotron frequency. This represented close correlation between the laboratory radiation efficiency, spectra, polarization and propagation with that of numerical predictions and the magnetospheric observations.

(Some figures in this article are in colour only in the electronic version)

1. Introduction

In the auroral region of the Earth's magnetic dipole, satellites have observed horseshoe type distributions in electron velocity space as a result of conservation of the magnetic moment, μ (equation (1)), by particles subject to magnetic compression as they descend towards the atmosphere. As the magnetic flux density increases, $v_\perp$ increases to keep μ constant, and so $v_\parallel$ decreases.

$$\mu = \frac{m v_\perp^2}{2B_0}, \tag{1}$$

where m is the electron mass, $v_\perp$ is the transverse velocity component and B_0 is the magnetic flux density.

Auroral kilometric radiation (AKR) (Benediktov *et al* 1965, Gurnett *et al* 1974), first observed in 1965 by the satellite 'Electron-2', is the most intense non-thermal natural emission from the Earth, occurring close to the electron cyclotron frequency, Ω (equation (2)). Similar types of radiation have been observed from the solar system's other magnetized planets Jupiter, Saturn and Uranus (Zarka *et al* 2001). Recent satellites, including Viking and FAST (Roux *et al* 1993, Delory *et al* 1998), have also observed the production of AKR. FAST experimentally measured the horseshoe distribution function with $(\partial f/\partial v_\perp) > 0$ in the source region where f is the electron distribution function in velocity space:

$$\Omega = \frac{eB}{m}, \tag{2}$$

where e is the magnitude of the electron charge and Ω is the non-relativistic cyclotron frequency.

In 1979, Wu and Lee proposed a mechanism comprising a cyclotron maser instability driven by a positive gradient in the transverse velocity profile of the magnetically mirrored auroral electrons—called the loss cone model (Wu and Lee 1979). In 2000, Bingham and Cairns applied kinetic theory to describe the X-mode dispersion (Bingham and Cairns 2000) and growth due to a cyclotron maser instability driven by a positive gradient in the transverse velocity profile of a horseshoe distribution. This theory accounted for the observed frequencies down to ω_{ce} and predicts near perpendicular emission in the X-mode (Benson 1985). New research has considered the spatial variation in the magnetic field as an explanation for the spectral content and temporal stability of AKR emissions (Savilov *et al* 2007). Equation (3) shows the dispersion relation for a relativistic cyclotron beam. Clearly $k_\parallel$ should be as close to 0 as possible for a strong resonance if $v_\parallel$ is not well defined (Bratman *et al* 2000, Chu 2004), consistent with the X-mode. When $k_\parallel$ is zero and there is a maximum of $k_\perp$ for a given radiation frequency the contours of the resonance are circular in electron velocity space and lie on the inside edge of the horseshoe distribution function. This yields optimal brightness of AKR emission since the radiation can be excited by all components of the electron population (Pritchett and Winglee 1989). As $k_\parallel$ increases, the contours of resonance become elliptical in shape and cut across the distribution function. This means the resonance condition is weaker (Vorgul *et al* 2005).

$$\omega = S\frac{\Omega}{\gamma} + k_\parallel v_\parallel, \tag{3}$$

where $k_\parallel$ is the parallel component of k vector, $v_\parallel$ is the parallel component of velocity, S is the cyclotron harmonic number and γ is the Lorentz factor.

The horseshoe distributions were shown by kinetic analysis (Bingham and Cairns 2000, Vorgul *et al* 2005) to be unstable to an electron cyclotron resonance maser type of instability (Twiss *et al* 1958, Sprangle and Drobot 1977), and are now proposed as the source of free

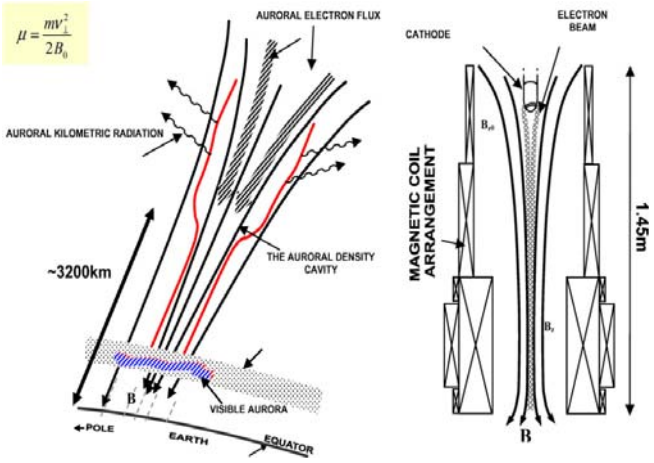

Figure 1. Comparative geometry of the auroral zone and the laboratory experiment.

energy responsible for the production of AKR (Bingham and Cairns 2002, Bingham *et al* 2004) and other astrophysical radio emissions (Bingham *et al* 2003, Kellett *et al* 2002). The electron population in the horseshoe distribution formed through magnetic compression has a high fraction of gyrational momentum allowing energy extraction to be feasible. Figure 1 depicts the auroral zone where the electrons transit the auroral density cavity, a region of plasma depletion. In this region, due to the absence of background plasma, electrons have $\omega_p < \omega_w$, where ω_p is the electron plasma frequency and $\omega_w \cong \Omega/\gamma$ is the frequency of the wave. Towards the edges of this region ω_p increases markedly thus creating a boundary effect (Burinskaya and Rauch 2007). Satellites that investigated these auroral regions have observed that the radiation is emitted in the extraordinary (X) plasma mode (Ergun *et al* 1998, Ergun *et al* 2000), polarized and propagating perpendicular to the static magnetic field. More distant observations indicate some small fraction is also polarized in the ordinary (O) mode (Hanasz *et al* 2003). In the magnetosphere a parallel electric field, $E_\parallel$, is necessary to constantly accelerate the electrons into the converging magnetic field to obtain the AKR distribution (Wu and Lee 1979, Pritchett and Winglee 1989) and reduce the plasma density.

To reproduce major features of this auroral situation, a laboratory experiment was constructed, scaled from lengths ~9000 km, the extent of the density cavity, down to ~2 m and from frequencies of ~300 kHz to between 4 and 12 GHz. As this experiment intended to study the generation efficiency from directly within the source region the authors have concentrated on resonances with X-like modes. The role of the parallel electric field was provided by an electron gun which injected an electron beam with an initial velocity spread into a set of electromagnets where it was subject to magnetic compression. This gave the effect of the auroral density cavity with the waveguide walls acting as the boundary, whilst the solenoids provided the 'bottleneck' of increasing magnetic field. Measurements were undertaken of the electron beam's current and energy. The results showed the formation of the desired horseshoe shape in the electron beams velocity distribution, reproducing the magnetospheric situation. Measurements of the output power, emission efficiency, operating frequency, emitted wave

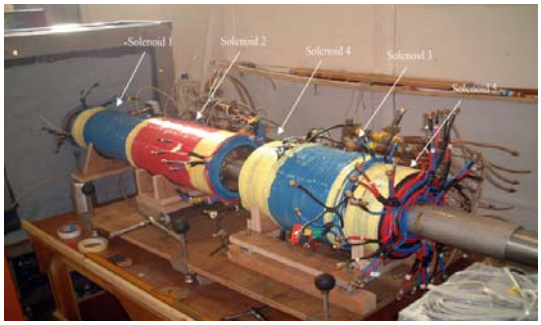

Figure 2. The solenoids of the magnetic field system during assembly in the laboratory.

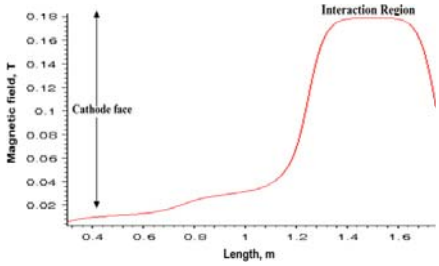

Figure 3. Magnetic field profile through the centre of the solenoids. The locations of the cathode and interaction region are marked. This profile was calculated by computer and checked experimentally by Hall sensor.

polarization and propagation were taken as a function of detuning between the radiation and beam frequencies and degree of magnetic compression. These were compared with numerical and theoretical predictions (Cairns *et al* 2005, Speirs *et al* 2005, Vorgul *et al* 2005 and Speirs *et al* 2008) and the magnetospheric observations.

2. Experimental apparatus

A system of solenoids was created as shown in figure 2, to encompass the electron beam as it traversed through the experiment from the cathode through the interaction space to the anode. Each of the five solenoids was constructed by winding OFHC copper tubing around non-magnetic formers. The individual copper tubes were around 20 m in length with an ID of 2.5 mm and OD of 7 mm, coated in dielectric insulation. A high pressure water cooling system, delivering a coolant inlet pressure of ∼22 bar to the tubing core, allowed the solenoids to be run up to a power of 120 kW with up to 300 A on each individual wire. Independent adjustment of each of the coils allowed fine control of the magnetic field compression profile, figure 3. The electron injector was placed in the low, fringing, magnetic field generated by solenoid 1 which ensured that the electrons had an initial spread in their pitch angles. The electrons

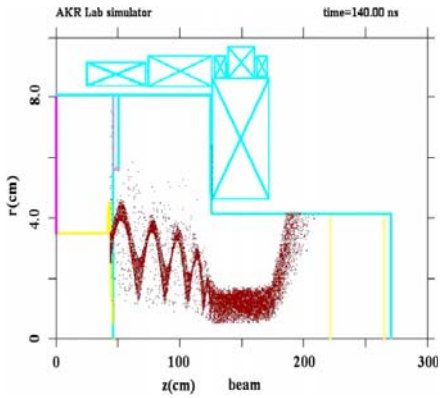

Figure 4. Electron beam trajectory through the apparatus as predicted by the PiC code KARAT.

were subject to magnetic compression as they passed into solenoid 2 and reached a maximum magnetic field in the plateau in the centre of solenoid 3. The shimming solenoids 4 and 5 were used to balance the profile of the magnetic field plateau. Two different plateau magnetic fields were used. For the low frequency resonance experiment at 4.42 GHz the flux density of the plateau was 0.18 T. For the higher frequency resonance of 11.7 GHz the flux density was 0.49 T (Speirs *et al* 2005). The solenoids determined the size of the evacuated anode vacuum vessel/beam tunnel and interaction space 16 cm and 8.28 cm in diameter, respectively, illustrated in figure 4, which also shows the computed electron trajectories as the beam travels through the system. The beam tunnel is the area between the mesh and the entrance to the interaction region. At the walls where the beam tunnel leads into the interaction region there is a slope in their shape; this is to allow as much of the beam as possible into the 8.28 cm diameter waveguide. It was essential that the system be kept under vacuum, $\sim 10^{-6}$ mbar, so that there were no unnecessary collisions between the electrons and any other particles in the residual gas.

The electron gun used in the system had a vacuum spark cathode; these types of devices are pulsed cathodes used to generate a high voltage, short duration electron beam. The cathode used in the present experiment is energized by 100 ns pulses from a Blumlein power supply (Somerville *et al* 1990) capable of reaching up to 200 kV. The output of the quad cable Blumlein system, figure 5(*a*), was matched by an ionic resistor connecting its high voltage terminal to an earth connection. The Blumlein cables were charged in parallel and discharged in series when a triggered mid-plane spark gap reached breakdown to give an amplified output signal (up to 3.5 V_{ch}) whilst maintaining a rectangular output pulse. The ionic resistor that is connected to the high voltage end of the Blumlein is made up of a saturated copper sulphate ($CuSO_4$) solution, which has the advantage of being able to withstand high peak powers without damage. The role of the matching resistor, $\sim 230\ \Omega$, was to match the impedance of the Blumlein, 200 Ω, so that the signal did not reflect back to the supply when the experiment was energized. If the matching resistor were not present, the power from the initial pulse would reflect back into the supply and cause undesirable amplitude modulation.

The length of the cathode stalk and the placement of the anode mesh were adjusted to set a diode gap of 2 cm. From figure 5(*b*), the face of the cathode can be seen with the velvet ring

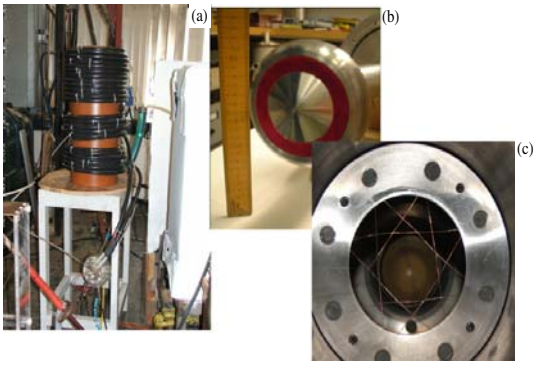

Figure 5. (*a*) Blumlein pulsed power supply, (*b*) cathode face with velvet ring, (*c*) anode mesh.

surrounding the dome-shaped cathode surface. When the output pulse from the power supply energized the cathode, electrons were emitted due to field emission from the velvet fibres. As the temperature at the fibre tips increased, the field emission led to the formation of a plasma cloud and ultimately resulted in explosive electron emission. The rate at which the plasma travelled across the cathode–mesh gap was determined by the material used (Mesyats and Proskurovsky 1989, Ronald *et al* 1998, Mesyats 2005): for velvet the expansion velocity is of the order 2 cm μs^{-1}. An expansion of a few centimetres per microseconds limits the minimum gap spacing to a couple of centimetres for pulses of 100 ns. The shape of the cathode face was designed to make those electrons on the inner circumference of the velvet emission ring have more transverse momentum than those on the outer circumference to induce a moderate spread in the velocity of the electron beam. The anode mesh, figure 5(*c*), had a sparse grid and was used to set the anode–cathode gap to provide a sufficiently high field ~50 kV cm^{-1} on the cathode to cause ignition of the plasma flare. A sparse mesh was used to avoid excessive loss of high pitch factor electrons which would arise if small aperture holes were employed. The electrons were brought to cyclotron resonance in the 8.28 cm diameter tube with near cut-off transverse electric (TE) modes as these share similar polarization and propagation properties (ac electric field and the wave vector are both perpendicular to the static magnetic field) with the X-mode observed in the magnetosphere. In particular resonances with $TE_{(0,n)}$ modes were studied as these could be modelled in 2D PiC code simulations due to their azimuthal symmetry (Speirs *et al* 2008). Equation (3) must be satisfied for resonant interaction and energy exchange to occur. To excite the near cut-off TE_{01} mode at a frequency of 4.42 GHz, the plateau magnetic flux density was set at 0.18 T, the low frequency resonance regime. The same analysis determined the higher frequency resonance regime of 11.7 GHz for the TE_{03} mode requiring a plateau flux density of 0.49 T (Ronald *et al* 2008).

3. Diagnostics

Accelerating potential was measured by sensing the current through the matching ionic resistor by a Rogowski belt and recorded by a deep memory oscilloscope. Diode current was obtained with a Rogowski belt diagnostic placed in the ground current return connection of the anode.

The beam current was measured by placing a Faraday cup beam interceptor into the interaction space. The Faraday cup was conical in shape to inhibit the escape of any secondary electrons that were produced.

Pairs of waveguide 12 and waveguide 18 stub receiver systems were created. These devices were built using single mode linearly polarized rectangular waveguide components with simple open ended waveguide apertures for 4.42 GHz and 11.7 GHz radiation, respectively. These were fitted with calibrated attenuators, placed in the far field of the experiment output antenna and fed signals to calibrated rectifying diodes. The rectified microwave radiation pulses were recorded using a 1.5 GHz deep memory digital oscilloscope. To measure the microwave spectra a deep memory 12 GHz digital oscilloscope was used to capture the radiation ac waveforms. Fourier transform of these allowed the radiation frequency to be measured. At the higher resonance regime, it was necessary to use cut-off filters to confirm the spectrum since the frequency was close to the oscilloscope's bandwidth limit. The pairs of waveguide stub antennae were used to measure the radiation antenna pattern emitted by the experiment in radial and azimuthal polarizations as a function of the azimuthal angle. One antenna was used to scan in the azimuthal direction and one provided a control reference. These readings were then analysed to give the power output of the system (Ronald *et al* 2008). Measurements were taken of azimuthal angles of up to 55°, angles greater than 55° could not be measured due to the walls of the output flange obstructing the radiation emission. Two regimes of resonant interaction were investigated, one at 4.42 GHz and the second at 11.7 GHz. For the lower frequency, a maximum magnetic flux density plateau of 0.18 T was set in the interaction region of solenoid 3. This gave resonance near cut-off with a relatively low order mode, TE_{01}, whilst retaining a substantial reserve capacity of magnetic field with which the resonant electron distribution function was measured. The higher frequency was investigated to more closely replicate the magnetospheric situation with $\lambda \ll$ dimensions of the resonant cavity (Burinskaya and Rauch 2007). This frequency required a maximum plateau magnetic field of 0.49 T.

4. Experimental results

The beam energy, current and transport through the apparatus were investigated as a function of the configuration of the magnetic field. Examples of the beam current and diode voltage traces observed on the oscilloscope are presented in figure 6(*a*). At (i) on the diagram the output pulse from the Blumlein reached its maximum amplitude. When the cathode was energized by this pulse it released electrons due to field emission which resulted in explosive electron emission (Ronald *et al* 1998, Mesyats 2005) and the onset of a vacuum spark in the electron gun. The experiment impedance at this point reduced sharply reducing the total load impedance seen by the Blumlein and the voltage across the diode to 75 kV, (ii) on the diagram. Figure 6(*b*) indicates how the beam current pulse varied as a function of the gun magnetic field for a beam voltage of 85 kV, plateau flux density of 0.52 T, and shows that as the cathode flux density was increased from 0.013 to 0.05 T, the beam current increased from 12 to 47 A. Figure 6(*c*) displays similar information but with a lower beam voltage of 75 kV, plateau flux density of 0.4 T and shows that as the cathode flux density was increased from 0.01 to 0.05 T, the current of the electron beam increased from 6 to 47 A. Results for the fraction of beam transported into the interaction region for a given cathode flux density as the maximum plateau magnetic field was increased, demonstrated the formation of the horseshoe distribution, because progressive magnetic mirroring was achieved. Analysing the variation of the beam current with mirror ratio, figure 7(*a*), as the plateau magnetic field was increased from the resonant value and relating this back to the critical value of v_z yielded the one-dimensional (1D) number density

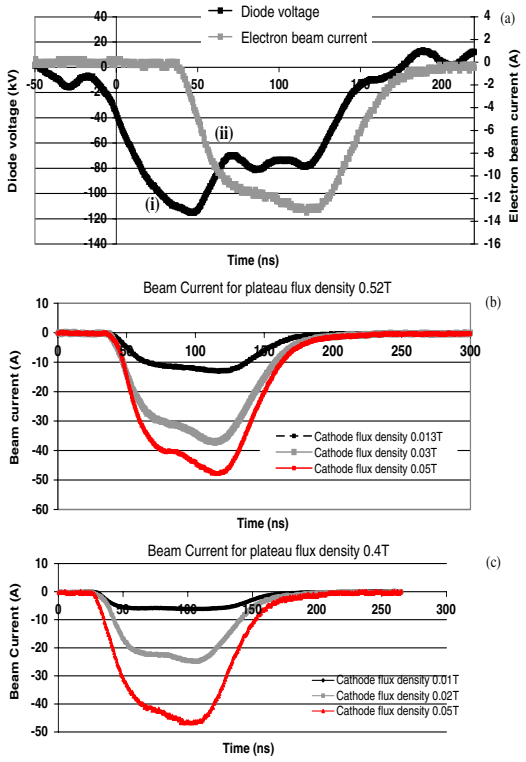

Figure 6. (*a*) Raw diode voltage and beam current plot, (*b*) beam current at plateau flux 0.52 T, (*c*) beam current at plateau flux 0.4 T.

of the electron beam as a function of the pitch angle. The 1D number density of the electron beam formed at the cathode flux densities of 0.01 and 0.02 T and plateau flux density of 0.18 T can be seen as a function of pitch angle in figure 7(*b*).

Analysis of figure 7 demonstrates that for the lower cathode flux density of 0.01 T, the electron beam had half the number density at high pitch angles compared with the flux density of 0.02 T. For the 0.01 T case, 2/3 of the current was associated with electrons having pitch angles greater than 37°. Electrons having a pitch <37° were not measured due to apparatus limitations. For the 0.02 T case, only 1/3 of the current was associated with electrons having pitch angles >37°.

Figure 8(*a*) shows the radiation ac waveform for the lower resonance regime of 4.42 GHz from which the Fourier transform was calculated, figure 8(*b*). The peak spectral component of the signal was observed at 4.42 GHz close to cut-off for the TE_{01} mode and the cyclotron frequency, with a second harmonic observed at ∼8.8 GHz. The maximum efficiency was achieved at a cyclotron detuning $(\omega_w - \omega_{ce})/\omega_{ce}$ of ∼2.5%. Figure 9 shows the experimental

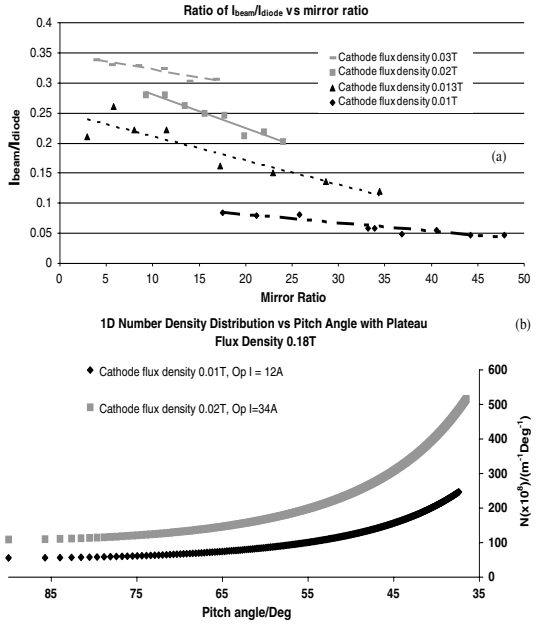

Figure 7. (*a*) Variation of electron beam transport from accelerator to interaction space as a function of the magnetic configuration, (*b*) analysis of the 1D number density distribution at a plateau flux density of 0.18 T.

and normalized theoretical microwave antenna pattern measurements. The two plots are in close agreement up to an angle of ∼45°, confirming the mode to be the TE_{01} at 4.42 GHz. Excitation of a near cut-off TE mode was consistent with AKR, which is predominately generated in the X-mode propagating and polarized perpendicular to the static magnetic field. The discrepancy above 45° was due to scattering of the experimental pattern from part of the vacuum window. Integration of the normalized theoretical antenna pattern obtained from these mode scan measurements gave output powers of 19 kW and 35 kW for cathode flux densities of 0.01 T and 0.02 T, with maximum efficiencies of emission of 2% and 1%, respectively. The higher power but lower efficiency associated with the 0.02 T regime is consistent with the distribution of the particles noted in the 1D number density plot, figure 7(*b*). Figure 10(*a*) shows the Fourier transform for the higher resonance regime where a peak signal was observed at 11.7 GHz, close to the cyclotron frequency and the cut-off for the TE_{03} mode. As the resonance in this case was close to the limit of the oscilloscope, cut-off filters were used in the waveguide to confirm that no significant higher spectral components were present, figure 10(*b*). The antenna patterns for the higher resonance regime of 11.7 GHz can be seen in figure 11. Due to the multimode nature of this resonance condition, the measured mode plot was more complicated and the energy was split between the azimuthal and radial polarizations. Components of both the TE_{03} and TE_{23} modes were observed, and the experiment appeared to exhibit mode hopping where the dominant resonant mode changed with time and there were

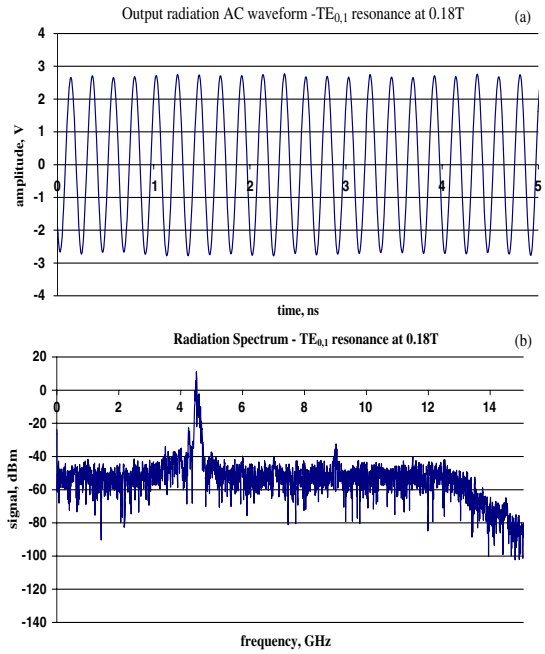

Figure 8. (*a*) Ac waveform for 4.42 GHz microwave results, (*b*) Fourier transform with frequency peak at 4.42 GHz.

two temporally separated peaks in the output radiation. At a cathode flux density of 0.013 T, power of up to 9.4 kW was observed and at a cathode flux density of 0.03 T a power of up to 30 kW was emitted. A maximum efficiency of emission was achieved with a cathode flux density of 0.03 T, beam current 37 A of ∼1%.

5. Summary

A laboratory experiment was constructed using electromagnets to produce a progressively increasing magnetic field profile, through which an electron beam was transported to create a horseshoe distribution function in electron velocity space. Microwave radiation was extracted by the postulated AKR mechanism. The production of the horseshoe electron distribution function, at a maximum magnetic field corresponding to a cyclotron frequency of 4.42 GHz was shown by the beam transport measurements. Microwave measurements confirmed the instability of the distribution function to cyclotron emissions, whilst frequency measurements showed the radiation frequency to be just above the relativistic cyclotron frequency. Integration of the antenna patterns gave a maximum efficiency of up to 2% agreeing with both numerical predictions and magnetospheric observations. The relationship between the wave and cyclotron frequencies and the wave polarization and propagation directions were also consistent with the satellite measurements.

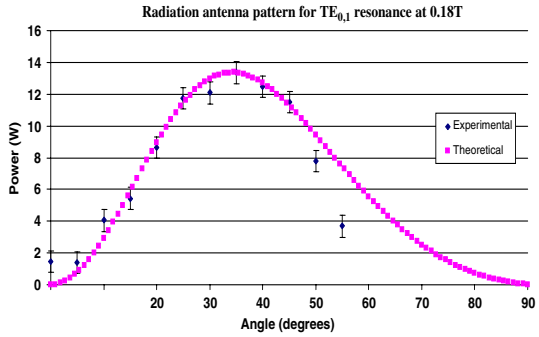

Figure 9. Measurement of the antenna pattern showing the $TE_{0,1}$ mode.

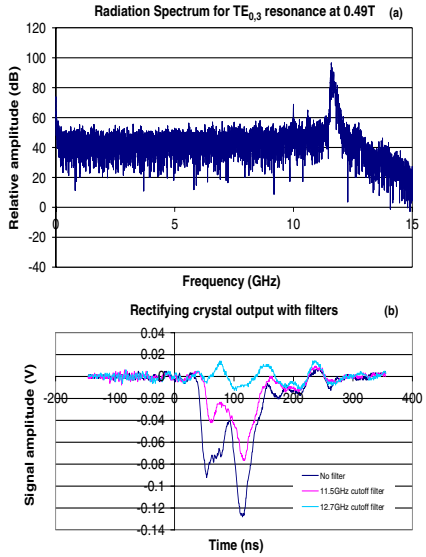

Figure 10. (*a*) Fourier transform with frequency peak at 11.7 GHz, (*b*) rectifying crystal output with different cut-off filters.

6. Future work

To enhance the comparability between the laboratory and magnetospheric geometry, the addition of a background plasma is planned. The proposed scheme will create a Penning gas discharge in the interaction region to form a low temperature, low density ionized gas. This geometry will take advantage of the inherent magnetic field present in the apparatus whilst

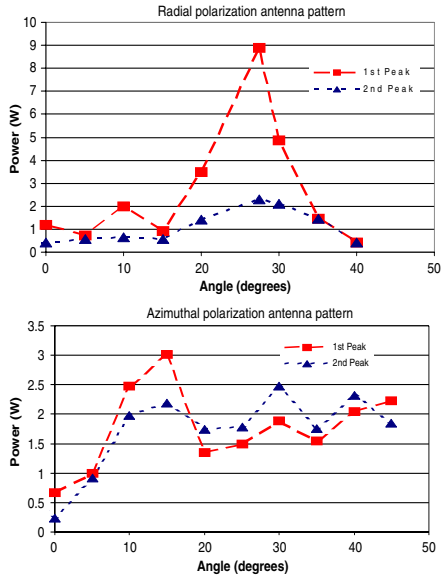

Figure 11. Radial and azimuthal antenna patterns for a resonance at 0.49 T plateau flux density showing components of the TE_{03} and TE_{23} modes and temporal mode hopping.

improving discharge ignition in the low pressure regimes. The addition of the background of 'cool' particles will allow investigation of the role of the weak background plasma in the auroral density cavities, specifically the possibility of upper hybrid resonant absorption.

Acknowledgments

The EPSRC and the STFC Centre for Fundamental Physics supported this work. Mr I S Dinwoodie is thanked for his help in creating the apparatus and Professor V L Tarakanov for assistance with the numerical model. Helpful conversations with Professor A Savilov are gratefully acknowledged.

References

Benediktov E A, Getmanstev G G, Sazonov Yu A and Tarasov A F 1965 *Cosm. Res.* **3** 614–7
Benson R F 1985 *J. Geophys. Res.—Space Phys.* **90** 2753–84
Bingham R and Cairns R A 2000 *Phys. Plasmas* **7** 3089–92
Bingham R and Cairns R A 2002 *Phys. Scr.* T **98** 160–2
Bingham R, Kellett B J, Cairns R A, Tonge J and Mendonca J T 2003 *Astrophysical J.* **595** 279–84
Bingham R, Kellett B J, Cairns R A, Vorgul I, Phelps A D R, Ronald K and Speirs D 2004 *Contrib. Plasma Phys.* **44** 382–7
Bratman V L, Cross A W, Denisov G G, He W, Phelps A D, Ronald K, Samsonov S V, Whyte C G and Young A R 2000 *Phys. Rev. Lett.* **84** 2746–9

Burinskaya T M and Rauch J L 2007 *Plasma Phys. Rep.* **33** 28–37
Cairns R A, Speirs D C, Ronald K, Vorgul I, Kellett B J, Phelps A D R and Bingham R 2005 *Phys. Scr.* T **116** 23–6
Chu K R 2004 *Rev. Mod. Phys.* **76** 489–540
Delory G T, Ergun R E, Carlson C W, Muschietti L, Chaston C C, Peria W, McFadden J P and Strangeway R 1998 *Geophys. Res. Lett.* **25** 2069–72
Ergun R E *et al* 1998 *Geophys. Res. Lett.* **25** 2061–4
Ergun R E, Carlson C W, McFadden J P, Delory G T, Strangeway R J and Pritchett P L 2000 *Astrophys. J.* **538** 456–66
Gurnett D A 1974 *J. Geophys. Res.* **79** 4227–38
Hanasz J, Panchenko M, de Faeraudy H, Schreiber R and Mogilevsky M M 2003 *J. Geophys. Res.* **108** 1408
Kellett B J, Bingham R, Cairns R A and Tsikoudi V 2002 *Mon. Not. R. Astron. Soc.* **329** 102–8
Mesyats G A 2005 *Plasma Phys. Control. Fusion* **47** 109–51
Mesyats G A and Proskurovsky D I 1989 *Pulsed Electrical Discharge in Vacuum* (Berlin: Springer)
Pritchett P L and Winglee R M 1989 *J. Geophys. Res.* **94** 129–43
Ronald K, Cross A W, Phelps A D R, He W L, Yin H B and Spark S N 1998 *IEEE Trans. Plasma Sci.* **26** 375–82
Ronald K, Speirs D C, McConville S L, Phelps A D R, Robertson C W, Whyte C G, He W, Gillespie K M, Cross A W and Bingham R 2008 Radio frequency resonator structure and diagnostic measurements for a laboratory simulation of Auroral Kilometric Radiation *Phys. Plasmas* **15** at press
Roux A, Hilgers A, de Feraudy H, le Queau D, Louard P, Perraut S, Bahnsen A, Jespersen M, Ungstrup E and Andre M 1993 *J. Geophys. Res.* **98** 11657–70
Savilov A V, Bespalov P A, Ronald K and Phelps A D R 2007 *Phys. Plasmas* **14** 113104
Somerville I C, MacGregor S J and Farish O 1990 *Meas. Sci. Technol.* **1** 865–8
Speirs D C, Vorgul I, Ronald K, Bingham R, Cairns R A, Phelps A D R, Kellett B J, Cross A W, Whyte C G and Robertson C 2005 *J. Plasma Phys.* **71** 665–74
Speirs D C *et al* 2008 *Plasma Phys. Control. Fusion* **50** 074011
Sprangle P and Drobot A T 1977 *IEEE Trans. Microw. Theory Tech.* MTT-25 **25** 528–44
Twiss R Q 1958 *Aust. J. Phys.* **11** 564–79
Vorgul I, Cairns R A and Bingham R 2005 *Phys. Plasmas* **12** 122903
Wu C S and Lee L C 1979 *Astrophys. J.* **230** 621–6
Zarka P, Treumann R A, Ryabov B P and Ryabov V B 2001 *Astrophys. Space Sci.* **277** 293–300

IOP Publishing Plasma Sources Science and Technology
Plasma Sources Sci. Technol. **17** (2008) 035011 (8pp) doi:10.1088/0963-0252/17/3/035011

Electron beam measurements for a laboratory simulation of auroral kilometric radiation*

K Ronald[1], S L McConville[1], D C Speirs[1], A D R Phelps[1], C W Robertson[1], C G Whyte[1], W He[1], K M Gillespie[1], A W Cross[1] and R Bingham[1,2]

[1] SUPA Department of Physics, John Anderson Building, 107 Rottenrow, University of Strathclyde, Glasgow, G4 0NG, UK
[2] Space Science and Technology Department, STFC Rutherford Appleton Laboratory, Didcot, OX11 0QX, UK

E-mail: K.Ronald@strath.ac.uk

Received 4 November 2007, in final form 17 April 2008
Published 20 June 2008
Online at stacks.iop.org/PSST/17/035011

Abstract
Efficient (∼1%) electron cyclotron radio emissions are produced in the X-mode from regions of locally depleted plasma in the Earth's polar magnetosphere. These emissions are commonly referred to as auroral kilometric radiation. Two populations of electrons exist with rotational kinetic energy to contribute to this effect, the downward propagating auroral electron flux which acquires transverse momentum due to conservation of the magnetic moment as it experiences an increasing magnetic field and the mirrored component of this flux. This paper demonstrates the production of an electron beam having a controlled velocity spread for use in an experiment to investigate the available free energy in the earthbound electron flux. The experiment was scaled to microwave frequencies and used an electron gun to inject an electron beam into a controlled region of increasing magnetic field produced by a set of solenoids reproducing the magnetospheric situation. Results are presented of the measurements of diode voltage, beam current as a function of magnetic mirror ratio and estimates of the line density versus electron pitch angle consistent with the formation of a horseshoe velocity distribution and demonstrating control of the electron distribution in velocity space.

(Some figures in this article are in colour only in the electronic version)

1. Introduction

Auroral kilometric radiation (Gurnett 1974, Melrose *et al* 1982, Roux *et al* 1993) has been observed by satellites over several decades, with the precision of the measurements increasing as technology developed allowing more complex observations to be undertaken. The measurements have revealed that the radiation frequency observed at any given altitude extends down to the local electron cyclotron frequency with the peak in the emissions around 300 kHz. The wave propagation and polarization appears to be in the X-mode (Benson 1985) with a peak power $\sim 10^9$ W, corresponding to an estimated radiation efficiency ∼1% (Pritchett and Strangeway 1985, Gurnett 1974) of the auroral electron precipitation energy (Ergun *et al* 1998, 2000, Delory *et al* 1998). The availability of accurate data has resulted in a significant research effort to explain the unusually high efficiency of this natural process (Burinskaya and Rauch 2007, Bingham *et al* 2000, 2002 2004 Vorgul *et al* 2005). Electrons precipitating into the Earth's magnetosphere are subject to increasing magnetic field with decreasing altitude. In the absence of collisions and given that the field increases slowly compared with the electron oscillation period, the adiabatic conservation of the magnetic moment comes into effect.

$$\underline{\mu} = \pi r^2 i \hat{\underline{z}} = \frac{\gamma m v_\perp^2}{2B} \hat{\underline{z}}, \tag{1}$$

where $\underline{\mu}$ is the vector magnetic dipole moment of an electron orbit, $\underline{B}$ is the magnetic flux, taken here to be orientated in

* This paper was presented as an invited talk at the 28th International Conference on Phenomena in Ionized Gases (ICPIG XXVIII) held in Prague, Czech Republic on 15–20 July 2007. See stacks.iop.org/PSST/17/2

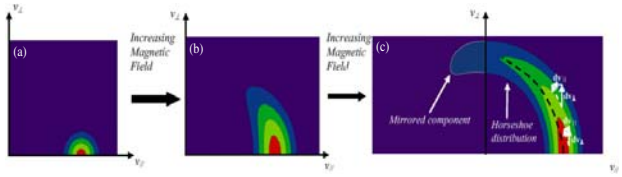

Figure 1. The velocity space evolution of an electron beam subject to an adiabatically increasing magnetic field.

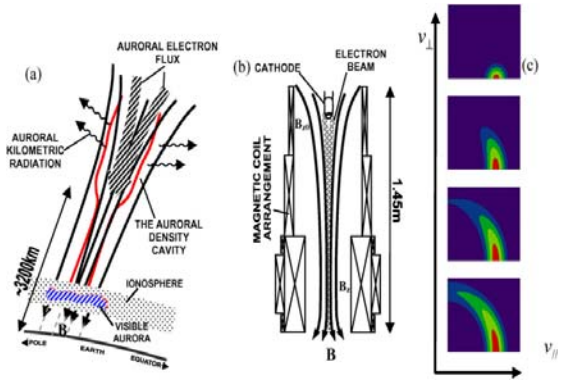

Figure 2. A comparison between the (*a*) magnetospheric and (*b*) experimental geometries, illustrating the plasma depleted auroral density cavity, showing the comparative geometry of the experiment, schematic of the electromagnets and (*c*) context of the evolution of the beam distribution.

the $\hat{z}$ direction, i is the current associated with the electron rotational orbit, r is the radius of the electron orbit, m the electronic rest mass, γ the Lorentz–Fitzgerald factor and $v_\perp$ the rotational electron velocity.

This results in an increase in the pitch angle of individual electrons as they descend towards the atmosphere. Figure 1 shows in a contour plot the evolution of the velocity space number density distribution of the electron beam under conditions of adiabatic compression, showing the incremental conversion of axial ($dv_\parallel$) to gyrational ($dv_\perp$) velocity, producing a horseshoe distribution in the electron velocity of the earthbound electron flux from an electron beam with a small initial transverse component of velocity. Figures 2(*a*) and (*c*) illustrate this evolution in the context of the magnetospheric geometry. Such electron distributions have been measured in the magnetosphere (Ergun *et al* 2000, Delory *et al* 1998). As the magnetic flux density increases a point is reached where in order to conserve the magnetic moment, all of a given electron's kinetic energy must become associated with its rotational motion, its descent ceases and the electron is 'mirrored', reversing its direction of motion along the magnetic field lines, figure 1. This leads to the second energetic electron population in the auroral magnetosphere, the space bound component. Due to the correlation between the electron cyclotron frequency and the radio frequency, it has been postulated for some time that the emissions are due to a cyclotron instability (Twiss 1958, Gaponov 1959, Chu 2004, Sprangle and Drobot 1977). The mirrored component of the electron beam contains only part of the earthbound current, since part of the beam with low initial transverse momentum does not satisfy the mirroring condition before absorption in the upper regions of the ionosphere. This component which does not mirror prior to encountering the atmosphere is said to be in the 'loss cone'. Since low pitch electrons do not have free energy to drive a cyclotron instability, but would be capable of absorbing the emitted radiation, initial focus (Wagner *et al* 1984, Wu and Lee 1979) was placed on the space bound flux since the lowest pitch electrons would be absent. In fact, however, at any significant altitude above the ionosphere, conservation of the magnetic moment of the space bound flux reduces the angular width of the loss cone in any case. This led to the postulate that the higher current earthbound flux of particles may be the source for the radiation and a theory of the emission process from an electron beam having a horseshoe distribution in velocity spread has supported this concept (Bingham *et al* 2000, 2002, 2004, Vorgul *et al* 2005). As the equations describing this instability scale with the cyclotron frequency, it became clear that one could test the concept in a laboratory experiment, facilitating better control of the experimental parameters than is possible in the magnetospheric observations (Cairns *et al* 2005, Speirs *et al* 2005). This paper presents the apparatus for such an experiment and describes the measurement of the beam energy, current and distribution function in velocity space.

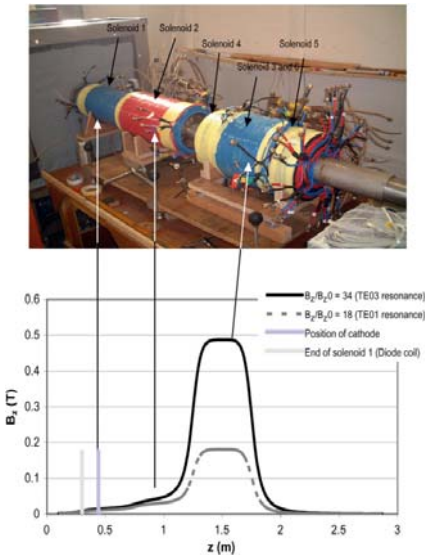

Figure 3. The magnetic solenoids being assembled in the laboratory, solenoids have been rolled apart to show the transition between the 16 cm diameter anode can and the 8 cm diameter interaction waveguide. The variation of the axial magnetic field for two regimes of operation is illustrated, calculated by analytical methods and confirmed by Hall probe measurements.

2. Apparatus

The experimental apparatus was based on the use of an electron gun to inject particles into an increasing magnetic field produced by a system of electromagnets. The overall layout of the experiment is illustrated in figure 2(*b*), along with a schematic of its relationship to the magnetospheric situation. The electromagnets were formed in six distinct coils, illustrated in figure 3, each coil was wound from OFHC copper tubing coated with a thin plastic sheath for electrical insulation. The windings were core cooled by water and were able to carry a current of up to 450 A. The first coil, half a metre in length and formed of two layers, surrounded the electron accelerator and defined the magnetic field experienced by the electrons as they were injected into the 16 cm diameter beam tunnel. Coil 2, also half a metre in length and formed of four layers, confined and transported the electrons to the interaction region and acted as a transition between the low-field electron gun region and the high-field interaction region. As the electron beam diameter reduced with increased flux density, it was possible to reduce the diameter of the interaction region to 8 cm, which also provided a useful reduction in power consumption of the apparatus. Solenoids 3–5 provide the maximum plateau flux density (up to 0.5 T) in the apparatus, and were wound as a 10 layer main coil with a pair of two layer balancing shim coils, respectively. Precise control of the magnetic flux density in this 'interaction' region allowed the efficiency of the cyclotron instability to be investigated. The control of the magnetic flux density at the cathode and in the interaction space provided control of the initial electron velocity distribution and degree of magnetic compression and determined the electron distribution in the plateau region where the resonance condition would be satisfied with the electromagnetic radiation. The role of solenoid 6 was to provide a very high (>0.7 T), peaked field profile to aid in mirroring the electrons, which in conjunction with downstream electron beam measurement systems allowed the estimation of the electron velocity distribution. The axial profile of the magnetic flux density was computed using analytical integration of the field due to infinitesimal current loops over the volume of the solenoids. The predictions from this calculation were confirmed using a commercial Hall effect sensor to map the axial variation of the flux density, figure 3.

Electron emission into the apparatus was achieved by placing a cathode electrode covered with an annular region (3 cm mean radius, 1 cm radial width) of velvet emitter (Bratman *et al* 2000, Cooke *et al* 1996, Denisov *et al* 1998) within 2 cm of a sparse mesh anode, figure 4. Design of this injector was undertaken with the aid of the 2D PiC code KARAT (Speirs *et al* 2005, 2008), figure 5. Application of an accelerating potential of 75 kV to the cathode led to field-enhanced electron emission at the discontinuities of the dielectric fibres. The field emission current was sustained by a tunnelling current from the metallic cathode body into the fibres (which were subject to a strong field along their length) and was enhanced by an avalanche process with the valance electrons in the fibres and a surface flashover avalanche along the outside of the fibres (Noer 1982, Garven 1996, Latham 1983, Xu and Latham 1992). A high current density was emitted from each fibre tip leading to explosive vaporization of the underlying bulk material. This vapour was ionized by the thermionic emission current from the hot underlying material resulting in the formation of a cathode plasma flare (Mesyats 1991, Mesyats and Proskurovsky 1989, Ronald *et al* 1998). The uniformity of the velvet fibres ensured that the cathode was quickly and evenly covered in plasma which supported the space-charge-limited emission of electrons into the diode gap forming a vacuum spark discharge. The plasma expanded away from the cathode (Mesyats 1991, Mesyats and Proskuorvsky 1989, Ronald *et al* 1998) at a velocity of $\sim$2 cm μs^{-1}, causing a small increase in the diode current since the acceleration pulse was only 100 ns in duration. Most of the current passed the anode mesh and entered the 16 cm anode can region of the experiment propagating into the increasing magnetic field.

The electron gun was placed in the fringing field of solenoid 1, figure 3. As the emission surface was normal to the axis of the solenoids this ensured that depending on the location of their emission point, the electrons would experience a slightly different magnetic compression. This was not sufficient to produce a wide horseshoe electron distribution in the resonant region given the attainable ratio of magnetic fields. However the central nose of the cathode was designed to have a distinct conical form making an angle of 12° to the emission surface, figure 4(*b*). This ensured that the electrons as they were emitted from the cathode were subject to a radial force, exaggerating the angle between the accelerating force

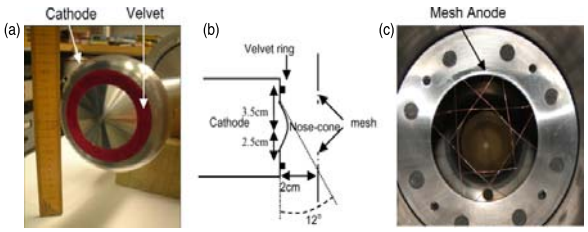

Figure 4. The electron accelerator components, showing (*a*) the cathode with velvet emission ring, (*b*) conical 'nose' and (*c*) mesh anode.

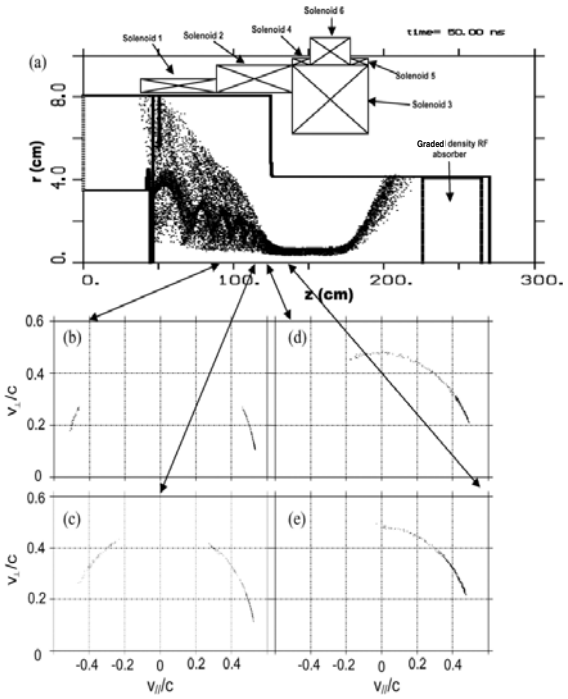

Figure 5. Electron trajectories simulated in the 2D PiC code KARAT (*a*), illustrating mirroring, compression and the formation of the horseshoe distribution in electron velocity space as the electron beam experiences the increasing magnetic field at (*b*) 90 cm, (*c*) 120 cm, (*d*) 130 cm and enters the plateau at (*e*) 140 cm.

and the magnetic field lines. The magnitude of the radial force varied depending on the proximity of the emission site to the inner edge of the velvet ring. Unlike the magnetron injection gun (MIG) (Petelin 1993, Flyagin *et al* 1984, Cross *et al* 1993) in the present geometry the cathode magnetic flux links the emitter surface and electrons are accelerated over a small range of angles close to tangential to the magnetic flux lines. In the region of the electron injector, due to the large Larmor radii and fringing magnetic fields combined with the accelerator field, the initial particle motion is not adiabatic.

The power supplies for the magnet system consisted of a bank of switched mode 300 A, 70 V supplies in series and/or parallel combinations to match the current and voltage requirements of each load coil. Coils 3 and 5 were however set by a 200 V, 310 A linear regulator to ensure an accurate resonant frequency. Independent control of the current in solenoids 1–4 ensured flexible control of the magnetic compression process and mirror ratio, solenoid 5 was always wired directly in series with solenoid 3. The power supply for the accelerator consisted of a double cable Blumlein generator, four cables each of electrical length equivalent to 120 ns were charged in parallel up to 75 kV and switched to series by a single spark gap to yield a peak amplitude of 3.5 times the charging voltage (into an open circuit, about twice charging voltage into a matched load) with an output impedance of 200 Ω (Somerville *et al* 1990). The pulse

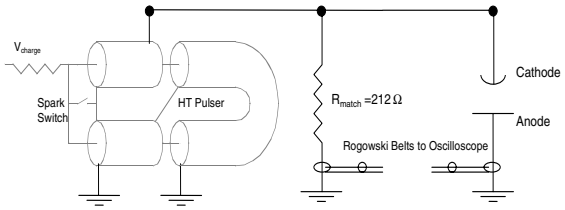

Figure 6. The circuit of the HT pulsed power supply showing the matching resistor, accelerator, diode voltage and anode current diagnostics.

duration was set by the cable lengths and the rise time by the speed of the spark gap switch and the inductance of the output circuit (∼20 ns). Explosive electron emission accelerators have very dynamic impedance, being initially almost open circuit, then collapsing to a very low impedance. Dynamically varying load mismatches tend to yield poor pulse shapes with Blumlein generators, therefore to cap the maximum impedance presented to the generator, a 212 Ω ionic resistor using saturated $CuSO_4$ solution was placed in parallel with the accelerator. The accelerator diode circuit is illustrated in figure 6. A single 'star' earth point was used for the supply and all diagnostics, as with fast pulses the inductance of the earth lines can lead to spurious measurements.

It was not possible to use a ferrite core current transformer to measure the electron beam current in the interaction space since the experiment had to work over a large range of magnetic flux in this vicinity. The use of a dielectric cored transformer was discounted due to the problem of simultaneously satisfying the size constraints, sensitivity requirements and bandwidth. Therefore a Faraday cup beam interception diagnostic was devised with high bandwidth and minimum noise pick up. This device is illustrated in figure 7. The conical form of the interceptor inhibited the escape of secondary electrons scattered from the surface. A large dielectric support secured the cup in the centre of the interaction space and the 4 cm cup diameter was sized to ensure it would intercept the largest diameter electron guiding centres which would pass into the 8 cm interaction region. To minimize noise pick up and eliminate inductance in the sensing circuits, a low impedance sliding contact was provided onto the main anode of the experiment at this location, this sliding contact formed the star earth point for the entire apparatus. A 50 Ω 3 W metal film resistor electrically connected the cup body to the anode and was shunted by a 50 Ω coaxial cable leading to the oscilloscope (50 Ω input impedance) used to measure the pulses. The current shunt therefore presented a 25 Ω impedance overall to the electron beam. With beam currents of up to 40 A the signal returned to the oscilloscope was up to 1 kV. High voltage, high bandwidth attenuators were used to reduce this down to below 5 V suitable for the instrument.

Since a current shunt technique for the measurement of the electron beam current was forced on the design by other important aspects of the experiment, it was necessary to measure the total current flowing to the anode and the total accelerating potential by methods which did not require any additional ground contacts to prevent errors due to differential grounds and noise due to ground loops being introduced into

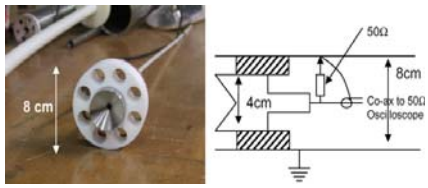

Figure 7. The Faraday cup electron beam current diagnostic showing the mounting into the 8 cm diameter interaction waveguide.

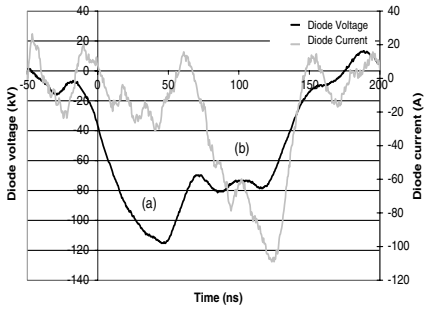

Figure 8. The accelerating potential and diode current plotted on the same timescale, cathode flux density 0.013 T.

the system. The anode current was simply measured using a commercial, magnetically cored Rogowski belt, figure 6. To measure the acceleration potential a similar belt was used to monitor the current flowing through the power supply matching resistor. Knowing the impedance of this resistor yielded the accelerating potential.

3. Measurements

Figure 8 illustrates the time evolution of the accelerating potential and the total diode current. The diode current was found to have a strong displacement current distortion due to the high capacitance of the vacuum diode. Since this distortion was a systematic effect it was possible to compensate by recording a trace where the field intensity was insufficient to cause the ignition of the vacuum spark and subsequently subtract this trace from the measurements. The ignition of a vacuum spark however is a statistical effect, and this process results in a degraded signal-to-noise ratio for the measurement. As the accelerating potential increased on the diode, the

cathode began to field emit at a low level. Ignition of the vacuum spark was not instantaneous in the experiment as the field was only slightly above threshold. This resulted in a slight overshoot in the voltage signal prior to the ignition of the cathode flare (region (a) in figure 8). Once the cathode started emitting it quickly reached the space charge limit with an impedance of ∼750 Ω (region (b)), the slow subsequent increase in the diode current was associated with the expansion of the cathode flare reducing the anode–cathode gap. The accelerating potential dropped from phase (a) to phase (b) as the Blumlein matching resistor was now shunted by the finite impedance of the accelerator, figure 6. The accelerating potential was typically in the range 75–85 kV depending on the precise control of the Blumlein charging circuit, with a maximum current collected on the entire anode (the diode current) of 120 A.

For a given maximum magnetic flux density in the interaction region, the beam current in the interaction space (as collected by the Faraday cup) was found to strongly increase with the flux density on the cathode as illustrated in figure 9 and was in all cases lower than the overall diode current. This implied that a significant amount of magnetic mirroring was occurring or that the beam was being scraped on some surface, probably the anode mesh support structure, in a manner dependent on the cathode magnetic field.

To demonstrate that a horseshoe distribution was being formed in electron velocity space within the resonant interaction region it was necessary to adjust the maximum plateau magnetic field in the interaction space whilst keeping all other parameters stable, placing the Faraday cup downstream from the maximum of the magnetic field and monitoring the changes in the beam current as a function of this field. The results of this measurement are illustrated in figure 10. The increasing maximum flux density experienced by the beam in all cases resulted in a decrease in the electron beam current except in the case where a flux density was applied to the cathode of 0.05 T where no clear trend was observed within the attainable range of plateau magnetic field of the apparatus. This progressive decrease in the beam current with increasing magnetic flux density indicated that the electron beam was being progressively mirrored, implying the required horseshoe distribution (figures 1 and 5) had been formed in electron velocity space. It was clear from the diagram in figure 10 that the electron beam current as a fraction of the total anode current increased markedly with the cathode flux density, consistent with figure 9, but that even with a flux density of 0.05 T on the cathode was still only part of the total anode current, though in this case there seemed to be no clear reduction due to mirroring. This alternative loss mechanism was assumed to be scraping (interception) of the electron beam on the anode mesh aperture.

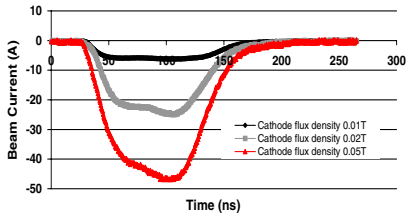

Figure 9. The electron beam current pulse as a function of the cathode magnetic flux density for a plateau flux density of 0.42 T.

4. Analysis

The variation of the electron beam current with the applied plateau magnetic field illustrated in figure 10 was fitted with a linear trend line. This was well matched with the numerical simulations, figure 11 (Speirs *et al* 2008). For a given operating regime (plateau 0.18 T) where energy exchange was observed between the electron beam and a radiation mode, this plot allowed the study of the electron velocity distribution by quantifying the progressive reduction in the beam current with increasing plateau magnetic field. The axial velocity of an electron at the operating flux density, B_{op}, (0.18 T) which would exactly mirror at some higher flux density B_{mr}, was estimated on the assumption that the electron kinetic energy was given by the accelerating potential (implicit in this assumption is that the electron distribution must be around a thin circle in $v_{\perp}$, $v_{\parallel}$ velocity space, e.g. figure 5) that energy was conserved and that particles mirrored when all

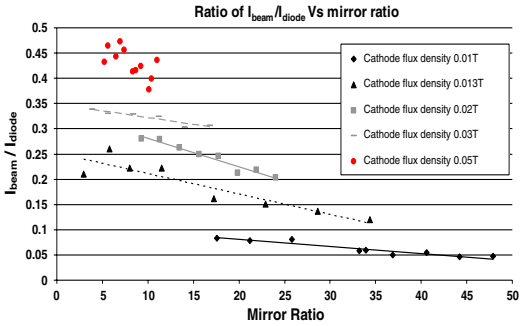

Figure 10. The fraction of electron beam current to anode current as a function of the ratio of the plateau to cathode flux density for five different cathode flux densities.

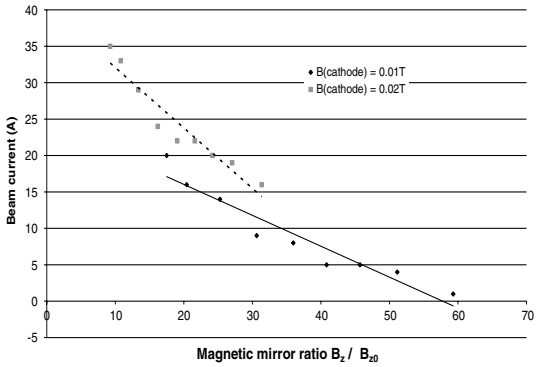

Figure 11. The decline of electron beam current as a function of mirror ratio as computed by the PiC code KARAT.

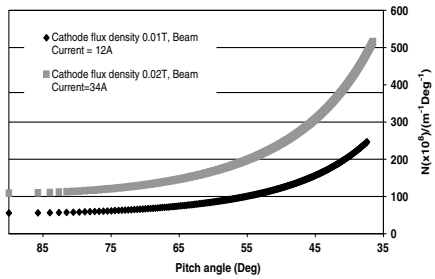

Figure 12. The analysis of the electron beam line density as a function of the pitch angle at a plateau flux density of 0.18 T and cathode flux densities of 0.01 T and 0.02 T.

of their kinetic energy became rotational. To determine the critical value of axial velocity which an electron should have at condition B_{op} in order to mirror at the higher flux B_{mr} the following formula may be used:

$$v_{zc} = v\sqrt{1 - \frac{B_{op}}{B_{mr}}}, \tag{2}$$

where v_{zc} is the critical value of the electron axial velocity at B_{op} which mirrors at B_{mr} and v is the total electron velocity. Given that the electron current in the apparatus is given by $I = -envz$ where n is the line density of the electrons (one-dimensional number density) and e is the electronic charge, one may use the reduction of the beam current with increasing magnetic flux density illustrated in figure 10 to estimate the line density 'Δn' of particles present within some range of axial velocities. This range of axial velocity may in turn be translated to a window in pitch angle $\theta = \arctan\left(\frac{v_\perp}{v}\right)$. The variation of '$n$' with the electron axial velocity or pitch angle at the initial plateau flux density of B_{op} may then be estimated. The results of this analysis are presented in figure 12 where $\Delta n/\Delta\theta$ is plotted against θ for cathode flux densities of 0.01 and 0.02 T and a plateau flux density of $B_{op} = 0.18$ T.

The graph clearly illustrated that at the higher cathode magnetic flux density (0.02 T), the number density of electrons at high velocity pitch angles, $>37^\circ$ was about twice that for the lower case, 0.01 T, commensurate with the variation in the total beam current. However, the fraction of the total beam power associated with electrons having a pitch angle exceeding 37° (corresponding to the fractional reduction of the beam power at the maximum magnetic flux used in the mirroring experiments, 0.47 T) was 1/3 and 2/3 for cathode flux densities of 0.02 T and 0.01 T, respectively. Therefore the experiment was able to control the total number of electron oscillators injected into the interaction region and also control their distribution in pitch angle. This allows the experiment to investigate the impact of variation in the particle distributions observed in the magnetosphere on the strength of the AKR: increasing the number of electron oscillators in the plateau of the magnetic field should increase the power of the emitted radiation; however, a large fractional population of electrons with little gyrational momentum are likely to absorb some of the emitted radiation. The progressively increasing number density with decreasing pitch angle is consistent with the adiabatic compression of an initially largely rectilinear electron beam having a small velocity spread, figure 1, where it is represented by the increasing height of the 'ridgeline' (black dashed line in figure 1(*c*)) of the contour plot as one tracks from a pitch angle of 90° to 0°.

5. Summary

Measurements of the current, accelerating potential and magnetic mirroring of the electron beam for an experiment to demonstrate the mechanism of AKR have been undertaken. The results showed electron beam currents varying from 5–50 A in the interaction region as a function of the magnetic flux density applied to the cathode. The formation of a horseshoe distribution function in electron velocity space by magnetic compression of the electron beam has been inferred from the measurements of the variation of the beam current with magnetic mirror ratio. Such an electron beam is consistent with the magnetospheric observations. The electron beam density and distribution has been controlled using the configurable electromagnets. The initial analysis

of the electron beam suggested that the number of high pitch angle electron oscillators in the interaction space at a resonant flux density of 0.18 T doubled as the cathode flux density increased from 0.01 to 0.02 T. However, the high cathode flux density also gave a much greater increase in low pitch factor electrons which are expected to contribute little to the interaction. This correlates well with the observations of the microwave radiation output power (Ronald *et al* 2008, McConville *et al* 2008).

Acknowledgments

This work was supported by the EPSRC and the STFC Centre for Fundamental Physics. Mr I S Dinwoodie is thanked for the construction of the apparatus and Professor V L Tarakanov for his advice on numerical simulations. Helpful discussions with Professor R A Cairns, Dr I Vorgul, Dr B J Kellett and Professor A Savilov are gratefully acknowledged.

References

Benson R F 1985 *J. Geophys. Res: Space Phys.* **90** 2753–84
Bingham R and Cairns R A 2002 *Phys. Scr.* **T98** 160–2
Bingham R and Cairns R A 2000 *Phys. Plasmas* **7** 3089–92
Bingham R, Kellett B J, Cairns R A, Vorgul I, Phelps A D R, Ronald K and Speirs D 2004 *Contrib. Plasma Phys.* **44** 382–7
Bratman V L, Cross A W, Denisov G G, He W, Phelps A D R, Ronald K, Samsonov S V, Whyte C G and Young A R 2000 *Phys. Rev. Lett.* **84** 2746–9
Burinskaya T M and Rauch J L 2007 *Plasma Phys. Rep.* **33** 28–37
Cairns R A, Speirs D C, Ronald K, Vorgul I, Kellett B J, Phelps A D R and Bingham R 2005 *Phys. Scr.* **T116** 23–6
Chu K R 2004 *Rev. Mod. Phys.* **76** 489–540
Cooke S J, Cross A W, He W and Phelps A D R 1996 *Phys. Rev. Lett.* **77** 4836–9
Cross A W, Spark S N, Ronald K, Phelps A D R and He W 1993 *Digest of the 18th Int. Conf. on Infrared and Millimeter Waves (SPIE 2104, Colchester, UK)* pp 448–9
Delory G T, Ergun R E, Carlson C W, Muschietti L, Chaston C C, Peria W, McFadden J P and Strangeway R 1998 *Geophys. Res. Lett.* **25** 2069–72
Denisov G G, Bratman V L, Cross A W, He W, Phelps A D R, Ronald K, Samsonov S V and Whyte C G 1998 *Phys. Rev. Lett.* **81** 5680–3
Ergun R E *et al* 1998 *Geophys. Res. Lett.* **25** 2061–4
Ergun R E, Carlson C W, McFadden J P, Delory G T, Strangeway R J and Pritchett P L 2000 *Astrophys. J.* **538** 456–66
Flyagin V A, Goldenberg A L and Nusinovich N S 1984 *Infrared Millim. Waves* **11** 179–226
Gaponov A V 1959 *Izv. Vyssh. Uchebn. Zaved. Radiofiz.* **2** 450–62
Gaponov A V 1959 *Izv. Vyssh. Uchebn. Zaved. Radiofiz.* **2** 837
Garven M, Spark S N, Cross A W, Cooke S J and Phelps A D R 1996 *Phys. Rev. Lett.* **77** 2320–3
Gurnett D A 1974 *J. Geophys. Res.: Space Phys.* **79** 4227
Latham R V 1983 *IEEE Trans. Electr. Insul.* **EI-18** 194–203
McConville S L *et al* 2008 *Plasma Phys. Control. Fusion* **50** 074010
Melrose D B, Ronnmark K G and Hewitt R G 1982 *J. Geophys. Res.: Space Phys.* **87** 5140
Mesyats G A 1991 *IEEE Trans. Plasma Sci.* **PS-19** 683–9
Mesyats G A and Proskurovsky D I 1989 *Pulsed Electrical Discharge in Vacuum* (Berlin: Springer)
Noer R J 1982 *Appl. Phys.* A **28** 1–24
Petelin M I 1993 *Plasma Phys. Control. Fusion* **35** B343–51
Pritchett P L and Strangeway R J 1985 *J. Geophys. Res.: Space Phys.* **90** 9650–62
Ronald K, Cross A W, Phelps A D R, He W, Yin H and Spark S N 1998 *IEEE Trans. Plasma Sci.* **PS-26** 375–82
Ronald K, Speirs D C, McConville S L, Phelps A D R, Robertson C W, Whyte C G, He W, Gillespie K M, Cross A W and Bingham R 2008 *Phys. Plasmas.* **15** 056503
Roux A, Hilgers A, Deferaudy H, LeQueau D, Louarn P, Perraut S, Bahnsen A, Jespersen M, Ungstrup E and Andre M 1993 *J. Geophys. Res.* **98** 11657–70
Somerville I C, MacGregor S J and Farish O 1990 *Meas. Sci. Technol.* **1** 865–8
Speirs D C *et al* 2008 *Plasma Phys. Control. Fusion* **50** 074011
Speirs D C, Vorgul I, Ronald K, Bingham R, Cairns R A, Phelps A D R, Kellett B J, Cross A W, Whyte C G and Robertson C 2005 *J. Plasma Phys.* **71** 665–74
Sprangle P and Drobot A T 1977 *IEEE Trans. Microw. Theory Tech.* **MTT-25** 528–44
Twiss R Q 1958 *Aust. J. Phys.* **11** 564–79
Vorgul I, Cairns R A and Bingham R 2005 *Phys. Plasmas* **12** 122903
Wagner J S, Lee L C, Wu C S and Tajima T 1984 *Radio Sci.* **19** 509–18
Wu C S and Lee L C 1979 *Astrophys. J.* **230** 621–6
Xu N S and Latham R V 1992 *Surf. Sci.* **274** 147–60

Radio frequency resonator structure and diagnostic measurements for a laboratory simulation of Auroral Kilometric Radiation[a)]

K. Ronald,[1,b),c)] D. C. Speirs,[1] S. L. McConville,[1] A. D. R. Phelps,[1] C. W. Robertson,[1] C. G. Whyte,[1] W. He,[1] K. M. Gillespie,[1] A. W. Cross,[1] and R. Bingham[1,2]
[1]*Scottish Universities Physics Alliance and Department of Physics, John Anderson Building, 107 Rottenrow, University of Strathclyde, Glasgow G4 0NG, United Kingdom*
[2]*Space Science and Technology Department, Science and Technology Facility Council, Rutherford Appleton Laboratory, Didcot OX11 0QX, United Kingdom*

(Received 18 November 2007; accepted 25 January 2008; published online 2 April 2008)

Auroral Kilometric Radiation is emitted from regions of depleted plasma density in the Earth's polar magnetosphere. The radiation frequency is close to the local electron cyclotron frequency, polarized in the X-mode with an efficiency of ~1%, with power up to 1 GW. Kinetic analysis of the instability in the descending auroral flux indicated that the phenomena scaled with the cyclotron frequency. Therefore, an experimental reproduction of the auroral geometry has been created scaled to laboratory dimensions by raising the radiation frequency to the microwave range. The experiment transports a 75–85 keV electron beam through a region of increasing magnetic flux density, with a mirror ratio of up to 30. The experiments measured the mode, spectrum, power, and conversion efficiency of the emitted radiation as a function of the mirror ratio in two resonance regimes, with frequencies of 4.42 and 11.7 GHz. The microwave diagnostics and measurements will be presented in this paper. © *2008 American Institute of Physics*. [DOI: 10.1063/1.2856649]

I. INTRODUCTION

Kilometer band radio emission from the Earth's polar magnetosphere, Auroral Kilometric Radiation (AKR), has been observed by multiple satellites.[1,2] The observations suggest that the radiation is produced above 3200 km in altitude in regions of low plasma density where the cyclotron frequency exceeds the plasma frequency by an order of magnitude. Measurements of the emitted radiation have revealed that it is close to the local cyclotron frequency, with the strongest emission at ~300 kHz, and the polarization and propagation are consistent with the X-mode.[3] The data also suggest that the peak rf output power can be up to 1 GW corresponding to ~1% (Refs. 1 and 4) of the auroral electron precipitation energy.[5–7] Due to the correlation between the emitted wave spectrum and the cyclotron frequency, it has been suspected for some time that the instability driving the production of this radiation was cyclotron[8–11] in nature. There exist two populations of high-energy electrons in the polar magnetosphere that have a high fraction of rotational momentum and could participate in this effect. Earthbound electrons are subject to magnetic compression as they experience progressively higher levels of magnetic flux, converting axial to gyrational momentum due to conservation of the magnetic moment, Eq. (1), and producing an electron beam with a horseshoe distribution in velocity space, Fig. 1. At the tips of this distribution, the electron density has a positive gradient in transverse velocity and may generate radiation by cyclotron emission.

$$\underline{\mu} = \pi r^2 i \hat{\underline{z}} = \frac{\gamma m v_\perp^2}{2B} \hat{\underline{z}}, \tag{1}$$

$\underline{\mu}$	the vector magnetic dipole moment of an electron orbit
B	magnetic flux, taken here to be orientated in $\hat{\underline{z}}$ direction
i	current associated with electron rotational orbit
r	radius of electron orbit
m	electronic rest mass
γ	Lorentz–Fitzgerald Factor
$v_\perp$	the rotational electron velocity

A fraction of this electron current can mirror over a range of altitudes, where the gyrational velocity of the electrons becomes equal to the total velocity, producing a space bound flux of particles that also has an appropriate velocity structure to contribute to this effect, Fig. 1. Due to the absence of low pitch electrons, this space bound flux was originally proposed to be responsible for the radiation emission when the cyclotron model was first mooted.[12,13] However, as the altitude increases, this mirrored distribution will tend to fill the "hole" in velocity pitch angle as the magnetic flux decreases. Since this distribution will carry significantly less energy than the earthbound flux, attention has recently become focused on the possibility of a cyclotron instability in the earthbound flux. A kinetic theory has been developed for cyclotron instabilities in the complex distribution function of the descending electrons.[14–17] The analysis demonstrated that the distributions could be unstable to emission at the cyclotron frequency and that all the major parameters would scale with

[a)]Paper VI2 4, Bull. Am. Phys. Soc. **52**, 347 (2007).
[b)]Invited speaker.
[c)]Electronic mail: K.Ronald@strath.ac.uk.

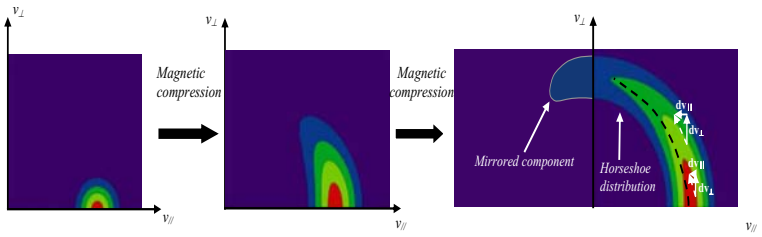

FIG. 1. (Color online) The velocity space evolution of an electron beam subject to an adiabatically increasing magnetic field.

the cyclotron frequency. This made it possible to conduct a laboratory experiment scaled into the microwave bands by increasing the magnetic flux density.[18,19] The experiment facilitates more control of the parameters than is possible in the magnetospheric observations and therefore permits the development of a greater understanding of the growth of the instability. The objective of these experiments was to demonstrate whether an electron beam in a horseshoe configuration in velocity space had sufficient free energy to support the efficiencies observed in the magnetosphere. This paper will describe the microwave resonant system, the rf diagnostics, and measurements of the radiation generated by the experiment as a function of the magnetic field configuration.

II. APPARATUS AND METHOD

As particles descend in the polar regions of the Earth's magnetosphere, they experience an increase in the magnetic flux due to their increasing proximity to the Earth's dipole and the ionosphere. At certain locations they encounter regions of depleted plasma density, the so-called plasma density cavities, and in these regions generate AKR. The structure of the polar magnetosphere is illustrated in Fig. 2 along with a laboratory analogue where an electron beam is injected along the axis of a system of electromagnets.

An electron gun was used to inject a beam into a fringing magnetic field,[20] generated by a set of six solenoids driven by dc current, Fig. 3. Each solenoid was wound from sections of OFHC copper tubing, and core cooled by water. The solenoids surround a 16 cm diameter drift tube and an 8.14 cm diameter interaction waveguide. Reducing the diameter of the vacuum envelope allowed the interaction region where the electrons were to be brought into resonance with the microwave fields to be held at a much higher magnetic flux density compared to the cathode, the compression ratio being controllable to a factor in excess of 30. Between the gun and the interaction region, the electron beam traversed a progressively increasing magnetic flux density, and an independent solenoid surrounding this region allowed the profile of the field to be adjusted to maintain conditions as close as possible to the adiabatic ideal. The electron injector was a

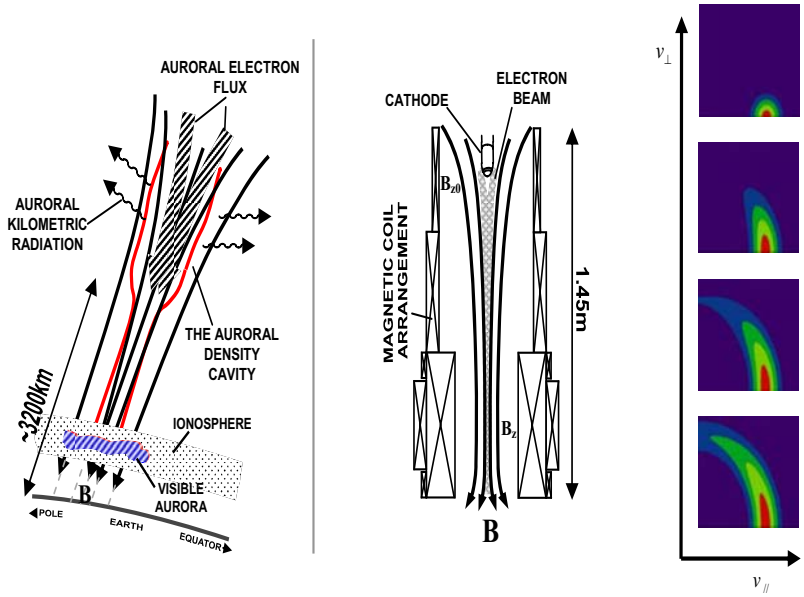

FIG. 2. (Color online) A comparison between the magnetospheric and experimental geometries, illustrating the plasma depleted Auroral Density Cavity, the comparative geometry of the experiment, and a schematic of the electromagnets.

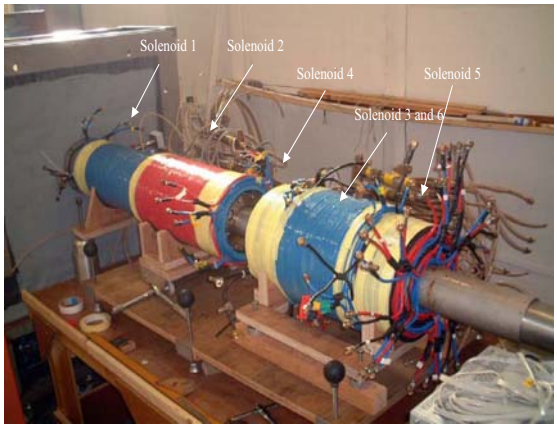

FIG. 3. (Color online) The magnetic solenoids being assembled in the laboratory, solenoids have been rolled apart to show the transition between the 16 cm diameter drift space and the 8 cm diameter interaction waveguide.

plasma flare electron gun producing an electron beam of up to 50 A in the interaction waveguide (120 A in the diode) with an energy of 75–85 keV. The cathode was fabricated by securing a velvet film to a metal surface and energized by applying a short 120 ns high-voltage pulse from a spark-gap-switched double Blumlein cable pulser.[20] Field emission initiated a cathode plasma that then supported space-charge-limited emission into the diode gap.

The maximum magnetic field in the 20 cm long plateau region was 0.5 T. The electron injector provided a controllable electron beam current of between 5 and 50 A depending on the settings of the magnetic fields, with a potential of 75–85 kV. This means the relativistic cyclotron frequency can be adjusted up to 12.5 GHz. The presence of the metallic boundaries of the 8.14 cm diameter interaction waveguide set very specific limits on the possible radiation modes that could be excited by the experiment. Such a structure bounds the radiation in the radial direction; this reproduces the natural radiation propagation boundaries that are proposed to exist in the magnetosphere due to the variations in the plasma density.[21]

Satellite observations indicate that the radiation is produced in the X-mode, meaning that the electric field vector is polarized and the wave is propagating transverse to the static magnetic field. In the resonant region of the experiment, the magnetic field is along the axis of the 8.14 cm diameter cylinder. Metallic cylinders support either transverse electric (TE) or transverse magnetic (TM) modes; all have their Poynting flux orientated along the length of the waveguide as a result of superposition of waves rebounding from the walls of the waveguide. TE modes have no axial component of the electric field, TM modes have no axial component of the magnetic field. The total wave vector makes an angle to the waveguide axis depending on the radiation frequency compared to the cutoff frequency of the specific mode. Close to waveguide cutoff, the axial wave vector tends to 0 and the radiation energy essentially bounces backwards and forwards across the waveguide axis. In the limit as the wave frequency approaches cutoff, the field components for TE modes show that only the axial component of the magnetic field is finite; all the transverse magnetic fields tend to zero. TM modes exhibit the opposite behavior, whereby the axial electric field remains finite while the transverse electric components tend to zero. Therefore, within the boundaries of the waveguide system, near cutoff TE modes offer the closest approach to the X-mode. This correlation between the X-modes and the near cutoff TE modes was expected given existing knowledge from applied physics where the CRM instability is used to generate millimeter wave radiation with high efficiency using near cutoff waveguide modes,[10,11,22–24] due to the minimization of the Doppler term as $k_{\|}$ tends to zero, Eq. (2), irrespective of the range of velocities.

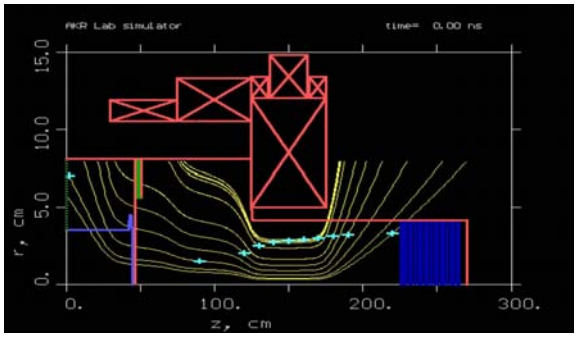

FIG. 4. (Color online) The experimental apparatus as programmed into the PiC code KARAT, illustrating the cathode, anode, and interaction waveguide, notice the extreme foreshortening in "z."

FIG. 5. (Color online) One of the WG12 receiving antenna, with calibrated attenuators and rectifying diodes installed in the Faraday cage.

$$\omega = n\omega_{ce} + k_{\parallel}v_{\parallel} \tag{2}$$

ω	wave frequency
$\omega_{ce} = eB/\gamma m_o$	relativistic cyclotron frequency
$k_{\parallel}$	parallel wave vector
$v_{\parallel}$	parallel velocity
n	cyclotron harmonic

Therefore, near cutoff TE modes were used for the electron beam interaction experiments. Two regimes of interaction were studied, one where the magnetic field system was operated at near maximum capacity, and resonance was sought with an electron cyclotron frequency of close to 11.7 GHz, and another with a cyclotron frequency of 4.42 GHz. These two specific frequencies were investigated as they correspond to the cutoff frequencies of the $TE_{0,3}$ and $TE_{0,1}$ modes in a 8.14 cm diameter waveguide. TE_0 modes were chosen in this first instance as they would allow the rf interaction to be modeled by the 2D axisymmetric version of the PiC code KARAT, due to the azimuthal symmetry of the modes. The layout of the apparatus programmed into the PiC code may be seen in Fig. 4. Ultimately the radiation propagated along the interaction waveguide and was launched into free space by an antenna of 8.14 cm diameter through a thin mylar vacuum window. The radiation was then detected by placing a receiving antenna in the far field of this aperture.

The microwave diagnostics consisted of waveguide stub receiving antennae, waveguide and coaxial attenuators, cutoff filters and real time Fourier transform spectrometers, and calibrated rectifying diodes. Two regimes of microwave emission were observed at 4.42 and 11.7 GHz. Precise measurements for these two frequencies required two separate pairs of receiving antenna, fabricated in Waveguide 12 (4.42 GHz) and Waveguide 18 (11.7 GHz). In all cases, the receivers were fitted with waveguide to coaxial adapters and were provided with attenuators based either on lumped element (4.42 GHz) or sliding vane (11.7 GHz) principles; the feed waveguides were also loaded with lossy volume attenuators (to ensure attenuation of harmonics). The entire receiver circuit was placed in a Faraday cage to prevent the relatively small microwave signals being swamped by the copious ~10 MHz noise generated by the switching of the Blumlein pulse modulator and ignition of the cathode emitter. Figure 5 illustrates one of the WG12 receivers. Transmission through each attenuator and waveguide to coaxial coupler was measured at the operating frequency by a vector network analyzer (Anritsu 37397A), Fig. 6.

The receivers were used in matched pairs, allowing one to be used as a control while modifications were made to the second. This allowed accurate measurements of the radiation patterns launched from the experiment to be obtained. The scanning apparatus for this measurement is illustrated in Fig. 7. The reference receiver was held in a fixed position to allow the results to be normalized against variability on the cathode behavior. The scanning antenna was moved in azimuthal angle. Measurements were taken in both polarizations (i.e., with the receiving antenna polarized along the

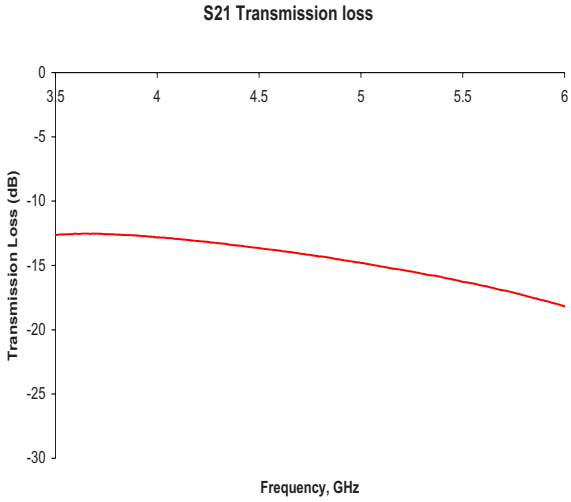

FIG. 6. (Color online) The transmission of one of the waveguide attenuators calibrated on the vector network analyzer.

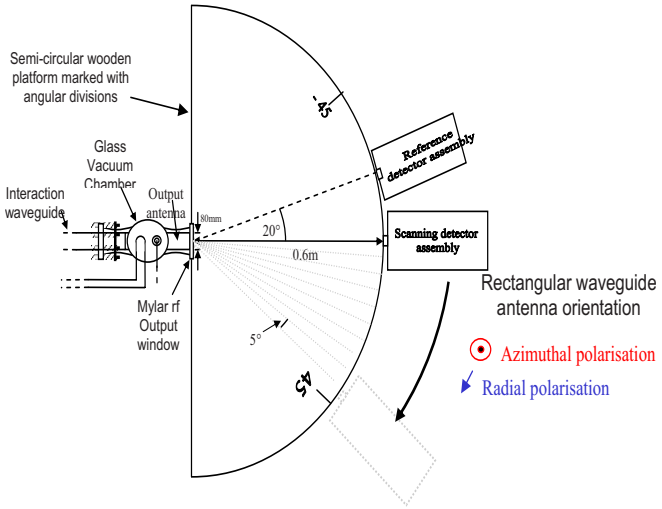

FIG. 7. (Color online) Illustration of the apparatus used to measure the experiments output antenna pattern.

azimuthal and radial directions). When it is assumed that, consistent with most cyclotron instabilities, the radiation is output with a time-integrated azimuthal symmetry, it becomes possible to identify the mode excited in the waveguide by comparison with the theoretical expectations for diffraction from such an aperture at a given frequency. The signals from the receivers were recorded in two distinct ways. For measurements of the antenna patterns, the coaxial output from the receivers was used to feed calibrated commercial rectifying diodes (Agilent 8474B), which were calibrated to fit their polynomial response curves, Fig. 8, of output video amplitude to input AC power and confirm their insensitivity to spectral variation. Such rectified signals were recorded on a deep memory 1 GHz Digital Oscilloscope. Rectified signals were also used in conjunction with waveguide cutoff filters to measure the output radiation frequency.

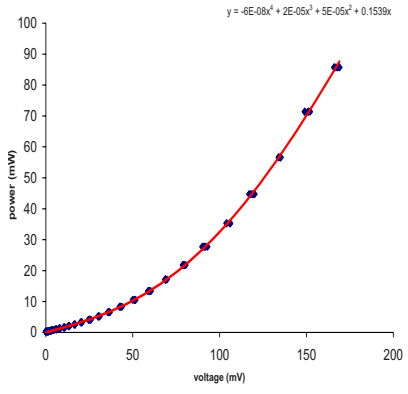

FIG. 8. (Color online) Calibration of a rectifying diode over the spectral range 4–5 GHz, showing the polynomial fit used to convert recorded video voltages to estimates of incident power.

An alternative system allowed the AC waveform captured by the receivers to be fed directly by low-loss, single-mode microwave coaxial cable to a deep memory 12 GHz microwave digital oscilloscope. Capturing of this entire waveform allowed a Fourier transform to be performed to obtain the output spectrum in a particularly convenient manner.

III. MEASUREMENTS

With the resonance adjusted to 4.42 GHz, the temporal variation of the microwave output signal is illustrated in Fig. 9. The large-amplitude variations were caused by oscillations in the energy of the injected electrons moving the electron beam in and out of resonance with the electromagnetic fields. The modulation of the electron energy arose due to the dynamically evolving impedance of the electron accelerator. Figure 10 shows a section of the AC waveform captured by the high-frequency oscilloscope and the Fourier transform of the entire output pulse. The spectrum clearly contains a strong signal at the expected frequency corresponding to the cyclotron frequency and the cutoff of the $TE_{0,1}$ mode in the interaction waveguide. The azimuthally polarized antenna pattern produced by the experiment is illustrated by the points in Fig. 11, plotted on the same axis as the theoretical prediction for the $TE_{0,1}$ mode from this aperture and radiation frequency. Clearly the two curves agree well until an azimuthal angle of 55°; the discrepancy at larger angles corresponds to interception of the microwave signal on the aluminum flange supporting the mylar vacuum window. Scattering of radiation from this flange made measurements of radiation diffracted at large angles impossible. With the receivers in radial polarization, the detected radiation was at the noise threshold (randomly scattered radiation) consistent with the theoretical expectation of zero signal.

Figure 12 shows the Fourier transform of the entire output pulse produced by the experiment when tuned for reso-

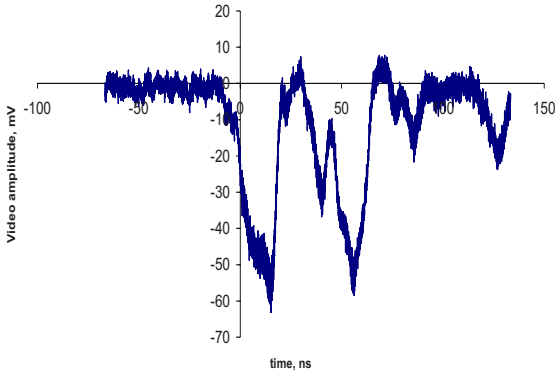

FIG. 9. (Color online) An example of the rectified output pulse from the experiment once tuned for resonance with the $TE_{0,1}$ mode; the time separated 60 mV spikes are due to ripple in the acceleration voltage.

nance at 11.7 GHz. Again the output signal has a strong spectral component at the cyclotron frequency, though there are some weak signals at slightly lower frequencies, possibly due to backwards wave resonances with alternative transverse modes. This frequency was close to the bandwidth limit of the oscilloscope, therefore it was checked by placing waveguide cutoff filters in the single-mode WG18 feedline. The results, also shown in Fig. 12, demonstrate the complete attenuation of the pulse amplitude as the filter was adjusted from 11.5 to 12.7 GHz. Measurements of the output antenna pattern for this high-frequency resonance are illustrated in Fig. 13. In this instance, both azimuthal and radial polarization gave strong signals and no clear single mode was observed. This was expected, since although the resonance was nominally tuned to excite the $TE_{0,3}$ mode, there exist a large number of modes with nearly degenerate cutoff frequencies, any of which might be generated. In addition, the first and second temporal output pulses exhibited at this resonance condition showed different variation in the radiation intensity with azimuthal angle, indicating that different mode mixtures were being excited in each case.

IV. ANALYSIS

The low-frequency 4.42 GHz resonance yielded output frequencies and mode content very close to those anticipated giving close correlation to the X-mode. Variation of the plateau flux density allowed the dependence of the instability on the differential between the wave frequency and the gyrofrequency (the cyclotron detuning) to be studied. The output amplitude was strongest for a fractional detuning $\Delta\omega/\omega \sim 2-3\%$. Since this experiment had a low magnetic field requirement, it was possible to map the 1D number density (line density) by progressively mirroring the electron beam.[20] This analysis, Fig. 14, showed that the number density of high pitch angle electrons increased with the cathode magnetic flux density, doubling as this flux density was increased from 0.01 to 0.02 T. One would therefore anticipate an increase in the output power with this change in the cathode flux density. Given that the mode content for these results was very clear, the theoretical antenna pattern was normalized to the experimental data at the peak lobe position

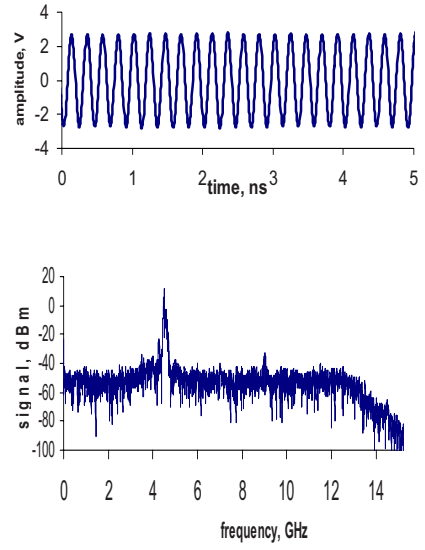

FIG. 10. (Color online) AC waveform captured on the deep memory microwave oscilloscope and the Fourier transform illustrating the spectral content of the experiments output, tuned for resonance with the $TE_{0,1}$ mode.

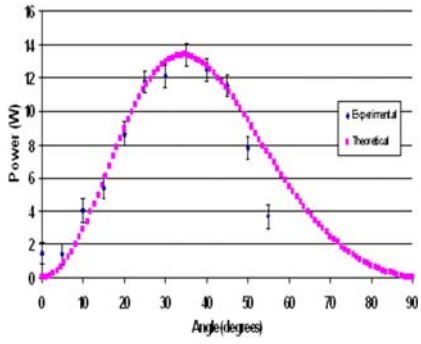

FIG. 11. (Color online) Antenna pattern produced from the experiment and compared to the theoretical predictions, tuned for resonance with the $TE_{0,1}$ mode.

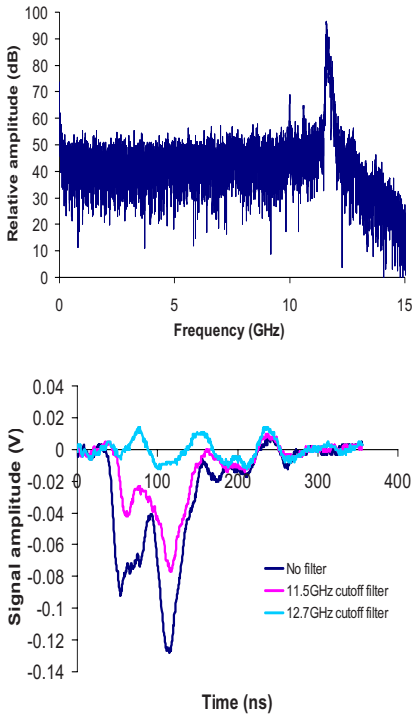

FIG. 12. (Color online) Output frequency of the experiment tuned for resonance with the $TE_{0,3}$ mode, measured by the FFT spectrometry method and by cutoff filters.

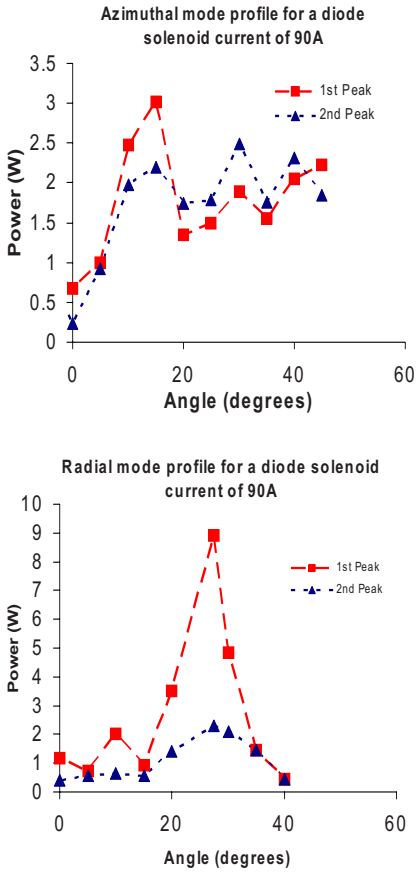

FIG. 13. (Color online) Antenna pattern produced from the experiment when tuned for resonance with the $TE_{0,3}$ mode illustrating the different mode content in the two temporal output pulses.

(where S/N was optimal) and the theoretical antenna pattern integrated over a half-sphere. The results showed that the total output power from the experiment was 19 and 35 kW for magnetic flux densities of 0.01 and 0.02 T, respectively, in broad agreement with the increase in the high pitch particle number density. In contrast, the efficiency falls from 2% to 1% with the same transition. This is again consistent with the variation in number density. For a cathode flux density of 0.01 T, 2/3 of the beam power was associated with the electron population having pitch angles $>37°$. Doubling the cathode flux (halving the mirror ratio) doubled the high pitch electron population, however in this configuration, only 1/3 of the beam power was associated with the high pitch electron population. Large numbers of low pitch electrons will tend to absorb the emitted radiation rather than emit it, reducing the efficiency.

The results obtained at the higher resonance frequency (11.7 GHz) are broadly in line with these conclusions. Analysis of the antenna patterns suggests multimode excitation and mode hopping, including the $TE_{0,3}$ and $TE_{2,3}$ modes of the waveguide, both of which are close to cutoff. Integration of the experimental antenna patterns was undertaken to estimate the radiated power (the complex mode mixture made fitting theoretical curves problematic), resulting in an estimate of 20 kW of output power with a radiation efficiency of 1%.

V. SUMMARY

The microwave output of a scaled experiment to demonstrate the mechanism of auroral kilometric radiation has been measured. The results showed output powers in the range 20–35 kW corresponding to electronic efficiencies of 1–2%

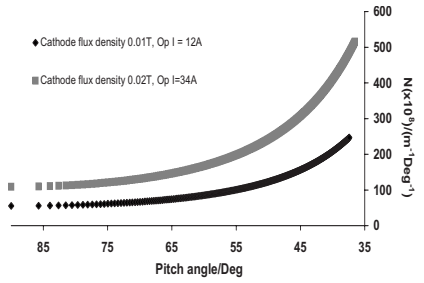

FIG. 14. Analysis of the electron beam line density as a function of the pitch angle at a plateau flux density of 0.18 T and cathode flux densities of 0.01 and 0.02 T.

varying as a function of cyclotron detuning and magnetic compression ratio (through the electron pitch angle distribution) for single-mode resonances at 4.42 GHz and multimode resonances at 11.7 GHz. The propagation and polarization angles of the radiation are perpendicular to the static magnetic field in all cases, corresponding to near cutoff TE waveguide modes. The radiation was strongly generated only where the electron beam was in close cyclotron resonance with the waveguide cutoff frequency. These results are in good agreement with the numerical simulations (Refs. 20 and 25) and observations from the magnetosphere where the radiation is emitted in the X-mode at close to the cyclotron frequency with an efficiency of around 1% of the auroral electron precipitation energy.

ACKNOWLEDGMENTS

Helpful discussions with Professor R. A. Cairns, Dr. I. Vorgul, Dr. B. J. Kellett, and Professor A. Savilov are gratefully acknowledged.

This work was supported by the EPSRC and the STFC Centre for Fundamental Physics. I. S. Dinwoodie is thanked for the construction of the apparatus and Professor V. L. Tarakanov for his advice on numerical simulations.

[1] D. A. Gurnett, J. Geophys. Res. **79**, 4227, DOI: 10.1029/JA079i028p04227 (1974).
[2] D. B. Melrose, K. G. Ronnmark, and R. G. Hewitt, J. Geophys. Res., [Space Phys.] **87**, 5140, DOI: 10.1029/JA087iA07p05140 (1982).
[3] R. F. Benson, J. Geophys. Res., [Space Phys.] **90**, 2753, DOI: 10.1029/JA090iA03p02753 (1985).
[4] P. L. Pritchett and R. J. Strangeway, J. Geophys. Res., [Space Phys.] **90**, 9650, DOI: 10.1029/JA090iA10p09650 (1985).
[5] R. E. Ergun, C. W. Carlson, J. P. McFadden, F. S. Mozer, G. T. Delory, W. Peria, C. C. Chaston, M. Temerin, R. Elphic, R. Strangeway, R. Pfaff, C. A. Cattell, D. Klumpar, E. Shelly, W. Peterson, E. Moebius, and L. Kistler, Geophys. Res. Lett. **25**, 2061, DOI: 10.1029/98GL00570 (1998).
[6] R. E. Ergun, C. W. Carlson, J. P. McFadden, G. T. Delory, R. J. Strangeway, and P. L. Pritchett, Astrophys. J. **538**, 456 (2000).
[7] G. T. Delory, R. E. Ergun, C. W. Carlson, L. Muschietti, C. C. Chaston, W. Peria, J. P. McFadden, and R. Strangeway, Geophys. Res. Lett. **25**, 2069, DOI: 10.1029/98GL00705 (1998).
[8] R. Q. Twiss, Aust. J. Phys. **11**, 564 (1958).
[9] A. V. Gaponov, Izv. Vyssh. Uchebn. Zaved., Radiofiz. **2**, 450 (1959); **2**, 837 (1959).
[10] P. Sprangle and A. T. Drobot, IEEE Trans. Microwave Theory Tech. **MTT-25**, 528 (1977).
[11] K. R. Chu, Rev. Mod. Phys. **76**, 489 (2004).
[12] C. S. Wu and L. C. Lee, Astrophys. J. **230**, 621 (1979).
[13] J. S. Wagner, L. C. Lee, C. S. Wu, and T. Tajima, Radio Sci. **19**, 509 (1984).
[14] R. Bingham and R. A. Cairns, Phys. Scr., T **T98**, 160 (2002).
[15] R. Bingham and R. A. Cairns, Phys. Plasmas **7**, 3089 (2000).
[16] I. Vorgul, R. A. Cairns, and R. Bingham, Phys. Plasmas **12**, 122903 (2005).
[17] R. Bingham, B. J. Kellett, R. A. Cairns, I. Vorgul, A. D. R. Phelps, K. Ronald, and D. Speirs, Contrib. Plasma Phys. **44**, 382 (2004).
[18] R. A. Cairns, D. C. Speirs, K. Ronald, I. Vorgul, B. J. Kellett, A. D. R. Phelps, and R. Bingham, Phys. Scr., T **T116**, 23 (2005).
[19] D. C. Speirs, I. Vorgul, K. Ronald, R. Bingham, R. A. Cairns, A. D. R. Phelps, B. J. Kellett, A. W. Cross, C. G. Whyte, and C. Robertson, J. Plasma Phys. **71**, 665 (2005).
[20] S. L. McConville, D. C. Speirs, K. Ronald, A. D. R. Phelps, A. W. Cross, R. Bingham, C. W. Robertson, C. G. Whyte, W. He, K. M. Gillespie, I. Vorgul, R. A. Cairns, and B. J. Kellett, "Demonstration of auroral radio emission mechanisms by laboratory experiment," Plasma Phys. Controlled Fusion (to be published).
[21] T. M. Burinskaya and J. L. Rauch, Plasma Phys. Rep. **33**, 28 (2007).
[22] V. L. Bratman, A. W. Cross, G. G. Denisov, W. He, A. D. R. Phelps, K. Ronald, S. V. Samsonov, C. G. Whyte, and A. R. Young, Phys. Rev. Lett. **84**, 2746 (2000).
[23] G. G. Denisov, V. L. Bratman, A. W. Cross, W. He, A. D. R. Phelps, K. Ronald, S. V. Samsonov, and C. G. Whyte, Phys. Rev. Lett. **81**, 5680 (1998).
[24] S. J. Cooke, A. W. Cross, W. He, and A. D. R. Phelps, Phys. Rev. Lett. **77**, 4836 (1996).
[25] D. C. Speirs, S. L. McConville, K. M. Gillespie, K. Ronald, A. D. R. Phelps, A. W. Cross, R. Bingham, C. W. Robertson, C. G. Whyte, I. Vorgul, R. A. Cairns, and B. J. Kellett, "Numerical simulation of auroral cyclotron maser processes," Plasma Phys. Controlled Fusion (to be published).

IOP Publishing Plasma Physics and Controlled Fusion

Plasma Phys. Control. Fusion **50** (2008) 074011 (15pp) doi:10.1088/0741-3335/50/7/074011

Numerical simulation of auroral cyclotron maser processes

D C Speirs[1], S L McConville[1], K M Gillespie[1], K Ronald[1], A D R Phelps[1], A W Cross[1], R Bingham[1,3], C W Robertson[1], C G Whyte[1], I Vorgul[2], R A Cairns[2] and B J Kellett[3]

[1] SUPA Department of Physics, University of Strathclyde, Glasgow, G4 0NG, UK
[2] School of Mathematics and Statistics, University of St Andrews, St Andrews, KY16 9SS, UK
[3] Space Physics Division, STFC, Rutherford Appleton Laboratory, Didcot, OX11 0QX, UK

E-mail: david.c.speirs@strath.ac.uk

Received 31 October 2007, in final form 31 January 2008
Published 3 June 2008
Online at stacks.iop.org/PPCF/50/074011

Abstract

Results are presented from a numerical investigation of radiation emission from an electron beam with a horseshoe-shaped velocity distribution. This process is relevant to the phenomenon of auroral kilometric radiation (AKR) which occurs in the polar regions of the Earth's magnetosphere. In these regions of the auroral zone, particles accelerated into the increasing magnetic field of the Earth's dipole develop a horseshoe-shaped velocity distribution through conservation of magnetic moment. It has been shown theoretically that this distribution is unstable to a cyclotron maser instability. A 2D particle-in-cell (PIC) code model was constructed to simulate a scaled laboratory experiment in which an electron beam subject to significant magnetic compression may be studied and brought into resonance with TE modes of an interaction waveguide. Results were obtained for electron beam energies of 75–85 keV, magnetic compression factors of up to 30 and electron cyclotron frequencies of 4.42 and 11.7 GHz. At 11.7 GHz, beam–wave coupling was observed with the TE_{03} mode and an RF output power of 20 kW was obtained corresponding to an RF conversion efficiency of 1.3%. At 4.42 GHz, excitation of the TE_{01} mode was observed with an RF output power of 35 kW for a cyclotron-wave detuning of 2%. This corresponds to an RF conversion efficiency of 2.6%. In both cases PiC particle velocity distributions show the clear formation of a horseshoe-shaped velocity distribution and subsequent action of a cyclotron maser instability. The RF conversion efficiencies obtained are also comparable with estimates for the AKR generation efficiency.

(Some figures in this article are in colour only in the electronic version)

1. Introduction

If a mainly rectilinear electron beam is subject to significant magnetic compression, conservation of magnetic moment results in the ultimate formation of a horseshoe-shaped velocity distribution. A similar scenario occurs where particles are accelerated into the auroral region of the Earth's magnetic dipole. Such a distribution has been shown to be unstable to an electron cyclotron maser instability (Bingham and Cairns 2000, Vorgul *et al* 2005) and it has been postulated that this may be the mechanism required to explain the production of terrestrial auroral kilometric radiation (AKR) and also radiation from other astrophysical objects such as stars and planets with a suitable magnetic field configuration (Bingham *et al* 2001, Zarka *et al* 2001, Willes and Wu 2004). AKR comprises a spectrum of discrete components of RF emission (Gurnett *et al* 1979, Menietti *et al* 2000) centred around a frequency of ∼300 kHz and sourced at high altitudes (∼1.5–3 Earth radii) within a region of plasma depletion in the auroral zone known as the auroral density cavity (Calvert 1981, Strangeway *et al* 1998, Burinskaya and Rauch 2007). Satellite observations have shown that the emissions are predominantly polarised in the R-X (right-hand-extraordinary) plasma mode (Benson 1985, Hanasz *et al* 2003) and that for a given altitude the spectrum of emission extends down to a lower cut-off of approximately the local relativistic electron cyclotron frequency (Pritchett *et al* 2002). As AKR cannot be detected from the ground, the earliest documented observations coincide with the launch of the first satellites equipped with suitable wave receiving antenna (Benediktov *et al* 1965, Dunckel *et al* 1970) and indeed all data pertaining to the AKR emissions and source region are the result of *in situ* or remote observations made by a large number of satellite missions.

To date, numerous theories have been proposed for the generation mechanism of AKR (Roux and Pellat 1979, Melrose *et al* 1982, Le Queau *et al* 1984) and almost all have considered the ∼5 keV auroral electron flux as the free energy source. The general consensus at present, however, is that AKR is generated by an electron cyclotron maser instability, a theory first proposed in 1979 by Wu and Lee (1979). Their particular model comprised a plasma kinetic description of growth in the X-mode due to a positive transverse gradient in the electron velocity distribution function ($\partial f_e/\partial v_\perp > 0$) of a loss-cone component in the auroral electron flux. This theory was widely accepted for many years (Pritchett 1984, Wagner *et al* 1984, Calvert 1995) although the loss-cone distribution was seldom observed as a well-defined component in particle data from within the auroral density cavity. Instead, a clear representation of an electron horseshoe distribution was often present in much of the published data (Ungstrup *et al* 1990, Ergun *et al* 2000) and was particularly evident in electron velocity distribution plots from the FAST satellite (Delory *et al* 1998). This led to the publication in 2000 of a new analytical theory by Bingham and Cairns considering X-mode dispersion and growth due to a horseshoe-shaped velocity distribution in the precipitating auroral electron flux (Bingham and Cairns 2000).

Figure 1 shows a diagrammatic representation of horseshoe distribution formation as a result of magnetic compression and associated evolution in the transverse velocity profile. The phase space is cut off at $v_\parallel = 0$ and does not show the magnetically mirrored component. If one considers the electron beam distribution in figure 1(*a*) with finite pitch factor and energy spread impingent on an increasing axial magnetic flux density, conservation of magnetic moment μ results in the conversion of axial velocity into perpendicular velocity. As $v_\perp \propto \sqrt{B_0}$, the resultant expansion in velocity space yields a half-horseshoe-like profile (figure 1(*b*)) with an increasing number of electrons present at high pitch factors across a positive gradient in the transverse velocity profile ($\partial f_e/\partial v_\perp > 0$). With reference to the analytical theory (Bingham and Cairns 2000), electrons across this positive gradient near the tip of the distribution may

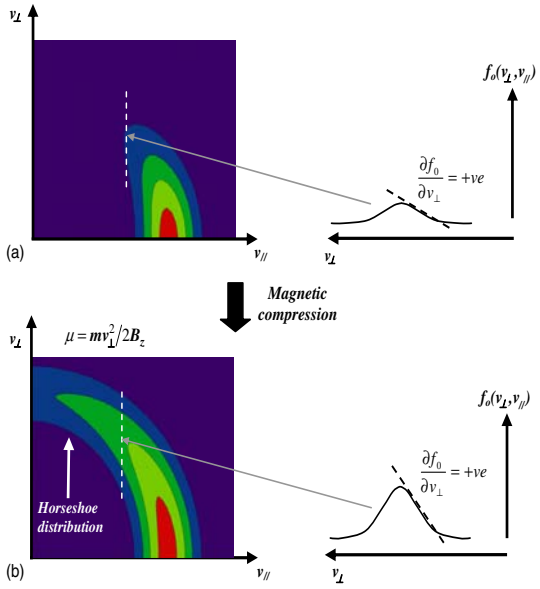

Figure 1. Contour plots and two dimensional plots showing the formation and evolution of the horseshoe distribution and transverse velocity profile (*a*) pre-magnetic compression and (*b*) post-magnetic compression.

undergo resonant energy transfer with an electromagnetic wave and as a result this portion of the distribution will appear to spread in $v_\perp$ and predominantly lose energy.

This work considers the numerical simulation of an experiment scaled to laboratory dimensions and microwave frequencies by increasing the cyclotron frequency $\omega_{ce} = eB/m_o\gamma$ to investigate the evolution of an electron beam subject to significant magnetic compression. The resultant beam was brought into resonance with microwave frequency electromagnetic waves in an interaction waveguide. Resonant interaction regimes were investigated with near cut-off TE modes of the waveguide due to the similarities between such modes and the X-mode in relative orientation of electromagnetic field components (i.e. a wave vector and electric field polarization perpendicular to the magnetostatic field). Figure 2 shows a diagrammatic representation of the scaled laboratory experiment in contrast to the terrestrial auroral process. The main concept of the experiment was the use of a tuneable solenoid arrangement to generate a convergent axial magnetic field culminating in a peak uniform section for resonant energy transfer within the interaction waveguide (Bingham *et al* 2004, Speirs *et al* 2005). Independent adjustment of the coil currents permitted variation in the magnetic compression factor, compression rate and the relativistic electron cyclotron frequency within the interaction region. Although the source region for AKR (the auroral density cavity) is typically many hundreds of wavelengths across (Calvert 1981, Ergun *et al* 2000), there is also evidence for smaller scale structures of the order of a few wavelengths across within the larger auroral density cavity (Louarn and Le Queau 1996a, 1996b). These smaller structures have a wavelength

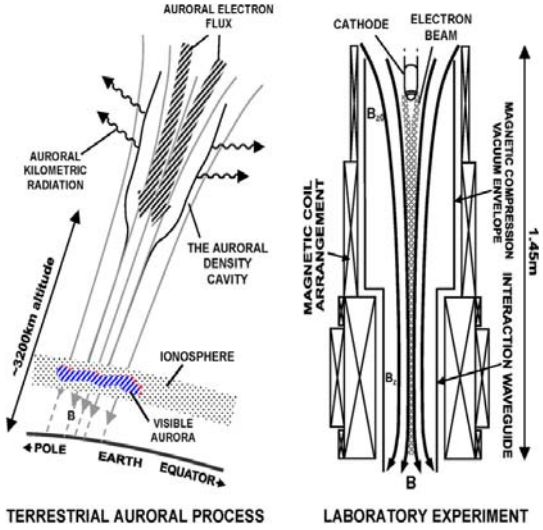

Figure 2. Comparative overview of the scaled laboratory experiment and the terrestrial auroral magnetosphere.

scaling close to the experiment modelled in the current paper. Furthermore, as previously mentioned the radiation propagation and polarization observed in the magnetosphere (X-mode) can be reproduced with the near cut-off TE modes of a waveguide. This reasoning suggested that relative to wavelength a small scale experiment could provide reasonable insight into the free energy available from a horseshoe electron distribution for the generation of such radiation.

2. PiC code simulations of beam compression and RF interaction geometry

For the purpose of simulating magnetic compression of the electron beam and any subsequent RF interaction, the 2D axisymmetric version of the finite-difference time domain PiC code KARAT was used (Tarakanov 1997, Speirs *et al* 2004). The 2D models allowed indirect observation of the distribution of particles in the transverse plane of motion. The code calculates the PiC electrons radial and azimuthal velocities and plots each particle location in transverse velocity space. Particles moving in circular orbits transition from v_{theta} and v_{radial} to $-v_{\text{theta}}$ and $-v_{\text{radial}}$ periodically. The formation of spatial bunches in a cyclotron instability corresponds to modulation of electron gyrational velocities ($v_\perp$) and in the limit of small modulation can be perceived in the 2D plots of v_{theta} versus v_{radial} as density variations. This is due to the bunch forming in a specific rotational phase with respect to the local ac field and thus at some instant in time having a 'location' in a plot of v_{theta} versus v_{radial}. In addition, energy modulation can be perceived through changes in the magnitude of $v_\perp = \sqrt{v_{\text{theta}}^2 + v_{\text{radial}}^2}$, illustrated by the area spanned by PiC particles in plots of v_{theta} versus v_{radial}.

An overview of the simulation geometry with electron beam trajectory is given in figure 3(*a*). The solenoid arrangement used comprised 6 coils. Solenoids 1 and 3 permitted

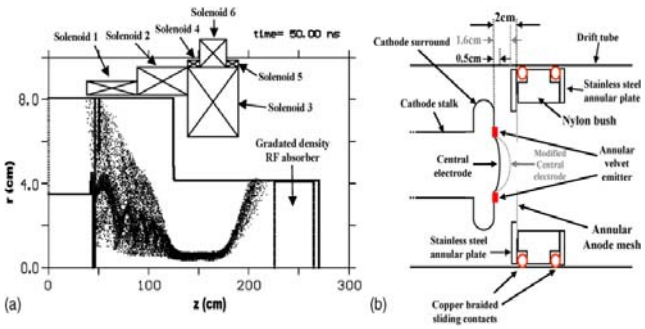

Figure 3. (*a*) 2D axisymmetric simulation geometry with electron beam trajectory plotted. (*b*) Detailed overview of electron gun geometry.

discrete adjustment of the magnetic flux density at the cathode and within the interaction waveguide, providing control over the net magnetic mirror ratio, whilst solenoid 2 facilitated adjustment of the magnetic compression rate. Solenoids 4 and 5 are shim coils which served to extend the region of peak uniform magnetic field within solenoid 3 to 25 cm in length. Solenoid 6 is an auxiliary coil that was used to achieve higher magnetic mirror ratios when performing a progressive mirroring analysis on the electron velocity distribution, although it was not used for the investigation of RF interactions. With reference to figure 3(*b*), the simulated electron gun comprises a 1 cm planar, annular emitter at a mean radius of 3 cm with a centrally mounted 12° domed electrode to impart an initial pitch spread to the electron beam. A planar anode mesh opposes the cathode emitter at a gap distance of 2 cm. After it passes the mesh the beam enters the convergent magnetic field of solenoids 1 and 2 and then passes into a 4.14 cm radius interaction waveguide (see figure 3(*a*)). The electron trajectories intercept the anode at $z \sim 210$ cm and a gradated density RF absorber is defined at $z > 2.5$ m to mitigate reflection and approximate a perfect microwave output window.

For the purpose of the initial investigation, two interaction regimes were investigated within the simulated geometry. The first comprised a peak axial magnetic flux density of 0.49 T for a near cut-off resonance with the TE_{03} mode in the interaction waveguide. The second was optimized for a near cut-off resonance with the TE_{01} mode requiring a peak axial magnetic field of 0.18 T. In both cases the PiC particle velocity distributions and electromagnetic field components were monitored at different axial positions within the simulation geometry. The magnetic field profiles used for both interaction regimes are plotted in figure 4, with the axial position of the cathode and end of solenoid 1 indicated. It should be noted that for the TE_{03} resonance regime the magnetic mirror ratio ($B_z/B_{z0} = 34$) is significantly larger than for the TE_{01} case ($B_z/B_{z0} = 18$). This is simply due to the higher peak magnetic field required for cyclotron resonance with the TE_{03} mode in the interaction waveguide.

2.1. TE_{03} resonance regime

Table 1 shows the simulation parameters used to investigate the TE_{03} resonance regime. The peak axial magnetic flux density of 0.49 T corresponds to a relativistic electron cyclotron frequency of 11.7 GHz. A beam–wave dispersion plot is presented in figure 5 corresponding to the simulation parameters for the TE_{03} resonance regime in table 1. Electron cyclotron

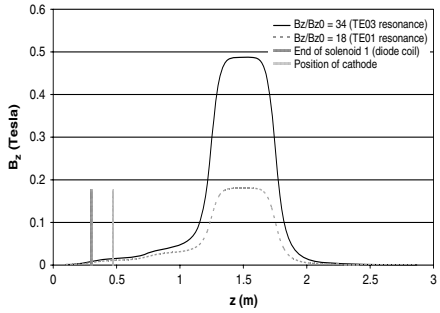

Figure 4. Axial magnetic field profiles corresponding to the two simulated beam–wave resonance regimes.

Table 1. Simulation parameters for the TE_{03} resonance regime.

	Value or range
Geometrical/simulation parameters	
Axial length	3 m
Radial width of drift tube	0.08 m
Radial width of interaction waveguide	0.0414 m
Axial mesh spacing	0.3 cm
Radial mesh spacing	0.1 cm
Simulation duration	100 ns
Time step	2.5 ps
Diode and electron beam parameters	
Electron beam limiting current I_b	18 A
Electron beam energy	85 keV
Anode–cathode gap	2 cm
Cathode emitter radius	2.5–3.5 cm
PiC particle merging factor	3 10^6 electrons/PiC particle
Convergent magnetic field parameters	
Magnetic mirror ratio B_z/B_{z0}	34
Peak axial magnetic field B_{z0}	0.49 T

beam dispersions (Chu 2004) for various pitch factors from $\alpha = v_\perp/v_\parallel = 0.5 \rightarrow 4$ are plotted along with dispersion curves for all TE and TM modes with cut-off frequencies in the vicinity of 11.7 GHz. A well-defined (narrowband) beam–wave resonance is present at 11.7 GHz with the TE_{03} mode. The resonance is near cut-off of the TE_{03} mode ($k_\parallel \rightarrow 0$) and is therefore relatively insensitive to variations in electron beam pitch factor. This should ensure a maximum in electron population resonant with the electromagnetic wave at 11.7 GHz across the pitch spread defining the horseshoe distribution.

The PiC particle velocity distributions were plotted at two axial positions (transverse planes) within the interaction waveguide after a 50 ns simulation duration. Each plane is delimited radially by the cross section of the waveguide. The corresponding plots are given in figure 6. At the point of entry to the peak, uniform axial magnetic field ($z = 1.3$ m) the $v_{transverse}$ versus v_{axial} plot shows a well-defined pitch spread in the PiC particle distribution

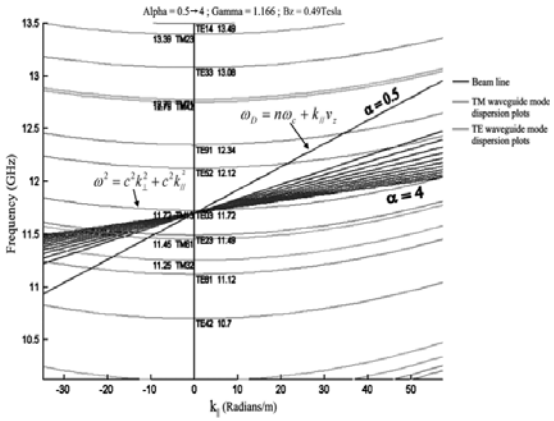

Figure 5. Beam–wave dispersion plot corresponding to the TE_{03} resonance regime in the simulated geometry.

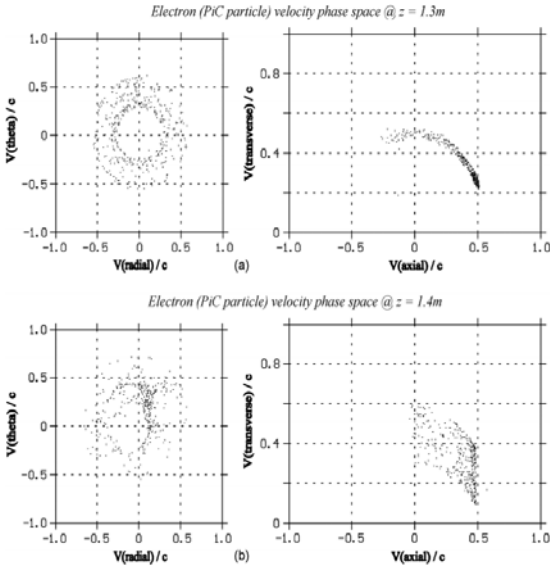

Figure 6. PiC particle velocity distributions measured on transverse planes within the simulation geometry at (*a*) $z = 1.3$ m and (*b*) $z = 1.4$ m for the TE_{03} resonance regime at 50 ns.

with a small mirrored component. The corresponding v_{theta} versus v_{radial} plot shows uniformity in the relative phase distribution of the PiC particles. Looking at the velocity distributions at $z = 1.4$ m the picture is very different. There is clear evidence of a cyclotron maser instability with significant smearing in the transverse velocity profile of the $v_{transverse}$ versus v_{axial} plot and indications of orbital phase bunching in the v_{theta} versus v_{radial} plot across a normalized velocity range of $0 \rightarrow 0.5$ in v_{theta} and v_{radial}. There is also evidence of significant energy extraction from the electron PiC particles in the v_{theta} versus v_{radial} plot from the reduced mean velocity of the electron population.

In order to evaluate mode content within the interaction waveguide, E_{theta} was plotted against radial coordinate at an axial position of $z = 1.4$ m and a simulation time of 50 ns. This corresponds to the axial coordinate where PiC particle velocity distributions appear most perturbed in figure 6. The resultant trace is shown in figure 7(*a*). A three-fold variation in E_{theta} can be seen across the radius of the waveguide which coupled with the azimuthal symmetry enforced by the 2D model indicates the presence of the TE_{03} mode. In order to investigate the spectral content of the RF output, a Fourier transform of E_{theta} was conducted over 45–50 ns at $z = 1.4$ m. The resultant plot is given in figure 7(*b*).

The spectrum of emission contains a clearly defined component at 11.7 GHz correlating with the relativistic electron cyclotron frequency and near cut-off resonance with the TE_{03} mode. Combined with the radial field structure shown in figure 7(*a*) it is evident that the interaction dispersion character of the beam–wave interaction is consistent with that plotted in figure 5.

The axial Poynting flux was monitored at $z = 2.2$ m, beyond the range of electron beam propagation and before the gradated density RF absorbing element. Figure 8 shows the corresponding temporal variation in axial Poynting flux at $z = 2.2$ m for a 100 ns simulation duration. There is significant initial growth in RF output between 40 and 48 ns followed by a saturated output power of ∼20 kW. At 60 ns there is an anomalous spike in output power of ∼60 kW; however, from 70 ns onwards the RF output appears to stabilize to a mean value of ∼20 kW. This corresponds to a beam–wave conversion efficiency of 1.3% which is consistent with estimates for the AKR generation efficiency (Gurnett 1974, Pritchett and Strangeway 1985). The fluctuating character of the RF output is also not inconsistent with chaotic spiking phenomenon reported in various cyclotron maser device variants (Ginzburg *et al* 1986, Ronald *et al* 2001).

2.2. TE_{01} resonance regime

Table 2 contains the simulation parameters used to investigate the TE_{01} resonance regime. In this case the peak axial magnetic field was reduced by up to 3% from the value corresponding to an exact, near cut-off resonance with the TE_{01} mode. This effective detuning of electron cyclotron frequency with respect to the wave frequency was implemented due to the observation of orbital phase bunching in the TE_{03} simulation results. For resonant energy transfer between an electron bunch and an electromagnetic wave, the relativistic electron cyclotron frequency ω_{ce} must be set marginally below that for perfect resonance. This is due to the relativistic increase in electron cyclotron frequency associated with energy transfer from the bunch to the wave (Chu 2004). In detuning the axial magnetic field by an optimum amount the beam–wave conversion efficiency can be enhanced. This was therefore investigated for the TE_{01} resonance regime.

The beam–wave dispersion character presented in figure 9 is for a near cut-off resonance between the electron beam and the TE_{01} waveguide mode at 4.42 GHz. As for the near cut-off

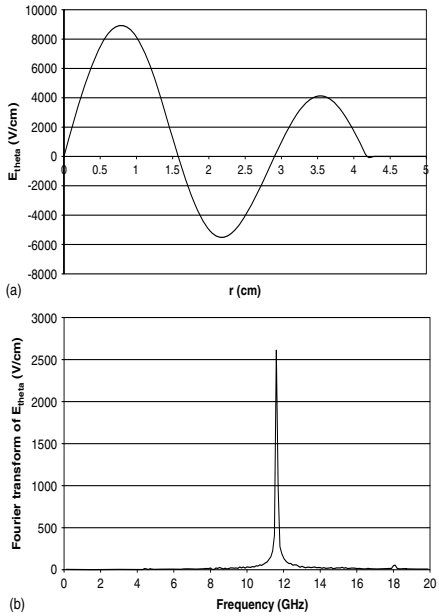

Figure 7. (*a*) Radial profile of E_{theta} at an axial position of $z = 1.4$ m and a simulation time of 50 ns. (*b*) Fourier transform of E_{theta} at an axial position of $z = 1.4$ m taken over the period $t = 45$–50 ns.

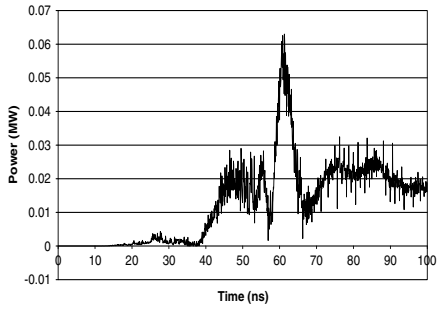

Figure 8. Axial Poynting flux measured at $z = 2.2$ m across the interaction waveguide.

TE_{03} resonance in figure 5, the TE_{01} resonance is relatively unaffected by variations in electron beam pitch factor α.

PiC particle distribution plots from the TE_{01} resonance regime were consistent with those previously outlined in figure 6 for the TE_{03} resonance regime. There was clear evidence

Table 2. Simulation parameters for the TE_{01} resonance regime.

	Value or Range
Geometrical/simulation parameters	
Axial length	3 m
Radial width of drift tube	0.08 m
Radial width of interaction waveguide	0.0414 m
Axial mesh spacing	0.3 cm
Radial mesh spacing	0.1 cm
Simulation duration	275 ns
Time step	2.5 ps
Diode and electron beam parameters	
Electron beam limiting current I_b	18 A
Electron beam energy	75 keV
Anode–cathode gap	2 cm
Cathode emitter radius	2.5–3.5 cm
PiC particle merging factor	3 10^6 electrons/PiC particle
Convergent magnetic field parameters	
Magnetic mirror ratio B_z/B_{z0}	18
Peak axial magnetic field B_{z0}	0.18 T (detuning from 0.175 to 0.178 T)

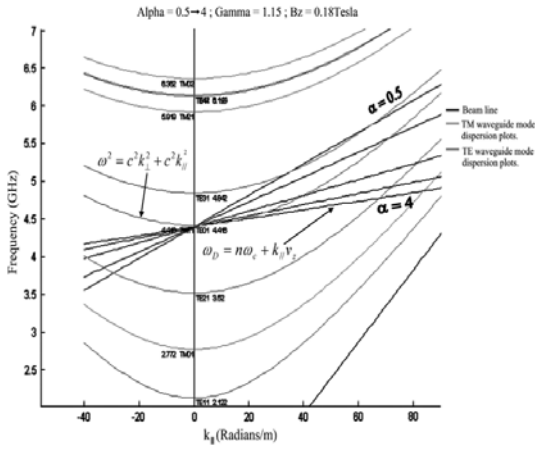

Figure 9. Beam–wave dispersion plot corresponding to the TE_{01} resonance regime in the simulated interaction geometry.

of energy transfer between the beam and the wave in the $v_{transverse}$ versus v_{axial} plots and indications of azimuthal phase modulation in the v_{theta} versus v_{radial} plots. Figure 10(*a*) shows the radial dependence of E_{theta} at $z = 1.4$ m and $t = 50$ ns for a cyclotron-wave detuning of 1%. A variation in field corresponding to the fundamental radial mode is present across the interaction waveguide serving to confirm excitation of the TE_{01} mode within the simulated geometry.

Figure 10(*b*) shows the corresponding Fourier transform of E_{theta} over $t = 45$–50 ns at $z = 1.4$ m within the interaction waveguide. As expected a singular, narrowband spectral

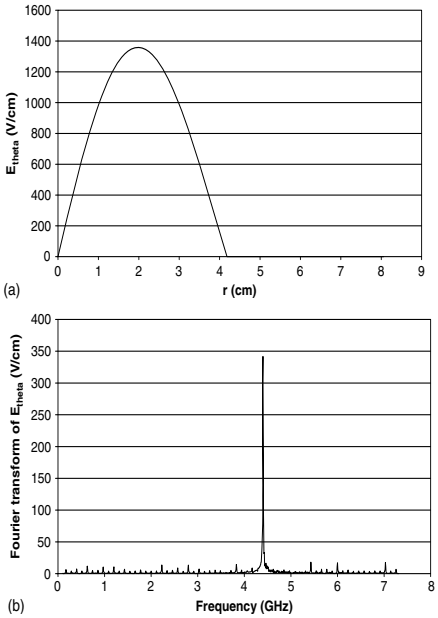

Figure 10. (*a*) Radial profile of E_{theta} at an axial position of $z = 1.4$ m and a simulation time of 50 ns. (*b*) Fourier transform of E_{theta} at an axial position of $z = 1.4$ m over the period $t = 45$–50 ns.

component is present at 4.42 GHz correlating with the cut-off frequency of the TE_{01} mode and the relativistic electron cyclotron frequency at the peak of the axial magnetic field. These results were observed consistently for cyclotron-wave detunings of 1%, 2% and 3%. There were however significant variations in axial Poynting flux and RF conversion efficiency for the different detunings. This is illustrated in figure 11 which shows the temporal variation in axial Poynting flux at $z = 2.2$ m for the three detunings investigated. In particular, there was a marked variation in the time at which RF output commences. This was most extreme for a detuning of 3% where significant RF output did not occur until 120 ns had elapsed. In contrast, for 1% and 2% detunings growth commenced at 50 ns and 60 ns, respectively. Both 2% and 3% detunings exhibited steady growth rates reaching a relatively stable saturated output power at 150 ns and 180 ns, respectively; however, for 1% detuning there was a sharp drop in output power at 120 ns followed by a secondary region of growth. These large amplitude power fluctuations perpetuate for the 1% detuning case and, in common with the TE_{03} results, are not inconsistent with chaotic spiking phenomena (Ginzburg *et al* 1986, Ronald *et al* 2001). After 250 ns, a 2% detuning yielded the highest stable output power of ∼35 kW corresponding to an RF conversion efficiency of 2.5%. This is only marginally higher than for 3% detuning although a 2% detuning resulted in earlier growth and saturation of the instability.

In general, the RF conversion efficiencies for the TE_{01} resonance regime are around double those obtained from the TE_{03} simulations, with a 2–3% cyclotron-wave detuning resulting in significant improvements in RF output stability. The peak RF conversion efficiency of 2.5% is

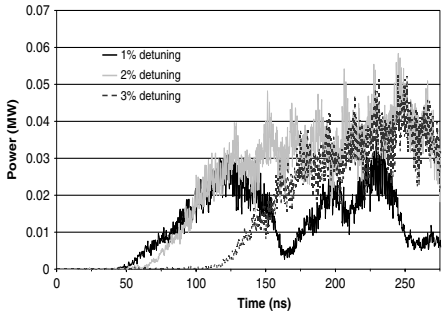

Figure 11. Temporal variation in axial Poynting flux measured at $z = 2.2$ m for three different cyclotron-wave detunings.

still however of a similar order to estimates of the AKR generation efficiency (Gurnett 1974, Pritchett and Strangeway 1985).

3. Beam velocity distributions and one dimensional number densities

Measurements of the transported electron beam current with increasing peak-plateau magnetic flux density were used in the TE_{01} experiment to study the electron velocity distribution function. As the magnetic flux density in the peak-plateau region was progressively increased above the value corresponding to a desired cyclotron resonance, B_{op}, a larger proportion of the electron population having an axial velocity component $v_z < v_{crit}$ at B_{op} was mirrored. This provided a mechanism to analyse the number of electrons occupying any range of axial velocities $v_{z2} < v_{z1}$ from the progressive decrease in measured electron beam current with increasing magnetic mirror ratio, figure 12(*a*).

This process was undertaken numerically as well as experimentally for the TE_{01} resonance regime to ensure that the simulations had a similar distribution of high pitch factor electrons to the experiment for a given magnetic field configuration. It was not possible to perform this measurement experimentally for the TE_{03} resonance. Two different cathode magnetic flux densities were used to provide control of the electron beam current and velocity distribution across an extended range of magnetic mirror ratios. By increasing the end displacement of the central domed electrode in simulation to 1.6 cm from the cathode emitter surface (see figure 3(*b*)) a close match was obtained between the modelled and experimental electron pitch distributions in the interaction space (figure 12(*b*)). When this matched electron distribution was used in simulations of the TE_{01} resonant interaction, RF output powers of 20 kW and 50 kW were predicted for cathode magnetic flux densities of 0.01 T ($B_z/B_{z0} = 18$) and 0.02 T ($B_z/B_{z0} = 9$), respectively. These are in good agreement with output powers obtained from the laboratory experiment for the TE_{01} resonant interaction of 19 kW and 35 kW for cathode magnetic flux densities of 0.01 T and 0.02 T, respectively (McConville *et al* 2008, Ronald *et al* 2008).

4. Summary and conclusions

In summary, PiC code simulations have been conducted to investigate the magnetic compression of an electron beam in a scaled experimental geometry and subsequent resonant

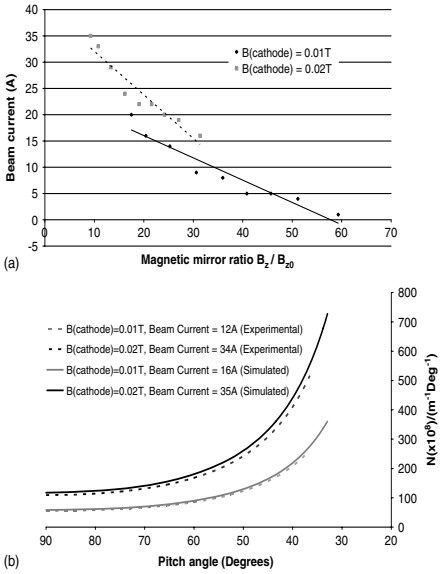

Figure 12. (*a*) Simulated variation in transported (unmirrored) electron beam current with magnetic mirror ratio. (*b*) Numerically modelled electron pitch distributions for a modified electron gun geometry in comparison with experimental results. Both cases correspond to the TE_{01} resonance regime for cathode magnetic flux densities of 0.01 T and 0.02 T, respectively.

energy transfer between the resultant electron velocity distribution and TE modes of an interaction waveguide. Two cyclotron resonance regimes were investigated, one optimized for coupling with the TE_{03} mode of the interaction waveguide and the other tuned for resonance with the TE_{01} mode. In both cases the evolution of PiC particle velocity distributions with axial position was monitored and the field structure analysed within the interaction waveguide.

For the TE_{03} resonance regime, pitch expansion of the electron beam was clearly evident in the PiC particle velocity distributions followed by a spreading in $v_\perp$ as a result of energy transfer with the electromagnetic wave. After a 50 ns run a three fold variation in E_{theta} was present across the radius of the interaction waveguide serving to indicate excitation of the TE_{03} mode. A Fourier transform of E_{theta} shows the presence of a well-defined spectral component at 11.7 GHz correlating with the cut-off frequency of the TE_{03} mode and the relativistic electron cyclotron frequency of the electron beam. The temporal variation in axial Poynting flux shows a saturated RF output power of 20 kW after 80 ns. This corresponds to an RF conversion efficiency of 1.3% and is relatively consistent with estimates for the AKR generation efficiency (Gurnett 1974, Pritchett and Strangeway 1985).

In the TE_{01} resonance regime, cyclotron-wave detunings of 1%, 2% and 3% were investigated to evaluate the effect on RF conversion efficiency and the temporal stability of RF output. For all three detunings, PiC particle velocity distributions indicated the clear action of a cyclotron maser instability with spreading in the transverse velocity profile and modulation

of the orbital velocity distribution. Spectral output was well defined with a singular component at 4.42 GHz corresponding to the relativistic electron cyclotron frequency and a near cut-off resonance with the TE_{01} mode. A 2% cyclotron detuning yielded the highest stable RF output power of ∼35 kW corresponding to an RF conversion efficiency of 2.6%. This was roughly double that obtained for the TE_{03} resonance regime, although still of a similar order to estimates of the AKR generation efficiency.

Finally, matching of electron pitch distributions between simulation and experiment was achieved through adjustment of the cathode central electrode displacement from the simulated emitter surface. Using the experimentally matched electron pitch distributions in simulation of the TE_{01} resonance regime, RF output powers of 20 kW and 50 kW were obtained for magnetic mirror ratios of $B_z/B_{z0} = 18$ and $B_z/B_{z0} = 9$, respectively. These output powers are in good agreement with results from the laboratory experiment of 19 kW and 35 kW for $B_z/B_{z0} = 18$ and $B_z/B_{z0} = 9$, respectively (McConville *et al* 2008, Ronald *et al* 2008).

Acknowledgments

The EPSRC and the STFC Centre for Fundamental Physics supported this work. Professor V L Tarakanov is thanked for his assistance with the numerical model and Mr I S Dinwoodie for assistance in creating the experimental apparatus. Helpful conversations with Professor A Savilov are also gratefully acknowledged.

References

Benediktov E A, Getmantsev G G, Sazonoy Yu A and Tarasov A F 1965 *Kosm. Issled.* **3** 614
Benson R F 1985 *J. Geophys. Res.—Space Phys.* **90** 2753–84
Bingham R and Cairns R A 2000 *Phys. Plasmas* **7** 3089–92
Bingham R, Cairns R A and Kellett B J 2001 *Astron. Astrophys.* **370** 1000–3
Bingham R, Kellett B J, Cairns R A, Vorgul I, Phelps A D R, Ronald K and Speirs D C 2004 *Contrib. Plasma Phys.* **44** 382–7
Burinskaya T and Rauch J 2007 *Plasma Phys. Rep.* **33** 28–37
Calvert W 1981 *Geophys. Res. Lett.* **8** 919–21
Calvert W 1995 *J. Geophys. Res.* **100** 14887–94
Chu K R 2004 *Rev. Mod. Phys.* **76** 489–540
Delory G T, Ergun R E, Carlson C W, Muschietti L, Chaston C C, Peria W, McFadden J P and Strangeway R 1998 *Geophys. Res. Lett.* **25** 2069–72
Dunckel N, Ficklin B, Borden L and Helliwell R A 1970 *J. Geophys. Res.* **75** 1854–62
Ergun R E, Carlson C W, McFadden J P, Delory G T, Strangeway R J and Pritchett P L 2000 *Astrophys. J.* **538** 456–66
Ginzburg N S, Nusinovich G S and Zavolsky N A 1986 *Int. J. Electron.* **61** 881–94
Gurnett D A 1974 *J. Geophys. Res.* **79** 4227–38
Gurnett D A, Anderson R R, Scarf F L, Fredricks R W and Smith E J 1979 *Space Sci. Rev.* **23** 103–22
Hanasz J, Panchenko M, de Feraudy H, Schreiber R and Mogilevsky M M 2003 *J. Geophys. Res.* **108** SMP14-1
Le Queau D, Pellat R and Roux A 1984 *J. Geophys. Res.* **89** 2831–41
Louarn P and Le Queau D 1996a *Planet. Space Sci.* **44** 199–210
Louarn P and Le Queau D 1996b *Planet. Space Sci.* **44** 211–24
McConville S L *et al* 2008 *Plasma Phys. Control. Fusion* **50** 074010
Melrose D B, Ronnmark K G and Hewitt R G 1982 *J. Geophys. Res.* **87** 5140–50
Menietti J D, Persoon A M, Pickett J S and Gurnett D A 2000 *J. Geophys. Res.—Space Phys.* **105** 18857–66
Pritchett P L 1984 *Phys. Fluids* **27** 2393–6
Pritchett P L and Strangeway R J 1985 *J. Geophys. Res.—Space Phys.* **90** 9650–62
Pritchett P L, Strangeway R J, Ergun R E and Carlson C W 2002 *J. Geophys. Res.* **107** 1437
Ronald K, Cross A W, Phelps A D R and He W 2001 *J. Phys. D: Appl. Phys.* **34** L17–22
Ronald K, Speirs D C, McConville S L, Phelps A D R, Robertson C W, Whyte C G, He W, Gillespie K M, Cross A W and Bingham R 2008 *Phys. Plasmas* at press
Roux A and Pellat R 1979 *J. Geophys. Res.* **84** 5189–98

Speirs D C, Phelps A D R, Konoplev I V, Cross A W and He W 2004 *Rev. Sci. Instrum.* **75** 826–31
Speirs D C, Vorgul I, Ronald K, Bingham R, Cairns R A, Phelps A D R, Kellett B J, Cross A W, Whyte C G and Robertson C W 2005 *J. Plasma Phys.* **71** 665–74
Strangeway R J *et al* 1998 *Geophys. Res. Lett.* **25** 2065–8
Tarakanov V P 1997 *'KARAT Code User Manual'* (Springfield, VA: Berkeley Research Associates Inc.)
Ungstrup E, Bahnsen A, Wong H K, Andre M and Matson L 1990 *J. Geophys. Res.* **95** 5973–81
Vorgul I, Cairns R A and Bingham R 2005 *Phys. Plasmas* **12** 122903
Wagner J S, Lee L C, Wu C S and Tajima T 1984 *Radio Sci.* **19** 509–18
Willes A J and Wu K 2004 *Mon. Not. R. Astron. Soc.* **348** 285–96
Wu C S and Lee L C 1979 *Astrophys. J.* **230** 621–6
Zarka P, Treumann R A, Ryabov B P and Ryabov V B 2001 *Astrophys. Space Sci.* **277** 293–300

IOP PUBLISHING PLASMA PHYSICS AND CONTROLLED FUSION

Plasma Phys. Control. Fusion **50** (2008) 124038 (11pp) doi:10.1088/0741-3335/50/12/124038

3D PiC code simulations for a laboratory experimental investigation of Auroral Kilometric Radiation mechanisms

K M Gillespie[1], D C Speirs[1], K Ronald[1], S L McConville[1], A D R Phelps[1], R Bingham[1,2], A W Cross[1], C W Robertson[1], C G Whyte[1], W He[1], I Vorgul[3], R A Cairns[3] and B J Kellett[2]

[1] SUPA Department of Physics, John Anderson Building, 107 Rottenrow, University of Strathclyde, Glasgow, G4 0NG, UK
[2] Space Science and Technology Department, STFC Rutherford Appleton Laboratory, Didcot, OX11 0QX, UK
[3] School of Mathematics and Statistics, University of St Andrews, St Andrews, KY16 9SS, UK

E-mail: karen.gillespie@strath.ac.uk

Received 2 June 2008
Published 5 November 2008
Online at stacks.iop.org/PPCF/50/124038

Abstract

Auroral Kilometric Radiation (AKR), occurs naturally in the polar regions of the Earth's magnetosphere where electrons are accelerated by electric fields into the increasing planetary magnetic dipole. Here conservation of the magnetic moment converts axial to rotational momentum forming a horseshoe distribution in velocity phase space. This distribution is unstable to cyclotron emission with radiation emitted in the X-mode. In a scaled laboratory reproduction of this process, a 75–85 keV electron beam of 5–40 A was magnetically compressed by a system of solenoids and emissions were observed for cyclotron frequencies of 4.42 GHz and 11.7 GHz resonating with near cut-off $TE_{0,1}$ and $TE_{0,3}$ modes, respectively. Here we compare these measurements with numerical predictions from the 3D PiC code KARAT. The 3D simulations accurately predicted the radiation modes and frequencies produced by the experiment. The predicted conversion efficiency between electron kinetic and wave field energy of around 1% is close to the experimental measurements and broadly consistent with quasi-linear theoretical analysis and geophysical observations.

(Some figures in this article are in colour only in the electronic version)

1. Introduction

Electrons precipitating into the Earth's magnetosphere are subject to an increasing magnetic field with decreasing altitude. In the absence of collisions and given that the field increases slowly compared with the electron oscillation period, the adiabatic conservation of magnetic moment comes into effect:

$$\underline{\mu} = \pi r^2 i \hat{\underline{z}} = \frac{\gamma m v_\perp^2}{2B} \hat{\underline{z}},$$

where $\underline{\mu}$ is the vector magnetic dipole moment of an electron orbit, B the magnetic flux density, taken here to be orientated in the $\underline{z}$ direction, i the current associated with the electron rotational orbit, r the radius of electron orbit, m the electronic rest mass, γ the Lorentz Fitzgerald factor and $v_\perp$ the rotational electron velocity.

Electrons entering the Earth's magnetic dipole structure have a spread in their initial velocity. Those electrons having a small initial component of velocity perpendicular to the magnetic flux lines experience an increase in their rotational component of velocity as they descend towards the atmosphere. The effect of this process is that an initially primarily rectilinear electron beam forms a horseshoe distribution in electron velocity space with a significant number of electrons having high pitch angles $\theta = \arctan(v_\perp / v)$, and a region with a positive gradient of number density with perpendicular velocity, $\mathrm{d}n/\mathrm{d}v_\perp$. This is illustrated schematically in figures 1(*a*) and (*c*). Such horseshoe electron distributions have been measured in the Auroral Kilometric Radiation (AKR) source region within the polar magnetosphere (Delory *et al* 1998, Ergun *et al* 2000). In addition, part of the electron stream is 'mirrored', reversing its direction of motion along the magnetic field lines once all of its kinetic energy becomes associated with rotational motion providing a second energetic electron population in the auroral magnetosphere, the space bound component.

Advances in satellite technology over the last few decades have made it possible to obtain quantitative data on the phenomenon of AKR (Gurnett *et al* 2001, Roux *et al* 1993). The magnetospheric measurements have revealed that the radiation emissions are sourced in regions of plasma depletion ($\omega_{pe} \ll \omega_{ce}$) at an altitude of 1.5–3 Earth radii. The frequency observed at any given altitude extends down to the local electron cyclotron frequency with the strongest emission at around 300 kHz. The wave propagation and polarization directions suggest that the radiation is generated in the X-mode (Benson 1985) with a peak power $\sim 10^9$ W, corresponding to $\sim$1% (Gurnett 1974, Pritchett and Strangeway 1985) of the auroral electron precipitation energy (Delory *et al* 1998, Ergun *et al* 1998, 2000). The availability of accurate data allows for meaningful comparison with theoretical expectations and has resulted in a significant research effort to explain the unusually high efficiency of this natural process, resulting in a number of models for the emission mechanisms. Due to the correlation between the electron cyclotron frequency and the radio frequency, it has been postulated for some time that the emissions are due to a cyclotron instability (Twiss 1958, Gaponov 1959a, 1959b, Chu 2004, Sprangle and Drobot 1977, Phelps *et al* 1984) in either the space bound or Earth bound electron streams. (Wu and Lee 1979, Wagner *et al* 1984, Bingham *et al* 2000, 2002, 2004, Vorgul *et al* 2005).

As the equations describing this instability scale with the cyclotron frequency it became clear that the authors could test this concept by creating a laboratory experiment, increasing the magnetic flux density and scaling the resonance into the microwave regime (Speirs *et al* 2005). In parallel with this experimental reproduction of the AKR emission process, 2D PiC simulations were conducted. These simulations predicted the formation of a horseshoe distribution in an electron beam subject to significant magnetic compression and subsequent cyclotron maser emission within an interaction waveguide (McConville *et al* 2008, Speirs *et al* 2008). Although the experimental results were in good agreement with the findings from the

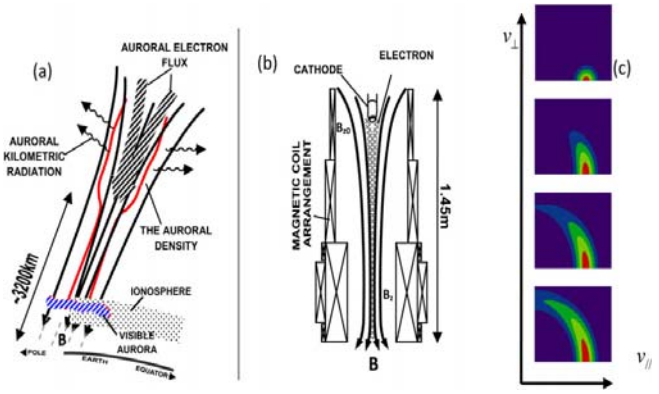

Figure 1. (*a*) Representation of the AKR source region and terrestrial auroral process. (*b*) Schematic of an experiment reproducing the AKR source region; an electron beam can be seen passing through an array of solenoids. (*c*) Formation of the horseshoe distribution, as the electron beam experiences magnetic compression.

2D PiC simulations, certain aspects of the experimental behaviour requires a 3D computational approach for reproduction. Specifically, 2D simulations cannot account for azimuthal structure in the modes supported by the waveguide; experimental effects associated with such modes require 3D simulations. This paper therefore presents new results from simulations conducted in three dimensions. Insight from these enhanced numerical simulations will be used to further optimize the laboratory experiment in the future.

2. Experimental study

The experimental apparatus is schematically illustrated in figure 1(*b*) and the relationships between the electrodes and solenoids (as programmed into the 2D version of the PiC code KARAT (Speirs *et al* 2008)) are illustrated in figure 2(*a*). An electron gun based on an annular velvet electron emitter (Cooke *et al* 1996, Denisov *et al* 1998, Bratman *et al* 2005) injected the particles by explosive electron emission (Ronald *et al* 1998, Ronald *et al* 2008a) into an increasing magnetic field produced by a system of six electromagnets. The magnetic compression forms a horseshoe in the electron beam velocity distribution (McConville *et al* 2008, Ronald *et al* 2008a) which is then brought into cyclotron resonance with near cut-off TE modes of the 8.14 cm diameter interaction waveguide (McConville *et al* 2008). Since in the experiment the magnetic flux density and waveguide are co-axial with each other, the polarization and propagation properties of such TE modes are very similar to those of the X-mode (Ronald *et al* 2008b). Two regimes of resonance were investigated, the first at a moderate value of the magnetic flux density 0.18 T corresponding to 4.42 GHz cyclotron frequency and the second with a magnetic flux density of 0.48 T and 11.7 GHz cyclotron frequency. These frequencies were chosen because they correlate to near cut-off resonance with the $TE_{0,1}$ and $TE_{0,3}$ modes, respectively, which were investigated in the 2D numerical simulations (Speirs *et al* 2008). The microwave output signals were analysed by placing stub receiving antenna in the far field of the experimental output aperture (Ronald *et al* 2008b) and

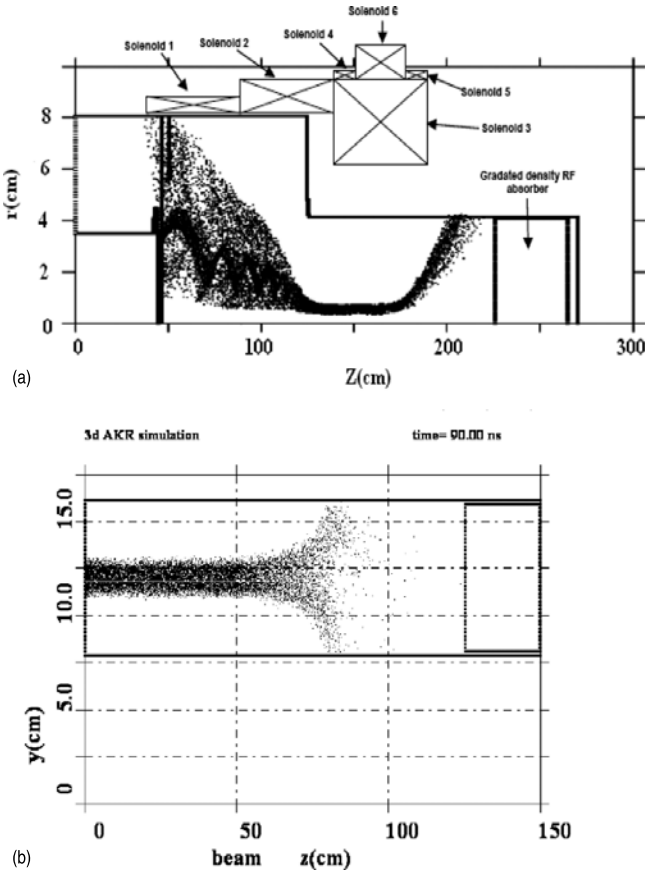

Figure 2. (*a*) Simulation geometry used for 2D calculations illustrating the solenoids and electron gun. (*b*) 3D simulation geometry of waveguide showing trajectories of an electron beam with a predefined horseshoe distribution.

the amplitude and spectral content of the signals captured by these receivers were recorded as they were scanned over the output antenna pattern (Ronald *et al* 2008b).

The high frequency resonance was excited using a beam accelerated over 85 kV gyrating in a magnetic field of 0.48 T. Measurements of the microwave output signal for this resonance condition confirmed that the radiation was at the expected frequency of 11.7 GHz corresponding to the relativistic electron cyclotron frequency, figure 3(*a*) (McConville *et al* 2008). There were also two temporally separated maxima in the output pulse amplitude. Analysis of the antenna patterns illustrated that the experiment was exciting multiple transverse modes of the interaction waveguide and that the dominant mode changed with time through the output pulse.

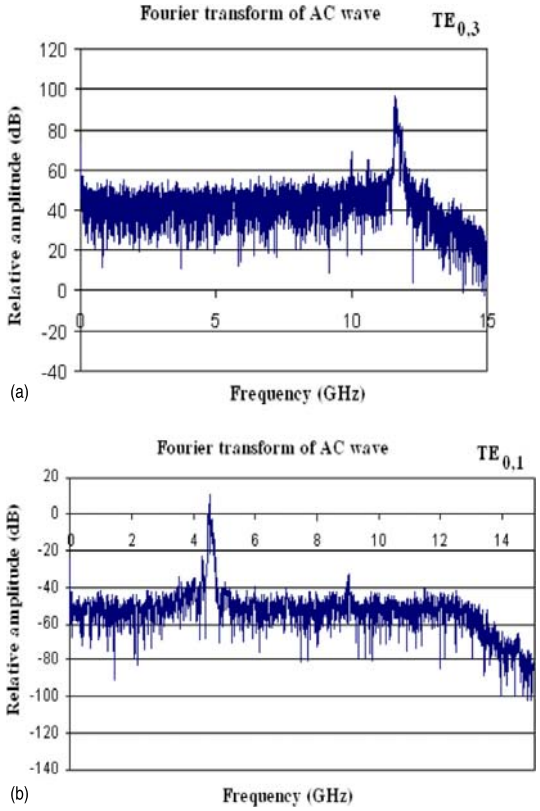

Figure 3. Fourier transforms of output ac waveforms from the experiments. (*a*) Frequency peak at 11.7 GHz for $TE_{0,3}$ resonance. (*b*) Frequency peak at 4.42 GHz for $TE_{0,1}$ resonance.

Specifically, a different mode mixture was generated in each temporal maxima of the output pulse, figures 4(*a*)–(*c*). At 11.7 GHz, the cavity supports many transverse modes of nearly degenerate cut-off frequency that may be excited. Two such modes are the $TE_{0,3}$ and $TE_{2,3}$ modes and evidence for both of these modes was found in the antenna patterns. The maximum output power measured was 30 kW for a cathode magnetic flux density of 0.03 T and a beam current of 37 A, corresponding to a conversion of electron kinetic energy to wave field energy of 1%. For a cathode flux density of 0.013 T the experiment generated 9.4 kW from a 13 A electron beam with beam-wave conversion efficiency of just under 1% whilst a cathode flux density of 0.05 T yielded an output power of 15 kW from a beam of 48 A, with corresponding beam-wave conversion efficiency of 0.4%.

When the experiment was tuned for the lower frequency resonance with a magnetic flux density of 0.18 T, the acceleration voltage was reduced to 75 kV. The resultant radiation

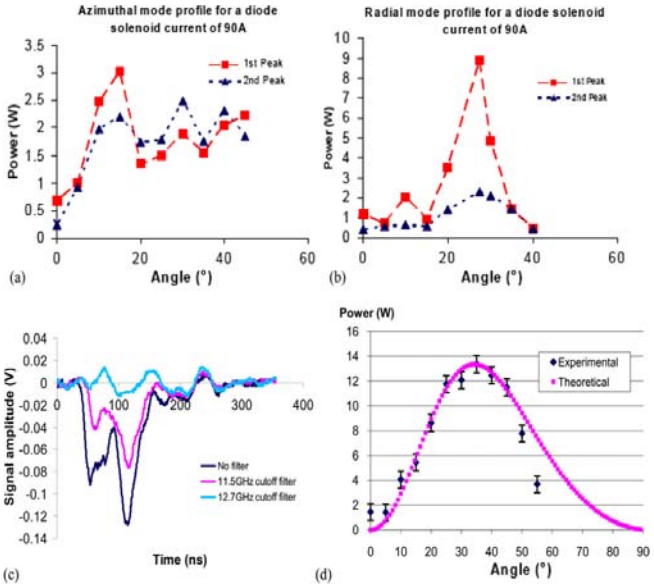

Figure 4. (*a*), (*b*) Radial and azimuthal antenna patterns for the resonance at 0.48 T plateau flux density contained components of the $TE_{0,3}$ and $TE_{2,3}$ modes and displayed temporal mode hopping. (*c*) Illustration of the 2 temporal peaks in the output pulse at 11.7 GHz resonance as a function of cut-off filter frequency. (*d*) Measurement of the antenna pattern at 0.18 T plateau flux density showing the $TE_{0,1}$ mode.

spectrum is presented in figure 3(*b*), where the fundamental resonance is seen at 4.42 GHz, close to the relativistic electron cyclotron frequency and the cut-off of the $TE_{0,1}$ mode in the microwave resonator. A weaker second harmonic signal is also seen close to 8.84 GHz. The radiation pattern for the 0.18 T resonance regime was in excellent agreement with the theoretical expectation for the $TE_{0,1}$ mode at this frequency for an angle of up to 50°, figure 4(*d*). The discrepancy at larger angles is associated with scattering from part of the vacuum apparatus (Ronald *et al* 2008b). The maximum output powers were achieved for cyclotron detuning (the fractional difference by which the waveguide cut-off frequency exceeded the cyclotron frequency (Chu 2004)) of 2–3%. With a magnetic flux density on the cathode of 0.01 T the output power was 19 kW from a beam current of 12 A. Increasing the cathode flux density to 0.02 T increased the beam current to 34 A and the output power to 35 kW corresponding to 2% and 1% conversion efficiencies respectively. This variation in power and efficiency corresponds well to observations of the variation in the electron distribution function (McConville *et al* 2008). With a cathode flux density of 0.05 T the experiment did not generate radiation. Theory predicts that electrons with a limited transverse component of velocity (in this case due to an insufficient magnetic compression ratio) will not contribute to the wave emission and may in fact absorb the RF energy. This effect was also clearly seen in numerical simulations with low magnetic compression ratios.

3. Three dimensional PiC code simulations

The simulations used the PiC code KARAT which is a finite difference time domain code solving Maxwell's equations and the equations of motion on a regular spatial mesh. 2D PiC code simulations with high execution speed and strong numerical stability were in very good agreement with the experimental results. Simulations were conducted for electron beam energies of 75–85 keV, magnetic compression factors of up to 30 and electron cyclotron frequencies of 4.42 GHz and 11.7 GHz. At 11.7 GHz, beam-wave coupling was observed with the $TE_{0,3}$ mode and an RF output power of 20 kW was predicted corresponding to an RF conversion efficiency of 1.3%. At 4.42 GHz, excitation of the $TE_{0,1}$ mode was observed with an RF output power of 35 kW for a cyclotron-wave detuning of 2%. This corresponds to an RF conversion efficiency of 2.6%. The RF conversion efficiencies predicted are therefore comparable to the experiment and to estimates for the AKR generation efficiency (Gurnett 1974, Speirs *et al* 2008). However, 2D simulations can only account for axisymmetric modes, which means that coupling to modes with azimuthal structure cannot be predicted. Therefore, 3D simulations were conducted to provide a more complete representation of the interaction dynamics accounting for modes with azimuthal indices.

The 3D simulation geometry, presented in figure 2(*b*), differs from that of the previous 2D simulations, figure 2(*a*). In the 2D simulation the electron gun, magnetic compression of the electron beam and cyclotron resonant interaction region have all been modelled, whereas in the 3D simulation only an interaction region has been simulated, into which an electron beam with a predefined horseshoe-shaped distribution in electron velocity space was injected. This simplification is due to the severe computational requirements of 3D simulations. Figure 2(*b*) comprises a cross sectional view of the 3D simulation showing electron beam PiC particle trajectories terminating on the waveguide wall at $z = 80$ cm. The corresponding axial magnetic field profile was defined to be uniform from $z = 0$ to 60 cm with a progressive reduction to zero between $z = 60$ and 80 cm. Due to the nature of this PiC code it is not permissible for any geometrical element to contain the z-axis. Hence in figure 2(*b*) the waveguide can be seen to be offset in the 'y' direction. The waveguide diameter and length, electron beam energy and the magnitude of the plateau magnetic field match the experiment. Due to the artificial injection of an electron beam with a predefined velocity distribution the plateau of the magnetic field is longer and flatter.

For an electron cyclotron frequency of 11.7 GHz, the mode structures and spectral content from the 3D simulation show definite coupling with the $TE_{0,3}$ mode and also the $TE_{2,3}$ mode. These predictions are illustrated in figure 5, with the vector diagram of the transverse electric field shown in figure 5(*a*) and the transverse spatial Fourier analysis of the mode content of the radiation in figure 5(*b*). These show the predominant excitation of the $TE_{0,3}$ mode in the resonator but with significant coupling to the nearly degenerate $TE_{2,3}$ mode. Both of these modes were observed in the experimental mode patterns, figures 4(*a*) and (*b*). The output spectrum is dominated by the 11.7 GHz components corresponding to the relativistic electron cyclotron frequency. There was a high frequency pedestal (observed in both the 3D simulations and the experiment) which corresponds to Doppler upshifted resonances associated with the low pitch angle components of the electron beam. The output power predicted by the 3D computations was 15–20 kW for an electron beam current of 16 A corresponding to an RF conversion efficiency of 1.25%. This agrees well with the 2D simulations (Speirs *et al* 2008) and the laboratory experiment (McConville *et al* 2008).

For an electron cyclotron frequency of 4.42 GHz, the mode structure and spectra predicted by the simulations are presented in figure 6. The vector diagram of the transverse electric field is shown in figure 6(*a*) and the transverse spatial Fourier analysis of the radiation mode content

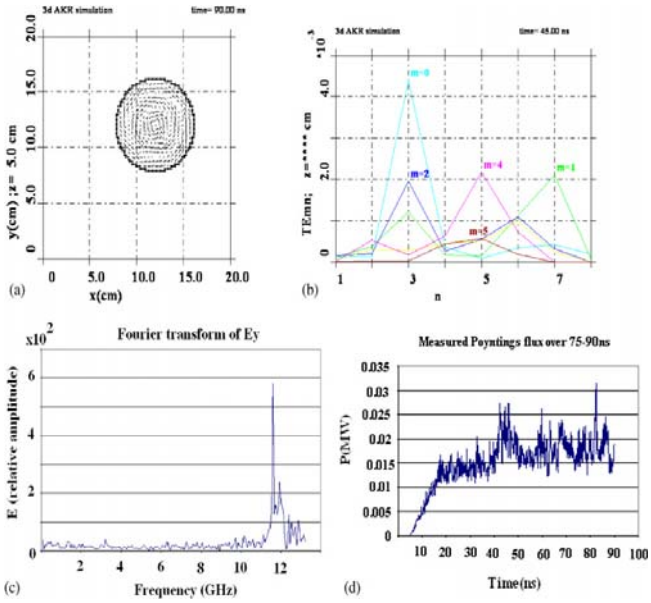

Figure 5. (*a*) Prediction from 3D simulations of the transverse electric field pattern excited by electrons at a cyclotron frequency of 11.7 GHz, clearly showing resonance with the $TE_{0,3}$ mode. (*b*) Transverse mode analysis of the TE mode content of 11.7 GHz radiation showing coupling with the $TE_{0,3}$ and also the $TE_{2,3}$ modes consistent with the experimental measurements. (*c*) Fourier transform showing radiation spectrum at 11.7 GHz. (*d*) Axial Poynting flux of output radiation showing saturation at 40 ns at ∼17 kW.

is represented in figure 6(*b*). These show the predominant excitation of the $TE_{0,1}$ mode but also a small contribution of other weakly coupled modes. Figure 6(*c*) illustrates the predicted spectrum, including a secondary peak corresponding to a second harmonic resonance. Due to the local electric field polarization with respect to the 3D co-ordinate system, the 3D simulations show strong 'apparent' variation in field intensity between the *x* and *y* ordinates. Referring to figure 3(*b*), a small secondary peak can also be seen in the spectral output of the experiment at the same frequency of around 8.84 GHz. This result was not predicted by the 2D simulations. The output power predicted by the 3D computations was ∼10 kW from an electron beam of 11.5 A corresponding to an efficiency of 1.16%. This is in good agreement with experimental results where an RF output power of 19 kW was obtained, corresponding to an RF conversion efficiency of 2%.

4. Summary and conclusions

In summary, 3D PiC code simulations have been conducted to investigate the two cyclotron resonance regimes studied in previous 2D simulations and laboratory experiments investigating the mechanisms of AKR. One regime was optimized for coupling with the

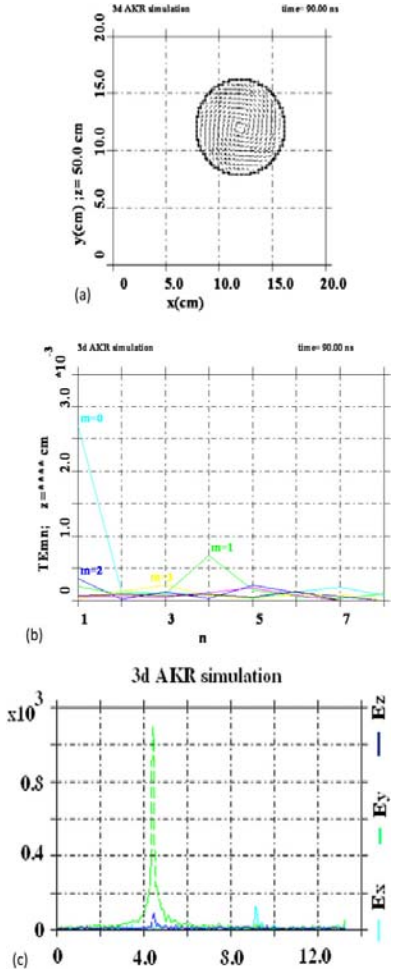

Figure 6. (*a*) KARAT mode profile plot clearly showing $TE_{0,1}$ mode. (*b*) KARAT mode analysis plot of TE mode content excited by 4.42 GHz electrons. Shows a predominantly $TE_{0,1}$ mode with weak $TE_{2,1}$ and $TE_{1,4}$ modes. (*c*) Result from 3D simulation illustrating coupling with $TE_{0,1}$ mode at 4.42 GHz also illustrating resonance with a second harmonic.

$TE_{0,3}$ mode of the interaction waveguide and the other tuned for resonance with the $TE_{0,1}$ mode.

Results obtained from these new simulations were consistent with the previous 2D simulations conducted under the same interaction regimes, although new modes and harmonics

were found, giving a more complete analysis of the interaction dynamics. 3D simulation results for the $TE_{0,3}$ resonance regime were in excellent agreement with the experimental results and identified modes observed in the experimental output not predicted by the 2D simulations.

The fundamental results of the 11.7 GHz simulations were verification of coupling with the $TE_{0,3}$ mode and also the $TE_{2,3}$ mode. The output power predicted by 3D simulations was 15–20 kW for an electron beam current of 16 A corresponding to an RF conversion efficiency of 1.25%. This agrees well with the 2D simulations (Speirs *et al* 2008) and experiment (McConville *et al* 2008).

In the $TE_{0,1}$ resonance regime, the mode analysis plots produced from KARAT show predominantly a $TE_{0,1}$ mode. Fourier transforms of the transverse electric field components show a primary peak at 4.42 GHz, which is clearly due to coupling with the $TE_{0,1}$ mode from analysis of the interaction dispersion characteristics. Second harmonic output was also predicted, in contrast to earlier 2D simulations, but in agreement with results from the laboratory experiment.

3D simulations therefore provide a more complete analysis of the horseshoe driven cyclotron maser instability in the scaled laboratory experiment. The observation of harmonic RF generation and a more complex interaction dynamic is in agreement with experimental results (McConville *et al* 2008). In future work the authors shall make the 3D simulation geometry more accurately represent the experimental electron distribution function and magnetic field configuration. The authors also propose to use a cylindrical rather than Cartesian co-ordinate system for improved conformity with the cavity geometry.

Acknowledgments

This work was supported by the EPSRC and the STFC Centre for Fundamental Physics. Mr I S Dinwoodie and Mr D Barclay are thanked for the construction of the apparatus and Professor V L Tarakanov for his advice on numerical simulations. Helpful discussions with Professor A Savilov are gratefully acknowledged.

References

Benson R F 1985 *J. Geophys. Res.—Space Phys.* **90** 2753–84
Bingham R and Cairns R A 2000 *Phys. Plasmas* **7** 3089–92
Bingham R and Cairns R A 2002 *Phys. Scr.* **T98** 160–2
Bingham R, Kellett B J, Cairns R A, Vorgul I, Phelps A D R, Ronald K and Speirs D 2004 *Contrib. Plasma Phys.* **44** 382–7
Bratman V L, Cross A W, Denisov G G, He W, Phelps A D R, Ronald K and Samsonov S V 2005 *Phys. Scr.* **T116** 23–6
Chu K R 2004 *Rev. Mod. Phys.* **76** 489–540
Cooke S J, Cross A W, He W and Phelps A D R 1996 *Phys. Rev. Lett.* **77** 4836–9
Delory G T, Ergun R E, Carlson C W, Muschietti L, Chaston C C, Peria W, McFadden J P and Strangeway R 1998 *Geophys. Res. Lett.* **25** 2069–72
Denisov G G, Bratman V L, Cross A W, He W, Phelps A D R, Ronald K, Samsonov S V and Whyte C G 1998 *Phys. Rev. Lett.* **81** 5680–3
Ergun R E, Carlson C W, McFadden J P, Delory G T, Strangeway R J and Pritchett P L 2000 *Astrophys. J.* **538** 456–66
Ergun R E *et al* 1998 *Geophys. Res. Lett.* **25** 2061–4
Gaponov A V 1959a *Izv. Vyssh. Uchebn. Zaved. Radiofiz.* **2** 450–62
Gaponov A V 1959b *Izv. Vyssh. Uchebn. Zaved. Radiofiz.* **2** 837
Gurnett D A 1974 *J. Geophys. Res.: Space Phys.* **79** 4227–38
Gurnett D A *et al* 2001 *Ann. Geophys.*
McConville S L *et al* 2008 *Plasma Phys. Control. Fusion* **50** 074010
Melrose D B, Ronnmark K G and Hewitt R G 1982 *J. Geophys. Res.: Space Phys.* **87** 5140–50

Phelps A D R, Garvey T and Hasaani A S 1984 *Int. J. Electron.* **57** 1141–50
Pritchett P L and Strangeway R J 1985 *J. Geophys. Res.: Space Phys.* **90** 9650–62
Ronald K, Cross A W, Phelps A D R, He W, Yin H and Spark S N 1998 *IEEE Trans. Plasma Sci.* **PS-26** 375–82
Ronald K, McConville S L, Speirs D C, Phelps A D R, Robertson C W, Whyte C G, He W, Gillespie K M, Cross A W and Bingham R 2008a *Plasma Sources, Sci. Technol.* **17** 035011
Ronald K, Speirs D C, McConville S L, Phelps A D R, Robertson C W, Whyte C G, He W, Gillespie K M, Cross A W and Bingham R 2008b *Phys. Plamas.* **15** 056503
Roux A, Hilgers A, Deferaudy H, LeQueau D, Louarn P, Perraut S, Bahnsen A, Jespersen M, Ungstrup E and Andre M 1993 *J. Geophys. Res.* **98** 11657–70
Speirs D C, Vorgul I, Ronald K, Bingham R, Cairns R A, Phelps A D R, Kellett B J, Cross A W, Whyte C G and Robertson C 2005 *J. Plasma Phys.* **71** 665–74
Speirs D C *et al* 2008 *Plasma Phys. Control. Fusion* **50** 074011
Sprangle P and Drobot A T 1977 *IEEE Trans. Microw. Theory Tech.* **MTT-25** 528–44
Twiss R Q 1958 *Aust. J. Phys.* **11** 564–79
Vorgul I, Cairns R A and Bingham R 2005 *Phys. Plasmas* **12** 122903
Wagner J S, Lee L C, Wu C S and Tajima T 1984 *Radio Sci.* **19** 509–18
Wu C S and Lee L C 1979 *Astrophys. J.* **230** 621–6

Numerical investigation of auroral cyclotron maser processes[a)]

D. C. Speirs,[1,b)] K. Ronald,[1] S. L. McConville,[1] K. M. Gillespie,[1] A. D. R. Phelps,[1] A. W. Cross,[1] R. Bingham,[1,2] C. W. Robertson,[1] C. G. Whyte,[1] W. He,[1] I. Vorgul,[3] R. A. Cairns,[3] and B. J. Kellett[2]

[1]*Department of Physics, SUPA, University of Strathclyde, Glasgow G4 0NG, Scotland*
[2]*Rutherford Appleton Laboratory, Space Physics Division, STFC, Didcot OX11 0QX, England*
[3]*School of Mathematics and Statistics, University of St. Andrews, St. Andrews KY16 9SS, Scotland*

(Received 20 November 2009; accepted 4 March 2010; published online 4 May 2010; publisher error corrected 11 May 2010)

When a mainly rectilinear electron beam is subject to significant magnetic compression, conservation of magnetic moment results in the formation of a horseshoe shaped velocity distribution. It has been shown that such a distribution is unstable to cyclotron emission and may be responsible for the generation of auroral kilometric radiation—an intense rf emission sourced at high altitudes in the terrestrial auroral magnetosphere. Particle-in-cell code simulations have been undertaken to investigate the dynamics of the cyclotron emission process in the absence of cavity boundaries with particular consideration of the spatial growth rate, spectral output and rf conversion efficiency. Computations reveal that a well-defined cyclotron emission process occurs albeit with a low spatial growth rate compared with waveguide bounded simulations. The rf output is near perpendicular to the electron beam with a slight backward-wave character reflected in the spectral output with a well defined peak at 2.68 GHz, just below the relativistic electron cyclotron frequency. The corresponding rf conversion efficiency of 1.1% is comparable to waveguide bounded simulations and consistent with the predictions of kinetic theory that suggest efficient, spectrally well defined emission can be obtained from an electron horseshoe distribution in the absence of radiation boundaries. © *2010 American Institute of Physics*. [doi:10.1063/1.3371937]

I. INTRODUCTION

When an electron beam that is mainly rectilinear in its propagation is subject to significant magnetic compression, conservation of magnetic moment results in the ultimate formation of a horseshoe shaped velocity distribution. A similar scenario occurs where particles are accelerated into the auroral region of the Earth's magnetic dipole. Such a distribution has been shown to be unstable to an electron cyclotron maser instability.[1,2] and it has been postulated that this may be the mechanism required to explain the production of terrestrial auroral kilometric radiation (AKR) and also radiation from other astrophysical objects such as stars and planets with a suitable magnetic field configuration.[3–5] AKR comprises a spectrum of discrete components of rf emission[6,7] centered around a frequency of ~300 kHz and sourced at high altitudes (~1.5–3 Earth radii) within a region of plasma depletion in the auroral zone known as the auroral density cavity.[8–10] Satellite observations have shown that the emissions are predominantly polarized in the R-X (right-hand-extraordinary) plasma mode[11,12] and that for a given altitude the spectrum of emission extends down to a lower cutoff of approximately the local relativistic electron cyclotron frequency.[13] As AKR cannot be detected from the ground, the earliest documented observations coincide with the launch of the first satellites equipped with suitable wave receiving antenna[14,15] and indeed all data pertaining to the AKR emissions and source region are the result of *in situ* or remote observations made by a large number of satellite missions.

To date, numerous theories have been proposed for the generation mechanism of AKR (Refs. 16–18) and almost all have considered the ~5 keV auroral electron flux as the free energy source. The general consensus at present however is that AKR is generated by an electron cyclotron maser instability, a theory first proposed in 1979 by Wu and Lee.[19] Their particular model comprised a plasma kinetic description of growth in the X mode due to a positive transverse gradient in the electron velocity distribution function ($\partial f_e/\partial v_\perp > 0$) of a mirrored, loss-cone component in the auroral electron flux. This theory was widely accepted for many years[20–22] although the loss cone distribution was seldom observed as a well defined component in particle data from within the auroral density cavity. Instead, a clear representation of a horseshoe distribution in electron momentum was often present in much of the published data[23,24] and was particularly evident in electron velocity distribution plots from the FAST satellite.[25] This led to the publication in 2000 of a new analytical theory by Bingham and Cairns considering X mode dispersion and growth due to a horseshoe-shaped velocity distribution in the precipitating auroral electron flux.[1]

Figure 1 shows a diagrammatic representation of horseshoe distribution formation as a result of magnetic compression and associated evolution in the transverse velocity profile. The phase space is cut off at $v_\parallel = 0$ and does not show the magnetically mirrored component. If one considers the electron velocity distribution in Fig. 1(a) with finite pitch factor

[a)]Paper UI3 6, Bull. Am. Phys. Soc. **54**, 302 (2009).
[b)]Invited speaker. Electronic mail: david.c.speirs@strath.ac.uk.

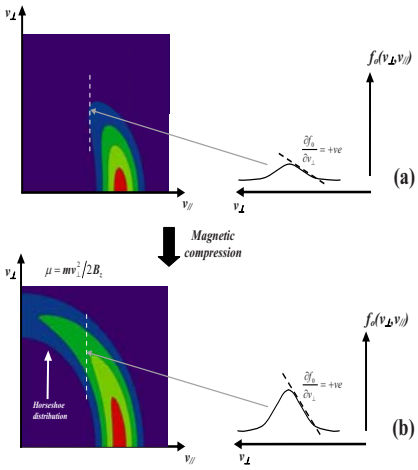

FIG. 1. (Color online) Plots showing the formation and evolution of the horseshoe distribution and associated transverse velocity profile as the magnetic field is increased from [(a)–(b)].

and energy spread impingent on an increasing axial magnetic flux density, conservation of magnetic moment μ results in the conversion of axial velocity into perpendicular velocity. As $v_\perp \propto \sqrt{B_0}$, the resultant expansion in velocity space yields a half-horseshoelike profile [Fig. 1(b)] with an increasing number of electrons present at high pitch factors across a positive gradient in the transverse velocity profile ($\partial f_e/\partial v_\perp > 0$). With reference to the analytical theory,[1] electrons across this positive gradient near the tip of the distribution may undergo resonant energy transfer with an electromagnetic wave and as a result this portion of the distribution will appear to spread in $v_\perp$ and predominantly lose energy.

Previous work at Strathclyde considered the numerical simulation of an experiment scaled to laboratory dimensions and microwave frequencies by increasing the cyclotron frequency $\omega_{ce}=eB/m_o\gamma$ to investigate the electrodynamics of an electron beam subject to significant magnetic compression.[26,27] The resultant beam was brought into resonance with microwave frequency electromagnetic waves in an interaction waveguide. Resonant interaction regimes were investigated with near cutoff TE modes of the waveguide due to the similarities between such modes and the X-mode in relative orientation of electromagnetic field components (i.e., a wave vector and electric field polarization perpendicular to the magnetostatic field).[28] Although the source region for AKR (the auroral density cavity) is typically many hundreds of wavelengths across,[8,23] there is also evidence for smaller scale structures of the order of a few wavelengths across within the larger auroral density cavity.[29,30] These smaller structures have a wavelength scaling close to the laboratory experiment at Strathclyde. The kinetic theory of the instability,[1] however, suggests that a small scale bounding structure (relative to wavelength) is not required for sufficient growth rates and rf conversion efficiencies to account for observed AKR emission intensities. This paper documents the results of numerical simulations conducted to investigate electron cyclotron emission in the absence of radiation boundaries. A comparative analysis is made to waveguide bounded simulations, with consideration of the convective growth rate, output spectra and rf conversion efficiencies.

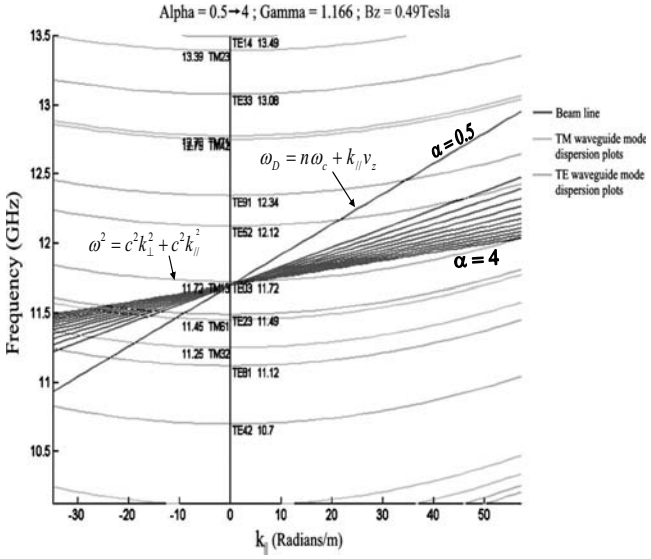

FIG. 2. Beam-wave dispersion plot corresponding to the TE_{03} resonance regime in the bounded simulated geometry.

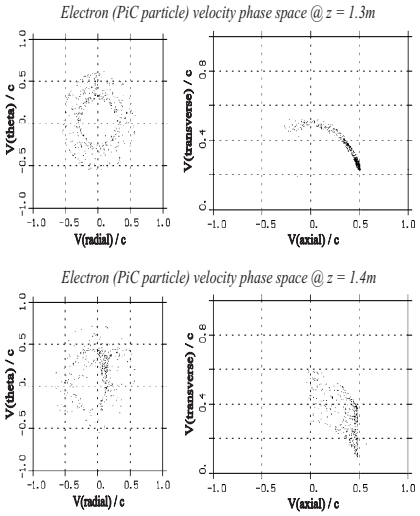

FIG. 3. PiC particle velocity distributions measured on transverse planes within the simulation geometry at (a) z=1.3 m and (b) z=1.4 m for the TE_{03} resonance regime at 50 ns.

II. PIC CODE SIMULATIONS OF WAVEGUIDE BOUNDED CYCLOTRON EMISSION

For the purpose of simulating the horseshoe distribution formation and any subsequent rf interaction, the two-dimensional (2D) axisymmetric version of the finite-difference time domain particle-in-cell (PiC) code KARAT was used.[31,32] The 2D models allowed indirect observation of the distribution of particles in the transverse plane of motion. The code calculates the PiC electrons radial and azimuthal velocities and plots each particle location in transverse velocity space. Particles moving in circular orbits transition from v_θ and v_r to $-v_\theta$ and $-v_r$ periodically. The formation of spatial bunches in a cyclotron instability corresponds to modulation of electron gyrational velocities ($v_\perp$) and in the limit of small modulation can be perceived in the 2D plots of v_θ versus v_r as density variations. This is due to the bunch forming in a specific rotational phase with respect to the local ac field and thus at some instant in time having a "location" in a plot of v_θ versus v_r. In addition, energy modulation can be perceived through changes in the magnitude of $v_\perp=\sqrt{v_\vartheta^2+v_r^2}$, illustrated by the area spanned by PiC particles in plots of v_θ versus v_r.

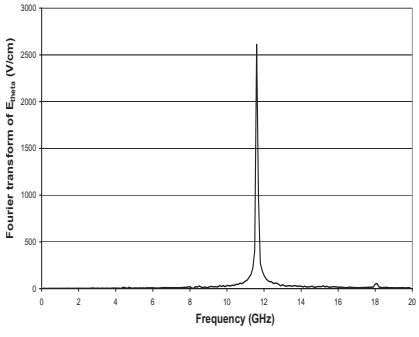

FIG. 4. Fourier transform of E_θ at an axial position of z=1.4 m taken over the period t=45–50 ns.

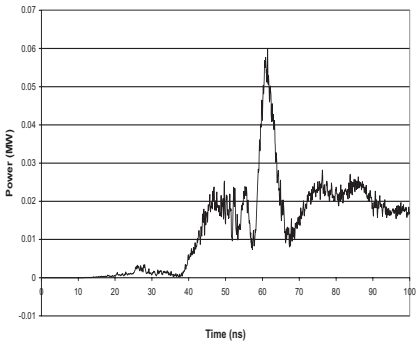

FIG. 5. Axial Poynting flux measured at z=2.2 m across the interaction waveguide.

Two interaction regimes were investigated in the laboratory and simulated using PiC codes.[28,33] The first comprised a peak axial magnetic flux density of 0.49 T for a near cutoff resonance with the TE_{03} mode in the interaction waveguide. The second was optimized for a near cutoff resonance with the TE_{01} mode requiring a peak axial magnetic field of 0.18 T. In both cases the PiC particle velocity distributions and electromagnetic field components were monitored at different axial positions within the simulation geometry. The magnetic field profiles used in both interaction regimes comprised a convergent axial magnetic field from the gun to the interaction waveguide, followed by a peak plateau region tuned for cyclotron resonance with the desired waveguide mode. Magnetic mirror ratios of $B_z/B_{z0}=34$ and $B_z/B_{z0}=18$ were used for the TE_{03} and TE_{01} interaction regimes, respectively.

The simulation parameters used to investigate the TE_{03} resonance regime comprised a peak axial magnetic flux density of 0.49 T, an electron beam energy of 85 keV, a beam current of 18 A and an interaction waveguide radius of 4.14 cm. A PiC particle merging factor of 3×10^6 electrons/PiC particle was also used along with an axial and radial grid resolution of 0.3 and 0.1 cm, respectively. The peak axial magnetic flux density of 0.49 T corresponds to a relativistic electron cyclotron frequency of 11.7 GHz. A beam-wave dispersion plot is presented in Fig. 2 corresponding to the simulation parameters for the TE_{03} resonance regime. Electron cyclotron beam dispersions[34] for various pitch factors from $\alpha=v_\perp/v_z=0.5\rightarrow4$ are plotted along with dispersion curves for all TE and TM modes with cutoff frequencies in the vicinity of 11.7 GHz. A well-defined (narrow band) beam-wave resonance is present at 11.7 GHz with the TE_{03} mode. The resonance is near cutoff of the TE_{03} mode ($k_\parallel\rightarrow0$) and is therefore relatively insensitive to variations in electron beam pitch factor. This maximized the electron population resonant at 11.7 GHz across the pitch spread defining the horseshoe distribution.

TABLE I. Simulation parameters for the unbounded interaction geometry.

Geometrical/simulation parameters	Value or range
Axial length	4 m
Axial mesh spacing	0.25 cm
Radial mesh spacing	0.25 cm
Simulation duration	200 ns
Time step	2.5 ps
Electron beam parameters	**Value or range**
Electron beam limiting current $\mathbf{I_b}$	14 A
Electron beam energy	20 keV
Injected electron beam energy spread	±5%
Injected electron beam pitch factor spread	α=0→9.5
PiC particle merging factor	3×10^6 electrons/PiC particle
Magnetic field parameters	**Value or range**
Static axial magnetic field $\mathbf{B_z}$	0.1 T
Radially bounding dielectric volume	**Value or range**
Radial limits	0.04 m→0.48 m
Axial limits	0 m→4 m
Conductivity	0.2 Siemens/m
Dielectric permittivity $\boldsymbol{\varepsilon}$	1
Magnetic permeability $\boldsymbol{\mu}$	1

PiC particle velocity distributions were plotted at two axial positions (transverse planes) within the interaction waveguide after a 50 ns simulation duration. Each plane is delimited radially by the cross section of the waveguide. The corresponding plots are given in Fig. 3. At the point of entry to the peak, uniform axial magnetic field (z=1.3 m) the $v_\perp$ versus v_z plot shows a well defined pitch spread in the PiC particle distribution with a small mirrored component. The corresponding v_θ versus v_r plot shows uniformity in the relative phase distribution of the PiC particles. Looking at the velocity distributions at z=1.4 m the picture is very different. There is clear evidence of a cyclotron maser instability with significant smearing in the transverse velocity profile of the $v_\perp$ versus v_z plot and indications of orbital phase bunching in the v_θ versus v_r plot across a normalized velocity range of 0→0.5 in v_θ and v_r. There is also evidence of significant energy extraction from the electron PiC particles in the v_θ versus v_r plot from the reduced mean velocity of the electron population.

A Fourier transform of E_θ was conducted over 45–50 ns at z=1.4 m. The resultant plot is given in Fig. 4. The spectrum of emission contains a clearly defined component at 11.7 GHz correlating with the relativistic electron cyclotron frequency and near cutoff resonance with the TE_{03} mode. A minor spectral feature is also present at 18 GHz attributable to a weakly coupled, backward-wave second harmonic resonance with a higher order mode.

The axial Poynting flux was monitored at z=2.2 m, beyond the axial range of electron beam propagation and corresponding to the output of the interaction waveguide. Figure 5 shows the corresponding temporal variation in axial Poynting flux at z=2.2 m for a 100 ns simulation duration. There is significant initial growth in rf output between 40 and 48 ns followed by a saturated output power of ~20 kW. At 60 ns there is an anomalous spike in output power of ~60 kW, however from 70 ns onwards the rf output appears to stabilize to a mean value of ~20 kW. This corresponds to a beam-wave conversion efficiency of 1.3% which is consistent with estimates for the AKR generation efficiency.[35,36]

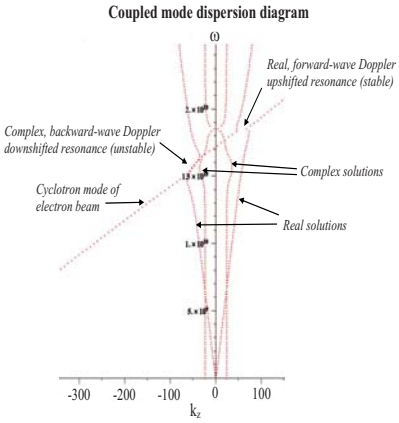

FIG. 6. (Color online) Real and complex roots of k_z for a beam energy of 20 keV, current density of 1.49 A cm^{-2} and axial magnetic field of 0.1 T.

III. PIC CODE SIMULATIONS OF UNBOUNDED CYCLOTRON EMISSION

Prior to a numerical investigation of unbounded electron-cyclotron emission, an analysis was conducted of the coupled mode dispersion characteristics via solution for the real and complex roots of the wave vector as a function of frequency corresponding to the PiC simulation parameters presented in Table I. The resultant plot is given in Fig. 6 for an electron pitch factor $\alpha=v_\perp/v_z=3$. Both forward and

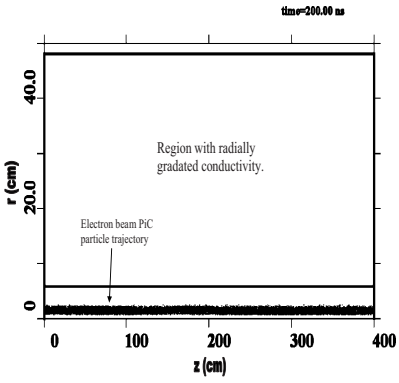

FIG. 7. Geometry of 2D KARAT model with gradated density dielectric volume radially bounding the interaction region.

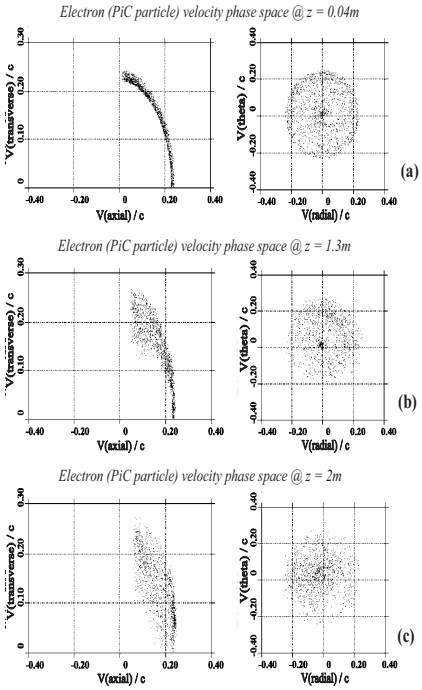

FIG. 8. PiC particle velocity distributions measured on transverse planes within the unbounded simulation geometry at (a) z=0.06 m (b) z=1.3 m and (c) z=2 m.

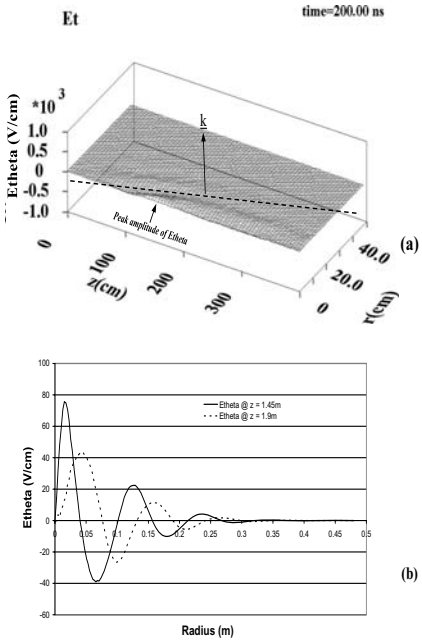

FIG. 9. (a) 3D contour plot of E_{theta} within the unbounded simulation geometry. (b) Plot showing the decay of E_{theta} with radial coordinate at z=1.45 m and z=1.9 m, respectively.

backward wave resonances are evident here with the point of axis crossing representing the relativistic electron cyclotron frequency of 2.71 GHz (here given in angular frequency). The backward wave resonance has complex roots in k_z and the potential for cyclotron resonant energy transfer at the Doppler downshifted frequency of 2.68 GHz, while the forward wave resonance at a Doppler upshifted frequency of 2.8 GHz has purely real solutions and is inherently stable.

Figure 7 shows a geometrical overview with electron beam trajectory of the unbounded cyclotron emission model defined using the PiC code KARAT. For the purpose of simulating the unbounded interaction geometry, a region with radially increasing conductivity was defined around the beam propagation path. This represented an idealized absorber of electromagnetic radiation, inhibiting reflection and the formation of boundary resonant eigenmodes. As confirmation, the radial depth of the absorber was varied between 24 and 54 cm, with no measurable effect on the simulation output. Other parameters of the simulation are provided in Table I. In contrast to the experimentally consistent bounded simulation presented in Sec. II, the electron beam was injected into the unbounded simulation geometry with a predefined horseshoe distribution, comprising a pitch spread α of $0 \rightarrow 9.5$, beam energy of 20 keV $\pm$ 5% and beam current of 14 A. The reduction in beam energy relative to the bounded case and introduction of a finite energy spread provided for a better comparison to the astrophysical data, where the precipitating auroral electron flux energies are typically 10–20 keV peak.[9]

A uniform axial magnetic field was also used in the unbounded simulations as no magnetic compression was necessary.

PiC particle velocity distributions were plotted after a 200 ns run time at three axial positions within the simulation geometry. The corresponding data is presented in Fig. 8. The injected beam distribution at z=0.04 m shows a well defined pitch spread in the $v_\perp$ versus v_z plot covering the complete pitch range from an axial electron beam to the point of magnetic mirroring (zero axial velocity). The corresponding v_θ versus v_r plot also shows a uniform spread in relative orbital phase with no evidence of coherent bunching effects. At z=1.3 m the picture is very different however, with clear evidence of azimuthal bunching in the v_θ versus v_r plot and in the corresponding $v_\perp$ versus v_z plot there is spreading in the transverse velocity profile for high pitch factor electrons. Considering the ~1.3 m displacement from the point of beam injection however, the spatial growth rate is clearly lower than in the bounded case of Fig. 3, where a more pronounced spreading in the velocity distribution is evident only 0.1 m from injection into the interaction waveguide. Finally, at an axial position of z=2 m the velocity distributions are representative of a saturated state, with smearing in the transverse velocity profile across the entire pitch range of the $v_\perp$ versus v_z plot and evidence of phase trapping with a concentration of PiC particles extending to the origin of the corresponding v_θ versus v_r plot.

Figure 9(a) contains a three-dimensional (3D) contour plot of E_{theta} mapped over the simulation geometry after a 200 ns run time. An electromagnetic wave sourced at

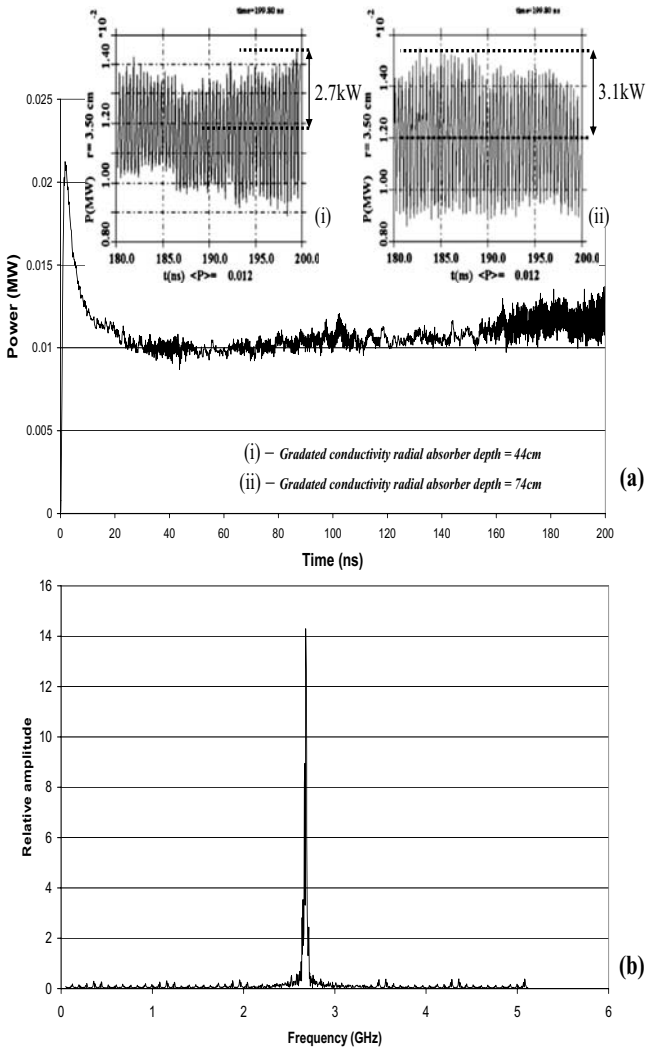

FIG. 10. (a) Temporal evolution of the radial Poynting flux measured in a plane at r=3.5 cm spanning the length of the unbounded simulation. (b) Fourier transform of E_{theta} from t=0→200 ns at z=1.9 m.

z~1.45 m is evident propagating near perpendicular to the electron beam with a mild backward wave character. A dashed line has been superimposed parallel to the primary wavefront with an arrow indicating the corresponding orientation of the wave vector. The axial coordinate range over which the wave is generated corresponds to the position at which a saturated PiC particle velocity distribution is evident in Fig. 8 and further illustrates the significantly increased beam path (number of Larmor steps) required for efficient cyclotron-wave coupling compared to the bounded case[28,33] presented in Sec. II. Looking at Fig. 9(b), the decay in amplitude of the wave with radial coordinate is apparent at two axial positions within the region of peak emission. In both cases the wave has decayed completely upon reaching the edge of the radial absorber and a phase mismatch is present in the radial profile between the two axial coordinates, consistent with the backward-wave propagation vector.

Figure 10(a) contains a plot of the radial Poynting flux measured in a plane at r=3.5 cm, over the entire length of the simulation geometry. In contrast to the waveguide bounded simulation presented in Sec. II, where the axial Poynting flux measurement plane was defined after the point of beam termination (Fig. 5), the radial Poynting flux measurement in the unbounded simulation was made over a radial plane parallel to the path of beam propagation. A dc offset is therefore present in the measurement due to low frequency electromagnetic field components associated with the electron beam propagation. The rf output power may therefore be obtained from the amplitude of the ac signal superimposed on this dc offset. Two panes are overlaid on

Fig. 10(a) showing the magnified ac amplitude measurement for two contrasting radial depths of gradated conductivity absorber bounding the simulation. Case (i) is a magnified trace of the main plot in Fig. 10(a) over 180–200 ns. This corresponds to the standard radial absorber depth used of 44 cm as shown in Fig. 7 and pertains to all data presented in Figs. 8 and 9. Case (i) shows a peak rf output power of 2.7 kW after 180 ns, while case (ii) corresponding to a greatly increased radial absorber depth of 74 cm shows a marginally higher saturated output power of 3.1 kW. This serves as confirmation that further increases in absorber depth do not broadly affect the rf output characteristics and in both cases, the ~3 kW output power corresponds to an rf conversion efficiency of 1.1%. This is comparable to the 1.3% efficiency obtained from the waveguide bounded simulation presented in Sec. II and consistent with the generally accepted estimate of ~1% for the AKR generation efficiency.[35,36] The corresponding output spectra does not vary with increased radial absorber depth and is presented in Fig. 10(b), showing a well defined spectral component at 2.68 GHz. This represents a 1.1% downshift from the relativistic electron cyclotron frequency of 2.71 GHz, consistent with the mild backward wave character observed in the emissions.

IV. SUMMARY AND CONCLUSIONS

In summary, PiC code simulations have been conducted to investigate the stability of an electron horseshoe distribution to cyclotron maser emission in the absence of reflective boundaries or cavity effects. A comparative analysis was conducted between these simulations and a waveguide bounded PiC code model, where cyclotron-resonant coupling was investigated between a horseshoe distribution and TE_{0n} waveguide mode.[28,33] The waveguide bounded simulation was optimized for coupling with the TE_{03} mode of an interaction waveguide with an axial magnetic field of 0.48 T and beam energy of 85 keV. The unbounded simulation had a lower beam energy of 20 keV and an axial magnetic field of 0.1 T. In both cases the evolution of PiC particle velocity distributions with axial position was monitored and the field structure analyzed within the simulation geometry.

For the waveguide bounded TE_{03} resonance regime, pitch expansion of the electron beam was clearly evident in the PiC particle velocity distributions followed by a subsequent spreading in $v_\perp$ as a result of energy transfer with the electromagnetic wave. After a 50 ns run a Fourier transform of E_θ shows the presence of a well-defined spectral component at 11.7 GHz correlating with the cutoff frequency of the TE_{03} mode and the relativistic electron cyclotron frequency of the electron beam. The temporal variation in axial Poynting flux shows a saturated rf output power of 20 kW after 80 ns. This corresponds to an rf conversion efficiency of 1.3% and is relatively consistent with estimates for the AKR generation efficiency.[35,36]

In the unbounded simulation presented in Sec. III, an electron beam with predefined horseshoe distribution was injected into a region of uniform axial magnetic field bounded by a gradated density dielectric absorber. PiC particle velocity distributions show the clear action of a cyclotron maser instability after a significantly greater number of Larmor steps than in the waveguide bounded case of Sec. II. Evidence of both phase trapping and spreading in $v_\perp$ is apparent at an axial displacement of 2 m from the point of beam injection, with the corresponding E_θ contour plot over the simulated region showing near perpendicular wave emission over $z=1.5\rightarrow2$ m with a slight backward wave character. An analysis of the spectral output reveals a singular, well defined peak at 2.68 GHz corresponding to a 1.1% downshift from the relativistic electron cyclotron frequency and consistent with a backward wave resonance. Some theoretical studies have predicted backward wave coupling for astrophysical cyclotron radiation.[37] The temporal variation in radial Poynting flux measured over the length of the simulation reveals a saturated output power of ~3 kW after 180 ns, corresponding to an rf conversion efficiency of 1.1%. This is comparable to the waveguide bounded case and supports the predictions of kinetic theory that efficient, spectrally well defined electromagnetic emission can be obtained from an electron horseshoe distribution in the absence of resonant cavity boundaries.[1] In addition, the rf conversion efficiency obtained is in agreement with estimates for the AKR generation efficiency.[35,36]

ACKNOWLEDGMENTS

The EPSRC (Grant No. EP/GO4239X/1) and the STFC Centre for Fundamental Physics supported this work. Professor V. L. Tarakanov is thanked for his assistance with the numerical models. Helpful conversations with Professor A. Savilov are also gratefully acknowledged.

[1] R. Bingham and R. A. Cairns, Phys. Plasmas **7**, 3089 (2000).
[2] I. Vorgul, R. A. Cairns, and R. Bingham, Phys. Plasmas **12**, 122903 (2005).
[3] R. Bingham, R. A. Cairns, and B. J. Kellett, Astron. Astrophys. **370**, 1000 (2001).
[4] P. Zarka, R. A. Treumann, B. P. Ryabov, and V. B. Ryabov, Astrophys. Space Sci. **277**, 293 (2001).
[5] A. J. Willes and K. Wu, Mon. Not. R. Astron. Soc. **348**, 285 (2004).
[6] D. A. Gurnett, R. R. Anderson, F. L. Scarf, R. W. Fredricks, and E. J. Smith, Space Sci. Rev. **23**, 103 (1979).
[7] J. D. Menietti, A. M. Persoon, J. S. Pickett, and D. A. Gurnett, J. Geophys. Res., [Space Phys.] **105**, 18857, doi:10.1029/1999JA000389 (2000).
[8] W. Calvert, Geophys. Res. Lett. **8**, 919, doi:10.1029/GL008i008p00919 (1981).
[9] R. J. Strangeway, L. Kepko, R. C. Elphic, C. W. Carlson, R. E. Ergun, J. P. McFadden, W. J. Peria, G. T. Delory, C. C. Chaston, M. Temerin, C. A. Cattell, E. Moebius, L. M. Kistler, D. M. Klumpar, W. K. Peterson, E. G. Shelley, and R. F. Pfaff, Geophys. Res. Lett. **25**, 2065, doi:10.1029/98GL00664 (1998).
[10] T. M. Burinskaya and J. L. Rauch, Plasma Phys. Rep. **33**, 28 (2007).
[11] R. F. Benson, J. Geophys. Res., [Space Phys.] **90**, 2753, doi:10.1029/JA090iA03p02753 (1985).
[12] J. Hanasz, M. Panchenko, H. de Feraudy, R. Schreiber, and M. M. Mogilevsky, J. Geophys. Res., [Space Phys.] **108**, 1408, doi:10.1029/2002JA009579 (2003).
[13] P. L. Pritchett, R. J. Strangeway, R. E. Ergun, and C. W. Carlson, J. Geophys. Res., [Space Phys.] **107**, 1437, doi:10.1029/2002JA009403 (2002).
[14] E. A. Benediktov, G. G. Getmantsev, Y. A. Sazonoy, and A. F. Tarasav, Kosm. Issled. **3**, 614 (1965).
[15] N. Dunckel, B. Ficklin, L. Borden, and R. A. Helliwell, J. Geophys. Res. **75**, 1854, doi:10.1029/JA075i010p01854 (1970).
[16] A. Roux and R. Pellat, J. Geophys. Res., [Space Phys.] **84**, 5189,

doi:10.1029/JA084iA09p05189 (1979).
[17]D. B. Melrose, K. G. Ronnmark, and R. G. Hewitt, J. Geophys. Res., [Space Phys.] **87**, 5140, doi:10.1029/JA087iA07p05140 (1982).
[18]D. Le Quéau, R. Pellat, and A. Roux, J. Geophys. Res., [Space Phys.] **89**, 2831, doi:10.1029/JA089iA05p02831 (1984).
[19]C. S. Wu and L. C. Lee, Astrophys. J. **230**, 621 (1979).
[20]P. L. Pritchett, Phys. Fluids **27**, 2393 (1984).
[21]J. S. Wagner, L. C. Lee, C. S. Wu, and T. Tajima, Radio Sci. **19**, 509, doi:10.1029/RS019i002p00509 (1984).
[22]W. Calvert, J. Geophys. Res., [Space Phys.] **100**, 14887, doi:10.1029/95JA00523 (1995).
[23]R. E. Ergun, C. W. Carlson, J. P. McFadden, G. T. Delory, R. J. Strangeway, and P. L. Pritchett, Astrophys. J. **538**, 456 (2000).
[24]E. Ungstrup, A. Bahnsen, H. K. Wong, M. Andre, and L. Matson, J. Geophys. Res., [Space Phys.] **95**, 5973, doi:10.1029/JA095iA05p05973 (1990).
[25]G. T. Delory, R. E. Ergun, C. W. Carlson, L. Muschietti, C. C. Chaston, W. Peria, J. P. McFadden, and R. Strangeway, Geophys. Res. Lett. **25**, 2069, doi:10.1029/98GL00705 (1998).
[26]K. M. Gillespie, D. C. Speirs, K. Ronald, S. L. McConville, A. D. R. Phelps, R. Bingham, A. W. Cross, C. W. Robertson, C. G. Whyte, W. He, I. Vorgul, R. A. Cairns, and B. J. Kellett, Plasma Phys. Controlled Fusion **50**, 124038 (2008).
[27]K. Ronald, D. C. Speirs, S. L. McConville, A. D. R. Phelps, C. W. Robertson, C. G. Whyte, W. He, K. M. Gillespie, A. W. Cross, and R. Bingham, Phys. Plasmas **15**, 056503 (2008).
[28]S. L. McConville, D. C. Speirs, K. Ronald, A. D. R. Phelps, A. W. Cross, R. Bingham, C. W. Robertson, C. G. Whyte, W. He, K. M. Gillespie, I. Vorgul, R. A. Cairns, and B. J. Kellett, Plasma Phys. Controlled Fusion **50**, 074010 (2008).
[29]P. Louarn and D. Le Queau, Planet. Space Sci. **44**, 199 (1996a).
[30]P. Louarn and D. Le Queau, Planet. Space Sci. **44**, 211 (1996b).
[31]V. P. Tarakanov, *KARAT Code User Manual* (Berkeley Research Associates, Inc., Berkeley, 1997).
[32]D. C. Speirs, A. D. R. Phelps, I. V. Konoplev, A. W. Cross, and W. He, Rev. Sci. Instrum. **75**, 826 (2004).
[33]D. C. Speirs, S. L. McConville, K. M. Gillespie, K. Ronald, A. D. R. Phelps, A. W. Cross, R. Bingham, C. W. Robertson, C. G. Whyte, I. Vorgul, R. A. Cairns, and B. J. Kellett, Plasma Phys. Controlled Fusion **50**, 074011 (2008).
[34]K. R. Chu, Rev. Mod. Phys. **76**, 489 (2004).
[35]P. L. Pritchett and R. J. Strangeway, J. Geophys. Res., [Space Phys.] **90**, 9650, doi:10.1029/JA090iA10p09650 (1985).
[36]D. A. Gurnett, J. Geophys. Res., [Space Phys.] **79**, 4227, doi:10.1029/JA079i028p04227 (1974).
[37]A. V. Savilov, P. A. Bespalov, K. Ronald, and A. D. R. Phelps, Phys. Plasmas **14**, 113104 (2007).